

Université du Québec
Institut National de la Recherche Scientifique
Centre Énergie, Matériaux et Télécommunications

DESIGN OF PHAGE-TEMPLATED GOLD ASSEMBLIES AS CONTRAST AGENT

By
Esen SOKULLU, M.Sc.

A thesis submitted for the achievement of the
degree of *Philosophiae doctor* (Ph.D.) in Energy and Materials Science

Jury Members

President of the jury and
Internal Examiner : Prof. Dongling Ma (INRS-EMT)
External Examiner : Prof. Amy S. Blum (McGill University)
External Examiner : Prof. Alexis Vallée-Bélisle (University of Montreal)
Director of Research : Prof. Tsuneyuki Ozaki (INRS-EMT)
Co-director of Research : Prof. Marc A. Gauthier (INRS-EMT)

ACKNOWLEDGEMENTS

I would like to thank Prof. Tsuneyuki Ozaki for giving me the opportunity to pursue my PhD study in my field of interest. It made me learn a lot and become more critical in decision-making steps. I am very grateful to my co-supervisor Prof. Marc A. Gauthier for all his support, help, and especially for being very patient and kind during this study. I learned a lot from our scientific discussions.

I would like to acknowledge Prof. Andreas Ruediger, who enabled the SERS application of this work and his group who trained me on performing the experiments and data analysis, namely Dr. Gitanjali Kolhatkar, Dr. Julien Plathier and Jiawei Zhang. I appreciate all their help not only in training, but also for fruitful discussions on scientific aspects of the work.

I would also like to acknowledge Prof. François Légaré who enabled the 2PEF microscopy measurements and his group for helping me to perform the experiments, namely Philippe Lassonde, Maxime Pinsard, and Nedgine Laurenceau. Thanks to Ali Özgür Argunsah for helping in processing of 2PEF images. I am also grateful to Prof. Fiorenzo Vetrone for helping me to perform 2PEF measurements to gain more insight about my work and of course, thanks to Artiom Skripka who kindly helped me for measurements.

I would like to thank Prof. Lindsay Black for providing me the materials to design T4 template materials.

I want to thank Dr. Xavier Ropagnol and Aziz Berchtikou for their help in this study. It was a huge amount of work and I appreciate all their efforts.

It was a big pleasure to work with nice colleagues who accompanied me at INRS, namely Ahlem Zaghmi, Sharifun Nahar, Fatemeh Zare, Ahlem Meziadi, Andrea Greschner, Tom Congdon, Anees Palapuravan, Xu Geng, Hoda Suleymani Abyaneh, Fabian Ambriz-Vargas. I am very thankful for their support and help.

Research is always challenging and I also had several obstacles during my study. However, I was very lucky to have nice people around me who always provided their endless support. Special thanks to Maria João Paolo, Bruno Guerreiro, Denis Ferachou, Cybelle Soares, Matteo Duca, Gaëtan Buvat, Teresa Simão, Juliana Barranco, Shadi Rohani, Marta Quintanilla, Antonio Benayas, Eva Hemmer, Erwan Bertin... They have been more than colleagues for me.

I would like to thank to the administrative and technical staff at INRS-EMT. They were very kind and helpful, particularly H  l  ne Tanguay, Nathalie Graveline, Louise Hudon, Nathalie M  tras, H  l  ne Sabourin, and Georges Lamoureux.

Finally, I would like to thank to my family in Turkey, my parents, my sister, my brother and my lovely nephew for all their support, love and encouragement during this study.

ABSTRACT

“Plasmonics”, the study of the interaction between an electromagnetic field and free electrons in a metal, is a growing field due to the recent developments in nanotechnology and nanofabrication that enable the design of new materials with properties suitable for locally concentrating light. One strategy to concentrate light is to create small gaps between metallic nanoparticles by organizing them into assemblies that display new, collective properties. The resulting enhancement of optical properties is mainly due to the coupling of the localized electric fields of the assembled nanoparticles, which is a phenomenon that depends on the inter-particle distance. Amongst the different metallic nanoparticles that have been explored for the production of plasmonic nanostructures, gold nanoparticles (AuNPs) have been the most popular owing to their general chemical inertness, biocompatibility, ease of synthesis, and simple surface modification. Given these important features, ‘isolated’ AuNPs have been investigated for several applications, including imaging biomaterials, via their ability to generate contrast for surface-enhanced and non-linear spectroscopies. Moving forward, the generation of assemblies of gold nanostructures could yield greater contrast than their isolated nanoparticle building blocks, because of the coupling of their plasmonic properties. As a consequence, this could enable the use of smaller AuNPs that do not intrinsically exhibit plasmonic features. As such, it is exciting and timely to investigate new plasmonic structures that exploit the collective properties of ensembles of AuNPs. Generally, plasmonic nanostructures are fabricated by ‘top-down’ techniques such as electron beam lithography, focused beam lithography, and nanoimprint lithography, which are limited by high cost, low-speed, and limited ability to generate three-dimensional structures. On the other hand, the self-assembly of AuNPs onto a template material is emerging as an alternative ‘bottom-up’ approach for producing colloidal plasmonic structures that could potentially have the ability to label biological structures. In this context, the use of very small AuNPs could be particularly advantageous because of their lesser expected detrimental effect on binding target biological molecules/structures, and better image resolution (i.e., smaller contrast agents). For the ‘bottom-up’ approach, nanoparticles are immobilized onto pre-determined binding sites on a template material. Viruses are one of the most studied biological template materials because of their great structural diversity and the ability to precisely position binding motifs in a controlled manner on their surface by genetic manipulation. Moreover, viruses naturally target and bind to cells, which make them suitable for producing colloidal contrast agents for specific types of cell. Notwithstanding, developing procedures for producing virus–AuNP assemblies can be technically complex (depends on AuNP size), and little information is available on the plasmonic properties of such assemblies prepared with very small AuNPs.

In the present work, two bacteriophage templates (virus that selectively infect bacteria), M13 and T4, were examined as biological templates to create well-defined assemblies of AuNPs. These phage were selected because of their considerably different geometries (filamentous vs icosahedral for M13 and T4, respectively), which will allow us to investigate both the effect of short-range and longer-range ordering of the AuNPs on plasmonic properties. Because of the paucity of data on the assembly of very small (<13 nm) AuNPs on bacteriophage, several gold-binding motifs were explored and, for T4, the relative disposition of these motifs on the phage surface was also varied. In Chapters 2 and 3, the genetic engineering of the phage is presented, and protocols for the assembly of 3, 9, and 13-nm AuNPs were established. The resulting assemblies were characterized by several complementary analytical techniques. Furthermore, the ability of the assemblies to bind to bacteria, despite the presence of AuNPs covering the surface of the phage, was verified. This finding supports the investigation of very small AuNPs in this work, because target binding is an important property for developing imaging contrast agents. In Chapters 4 and 5, the plasmonic properties of the phage–AuNP assemblies were examined by surface-enhanced Raman scattering (SERS) and two-photon excitation fluorescence (2PEF) microscopy. These Chapters evaluate the

influence of the structural parameters of the assemblies on their stability (i.e., suitability to typical sample handling procedures such as drop casting and drying on microscope slides), their ability to enhance SERS and 2PEF, and the influence of binding to bacteria on the observed SERS/2PEF signals. For SERS, only the assemblies prepared with 13 nm AuNPs were able to generate strong local electric field enhancements yielding signals which were clearly distinguishable from the background. The recorded SERS spectra corresponded to peaks associated with the stabilizing ligand on the surface of AuNPs, which was used as SERS reporter, indicating that signal enhancement originated from within the gaps formed between adjacent AuNPs. Binding of the assemblies to bacteria did not significantly affect the SERS spectrum or signal enhancement. Higher SERS enhancement was observed for M13-templated assemblies compared to T4-templated assemblies, and the ensemble of data suggests that short-range ordering is the dominant factor affecting enhancement. It was further demonstrated that covalent attachment of AuNPs to phage via a gold–thiolate bond was indispensable for stability of the assemblies, given that assemblies designed with non-covalent gold-binding motifs disassembled during sample handling, resulting in little or no SERS enhancement compared to AuNPs alone. For 2PEF, several of the phage–AuNP assemblies demonstrated signal enhancement. However, in contrast to SERS, the absolute intensity of 2PEF signals obtained for the clusters was closer to that of the background noise. Therefore, an image processing techniques was employed to objectively discriminate 2PEF signals from background, which enabled straightforward quantitative analysis. Reproducible 2PEF signal enhancement was observed for M13-templated assemblies prepared with 9 and 13 nm AuNPs, but not with 3 nm. Only a small effect of AuNP size was observed between the 9 and 13 nm AuNPs. In contrast, assemblies prepared with T4 typically did not exhibit 2PEF and signals and were only rarely distinguishable from the background. Only one T4-templated assembly, prepared with 13 nm AuNPs, produced reliable 2PEF signal, and the magnitude of the intensity was comparable in magnitude albeit slightly lower than that observed for equivalent assemblies prepared with M13. This difference could be explained with different spatial geometries of AuNP assemblies templated on M13 and T4 phages and their corresponding stabilities. It should be noted that isolated AuNPs (3–13 nm) never enhanced SERS or 2PEF in any of the experiment conducted. Indeed, these AuNPs are much smaller than those typically examined for their ability to enhance SERS/2PEF.

Overall, this thesis presents the design, production, and characterization of new colloidal plasmonic structures combining AuNPs and bacteriophage. It should be emphasized that this work explores very small AuNPs, for which a great paucity of data exists in the literature, both in terms of chemistry (i.e., conditions for assembly onto biological templates) and plasmonic properties. Drop casting and drying these assemblies, followed by their analysis by SERS and 2PEF provided essential information on how the design of the assemblies affected their performance as targeted imaging contrast agents, in terms of signal enhancement, stability, and effect of binding to cells. Screening a wide range of design parameters susceptible to influence these properties above has led to the identification of phage–AuNP assemblies that are suitable for use as biological contrast agents for SERS and 2PEF, and the relevant opportunities and limitations are discussed in each appropriate chapter. This body of work sets the stage for future experiments, which can now be performed because of the refinement achieved from within the large library of phage–AuNP assemblies above. For instance, analysis of the plasmonic properties of the assemblies in solution, while technically challenging, should provide additional data on some of the less-stable or meta-stable assemblies, which did not survive sample handling. This could enable a comparison of optical properties with, for instance, plasmonic characteristics determined by simulation. Furthermore, an additional level of matrix complexity can now be examined, such as the use of the assemblies as contrast agents within complex aqueous matrices (e.g., bacteria detection in wastewater) or for mixtures of cell populations. Indeed, the ability of the assemblies to be re-engineered to bind to different targets (beyond their native bacterial targets), may make them suitable for several imaging- and detection-related applications.

RÉSUMÉ

INTRODUCTION

Les récents progrès en nanotechnologie, en particulier dans les méthodes de nanofabrication, ont permis la conception de nouveaux matériaux aux propriétés améliorées. L'un des domaines ayant connu un développement surprenant est la plasmonique qui s'intéresse à l'étude des interactions métal-lumière et qui avait attiré une grande attention en raison de ses potentielles applications technologiques, allant de l'énergie à la médecine [1]. Les interactions métal-lumière découlent de la capacité du champ électromagnétique à induire des oscillations cohérentes des électrons libres sur les surfaces métalliques. Bien que le champ électromagnétique puisse être propagé par l'oscillation d'électrons sur une large gamme de fréquences, une forte résonance est observée à une fréquence spécifique, appelée résonance plasmonique de surface (SPR) [2]. À cette fréquence SPR, le couplage de la lumière incidente aux électrons du métal entraîne une forte amplification du champ électrique local à la surface des nanoparticules ainsi qu'une absorption et une diffusion accrues de la lumière par les nanoparticules [3].

Les propriétés optiques améliorées par SPR ont permis l'utilisation de nanostructures métalliques dans différentes applications. Par exemple, les propriétés améliorées d'absorption et de diffusion ont fait des métaux des marqueurs optiques alternatifs pour des applications telles que la détection et l'imagerie [4, 5]. Contrairement aux fluorophores, qui constituent un autre groupe de marqueurs optiques, les nanoparticules métalliques ne photoblanchissent pas, devenant ainsi des alternatives intenses et stables [6]. De plus, en convertissant l'énergie de la lumière en énergie thermique, les nanoparticules de métal peuvent générer de la chaleur pour détruire, par exemple, des cellules cancéreuses pour d'éventuelles interventions thérapeutiques en médecine [7]. D'un autre côté, l'amélioration du champ électrique local ouvre d'autres possibilités pour l'utilisation de nanostructures métalliques. L'énergie confinée dans de petits volumes autour de nanoparticules métalliques fournit une plate-forme pour améliorer les transitions électroniques d'absorbeurs ou d'émetteurs optiques placés à proximité. Plusieurs processus optiques tels que la diffusion Raman améliorée en surface (SERS), la fluorescence améliorée par champ de plasmons (PEF), la photoluminescence et la génération de seconde harmonique (SHG) pourraient être améliorées dans la région spectrale autour de la fréquence SPR [8-11]. En outre, l'activité catalytique de certaines enzymes utilisées pour la production des biocarburants pourrait être également améliorée en présence d'un champ électromagnétique amplifié qui améliorera les performances de la pile à combustible [12].

Bien que les phénomènes SPR existent pour tous les métaux, les études de plasmons de surface sont principalement réalisées avec des nanoparticules d'or (AuNPs). Plusieurs facteurs justifient l'utilisation de l'or. Tout d'abord, l'or forme des colloïdes stables à l'air qui ne s'oxydent pas. Deuxièmement, sa fréquence SPR se situe dans la partie visible du spectre. Par conséquent, les AuNP présentent une couleur visible à l'œil nu, ce qui les rend intéressants en tant que marqueurs optiques. Troisièmement, ils peuvent être facilement synthétisés dans un large éventail de tailles et de formes, ce qui permet de contrôler leurs propriétés optiques [2]. Quatrièmement, leur surface pourrait être facilement modifiée avec des groupements amines et thiols pour une liaison sélective et la détection de molécules. Enfin, ils présentent une excellente biocompatibilité, essentielle pour les applications biomédicales [13]. À cet égard, les AuNP ont été largement étudiées pour leurs propriétés optiques améliorées par SPR et avec les progrès récents dans les techniques de synthèse et de fabrication de particules, de nouvelles nanostructures optiques intéressantes ont été développées.

La taille des AuNPs est un paramètre important qui affecte de manière significative leurs propriétés plasmoniques. La bande SPR devient rouge pour les particules de grandes tailles, ce qui permet de choisir la taille des AuNPs qui correspond à la longueur d'onde de la lumière destinée à l'application [14]. La forme des AuNP affecte également la bande SPR et l'augmentation des bords ou de la netteté des particules entraîne un décalage vers le rouge. Différentes nanoparticules d'or de formes variées telles que des triangles, des cubes, des nanotubes, des nanostructures et des nano-étoiles ont été synthétisées pour créer des structures avec des SPR proches de l'infrarouge [15-17]. En plus du changement de la bande SPR, les nanoparticules non sphériques attirent beaucoup d'attention en raison de la formation d'un «point chaud» avec un champ électromagnétique accru au niveau des extrémités ou des bords de ces structures. Un champ électrique amélioré rend ces nanostructures favorables aux spectroscopies améliorées en surface [18]. Des points chauds peuvent également être produits en plaçant deux nanoparticules à proximité les unes des autres, dans les limites de leur longueur du champ local. Dans ce cas, les oscillations plasmoniques de deux particules se couplent et se traduisent par un champ local amélioré en raison de la capacité de focalisation de la lumière aux jonctions entre particules [19]. L'amélioration créée par le couplage plasmon dépend de la taille des AuNPs et de la distance inter-particules [20]. Des améliorations extraordinairement importantes, ne pouvant pas être obtenues avec des AuNPs individuelles non sphériques, peuvent être produites en adaptant ces paramètres [21]. Cependant, il est difficile de fabriquer des structures reproductibles sur une surface suffisamment grande pour les rendre pratiques aux applications réelles.

L'auto-assemblage de blocs de construction de base et leur utilisation comme modèle de matériau pour la fabrication de nanostructures hautement ordonnées sont apparus comme une approche alternative offrant une haute précision et une haute résolution. Dans cette approche, une matrice de matériau sert d'hôte pour l'assemblage structurellement contrôlé de nanoparticules. À cet égard, les virus ont été étudiés en tant que matériau bio-modèle car ils offrent une grande diversité de structures et de tailles pour la fabrication de nanostructures rentables, stables et précises. Les virus végétaux les plus étudiés comprennent le virus de la mosaïque du tabac, le virus de la mosaïque du soja et le virus de la mosaïque du concombre, tandis que les bactériophages, en particulier le phage M13, sont les virus bactériens les plus utilisés dans les applications matérielles [22]. En comparaison avec les matériaux synthétiques classiques, les virus sont des blocs de construction attractifs pour la fabrication de nanostructures. Les virus ont des structures et des dimensions précises, à l'échelle nanométrique, qui sont difficiles à reproduire en utilisant des méthodes standard de synthèse [23]. En outre, les propriétés de surface des virus peuvent être contrôlées en utilisant des approches chimiques et génétiques sans détruire leur intégrité structurelle. Cette caractéristique permet le contrôle spatial de la position des groupements fonctionnels sur la surface du virus [24]. La propriété la plus intéressante des virus, en matière de synthèse matérielle, est que les virus peuvent être produits en grande quantité en infectant leurs cellules hôtes, et peuvent ensuite être purifiés à grande échelle à peu de frais. Ces caractéristiques critiques sont requises pour un matériau destiné à être utilisé comme bloc de construction pour la fabrication de nanomatériaux.

Dans la présente thèse, nous cherchons à mieux comprendre l'auto-assemblage des AuNP par les phages et leurs propriétés plasmoniques. Par conséquent, pour concevoir les matrices de formation des nanostructures plasmoniques, nous avons utilisé deux plateformes différentes de « phage display », M13 et T4, avec des AuNP de trois tailles différentes (environ 3 nm, 9 nm et 13 nm). L'utilisation de différentes plateformes de phages avait conduit à la génération de nanostructures plasmoniques dans lesquelles les AuNP ont été disposées de différentes manières. Le phage M13 fournissait un gabarit en forme de tige alors que le phage T4 avait une capsid avec une structure icosaédrique pour l'assemblage des AuNP. De plus, les protéines d'enrobage disponibles pour le « phage display » et leur organisation sur M13 furent différentes de celles sur les phages T4. Cette diversité structurelle permettait l'auto-assemblage de AuNP avec deux géométries spatiales différentes et un espacement inter-particules différent, résultant en des propriétés plasmoniques vraisemblablement différentes. Les performances des nanostructures créées ont été étudiées pour différentes applications. L'ensemble des données obtenues pourrait fournir une

meilleure compréhension des opportunités et des limitations relatives à l'utilisation de ces assemblages plasmoniques.

MÉTHODES EXPÉRIMENTALES

Préparation des assemblages des AuNP sur modèle M13

Conception du modèle du phage M13

Afin de cibler les récepteurs des intégrines surexprimés sur les cellules cancéreuses, une séquence peptidique contenant le motif **R** (Arginine) - **G** (Glycine) - **D** (acide aspartique) (**GRGDSP**) a été exprimée sur la protéine d'enveloppe mineure p3 du phage M13. L'exposition des peptides RGD sur la protéine p3 a été accomplie en utilisant le « Ph.D. Peptide Display Cloning System » (New England Biolabs Inc., Ontario). L'oligonucléotide comprenant la séquence RGD (CAT GTT TCG GCC CCG CCG CCC GGG CTG TCA CCA CGG CCA GAG TGA GAA TAG AAA GGT ACC CGG G) a été hybridé avec l'amorce d'extension (CAT GCC CGG GTA CCT TTC TAT TCT C) puis étendu en tant que duplex en utilisant le fragment « Klenow » (New England Biolabs, Ontario). Le duplex prolongé et le vecteur M12KE ont été digérés avec les enzymes de restriction Acc65I et EagI (New England Biolabs, Ontario) selon les instructions du fabricant, puis les produits de digestion ont été purifiés sur gel. Le duplex prolongé a été purifié sur un gel de Polyacrylamide non dénaturant à 8% [25] et extrait du gel en utilisant un kit d'extraction de gel QIAEX II (QIAGEN, Ontario). Le vecteur M13KE digéré a été purifié sur gel d'agarose avec le kit d'extraction de gel QIAquick (QIAGEN, Ontario). Le vecteur purifié et le duplex d'ADN ont été ligaturés en utilisant une ADN ligase T4 (New England Biolabs, Ontario) à 16°C pendant une nuit et le mélange obtenu a été introduit dans des cellules ultra-compétentes XL10-Gold (Agilent, ON). Après 24 heures d'incubation sur gélose LB / IPTG / X-gal (gélose LB, IPTG, isopropyl-β-D-thiogalactoside, X-gal, 5-bromo-4-chloro-3-indolyl-β-D-galactoside) à 37°C, des plaques bleues ont été prélevées et analysées pour la présence de l'insert. L'analyse par PCR a été réalisée par amplification de la région d'ADN M13KE, qui comprend l'insert en utilisant des séquences d'amorces conçues. Les plaques de lyse des phages positifs ont été envoyés à la *Plate-forme d'analyses génomiques (Université Laval)* pour l'analyse de séquence.

Le phage M13 recombinant exprimant le peptide linéaire GRGDSP sur la protéine d'enveloppe mineure p3 a été modifié pour exposer le peptide de liaison GB-or (VSGSPDS) sur la protéine d'enveloppe principale p8. L'insert a été positionné à l'extrémité N-terminale de la protéine p8 sauvage en créant un site de restriction PstI (CTGCAG) dans cette région. Ceci a été réalisé par mutation de la base d'acide nucléique à la position 1372 du plasmide M13 de T à A. Le site PstI présent sur le plasmide M13 à la

position 6245 a été délété en mutant A à T en position 6249 également. La mutagenèse dirigée sur ces sites a été réalisée en utilisant le kit « QuikChange Lightning Multi Site-Directed Mutagenesis » (QIAGEN, Ontario). L'ADN du phage pour la mutagenèse a été préparé en propageant le phage M13. Après propagation, les particules de phages ont été recueillies par centrifugation et l'ADN double brin à l'intérieur du culot a été purifié en utilisant le kit « QIAprep Spin Miniprep » (QIAGEN, Ontario).

Oligonucléotide	Séquence (5'- 3')
Amorce pour la mutation à 1372	GCT GTC TTT CGC TGC AGA GGG TGA CGA TCC
Amorce sens pour la vérification de la mutation 1372	TTC TTA AAC AGC TTG ATA CCG ATA G
Amorce anti-sens pour la vérification de la mutation 1372	TGT TTC GCG CTT GGT ATA ATC G
Amorce pour la mutation à 6249	GCT TGC ATG CCT GCT GGT CCT CGA ATT CAC
Amorce sens pour la vérification de la mutation 6249	GCC ATT CGC CAT TCA GGC TG
Amorce anti-sens pour la vérification de la mutation 6249	TGA GTT AGC TCA CTC ATT AGG CAC
Amorce sens pour le clonage du p8	CCT CTG CAG CGA AAG ACA GCA TCG G
Amorce anti-sens pour le clonage du p8	ATA TAT CTG CAG TGT CGG GTA GTA GTC CGG ATT CGG ATC CCG CAA AAG CGG CCT TTA ACT CCC
Amorce sens pour la vérification de l'Insert p8	TTC TTA AAC AGC TTG ATA CCG ATA G
Amorce anti-sens pour la vérification de l'Insert p8	TGT TTC GCG CTT GGT ATA ATC G

Tableau 1. Séquences d'oligonucléotides pour le clonage du phage p8 M13.

Pour la mutagenèse, l'ADN double brin (ADNdb) purifié a été amplifié en utilisant des séquences d'amorces conçues (IDT, Integrated DNA Technologies, Inc.) (Tableau 1) et des brins mutants ont été synthétisés. Après la réaction, la matrice d'ADN mère a été digérée avec l'endonucléase DpnI à 37 °C pendant 5 min. L'ADN simple brin (ADNsb) muté a été transformé dans des cellules ultra-compétentes XL10-Gold et incubé pendant une nuit à 37 °C sur des géloses LB / IPTG / X-gal. L'ADNsb circulaire muté a été converti en forme duplex et s'est propagé en tant que phage. Après l'incubation, les plaques bleues sur des géloses LB / IPTG / X-gal comprenant l'ADN du phage muté ont été prélevées et propagées. Les régions mutées de l'ADN du phage propagé ont été amplifiées par PCR en utilisant les séquences

d'amorces conçues (IDT, Integrated DNA Technologies, Inc.) (tableau 1) et envoyées à la Plate-forme d'analyses génomiques (Université Laval) pour l'analyse de la séquence d'ADN.

Le peptide de liaison à l'or a été inséré dans le phage M13 modifié en utilisant un site de restriction PstI. L'insert a été positionné entre le premier et le cinquième acide aminé de la protéine p8 en remplaçant les résidus 2-4 de (Alanine¹ - acide glutamique² - Glycine³ - acide aspartique⁴ - acide aspartique⁵) à (Alanine¹ - insert - acide aspartique⁵). Deux séquences d'amorces ont été conçues: une amorce sens comprenant la séquence d'insertion et une amorce anti-sens pour linéariser le vecteur (tableau 1). Le phage M13 avec un site modifié de restriction PstI a été propagé selon le protocole décrit dans la section précédente et l'ADN viral a été purifié en utilisant le kit « QIAprep Spin Miniprep » (QIAGEN, Ontario). Pour incorporer l'insert, la PCR a été réalisée en utilisant l'ADN polymérase « Phusion® High-Fidelity » (New England Biolab, Ontario), les deux amorces et le plasmide M13 muté comme matrice d'ADN (New England Biolab, Ontario). Le produit obtenu a été purifié sur gel (1% d'agarose dans du tampon TAE, 45 min, 80 mV), extrait avec un kit d'extraction du gel QIAEX II (QIAGEN, Ontario), digéré avec l'enzyme PstI (New England Biolabs, Ontario) et re-circularisé avec la T4 DNA Ligase (New England Biolabs, Ontario) en incubant pendant une nuit à 16°C. Le mélange de ligation a été transformé dans des cellules ultra-compétentes XL10-Gold (Agilent, Ontario) et incubé sur des géloses LB / IPTG / X-gal à 37°C pendant une nuit. Les plaques bleues ont été prélevées et leurs plasmides ont été amplifiés. Après purification avec le kit « QIAprep Spin Miniprep » (QIAGEN, Ontario), des échantillons d'ADN ont été envoyés à la *Plate-forme d'analyses génomiques de l'Université Laval* pour le séquençage de l'ADN.

Préparation des AuNPs de 9 nm

Des AuNPs ayant un diamètre de 9 nm ($5,7 \times 10^{12}$ particules / mL) ont été achetés auprès de Ted Pella Inc. (CA, USA) et passivés avec BSPP (bis (p-sulfonatophényl) phénylphosphine) avant leur utilisation. Pour la passivation, BSPP a été rajouté à 100 ml de solution de nanoparticules d'or à une concentration de 1 mg / mL. Après 24h d'incubation à l'abri de la lumière, les nanoparticules d'or ont été concentrées par centrifugation avec des filtres de centrifugation Amicon ultra-15 (MWCO, 30 kDa, EMD Millipore, Canada) et dessalées en utilisant une solution de BSPP. Le processus de dessalage a été réalisé par centrifugation de la solution de nanoparticules qui ont été par la suite resuspendues dans 5 mL de solution de BSPP à 1 mg / mL. Ceci a été répété six fois pour assurer l'élimination complète du citrate de sodium. Le volume final de la solution a été ajusté à 10 mL ($5,7 \times 10^{13}$ particules / ml) avec 1 mg / mL de solution de BSPP dans de l'eau et conservé au réfrigérateur en recouvrant le récipient par une feuille d'aluminium pour minimiser l'exposition à la lumière.

Synthèse des AuNPs de 3 nm

Les AuNPs ont été synthétisées selon le protocole de Zahr et Blum [26]. Une solution d'acide tétrachloroaurique (HAuCl_4) (Sigma Aldrich, Canada) (2.5×10^{-4} M) a été préparée dans 20 ml d'eau désionisée et mélangée avec 10 μL de solution de citrate de sodium 0.5 M. La solution a été réduite en rajoutant 600 μL de 0.1 M borohydrure de sodium dans de l'eau sous agitation vigoureuse et stockée pendant une nuit à l'obscurité pour la formation des AuNP. Afin de passiver les particules synthétisées, BSPP a été ajouté à la solution à une concentration de 1 mg / mL. Après une nuit d'incubation dans l'obscurité, les AuNP ont été dessalées selon le protocole utilisé pour les AuNPs de 9 nm. Enfin, la solution a été centrifugée à 10 000 x g pendant 35 min pour éliminer les plus grosses particules de l'échantillon et le volume de la solution a été ajusté à 2 ml avec une solution de BSPP (1 mg / mL dans de l'eau). Le nombre des AuNP dans la solution mère (2.8×10^{15} particules/mL) a été estimé en utilisant l'équation basée sur le poids de HAuCl_4 utilisé dans la synthèse [27].

Synthèse des AuNPs de 13 nm

La méthode de Turkevich modifiée a été utilisée pour synthétiser des AuNPs de 13 nm [28]. Du citrate de sodium a été dissous dans 150 mL d'eau à une concentration de 2.2 mM et la solution a été chauffée jusqu'à ébullition. De l'acide tétrachloroaurique (HAuCl_4) a été rajouté à la solution à une concentration finale de 2.5×10^{-4} M et la température a été maintenue constante jusqu'à ce que la solution devienne rouge signifiant la formation des AuNP. Les AuNPs synthétisées ont été passivées avec du BSPP et dessalés comme décrit pour les AuNPs de 3 nm et 9 nm. Le volume final de la solution des AuNP a été rajusté à 15 mL et stocké dans le réfrigérateur. Le nombre des AuNP dans la solution mère (3×10^{13} particules/mL) a été estimé en utilisant l'équation basée sur le poids de HAuCl_4 utilisé dans la synthèse [27].

Assemblage des AuNPs sur le phage M13

Etant donné que le phage M13 était déjà purifié avec le PEG après sa propagation, il a été directement utilisé en le diluant dans une solution de réaction à une concentration de 10^9 PFU/mL.

L'auto-assemblage des AuNPs de 3, 9 et 13 nm sur des matrices de phages M13 a été réalisé dans 1 mL de tampon phosphate (0.025 M, pH 7.0) comprenant 10 μL de solution de phages purifiés (10^{11} PFU / mL dans du TBS) et 100 μL de solution concentrée de nanoparticules. Les solutions réactionnelles ont été incubées dans un agitateur orbital à température ambiante dans l'obscurité pendant 1 jour.

Évaluation de l'affinité de liaison à l'intégrine aux assemblages d'or sur le modèle M13

Le test ELISA (dosage d'immuno-absorption par enzyme liée) a été réalisé pour déterminer l'affinité à l'intégrine du RGD des assemblages d'or des modèles M13. Dans cet essai, les puits d'une plaque ont été recouverts de 200 µL d'intégrine humaine hétérodimérique alpha V beta 1 (Acrobiosystems Inc., Newark, US) dissoute dans une solution phosphate saline (PBS; 137 mM NaCl, 2.7 mM KCl, 4.3 Na₂HPO₄ mM, KH₂PO₄ 1.47 mM, pH 7.4) à une concentration de 14 µg / mL. Après incubation de 24h à 4 °C, les protéines non liées ont été retirées et les puits ont été incubés avec 200 µL de tampon de blocage (3% d'albumine de sérum bovin (BSA) dans du PBS) pendant 2 h à température ambiante. Pendant ce temps, les assemblages d'or des modèles de phages composés des AuNPs de 3, 9 et 13 nm et de leurs solutions contrôles correspondantes ont été préparés. Les échantillons ont été dilués avec un volume égal de tampon de blocage et incubés pendant 20 min avant leur addition aux puits. Après élimination du tampon de blocage, 200 µL des échantillons dilués ont été rajoutés aux puits revêtus d'intégrine et incubés pendant 2 h à température ambiante. Les puits ont été abondamment lavés avec du tampon de lavage (Tween 20 à 0,05% dans PBS) et 200 µL d'anticorps monoclonal anti-M13 conjugué à la peroxydase de raifort (Fisher Scientific, Ontario) dans du tampon de blocage ont été rajoutés pour marquer les phages liés dans les puits. La plaque a été incubée pendant 1 h à température ambiante et les anticorps anti-M13 non liés ont été éliminés par lavage six fois avec du tampon de lavage. La liaison des anticorps anti-M13 aux phages M13 recombinants à l'intérieur des puits a été détectée en ajoutant 200 µL de substrat TMB (3,3', 5,5'-tétraméthylbenzidine) (Invitrogen Inc.) et en mesurant la réaction enzymatique avec des mesures d'absorbance à 450 nm. La réaction enzymatique a été arrêtée après 45 min en ajoutant 100 µL de réactif d'arrêt (Invitrogen Inc.) et les mesures d'absorbance ont été effectuées en utilisant un lecteur de plaque (lecteur d'imagerie Cytation 5, Biotek, US).

Préparation des assemblages des AuNP sur modèle T4

Conception du modèle de phage T4

Les vecteurs d'intégration ont été construits en utilisant un plasmide pRH fourni par le Prof. Lindsay Black (Université du Maryland, Baltimore) et des fragments d'ADN de dérivés de Soc. Afin de construire des dérivés de Soc, les gènes codant pour le peptide de liaison à l'or (GSGSC) ont été insérés dans le gène Soc du phage T4 de type sauvage par mutagénèse dirigée par PCR. Dans cette réaction, le phage T4 de type sauvage a été utilisé comme ADN matrice et son gène Soc a été amplifié en utilisant un ensemble d'amorces comprenant une séquence peptidique de liaison à l'or (tableau 2). Tous les tests de PCR ont été réalisés dans un thermocycleur « Biometra TGradient » en utilisant 1 µL d'ADN matrice dans

50 µL de mélange PCR. Les concentrations finales des réactifs de PCR étaient 1 x tampon PCR, 2 mM de MgCl₂, 200 µM de mélange désoxynucléoside triphosphate, 250 µM d'amorces oligonucléotidiques sens et anti-sens (IDT, Integrated DNA Technologies, Inc.) et 2.5 unités d'ADN polymérase Taq Plus. La PCR a été réalisée selon les instructions du fabricant. Les produits de la PCR ont été observés par électrophorèse sur gel d'agarose. Les fragments de PCR ont été séparés dans un gel d'agarose à 1% préparé dans un tampon Tris acétate EDTA (TAE) 1X (4.84 g / L de Tris, 1.14 mL / l d'acide acétique et 2 mL d'EDTA (0,5 M. pH 8.0) à 100 volts (Bio-Rad, ON, CA). Après migration de 45 min, les molécules d'ADN ont été visualisées sous lumière UV à l'aide d'une coloration « T safe » (Bioshop, CA) ajoutée dans du gel d'agarose pendant la préparation. Les fragments d'ADN amplifiés appartenant à des dérivés de Soc ont été purifiés en utilisant des colonnes de centrifugation (QIAGEN, Ontario).

Insert	Type de Fusion	Amorces	Séquence (5'- 3')
GSGSC	C- Terminal	SOC-Cys FWD	TAC ATA TGG CTA GTA CTC GCG GTT ATG
		SOC-Cys REV	AAT TGA ATT CGA TTA GCA GCT GCC GCT GCC ACC AGT TAC TTT CCA CAA ATC

Tableau 2. Séquences des amorces pour l'exposition du phage T4 des peptides de liaison à l'or.

L'amplification du plasmide pRH a été réalisée dans un bouillon LB par la culture de cellules *E. coli* portant l'ADN plasmidique. Le culot cellulaire a été recueilli par centrifugation à 5000 rpm pendant 15 min et l'ADN plasmidique à l'intérieur des cellules a été purifié en utilisant un kit « QIAprep Spin Miniprep » (QIAGEN, Ontario). Avant la ligature des dérivés de Soc dans le plasmide pRH, les produits géniques amplifiés ont été digérés à travers les sites de restriction (EcoRI et NdeI), qui ont été insérés dans le gène Soc par PCR. Toutes les digestions ont été réalisées à l'aide des enzymes de restriction EcoRI et NdeI, en suivant les instructions du fabricant (New England Biolabs, Ontario). L'ADN plasmidique a également été digéré au niveau des mêmes sites de restriction et purifié sur gel en utilisant le kit d'extraction de gel QIAquick (QIAGEN, Ontario). Les dérivés de Soc digérés ont été ligaturés dans le plasmide pRH en utilisant un kit de ligature rapide (New England Biolabs, Ontario), et le mélange de ligature a été transformé dans des cellules compétentes *E. coli* HB101 (Promega, Madison, WI). Les cellules transformées ont été sélectionnées sur des agars LB contenant 100 µg / mL d'ampicilline. La transformation a été confirmée par l'analyse par PCR et le séquençage de l'ADN à la *Plate-forme d'analyses génomiques (Université Laval)*.

Après confirmation par analyse de séquence, les clones positifs ont été infectés avec des phages mutants T4-Z pour réintégrer le gène Soc incluant la séquence peptidique de liaison à l'or dans le génome

du phage. Selon la procédure décrite par Ren et al. (1996), des cellules de *E. coli* HB101 transformées avec des dérivés de pRH-Soc ont été cultivées dans un milieu citrate (CM) contenant 100 µg / mL d'ampicilline jusqu'à une concentration de 108 CFU / mL. Cette culture bactérienne (20 mL) a été infectée avec le phage T4-Z à une multiplicité d'infection (MOI) de 1. Après incubation pendant 5 heures à 37°C, les bactéries infectées ont été concentrées par centrifugation à 3200 g pendant 15 min et resuspendues dans un bouillon LB. Du chloroforme a été rajouté à la suspension pour libérer tous les phages à l'intérieur des bactéries, et les débris cellulaires ont été éliminés par centrifugation à 10 000 rpm pendant 5 min. Le surnageant, obtenu suite à une centrifugation à 20 000 x g pendant une heure pour éliminer l'antibiotique, a été étalé sur une plaque CM (11 g/L de gélose bactériologique (Fisher BioReagents) en bouillon CM) contenant *E. coli* B dans l'agar CM supérieur sans lysozyme. Les plaques ont été isolées et les intégrants ont été confirmés par PCR.

Purification des modèles de phages T4

Les stocks de phages T4 préparés ont été purifiés par filtration sur gel avec « Superose™ 6 prep grade » (GE Healthcare Biosciences, QC). Les stocks de phages ont été concentrés par centrifugation à 20 000 x g pendant 90 min et les culots de phages recueillis ont été remis en suspension dans 1 mL de tampon X. Le milieu a été conditionné dans une colonne C16/40 (GE Healthcare Biosciences, QC) et lavé initialement avec de l'eau distillée. Après équilibrage de la colonne avec du PBS, l'échantillon de phage concentré a été chargé dans la colonne et l'élution de l'échantillon a été réalisée en faisant passer du PBS à un débit constant ajusté par une pompe péristaltique. Les fractions ont été recueillies dans des volumes de 5 mL et analysées pour la teneur en protéines et en phages. Un spectromètre UV-Vis a été utilisé pour l'analyse des protéines où l'absorbance des fractions a été enregistrée à 280 nm. La concentration en phages a été déterminée par titrage des fractions, ce qui a été effectué par une méthode sur plaque de gélose double couche comme décrit précédemment. La fraction la plus riche en phages a été concentrée par centrifugation avec des unités de filtration Amicon ultra-15 (MWCO, 30 kDa, EMD Millipore, Canada) et lavée 3 fois avec du tampon phosphate 0.1 M (pH ajusté à 7.0 en mélangeant 0.1 M de NaH₂PO₄ avec 0.1 Na₂HPO₄ M). Le volume final de l'échantillon a été ajusté à 500 µL et l'échantillon a été stocké à 4°C après le titrage.

Assemblage des AuNPs sur le modèle de phage T4

L'auto-assemblage des AuNP sur les matrices de phages T4 a été réalisé dans différentes conditions réactionnelles en fonction de la taille des AuNP. L'assemblage des AuNPs 3 nm a été réalisé

dans 1 mL de tampon phosphate (0.2 M, pH 7.0) incluant 100 μ L de solution phagique purifiée (10^{10} PFU / mL dans du tampon phosphate (0.1 M, pH 7.0)) et 100 μ L de solution stock de nanoparticules. Pour les AuNPs de 9 nm, le processus d'assemblage a été réalisé dans 1 mL de tampon phosphate (0.05 M, pH 7.0) incluant 100 μ L de solution phagique purifiée (10^{10} PFU / mL dans du tampon phosphate (0.1 M, pH 7.0)) et 100 μ L de solution mère de nanoparticules. Une approche similaire a été utilisée pour assembler des AuNPs de 13 nm tandis que la réaction a été réalisée dans 1 mL de tampon phosphate (0.025 M, pH 7.0) incluant 100 μ L de solution de phage purifiée (10^{10} PFU / mL dans du tampon phosphate (0.1 M, pH 7.0)) et 100 μ L de solution mère de nanoparticules. Pour toutes les AuNP, les solutions réactionnelles ont été incubées dans agitateur orbital à température ambiante pendant 2 jours. Les échantillons ont été conservés dans une boîte fermée pour minimiser l'exposition à la lumière. Des contrôles de nanoparticules ont été préparés en utilisant les mêmes concentrations de AuNP et en remplaçant les solutions de matrices de phages par un tampon ayant le même pH et la même force ionique que les solutions réactionnelles.

Préparation de l'échantillon pour l'analyse SERS et 2PEF

Traitement hydrophobe des lames de verre

Avant le traitement hydrophobe, les lames de verre ont été nettoyées. Initialement, les lames de verre (0.13-0.16 mm, Ted Pella Inc., CA, USA) ont été placées dans un bécher contenant de l'acétone et laissées pendant 30 min dans un bain à ultrasons. Ensuite, les lames ont été soigneusement rincées à l'eau distillée et séchées au four (60 ° C). Dans la seconde étape, les lames ont été immergées dans une solution de piranha (H_2O_2 à 30% dans du H_2SO_4 concentré (3: 1, Sigma Aldrich, Canada) et laissées 30 min. Enfin, les lames ont été lavées par l'eau distillée et séchées dans un four (60°C).

Une solution de trichloro(1H, 1H, 2H, 2H-perfluorooctyl)silane (Alfa Aesar, MA, USA) (~ 1 mM) a été fraîchement préparée dans 100 ml de toluène (Sigma Aldrich, Canada) dans un bécher en verre de 150 ml. Des lames de verre fraîchement nettoyées ont été immergées dans cette solution, le bécher recouvert de parafilm, puis stockées dans une hotte pendant 3 h. Ensuite, les lames ont été retirées et rincées successivement avec du toluène et de l'éthanol absolu (Commercial Alcohols, ON, Canada). Finalement, les lames ont été séchées dans le four (60°C) et stockées dans une boîte jusqu'à ce qu'elles soient utilisées.

Préparation des AuNP-phages pour l'analyse

Après l'achèvement de l'assemblage des AuNP sur la matrice de phages, 100 μL de la solution réactionnelle de phage-AuNP ont été centrifugés à 3000 rpm pendant 5 min pour éliminer les AuNP non liés des assemblages des AuNP sur le phage. Le culot a été remis en suspension dans 100 μL de 25 mM tampon phosphate et la centrifugation a été répétée. Ensuite, le culot a été mis en suspension dans 30 μL de 25 mM tampon phosphate et une gouttelette de 3 μL de cette solution a été pipetée sur les lames de verre hydrophobes et laissée sécher à température ambiante.

Les spectres Raman des assemblages des AuNP à matrice de phages ont été enregistrés en l'absence et en présence de cellules bactériennes. Afin de préparer ces échantillons pour des assemblages des AuNP à matrice M13, 100 μL d'une solution de réaction phage-AuNP ont été mélangés avec 1 mL d'*Escherichia coli* ER2738 (10^6 CFU / mL dans du tampon phosphate 25 mM). Après incubation du mélange pendant 1 h sur un agitateur rotatif à température ambiante, la solution a été centrifugée à 3000 rpm pendant 5 min pour éliminer les AuNP non liées du complexe d'assemblage bactéries / phages-AuNP. Après que le culot a été remis en suspension dans 100 μL de 25 mM tampon phosphate, la centrifugation a été répétée. Le culot collecté incluant les assemblages bactéries / phages-AuNP a été mis en suspension dans 30 μL de 25 mM tampon phosphate et une gouttelette de 3 μL de cette solution a été pipetée sur les lames de verre hydrophobes et séchée à température ambiante. Dans le cas d'assemblages AuNP T4, 1 mL de suspension d'*Escherichia coli* B pendant une nuit dans du tampon phosphate 25 mM (10^6 CFU / mL) a été mélangé avec 100 μL de solution de réaction phage-AuNP après 2 jours de processus d'assemblage. Le mélange a été incubé pendant 15 min sur un agitateur rotatif à température ambiante, puis les AuNP non liées ont été retirées du complexe d'assemblage bactéries / phages-AuNP par centrifugation, comme cela a été réalisé pour les assemblages sur matrice M13. Finalement, le culot a été mis en suspension dans 30 μL de 25 mM tampon phosphate et une gouttelette de 3 μL de cette solution a été pipetée sur les lames de verre hydrophobes et séchée à température ambiante.

Cartographie SERS sur des lames de verre

Les mesures Raman ont été effectuées avec un microscope à sonde à balayage (AIST-NT CombiScope™ 1000) prenant en charge le mode de fonctionnement Raman. Un laser He-Ne, émettant à 632.8 nm, a servi de source d'excitation. Sauf indication contraire, le laser avait une puissance de 1.75 mW après l'objectif. Le faisceau laser a été focalisé sur l'échantillon à travers un objectif 20X avec une

ouverture numérique de 0.45. Les spectres Raman ont été collectés à partir de 0-1700 cm^{-1} avec un temps d'exposition de 1 s. La zone de cartographie était de 100 x 100 μm avec une taille de pas de 2.5 μm .

Microscopie 2PEF sur lames de verre

Les mesures de microscopie à deux photons ont été réalisées à l'aide d'un système optique construit sur place à partir d'un microscope à balayage laser (Till Photonics GmbH, Munich, Allemagne) équipé d'un étage motorisé XY (MLS203, Thorlabs). Le faisceau de pompe fourni par un oscillateur titane:saphir (Tsunami, Spectra Physics, Santa Clara, USA) a été utilisé pour générer ~ 180 impulsions femtoseconde (fs) avec une longueur d'onde centrale de 816.4 nm et un taux de répétition de 80 MHz. Le faisceau laser fs a été réglé à 15 mW avant d'être dirigé vers le microscope et 8 mW au foyer. Un objectif de microscope à immersion dans l'air Olympus UPlanSAPO 20X avec une ouverture numérique de 0.8 a été utilisé pour concentrer la lumière sur l'échantillon. Un télescope a été utilisé pour augmenter la taille du faisceau pour remplir la pupille arrière de l'objectif, permettant d'atteindre une résolution spatiale optimale de typiquement 600 nm (FWHM). Le signal 2PEF a été recueilli en utilisant un condenseur avec une ouverture numérique de 0.55, dans le sens direct. Alors que le laser d'excitation a été rejeté par un filtre 380-700 nm (SEMRock, Rochester, NY, USA) et la longueur d'onde a été sélectionnée par un filtre de 661 ± 10 nm (SEMRock) et détectée en utilisant des tubes photomultiplicateurs (modèle R6357, Hamamatsu Corporation, New Jersey, USA) réglés à 700 V. La surface de cartographie était de 400 x 400 μm^2 avec une taille de pas de 1 μm .

RÉSULTATS ET DISCUSSION

Auto-assemblage des NPsAu sur le modèle de Phage M13

L'auto-assemblage de de 3 nm de NPs d' Au sur le phage M13 a été réalisé en tampon phosphate 25mM, après une réaction d'un jour. Les mesures DDL ont démontré que la taille du phage M13 augmentait lors de la liaison des NPs d' Au. La spectroscopie UV-Vis a été utilisée pour étudier l'effet du processus d'assemblage sur les propriétés plasmoniques des NPs d' Au. Il était intéressant d'observer que l'assemblage de NPs d' Au sur le phage M13 n'a pas produit un changement ou un élargissement marqué dans leurs bandes SPR (Figure 1b).

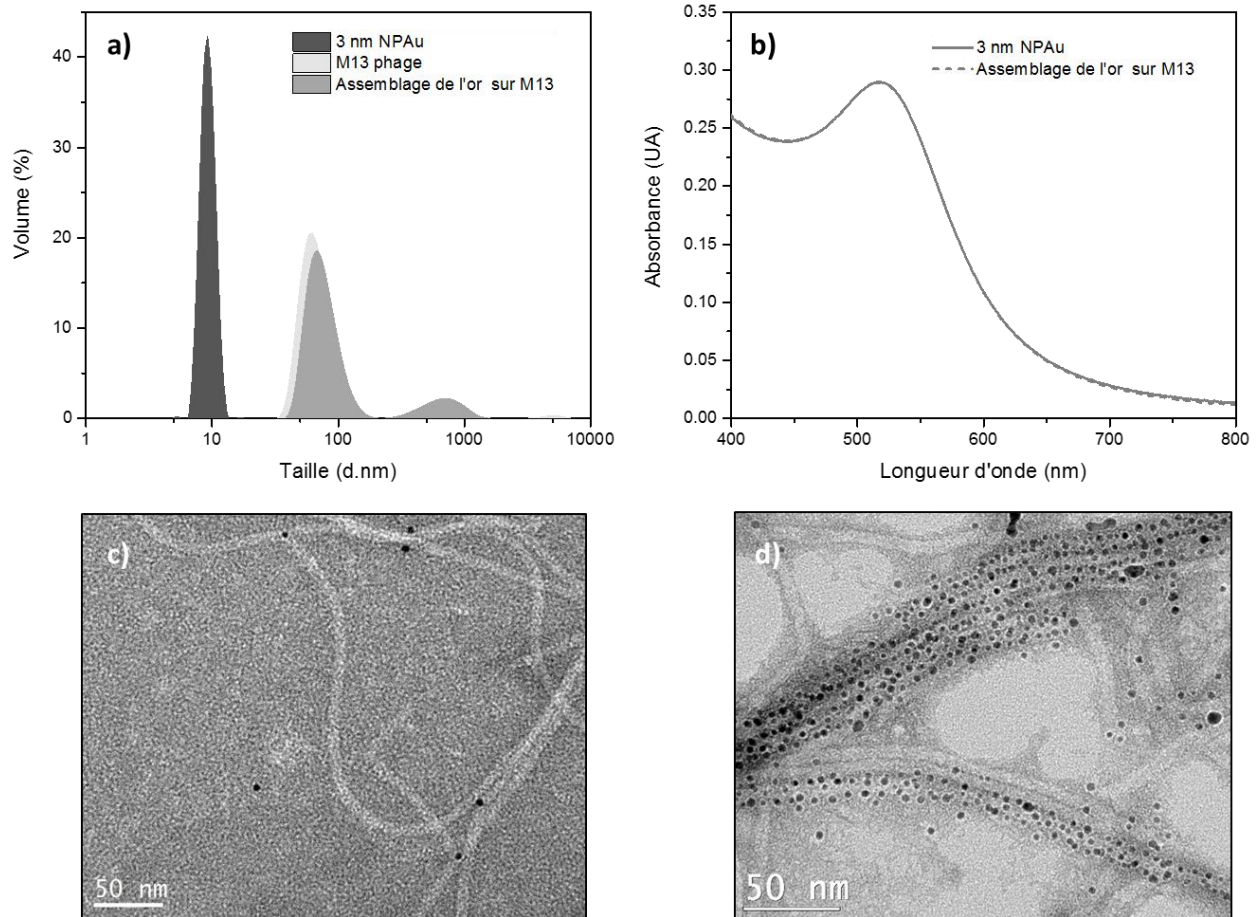


Figure 1. Caractérisation des NPs d'Or de 3 nm auto-assemblées sur le modèle du phage M13 après une réaction d'un jour a) Histogrammes de la DDL montrant la taille des NPs d'Or de 3 nm, du phage M13 et des assemblages d'or sur la matrice M13. b) Spectres UV-Vis des NPs d'Or de 3 nm dans une solution colloïdale (ligne continue) et auto-assemblées sur le modèle du phage M13 (ligne continue). c) Image MET du phage M13 coloré avec de l'acétate d'uranyle (2%) d) Image MET des NPs d'Or de 3nm assemblées sur le phage M13.

Le couplage plasmonique entre des nanoparticules métalliques adjacentes a été observé dans des conditions spéciales où la distance entre les NPs d'Or (D) est inférieure au diamètre moyen des particules ($2r$) [29]. La distance inter-particules (D) entre les NPs d'Or assemblées sur le phage M13 a été analysée en utilisant les images enregistrées par MET (figure 1d). En faisant la moyenne de 200 mesures, la valeur D a été calculée à $3,26 \pm 1,16$ nm. La valeur D obtenue, supérieure à 3 nm, était également une indication de la grande distance inter-particules qui empêchait le couplage plasmonique entre les NPs d'Or. Par conséquent, la position de la bande SPR a été préservée.

De manière similaire, l'assemblage des NPs d'Or de 9 nm sur le phage M13 a également été réalisé dans un tampon phosphate 25 mM. L'évaluation des histogrammes de distribution des tailles a montré la

modification de la taille des populations due à l'auto-assemblage des NPs d'Or sur le modèle phagique (Figure 2a).

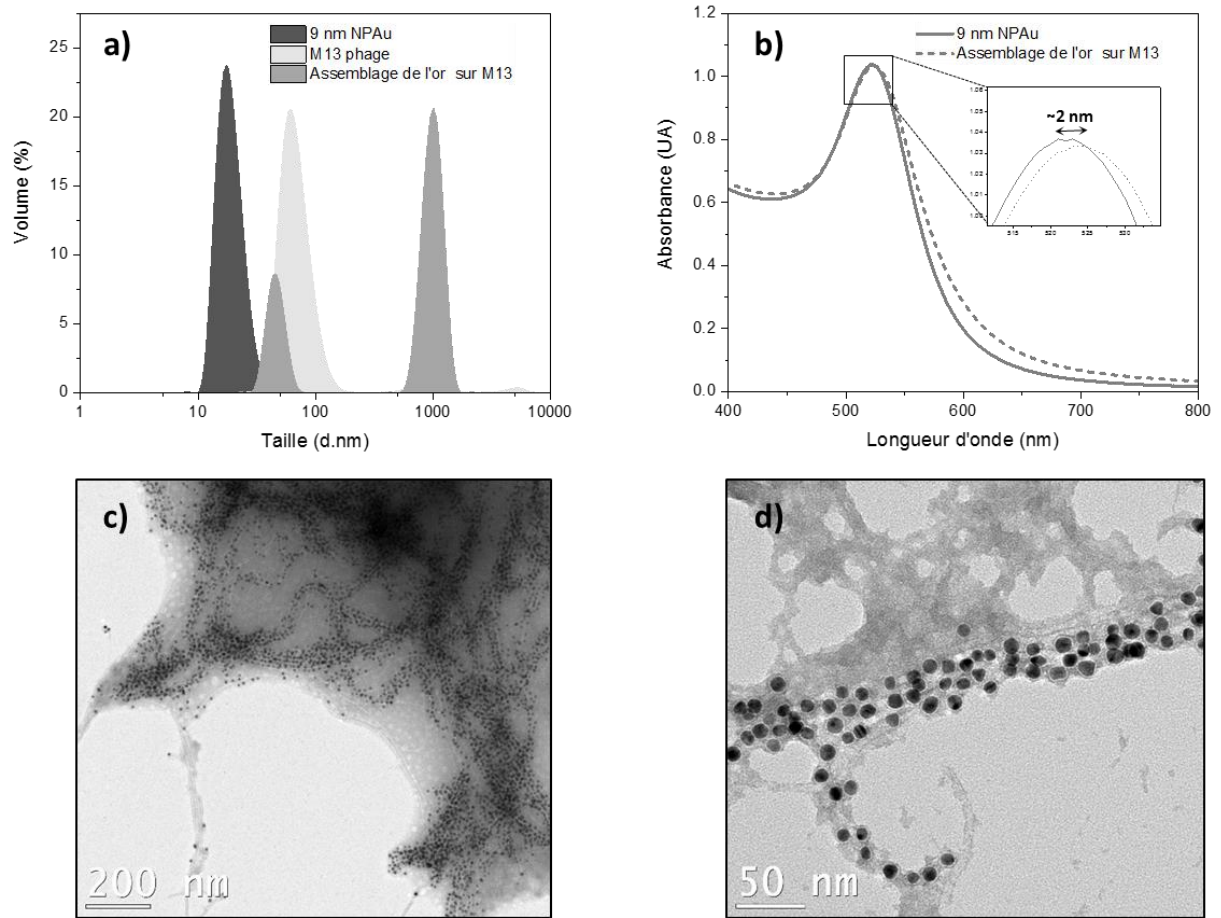


Figure 2. Caractérisation des NPs d'Or de 9 nm assemblées sur le modèle de phage M13 après une réaction d'un jour a) Histogrammes DDL montrant la taille des NPs d'Or de 9 nm, du phage M13 et des assemblages d'or sur la matrice M13. b) Spectres UV-Vis des NPs d'Or de 9 nm en solution colloïdale (ligne continue) et auto-assemblées sur le modèle du phage M13 (ligne pointillée). L'encart montre le décalage rouge ~ 2 nm dans la bande SPR en raison de l'assemblage des NPs d'Or sur le modèle du phage. c) Image MET de 9 nm des NPs d'Or assemblées sur le phage M13 d) Image MET à fort grossissement de 9 nm des NPs d'Or assemblées sur le phage M13.

L'assemblage des NPs d'or sur la matrice du phage est devenu visible avec la formation d'un pic à ~ 1008 nm qui était la longueur approximative de M13, alors que les pics des NPs d'Or colloïdaux et le pic principal du phage M13 ont disparu. La caractérisation de l'assemblage des NPs d'or sur la matrice M13 par spectroscopie UV-Vis a également confirmé l'auto-assemblage des NPs d'Or sur M13. En raison de l'assemblage des NPs d'Or sur la surface du phage, un décalage rouge (~ 2 nm) et un élargissement de la bande SPR s'est produit (figure 2b). Les images MET ont été utilisées pour calculer la distance interparticules entre les NPs d'Or assemblées sur le phage M13. Le rassemblement des NPs d'Or de 9 nm sur

la longueur de M13 a abouti à un système avec une distance inter-particules de $6,34 \pm 2,05$ (n: 200) qui était plus courte que le diamètre des NPs d'Or. Cette valeur était suffisamment courte et a créé un couplage dans les oscillations plasmoniques des NPs d'or assemblées sur le modèle phagique.

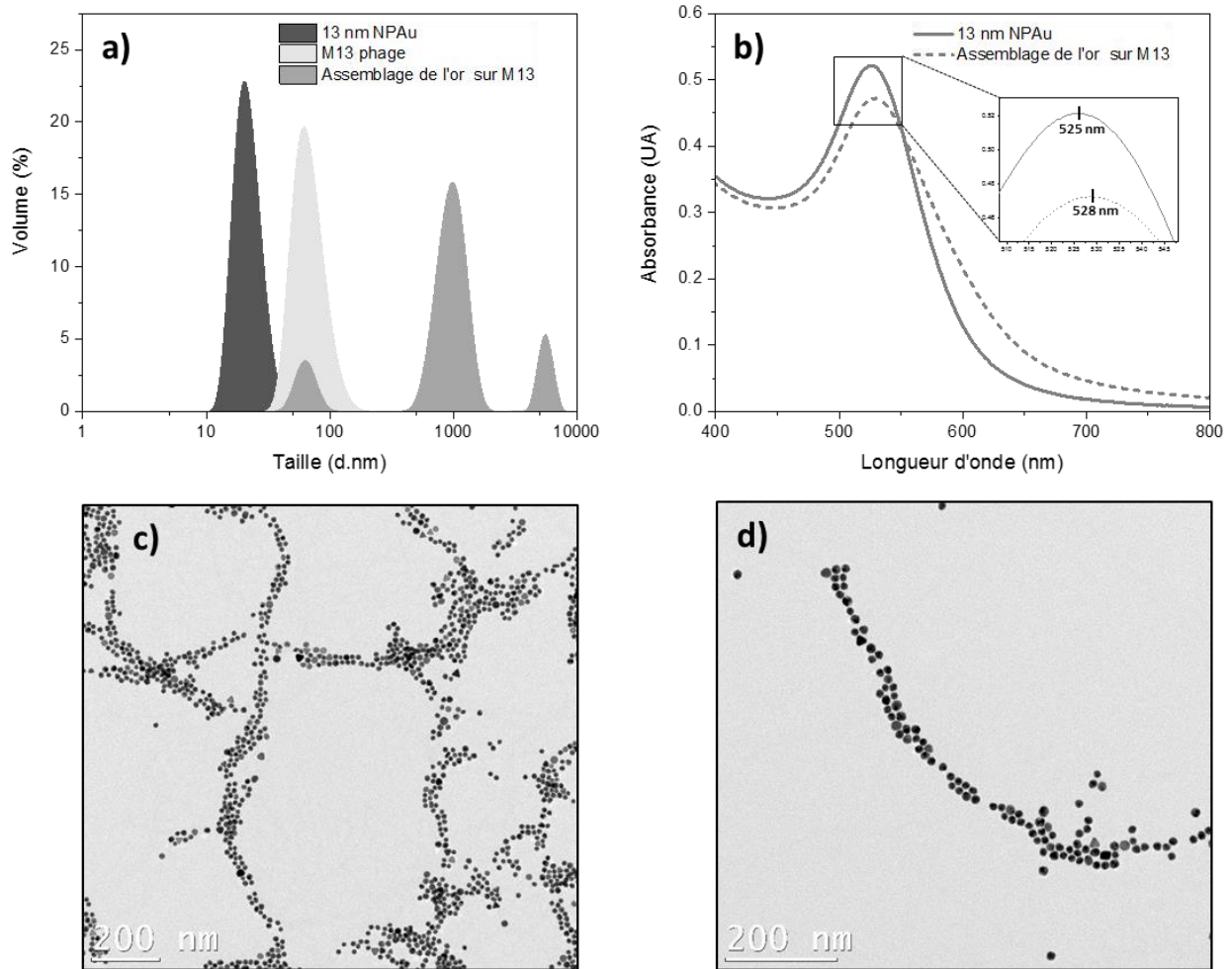


Figure 3. Caractérisation des NPs d'Or de 13 nm assemblées sur le modèle de phage M13 après une réaction d'un jour a) Histogrammes DDL montrant la taille des assemblages des NPs d'or de 13 nm, du phage M13 et de l'assemblages d'or sur la matrice M13. b) Spectres UV-Vis de NPsd'Or colloïdaux à 13 nm (ligne continue) et auto-assemblées sur le modèle du phage M13 (ligne pointillée). L'encart montre le décalage rouge de ~ 3 nm dans la bande SPR de 525 à 528 nm en raison de l'assemblage de NPs d'Or sur la matrice du phages. c) Image MET de NPs d'Or de 13 nm assemblées sur le phage M13 d) Image MET à fort grossissement de NPsd'Or de 13 nm assemblées sur le phage M13.

Les conditions de réaction pour l'assemblage de NPs d'Or de 13 nm sur le phage M13 étaient similaires aux assemblages constitués de NPs d'Or de 3 et 9 nm alors que le processus d'assemblage était réalisé dans un tampon phosphate à 25 mM. Comme on le voit dans les histogrammes de distribution des tailles (Figure 3a), les populations dominantes des histogrammes des NPs d'Or colloïdaux (~ 21 nm) et des matrices de phages M13 (~ 70 nm) ont été remplacées par la population représentant les assemblages

d'Or sur la matrice M13. La variation du spectre d'absorbance des NPs d'Or colloïdaux a également été observée pour les NPs d'Or de 13 nm lors de leur assemblage sur la surface du phage M13 (figure 3b). La distance inter-particules entre les NPs d'Or de 13 nm assemblées sur le phage M13 a été calculée à $3,17 \pm 2$ nm (n: 200), ce qui a abouti à une résonance plasmonique de surface collective sur la surface du phage. Le décalage vers le rouge (~ 3 nm) dans la bande SPR était proche de la valeur observée pour les grappes formées avec des NPs d'or de 9 nm (~ 2 nm). Les images MET des solutions de liaison après 1 jour de réaction ont également confirmé l'auto-assemblage des NPs d'Or (figure 3c-d).

Capacité de ciblage de l'intégrine du peptide RGD sur les assemblages aurifères à matrice M13

L'affichage du peptide RGD sur le phage M13 et sa fonctionnalité en présence des NPs d'Or assemblées ont été sondés par ELISA, qui a été réalisée dans des puits de microplaque revêtus d'intégrine.

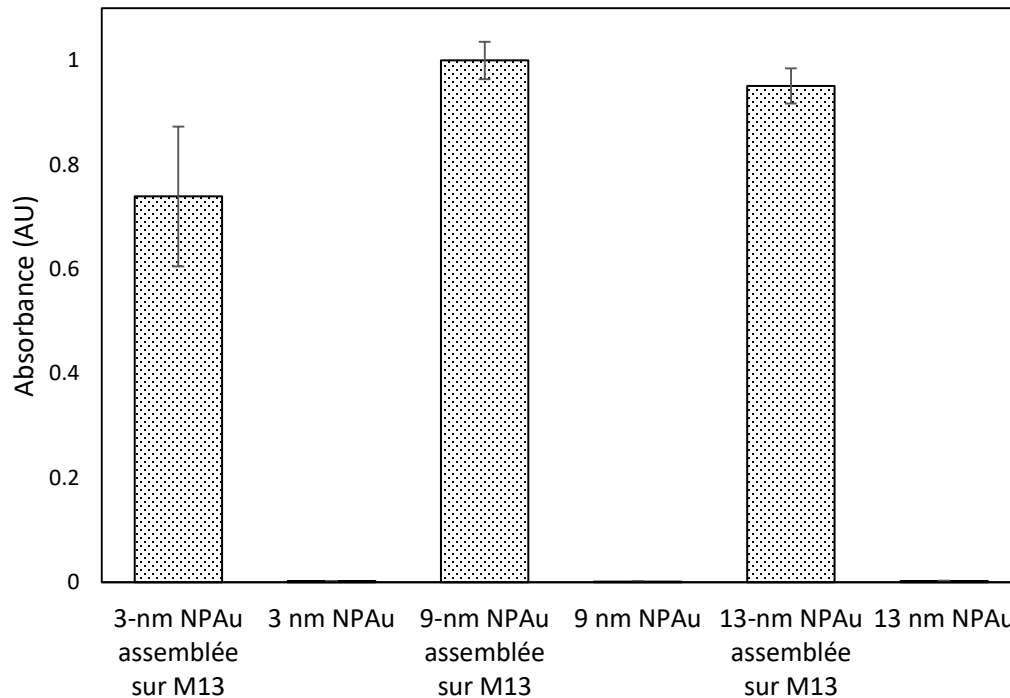


Figure 4. Réactivité de RGD portant des assemblages d'Or à l'état de phages M13 et des NPs d'Or colloïdaux avec une protéine intégrine humaine.

L'attachement des assemblages d'Or à la protéine intégrine via le peptide RGD a été détecté par l'activité de l'enzyme HRP conjuguée à l'anticorps anti-M13. La liaison de l'anticorps anti-M13 à la protéine d'enveloppe p8 du phage a donné lieu à des assemblages d'Or marqués avec l'enzyme HRP. Le niveau de marquage a été déterminé en ajoutant des substrats de HRP qui étaient du peroxyde et du TMB. En présence de peroxyde, le TMB a été oxydé et transformé en un produit de couleur bleue. Les valeurs d'absorbance des échantillons dans chaque puits ont été tracées comme le montre la figure 4. Les

résultats de ELISA ont montré que l'assemblage de NPs d'Au sur la protéine p8 du phage M13 n'interférait pas stériquement avec la capacité de liaison spécifique du peptide RGD à la protéine intégrine. En conséquence, les assemblages d'Au au format M13 étaient capables de reconnaître et de se lier à la protéine intégrine.

Auto-assemblage des NPs d'Au sur le modèle Phage T4

Des études ont démontré que le phage T4 présentant des résidus de cystéine sur l'extrémité C-terminale de la protéine Soc (Cys-C) était la meilleure matrice de liaison à l'Au.

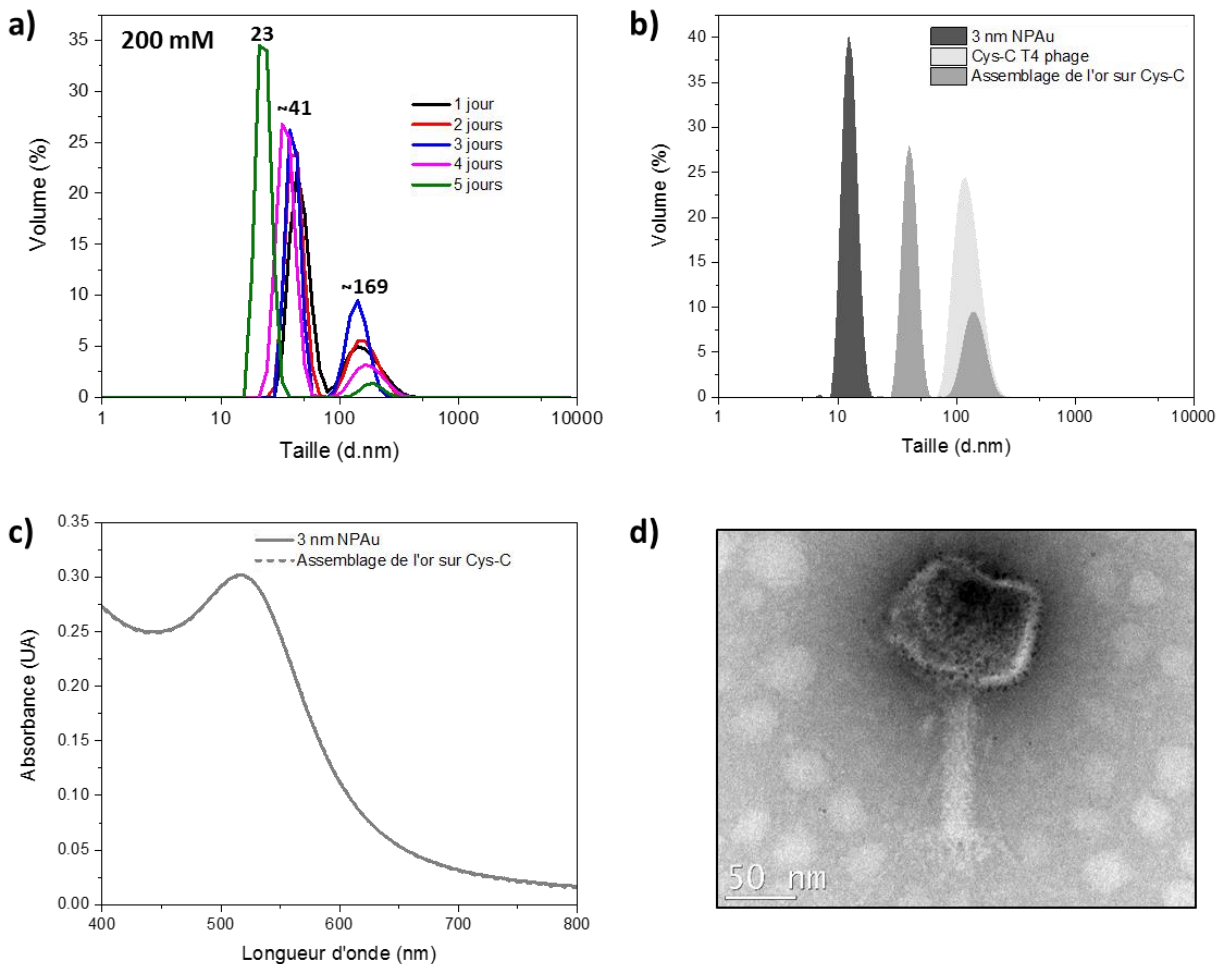


Figure 5. Caractérisation des NPs d'Au de 3 nm auto-assemblées sur la matrice Cys-C. a) Histogrammes DDL pour l'analyse de la taille basée sur le volume des solutions de Cys-C phage-3 nm des NPs d'Au dans du tampon phosphate 200 mM. Les histogrammes DDL ont été enregistrés pendant une période de 5 jours. b) Histogrammes DDL montrant la taille des NPs d'Au de 3 nm, du phage Cys-C et des assemblages d'or sur matrice de Cys-C après 2 jours de réaction. c) Spectres UV-Vis des NPs d'Au colloïdaux de 3 nm (ligne continue) et auto-assemblées sur modèle de phage Cys-C (ligne pointillée) après 2 jours de réaction. d) Image MET des NPs d'Au de 3 nm assemblées sur le phage Cys-C

L'assemblage des NPs d'Au de 3 nm sur le phage Cys-C a été réalisé dans du tampon phosphate 200 mM. L'analyse du spectre UV-Vis appartenant à des assemblages d'Au basé sur un modèle de phage Cys-

C n'a révélé aucun changement dans la bande SPR par rapport aux NPs d'Or isolées (figure 5b). Le regroupement des NPs d'Or sur le phage Cys-C a été observé par imagerie MET (Figure 5.d). La distance inter-particulaire entre les NPs d'Or assemblées sur le phage Cys-C a été déterminée à $3,05 \pm 0,98$ nm en faisant la moyenne de 200 mesures. Une distance interparticulaire proche du diamètre des NPs d'Or (3 nm) pourrait expliquer la position préservée de la bande SPR dans les assemblages phage-or car la distance interparticulaire égale ou supérieure au diamètre des particules empêcherait le couplage plasmonique entre les nanoparticules d'or.

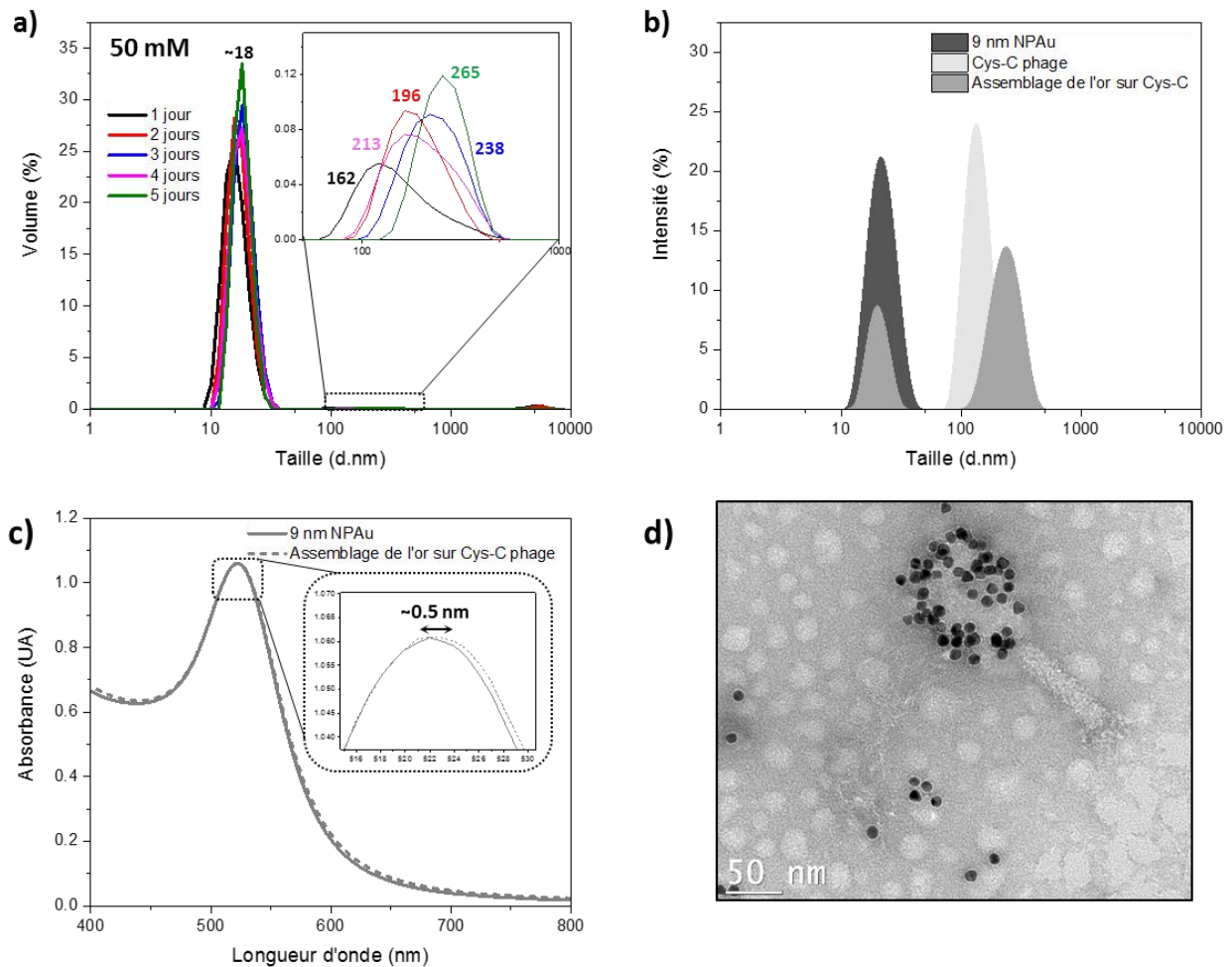


Figure 6. Caractérisation des NPs d'Or de 9 nm auto-assemblées sur le modèle Cys-C. a) Histogrammes DDL pour l'analyse de la taille basée sur le volume des solutions de Cys-C phage-9 nm des NPs d'Or dans du tampon phosphate 50 mM. Les histogrammes DDL ont été enregistrés pendant une période de 5 jours. b) histogrammes DDL montrant la taille des AuNPs de 9 nm, du phage Cys-C et des assemblages d'or sur la matrice de Cys-C après 2 jours de réaction. c) Spectres UV-Vis de NPs d'Or colloïdaux de 9 nm (ligne continue) et auto-assemblées sur modèle de phage Cys-C (ligne pointillée) après 2 jours de réaction. d) Image MET des NPs d'Or de 9 nm assemblées sur un phage Cys-C.

L'association de ces dernières de 9 nm a été réalisée dans un tampon phosphate 50 mM sur une période de 2 jours (figure 6a). La population principale dans les histogrammes DDL des solutions de

réaction de liaison phage-or était les NPs d'Or colloïdaux (~18 nm). L'analyse de la taille basée sur l'intensité des solutions de réaction a clairement démontré l'augmentation de la taille des matrices de phages en raison de l'assemblage des NPs d'Or sur leurs surfaces (figure 6b). Les échantillons ont été caractérisés par spectroscopie UV-Vis et imagerie MET. La formation d'assemblages d'Or sur la matrice de phages Cys-C a été réalisée par un léger décalage vers le rouge et un élargissement de la bande SPR de la solution de liaison phage-Or (figure 6c). L'imagerie des NPs d'Or de 9 nm assemblées sur un phage Cys-C par microscopie électronique a permis de recouvrir partiellement les particules de phages avec des NPs d'Or, ce qui pourrait être considéré comme une indication du désassemblage des NPs d'Or pendant la préparation de l'échantillon de la MET (Figure 6d).

Le processus d'auto-assemblage des NPs d'Or de 13 nm a été réalisé dans un tampon phosphate à 25 mM sur une période de 2 jours et a conduit à la formation des assemblages d'Or à matrice de phages d'une taille de 293 nm (figure 7a). L'augmentation de la taille de la matrice de phage Cys-C après l'assemblage des NPs d'Or à sa surface, a été montrée par l'analyse de taille basée sur l'intensité des solutions de réaction phage-or (figure 7b). La caractérisation des assemblages d'Or à matrice de phages Cys-C par spectroscopie UV-Vis a également montré la formation d'assemblages qui créaient un décalage vers le rouge et un élargissement de la bande SPR de la solution réactionnelle (figure 7c). Cependant, l'assemblage des NPs d'Or de 13 nm sur le phage Cys-C n'a pas été confirmé par les images MET. Comme nous l'avons observé pour les NPs d'Or de 9 nm, dans les images TEM, les particules de phages ont été partiellement recouvertes de nanoparticules d'Or (Figure 7d). Les résultats obtenus à partir de la spectroscopie DDL et UV-Vis suggèrent que les NPs d'Or assemblées sur le phage Cys-C ont été démontées pendant la préparation de l'échantillon pour la MET, très probablement à l'étape de séchage.

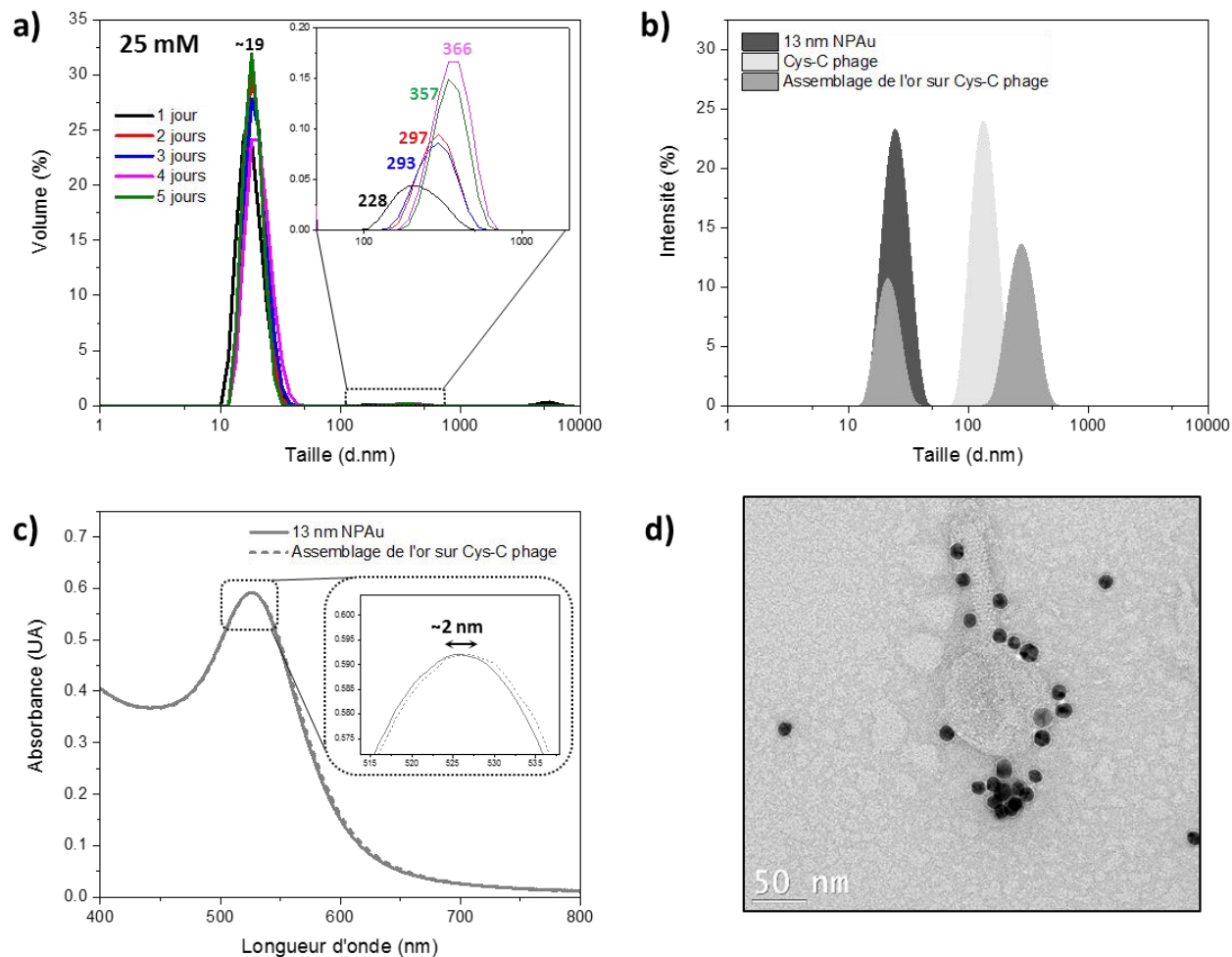


Figure 7. Caractérisation des NPs d' Au de 13 nm auto-assemblées sur le modèle Cys-C. a) Histogrammes DDL pour l'analyse de la taille basée sur le volume de solutions de Cys-C phage-13 nm des NPs d' Au dans un tampon phosphate 25 mM. Les histogrammes DDL ont été enregistrés pendant une période de 5 jours. b) Histogrammes DDL montrant la taille des NPs d' Au de 13 nm, du phage Cys-C et des assemblages d' or sur la matrice de Cys-C après 2 jours de réaction. c) Spectres UV-Vis des NPs d' Au colloïdaux de 13 nm (ligne continue) et auto-assemblées sur le modèle de phage Cys-C (ligne pointillée) après 2 jours de réaction. d) Image MET des NPs d' Au de 13 nm assemblées sur le phage Cys-C.

Activité SERS des assemblages d' AuNP au format phagique

Afin d'évaluer l'activité SERS des assemblages des NPs d' Au sur la matrice M13, leurs spectres Raman ont été comparés à ceux des NPs d' Au isolées et stabilisées par BSPP sur une lame de microscope. BSPP est un agent stabilisant de NPS d' Au, qui permet leur assemblage contrôlé sur le phage, et servira de rapporteur Raman ici. La figure 8a montre les spectres Raman de BSPP massif et des NPs d' Au passivés par BSPP (3 nm, 9 nm et 13 nm de diamètre) coulés sur une lame de microscope.

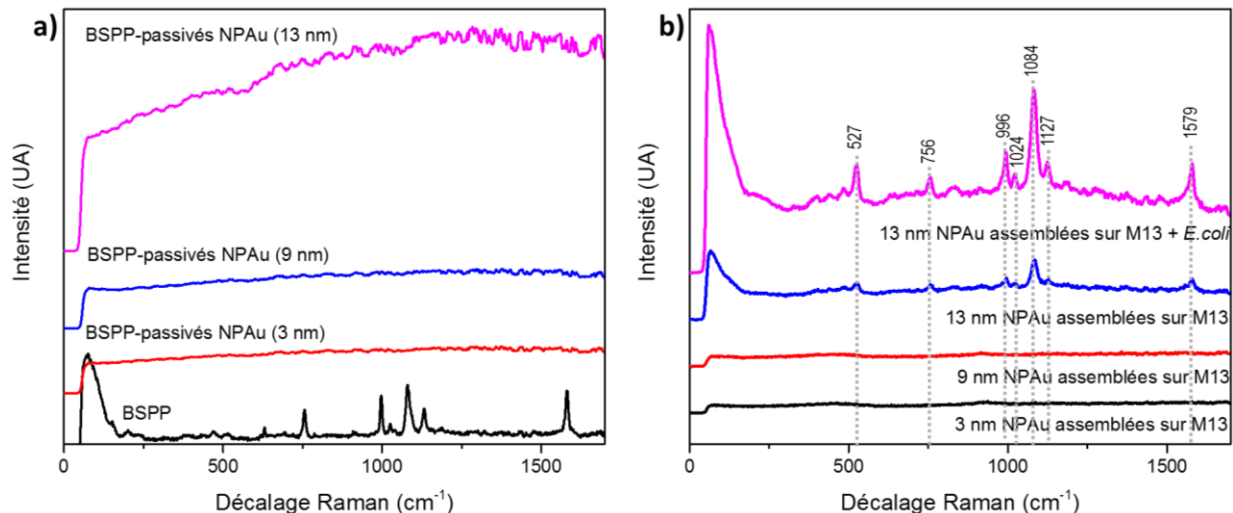


Figure 8. a) Spectres Raman représentatifs de BSPP (en masse) (20x) et spectres SERS de BSPP adsorbés sur des NPs d’Au de 3-13 nm (coulés sur une lame de microscope). b) Les spectres SERS représentatifs des assemblages des NPs d’Au sur des M13 modélisés en l’absence et en présence de la cellule de *E. coli*.

Aucun des pics attribués aux modes vibrationnels de BSPP n'a été observé lors de l'adsorption sur les NPs d’Au. Cela était dû à la faible concentration globale de BSPP sur la surface des nanoparticules (probablement une monocouche), et au fait que les diamètres des NPs d’Au employés dans ce travail étaient trop petits pour produire une amélioration même lorsqu'ils étaient agrégés de façon aléatoire (un processus qui peut générer aléatoirement des hotspots). En revanche, les spectres Raman des assemblages des NPs d’Au sur la matrice M13 (13 nm) ont montré les pics caractéristiques de BSPP (Figure 8b) et les pics associés à son cycle aromatique (1579, 1084, 1024, 996 et 756 cm^{-1}) et les groupes sulfonate (1127 et 527 cm^{-1}) [30] étaient clairement visibles par rapport au bruit de fond. Cependant, les pics de BSPP n'ont pas été observés pour les assemblages préparés avec des NPs d’Au plus petites (3 ou 9 nm). Comme aucun des NPs d’Au individuels n'encouragent suffisamment la SERS à observer les pics de BSPP, l'observation selon laquelle les assemblages de modèles phagiques montrent des pics de BSPP, indique que des points chauds sont en effet créés au sein des assemblages.

La taille des NPs d’Au employées dans ce travail (3 nm, 9 nm et 13 nm) est relativement faible et n'a généré aucun signal SERS lors de leur agrégation sur lame de verre pendant la préparation de l'échantillon. On sait que lorsque l'écart entre les particules est inférieur à 0,3 nm, on observe de nouveaux modes de transfert de charge (tunneling), qui poussent le champ électromagnétique vers l'extérieur de la zone de gap et réduisent le rehaussement du champ électromagnétique [31, 32]. Le spectre Raman des assemblages des NPs d’Au sur matrice M13 a également été enregistré après incubation des assemblages avec des cellules de *E. coli*. La liaison des assemblages aux cellules bactériennes n'a pas produit de

changement évident au spectre Raman en termes de nombre de pics observés ou de leur position (Figure 8b). Ce résultat suggère que SERS est généré dans les lacunes des nanoparticules auto-assemblées [33] et que le spectre présente les pics d'empreintes digitales de BSPP (situés dans ces régions) plutôt que des bactéries ou d'autres protéines matricielles, sont en dehors de ces points chauds. Cette caractéristique pourrait permettre l'utilisation d'assemblages phage-NP d'Au pour sonder leurs cibles spécifiques.

Dans le cas du phage T4, les spectres Raman ont été enregistrés pour les assemblages préparés avec Cys-C. Comme le montre la figure 9, les pics caractéristiques de la BSPP ont été observés uniquement pour les assemblages préparés avec des NPs d'Au de 13 nm. L'addition de bactéries à ces assemblages n'a pas modifié les spectres Raman des matériaux, en accord avec les observations faites avec les assemblages M13.

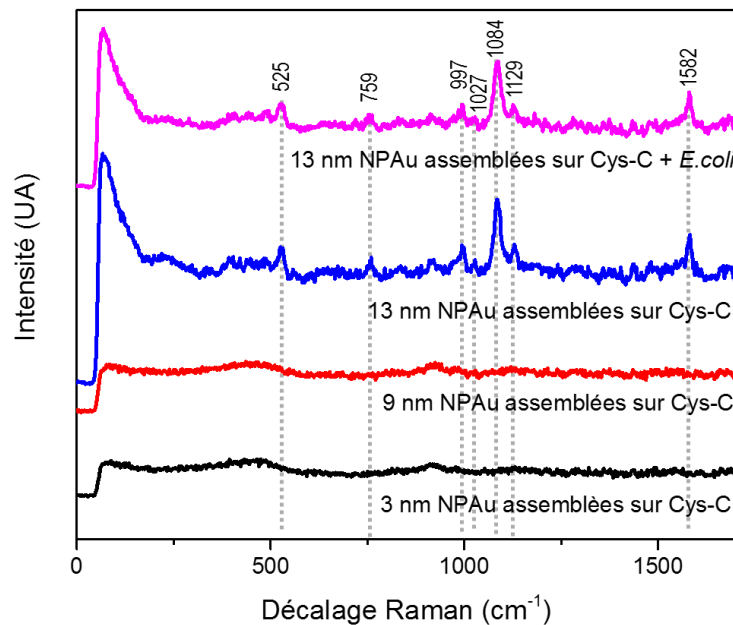


Figure 9. Les spectres SERS représentatifs des NPs d'Or assemblées sur le phage Cys-C en absence et en présence de cellules *E. coli*.

Les NPs d'Or assemblées sur les phages Cys-C ont montré des activités SERS relativement faibles par rapport aux assemblages structurés sur les phages M13. La différence entre les intensités moyennes des signaux SERS des NPs d'Or assemblées sur chaque phage a également été démontrée par l'analyse statistique (Figure 10). En effet, l'activité SERS plus faible des assemblages NPs d'Or Cys-C est due au fait que, pendant la préparation de l'échantillon, les assemblages de phages-NPs d'Or sont séchés sur des lames de verre et on pense que l'étape de séchage peut détruire les assemblées. En conséquence, les

signaux SERS résultants des assemblages des NPs d'or au format Cys-C pourraient être considérés comme des signaux d'assemblages détruits au lieu de signaux entièrement intégrés de NP d'Au.

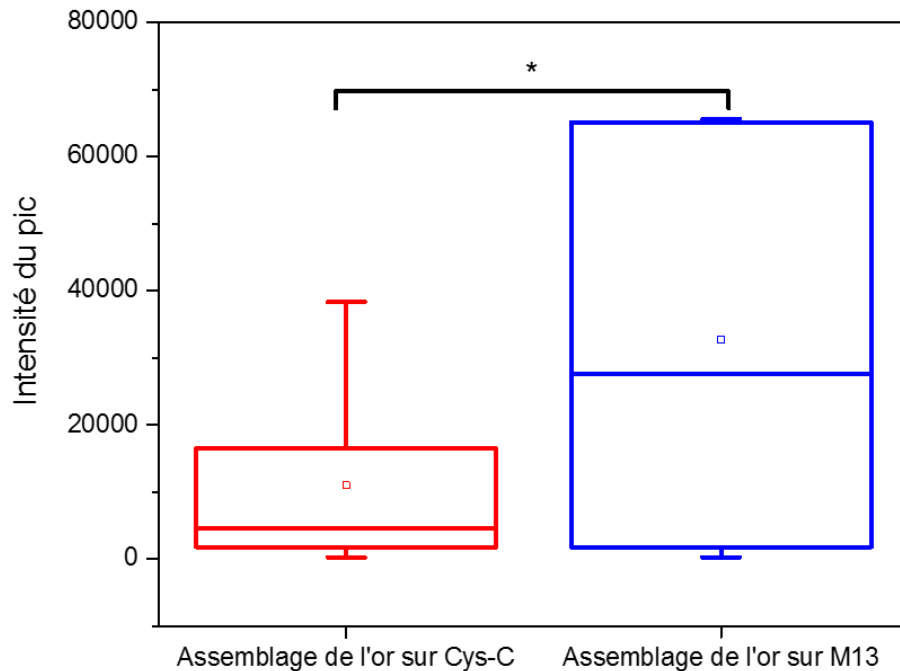


Figure 10. Distribution représentative des intensités du signal SERS des NPs de 13 nm assemblées sur des gabarits Cys-C (rouge) et M13 (bleu). Dans chaque boîte, le haut du rectangle indique le troisième quartile, une ligne horizontale du milieu du rectangle indique la médiane et le bas du rectangle indique le premier quartile. Les valeurs moyennes sont représentées par des carrés (□) sur le dessus des rectangles (* P < 0,05).

Emission 2PEF d'assemblages des NPs d'Au à matrice de phages

Pour évaluer l'intensité du signal 2PEF et la robustesse des assemblages, des solutions de phages-NP d'Au assemblées (contenant ou non des bactéries) ont été abandonnées et séchées sur des lames de microscope hydrophobes. Ce processus concentre la solution très diluée sur une petite zone de lame, puis peut être analysé par microscopie 2PEF. Essentiellement, une goutte de solution d'échantillon sur une lame de verre hydrophobe, favorise la concentration de l'échantillon au centre de la gouttelette pendant le processus de séchage. Les images de 2PEF du centre de la gouttelette sèche ont été acquises en balayant une zone de $400 \times 400 \mu\text{m}$ avec une taille de pas de $1 \mu\text{m}$, ce qui a donné 1 600 points de données pour chaque échantillon. Les distributions d'intensité du signal 2PEF ont été obtenues par traitement d'image pour identifier les pixels positifs à partir du bruit de fond, et retirer les pixels "chauds" isolés. Les histogrammes résultants fournissent des informations sur l'intensité moyenne de 2PEF pour un

échantillon donné, ainsi que le nombre de pixels positifs contre les négatifs, ce qui fournit indirectement des informations sur la robustesse des assemblages en vue du séchage (Figure 11).

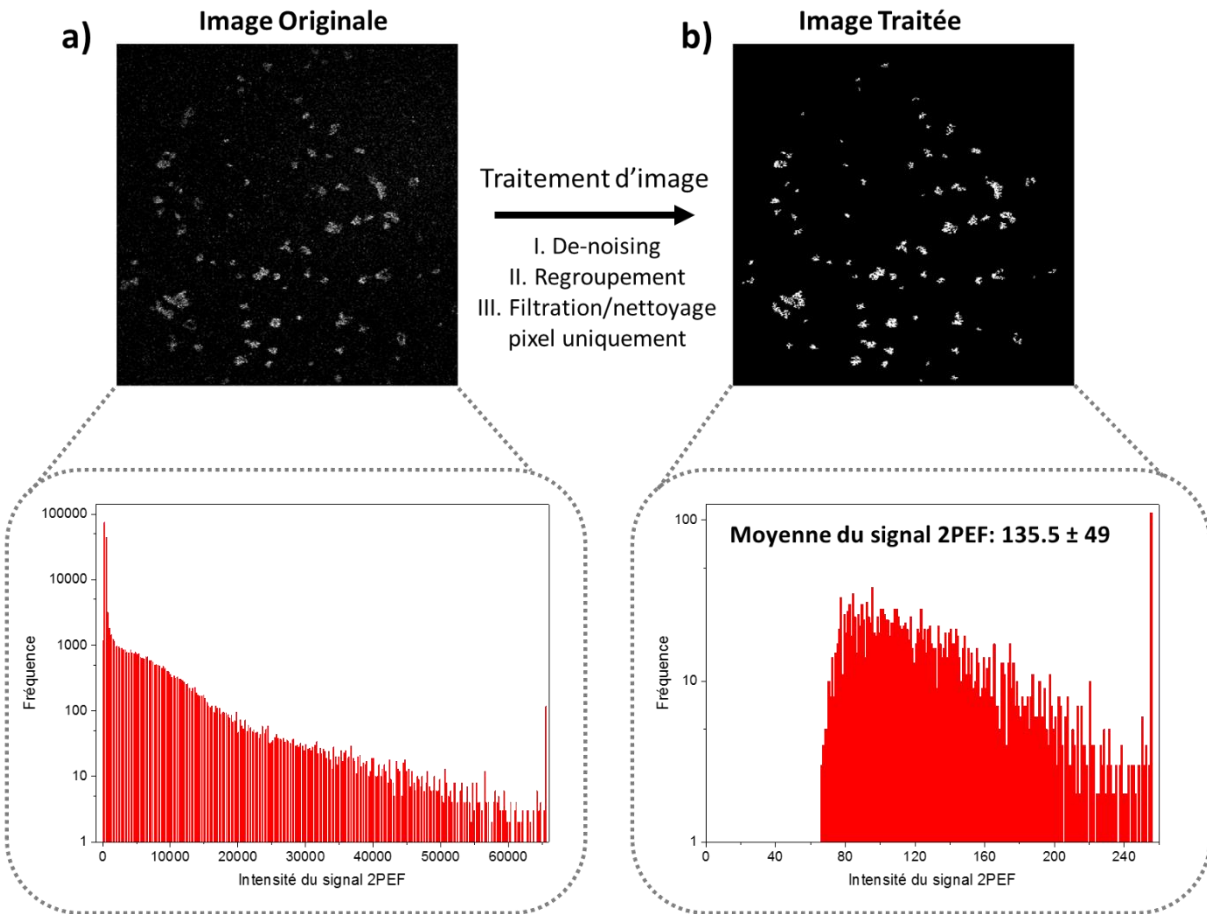


Figure 11. a) Image originale des NPs d’Au de 13 nm assemblées sur le phage M13 et histogramme représentant la distribution de l’intensité du signal 2PEF. b) Image traitée des NPs d’Au de 13 nm assemblée sur le phage M13 et histogramme représentant la distribution de l’intensité du signal 2PEF.

On sait que l’efficacité de 2PEF des NPs d’Au dépend de leur niveau d’agrégation. Pour cela, 2PEF des NPs d’Au isolées ont d’abord été comparés à ceux de l’assemblé sur le phage. Les résultats illustrés sur la figure 12, montrent que les histogrammes représentatifs des données traitées à partir d’AuNP isolés étaient indépendants de la taille (3-13 nm) et correspondaient au signal généralement observé pour le bruit de fond. Pour cela, les NPs d’Au isolées (3-13 nm) étaient en dessous de la limite de détection, au moins pour ce système 2PEF particulier. C’était également le cas pour les assemblages M13-NPs d’Au (3 nm).

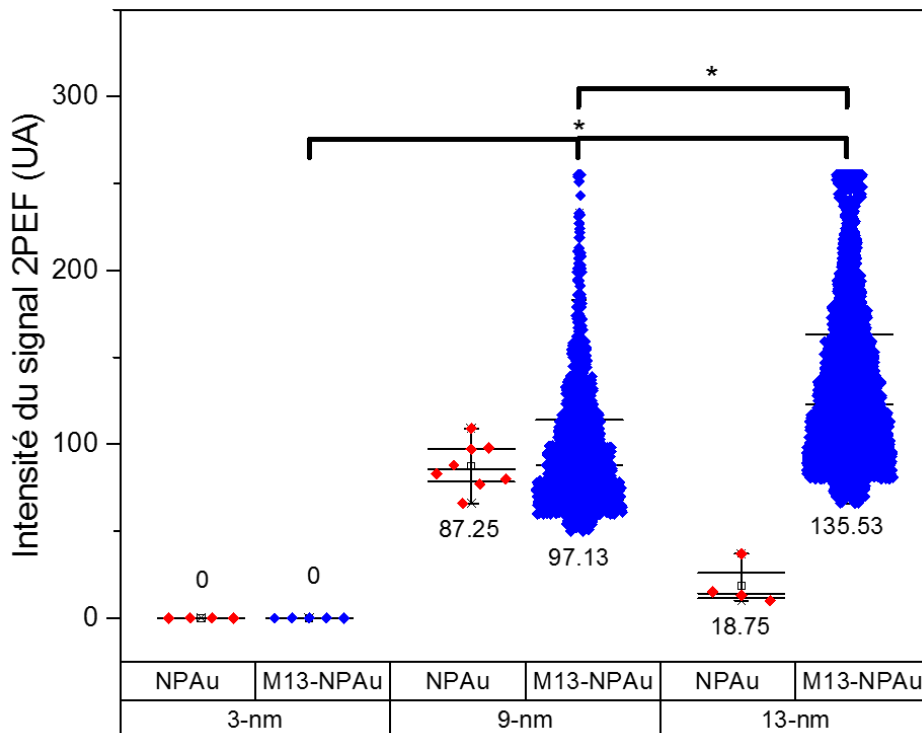


Figure 12. Diagramme en boîte, pour comparer les intensités des signaux 2PEF des NPs d’Au isolées avec les intensités des signaux 2PEF des assemblages des NPs d’Au sur la matrice M13 préparés avec des NPs de 3, 9 et 13 nm. Dans chaque boîte, la ligne horizontale en haut indique le troisième quartile, la ligne horizontale près du milieu indique la médiane et la ligne horizontale en bas indique le premier quartile. Les losanges bleu et rouge qui se chevauchent avec les boîtes représentent l'ensemble des données des échantillons. Les valeurs numériques à côté de chaque boîte indiquent la valeur moyenne de l'ensemble de données. (* P <0,05).

En revanche, les assemblages M13-NPs d’Au (9 et 13 nm) produisaient un signal plus élevé que le bruit de fond et augmentaient avec l'augmentation de la taille des NPs d’Au. Les différences entre les assemblages préparés avec des NPs d’Au de 9 et 13 nm étaient statistiquement significatives, mais faibles. Pour les assemblages M13- NPs d’Au (9 et 13 nm), l'amélioration de 2PEF suggère la formation d'une structure plasmonique à court ou long terme de commande des NPs d’Au sur M13. En effet, la probabilité de la première transition intra bande sp-sp au cours de l'excitation de deux photons de NP d’Au est liée à la résonance plasmonique de la surface localisée de la particule. Du fait que la section efficace d'absorption des petites NPs d’Au sphériques à 816 nm est négligeable, l'excitation de 2PEF à cette longueur d'onde n'est possible que lorsque le plasmon de surface génère une bande d'absorption à cette longueur d'onde. Le couplage inter-particulaire est attendu lorsque l'espacement entre les NPs d’Au est plus petit que le diamètre de la particule qui est un paramètre crucial pour observer le couplage plasmonique, ce qui est le cas pour les assemblages des NPs d’Au de 9 nm sur le phage M13 (~6.34 nm basé sur l'analyse MET). Comparé aux assemblages préparés avec des NPs d’Au de 9 nm, une intensité du

signal 2PEF plus élevée a été observée pour ceux préparés avec des NPs d' Au de 13 nm. L'intensité moyenne du signal 2PEF des assemblages des NPs de 13 nm était de 135,53 U.A alors que celle déterminée pour les assemblages préparés avec des NPs d' Au de 9 nm était de 97.13 U.A (Figure 12). L'amélioration de 2PEF a été attribuée à l'augmentation du champ électrique dépendante de la taille, et au changement de la longueur d'onde d'excitation dépendant aussi de la taille On sait que les NPs plus grandes ont un champ électrique induit par plasmon plus grand, ce qui crée un couplage de plasmon plus fort et des améliorations de champ électrique plus fortes dans leur proximité. En raison du fort couplage plasmon entre les NPs d' Au, la surface des plasmons des particules sera décalé vers le rouge et entraînera une augmentation de la longueur d'onde d'excitation (dans la région proche infrarouge), qui fournira plus d'états intermédiaires pour induire le processus d'excitation à deux photons.

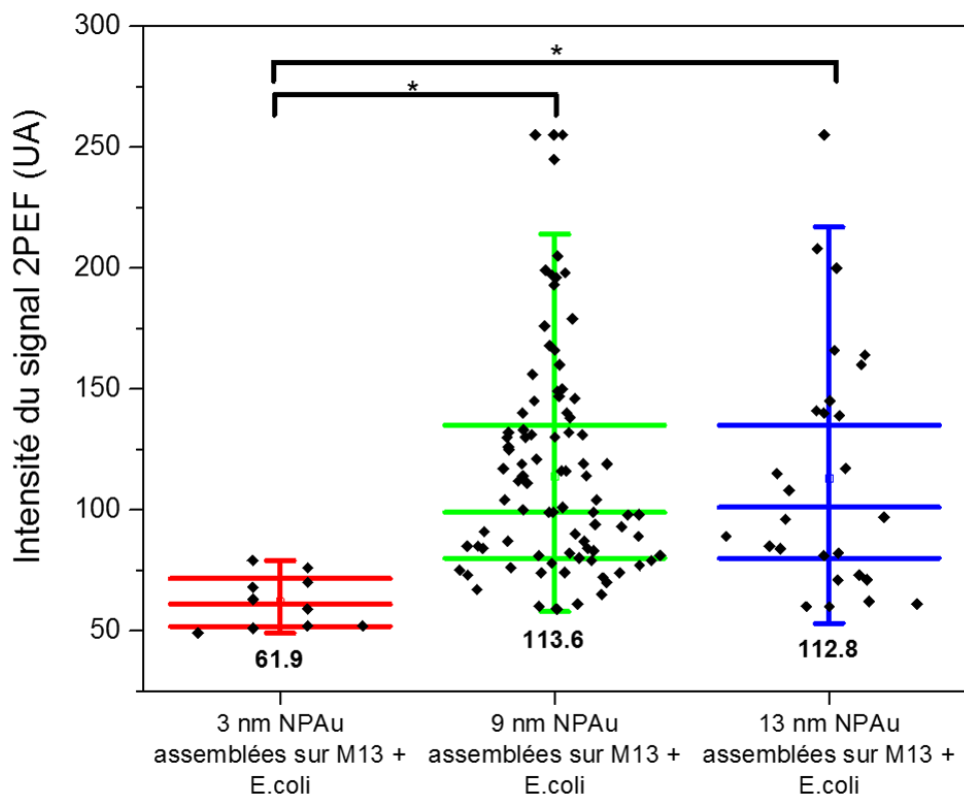


Figure 13. Diagramme en boîte tracé pour comparer les intensités du signal 2PEF des assemblages des NPs d' Au sur la matrice M13 en présence des cellules *E. coli*. Dans chaque boîte, la ligne horizontale en haut indique le troisième quartile, la ligne horizontale près du milieu indique la médiane et la ligne horizontale en bas indique le premier quartile. Les losanges noirs qui se chevauchent avec les boîtes représentent l'intégralité des données des échantillons. Les valeurs numériques sous chaque case indiquent la valeur moyenne de l'ensemble de données. (* P < 0,05).

Afin d'évaluer l'effet des bactéries sur l'intensité du signal 2PEF des assemblages M13-NPs, des images ont été acquises après une incubation des assemblages avec des cellules de *E. coli*, qui sont la cible

naturelle de M13. La liaison des assemblages M13-AuNP aux bactéries a légèrement affecté l'intensité du signal 2PEF (Figure 13). L'analyse quantitative des images traitées des assemblages préparés avec des NPs d'Or de 3 nm, révélait que ces derniers produisaient très peu de pixels positifs, indiquant que l'intensité moyenne du signal 2PEF pour ces assemblages, si elle se produisait, tombait largement dans le régime du bruit de fond. Pour les assemblages M13-NPs d'Or préparés avec des NPs de 9 nm et 13 nm, les intensités moyennes des signaux 2PEF des images traitées de ces deux échantillons étaient similaires en absence et en présence de bactéries. Au final, cette section démontre que les assemblages M13-NPs sélectionnées améliorent significativement le signal 2PEF à un niveau qui se distingue facilement du bruit de fond, ce qui est prometteur pour leur utilisation en tant qu'agents de contraste d'image.

Dans le cas du phage Cys-C, les assemblages des NPs d'Or produisaient des intensités de signaux 2PEF qui étaient comparables, bien que légèrement inférieures à celles produites par les assemblages sur le modèle M13.

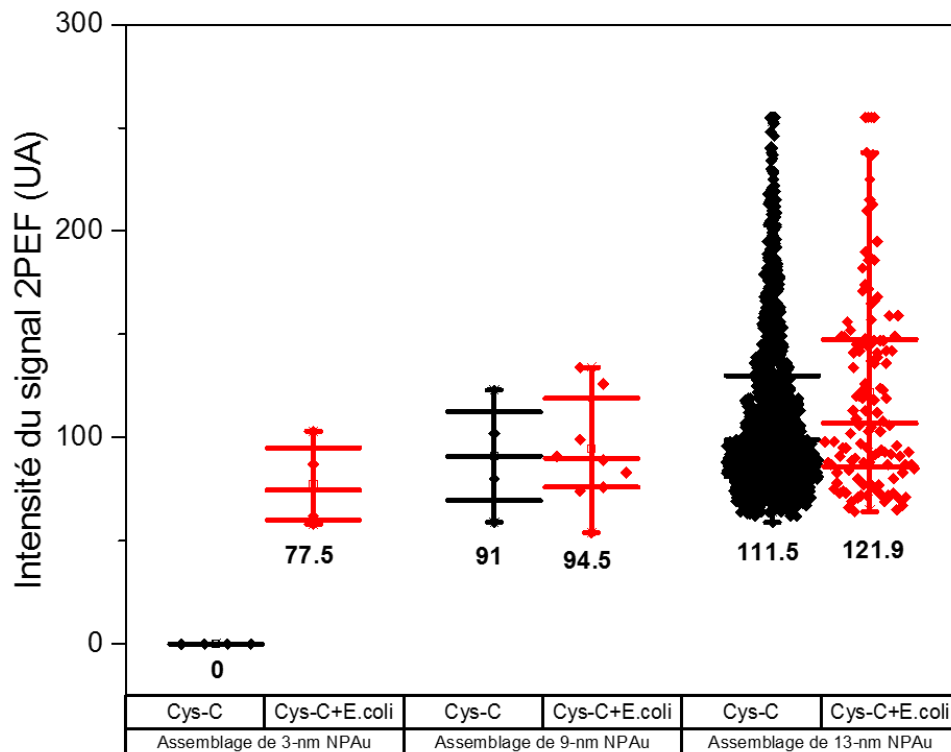


Figure 14. Diagramme en bâtons tracé pour comparer les intensités des signaux 2PEF des assemblages des NPs d'Or calquées sur Cys-C. Dans chaque boîte, la ligne horizontale en haut indique le troisième quartile, la ligne horizontale près du milieu indique la médiane et la ligne horizontale en bas indique le premier quartile. Les diamants noirs et rouges qui se chevauchent avec les boîtes représentent l'intégralité des données des échantillons. Les valeurs numériques sous chaque case indiquent la valeur moyenne de l'ensemble de données. (* P < 0,05).

Cependant, le nombre de signaux positifs pour les assemblages composés de NPs d' Au de 3 et 9 nm était assez faible, ce qui indique que très peu d'assemblages produisent un signal positif. Cela suggère que soit l'amélioration moyenne du signal 2PEF de ces assemblages était très faible (équivalente au signal du fond), soit que les assemblages se dissociaient au cours de la manipulation. En revanche, les assemblages Cys-C produits avec des NPs de 13 nm ont généré de nombreux pixels positifs indiquant que le processus d'assemblage produisait de manière fiable des assemblages actifs sur le plan plasmonique. En effet, à l'exception des assemblages préparés avec des NPs d' Au de 3 nm, la différence entre l'intensité moyenne du signal 2PEF des assemblages des NPs d' Au sur la matrice Cys-C, avec / sans cellule *E.coli*, n'était pas statistiquement significative. En général, les faibles intensités du signal des assemblages sur la matrice Cys-C pourraient être dues à la disposition des NPs d' Au sur la surface des phages avec une distance inter-particules non favorable pour un couplage plasmonique fort et une augmentation du signal 2PEF, de manière correspondante. Comme il l'a été mentionné précédemment, les assemblages des NPs d' Au de 13 nm modélisés sur le phage Cys-C ont été significativement affectés par l'étape de séchage dans la préparation de l'échantillon où la déshydratation des particules de phage a entraîné le démontage des assemblages.

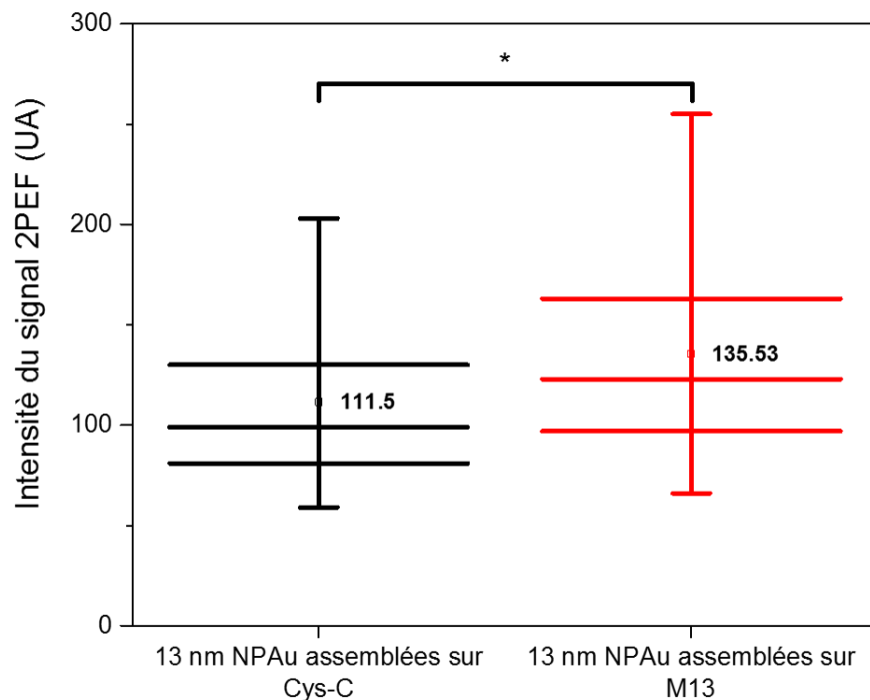


Figure 15. Diagramme en boîte tracé pour comparer les intensités du signal 2PEF des AuNP assemblées sur les phages Cys-C et M13. Dans chaque boîte, la ligne horizontale en haut indique le troisième quartile, une ligne horizontale près du milieu indique la médiane et la ligne horizontale en bas indique le premier quartile. Les valeurs numériques au-dessus de chaque boîte indiquent la valeur moyenne de l'ensemble de données. (* P < 0,05).

Néanmoins, les assemblages Cys-C-NP Au(13 nm) ont produit un signal 2PEF fiable, qui était comparable en amplitude, quoique légèrement inférieur à celui observé pour les assemblages équivalents préparés avec M13. Cette différence pourrait s'expliquer par différentes géométries spatiales des assemblages des NPs d'Or modélisés sur les phages M13 et T4 et leurs stabilités correspondantes. La structure allongée et mince du phage M13 fournit un matériau de matrice flexible pour l'assemblage des NPs d'Or et améliore leur stabilité vis-à-vis de la déshydratation survenant lors de la préparation de l'échantillon. Ces résultats s'expliquent très probablement par un manque de stabilité des assemblages. En effet, il a déjà été montré que les assemblages des NPs d'Or modélisés sur le phage Cys-C ne sont pas suffisamment stables pour rester intacts pendant l'étape de séchage au cours de la préparation de l'échantillon

CONCLUSION AND PERSPECTIVES

Conclusion

La conclusion la plus significative de cette thèse est que, des très petites NPs d'Or assemblées sur des bactériophages possèdent des caractéristiques essentielles pour leur utilisation en tant qu'agents de contraste d'imagerie sélective pour la SERS et le signal 2PEF, en termes d'amélioration du signal, de stabilité de la manipulation des échantillons et de capacité de se lier à une cible spécifique. À cet égard, on a constaté que des NPs d'Or de 13 nm de diamètre créent des points chauds, produisant un rehaussement de la SERS. La génération de points chauds entre les NPs assemblées sur la surface des phages a permis la détection du rapporteur Raman BSPP dans les lacunes. Aucun des NPs d'Or utilisées dans ce travail n'a montré l'activité de la SERS individuellement. Parmi tous les assemblages des NPs sur la matrice phagique, M13 a montré l'activité SERS la plus élevée.

En ce qui concerne les assemblages sur T4, les phages présentant des résidus de cystéine sur C / N-terminus de la protéine Soc étaient les seuls modèles qui produisaient des assemblages stables avec les NPs d'Or, bien que l'affichage des résidus cystéine sur l'extrémité C-terminale aboutisse à des assemblages de NPs plus stables, et à une amélioration plus élevée de la SERS. Dans le cas d'études de microscopie 2PEF, des NPs d'Or isolées de tailles 3-13 nm n'ont pas présenté une émission du 2PEF par elles-mêmes. Lors de leur assemblage sur le phage M13, on a observé une amélioration du 2PEF reproductible, uniquement avec des NPs d'Or de diamètres 9 et 13 nm. Les assemblages Cys-C-NPs d'Or de 13 nm ont produit un signal 2PEF fiable, dont la magnitude était comparable, quoique légèrement inférieure à celle observée pour les assemblages équivalents préparés avec M13. La différence entre les

améliorations des assemblages modélisés sur les phages M13 et T4 pourrait s'expliquer par différentes géométries spatiales des assemblages des NPs d'Or sur les phages M13 et T4 et leurs stabilités correspondantes. La structure allongée et mince du phage M13 fournit un matériau de matrice flexible pour l'assemblage des NPs d'or, et améliore leur stabilité vis-à-vis de la déshydratation survenant lors de la préparation de l'échantillon.

Ces résultats peuvent être expliqués par un manque de stabilité des assemblages. En comparant notre système à d'autres systèmes existants dans la littérature, l'utilisation de très petites NPs d'Or (≥ 13 nm pour SERS et $\geq 9-13$ nm pour 2PEF) est avantageuse car ils n'interfèrent pas avec la liaison de la cible, ce qui est nécessaire pour le marquage de la cible biologique spécifique. De plus, les NPs d'Or individuelles 'isolées' de cette taille sont trop petites pour produire un signal dans SERS ou 2PEF, ce qui élimine une source possible du bruit de fond provenant de la dégradation de l'assemblage. Pour cela, les résultats rapportés ici sont originaux et contribuent à l'avancement des connaissances dans un domaine important dans lequel il y a peu de données.

Perspectives

Le contenu scientifique de cette thèse ouvre la voie à de futures expériences. Par exemple, une limitation majeure de ce travail était le manque de stabilité de plusieurs assemblages de « phages-NPs d'Or » vers le séchage pendant la préparation de l'échantillon, ce qui a réduit l'ampleur des conclusions qui devaient être établies à partir de la bibliothèque conçue. Malheureusement, l'analyse des propriétés plasmoniques des assemblages en solution était techniquement difficile en raison du niveau élevé de dilution, bien que des solutions à ce problème puissent être prévues. L'accès aux propriétés SERS / 2PEF de ces assemblages métastables, probablement en fonction de la densité de greffage de la nanoparticule d'or, fournirait un ensemble de données supplémentaire qui pourrait être plus facilement comparé aux simulations plasmoniques.

L'accès à des données et méthodologies supplémentaires pour analyser les propriétés optiques des assemblages sous leur forme colloïdale (c'est-à-dire en solution), permettra à son tour leur analyse dans des matrices plus complexes. Par exemple, le signal quantitatif issu des assemblages pourrait être exploité pour la détection des bactéries dans des matrices aqueuses complexes telles que les eaux usées (ou autres). En outre, parce que les protéines de capsid non impliquées dans la liaison des NPs d'Or peuvent être modifiées pour afficher des fragments de ciblage pour de nombreuses autres cibles d'importance biologique, ainsi l'exploration de leur utilisation en tant qu'agents de contraste dans des mélanges de populations cellulaires serait intéressant.

Enfin, une observation inattendue a été faite au cours de cette thèse qui justifie une enquête supplémentaire, plus précisément, dans le chapitre 2, est que les assemblages « M13-NPAu » ont été analysés par un Immuno-essai enzymatique pour leur capacité du phage à conserver leur capacité de ciblage malgré la présence des NPs d' Au sur leur surface. Dans ce test, un conjugué anti-M13-[Horseradish peroxidase] a été utilisé comme anticorps secondaire pour la quantification de la quantité d'assemblage lié à la cible. Lorsque le substrat enzymatique de la Peroxydase de raifort a été ajouté aux puits de l'échantillon, une amélioration spectaculaire de l'activité catalytique a été observée lorsque les NPs d' Au étaient liées au phage. Alors que, l'amélioration de l'activité catalytique de certaines enzymes peut être améliorée par l'adsorption sur les NPs d' Au. Les améliorations observées sont généralement de 2 à 4 fois [34-36]. L'amélioration observée dans ce travail, de 50 à 100 fois, est remarquable et peut être attribuée à un transfert d'électron par appui des effets plasmoniques. Pour cela, l'étude du mécanisme de ce phénomène ainsi que ses applications potentielles sont clairement importantes.

TABLE OF CONTENTS

ACKNOWLEDGEMENTS	II
ABSTRACT	IV
RÉSUMÉ	VI
TABLE OF CONTENTS	XXXVIII
LIST OF TABLES	XLII
LIST OF FIGURES	XLIV
1 INTRODUCTION	1
1.1 Problematic.....	1
1.2 Template-assisted production of plasmonic nanostructures	3
1.3 Phage-templated strategies for fabrication of plasmonic nanostructures.....	6
1.4 Overview of this thesis.....	11
1.5 Structure of this thesis	13
2 M13 PHAGE-TEMPLATED AuNP ASSEMBLIES	14
2.1 Introduction	14
2.1.1 Structure and Characteristics of M13 Bacteriophage.....	14
2.1.2 M13 Phage Display Platform.....	15
2.1.3 M13-templated self-assembly of AuNPs.....	17
2.2 Materials and Methodology	20
2.2.1 Materials	20
2.2.2 Engineering of M13 Phage Template.....	20
2.2.3 Synthesis and Characterization of AuNPs	23
2.2.4 Self-Assembly of AuNPs on M13 Phage template	26
2.3 Results and Discussion	29
2.3.1 M13 Phage template displaying gold-binding moieties and RGD peptide	29
2.3.2 BSPP-passivated AuNPs.....	30
2.3.3 Self-assembly of AuNPs on M13 Phage Template	32
2.3.4 Integrin Targeting Ability of RGD peptide on M13-templated Gold Assemblies.....	40
2.4 Conclusion.....	42

3	T4 PHAGE-TEMPLATED AuNP ASSEMBLIES	43
3.1	Introduction	43
3.1.1	Structure and Characteristics of T4 Bacteriophage	43
3.1.2	T4 Phage Display Platform	44
3.1.3	Self-assembly of T4 phage surface with organic/inorganic materials	46
3.2	Materials and Methodology	47
3.2.1	Materials	47
3.2.2	Engineering of T4 Phage Templates.....	48
3.2.3	Self-Assembly of AuNPs on T4 Phage templates	51
3.3	Results and Discussion	53
3.3.1	Engineering of T4 phage to display gold binding moieties on Soc protein.....	53
3.3.2	Self-assembly of AuNPs on T4 phage templates.....	56
3.4	Conclusion.....	75
4	PHAGE-TEMPLATED AuNP ASSEMBLIES AS SERS-IMAGING CONTRAST AGENTS	78
4.1	Introduction	78
4.1.1	Surface enhanced Raman scattering (SERS)	78
4.1.2	Plasmonic nano-architectures as SERS-active material	79
4.2	Materials and Methods.....	84
4.2.1	Materials	84
4.2.2	Preparation of Bacterial Strains and Bacteriophages	84
4.2.3	Hydrophobic Treatment of Glass Slides.....	85
4.2.4	Preparation of Phage-templated Au Assemblies for SERS Analysis.....	85
4.2.5	SERS Mapping on Glass Slides.....	86
4.2.6	Determination of the SERS Enhancement Factor	87
4.3	Results and Discussion	88
4.3.1	SERS activity of M13-templated AuNP assemblies	89
4.3.2	SERS-activity of T4-templated AuNP assemblies	91
4.3.3	Effect of binding ligand	96
4.3.4	Chemical enhancement of SERS via graphitization of Reporter molecule	97
4.4	Conclusion.....	99
5	PHAGE-TEMPLATED AuNP ASSEMBLIES AS CONTRAST AGENT FOR NONLINEAR MICROSCOPY..	101

5.1	Introduction	101
5.2	Materials and Methods.....	103
5.2.1	Materials	103
5.2.2	Preparation of Bacterial Strains and Bacteriophages	103
5.2.3	Hydrophobic Treatment of Glass Slides.....	104
5.2.4	Preparation of Phage-templated AuNP Assemblies for 2PEF Analysis	104
5.2.5	2PEF Microscopy of Samples on Glass Slides.....	106
5.2.6	Quantification of 2PEF image signals.....	106
5.3	Results and Discussion	107
5.3.1	2PEF of M13–AuNP assemblies.....	109
5.3.2	2PEF of T4-AuNP assemblies.....	112
5.3.3	Comparison to other 2PEF contrast agents	115
5.4	Conclusion.....	117
6	CONCLUSION AND FUTURE WORK	119
6.1	Most significant findings and contribution to the advancement of knowledge	119
6.2	Future directions.....	120
7	REFERENCES	122
8	APPENDICES	139
8.1	Appendix A: DLS histograms of phage/AuNP reaction solutions at different ionic strengths..	139
8.2	Appendix B: SERS maps of the samples analyzed in Chapter 4	148
8.3	Appendix C. 2PEF images of the samples analyzed in Chapter 5.....	151

LIST OF TABLES

Table 2.2.1 Oligonucleotide sequences for M13 phage p3 cloning.	21
Table 2.2.2 Oligonucleotide sequences for M13 phage p8 cloning.	22
Table 3.2.1 Primer sequences for T4 phage display of gold binding peptides.	50

LIST OF FIGURES

Figure 1.3.1 Schematic structures of the liquid-crystalline phases of M13 bacteriophages a) Isotropic, b) nematic, c) smectic A, and d) smectic C phases. 7

Figure 2.1.1 Structure of M13 bacteriophage (a) Schematic representation of M13 phage virion showing the single-stranded DNA core surrounded by 5 coat proteins; p8, p3, p6, p7 and p9 (b) Repeating array of major coat protein (p8) represented as ribbon. Reproduced with permission from [144] (c) Domain structure of p3 protein. Three domains of p3 are presented as N1, N2 (N terminal domains) and CT (C terminal domain) which are separated by glycine rich linker sequences (Gly1 and Gly2). Numbers refer to the residues in mature protein sequence. Adapted from [145]..... 15

Figure 2.1.2 Classification of phage display systems In phage system (type 3), fusion of insert gene into gene 3 results in fusion proteins on all copies of p3 coat protein. In phagemid system (type 3+3), gene 3 inserted with fusion gene is carried on a phagemid and wild type gene 3 is provided by helper phage. Phage display using phagemid system results in hybrid phages displaying only few copies of fusion coat proteins. In hybrid system (type 33), the phage genome contains two copies of gene 3, one with an insert and one without. As in phagemid system, it also results in hybrid phages displaying few copies of fusion coat proteins. Type 8, 8+8 and 88 are the corresponding types for inserts in gene 8. Adapted from [160].
..... 17

Figure 2.3.1 Detection of RGD peptide insertions in M13KE cloning vector by PCR. Marker, molecular size standard; lane 1-3, PCR product of M13KE phage (300 bp); lane 2-4-5, PCR product indicating the presence of linear GRGDSP peptide fusion in M13KE phage (327 bp)..... 30

Figure 2.3.2 TEM images and corresponding size distribution histograms of BSPP-passivated AuNPs..... 31

Figure 2.3.3 UV-Vis absorption spectra of BSPP-passivated AuNPs with diameters of 3 nm (black line), 9 nm (red line) and 13 nm (blue line). 32

Figure 2.3.4 DLS histograms for volume based size analysis of M13 phage-3 nm AuNP solutions in a) 5 mM, b) 10 mM, c) 25 mM, d) 50 mM and e) 100 mM phosphate buffers. DLS histograms of each sample solution were recorded for a 5 day period. 34

Figure 2.3.5 Characterization of 3 nm AuNPs self-assembled on M13 phage template after 1 day reaction a) DLS histograms showing the size of 3 nm AuNPs, M13 phage and M13-templated gold assemblies. b) UV-Vis spectra of 3 nm AuNPs in colloidal solution (solid line) and self-assembled on M13 phage template (dashed line). c) TEM image of M13 phage stained with uranyl acetate (2%) d) TEM image of 3 nm AuNPs assembled on M13 phage stained with uranyl acetate (2%)..... 36

Figure 2.3.6 DLS histograms for volume based size analysis of M13 phage-9 nm AuNPs solutions in a) 10 mM and b) 25 mM phosphate buffers. DLS histograms of each sample solution were recorded for a 5 day period.....	37
Figure 2.3.7 Characterization of 9 nm AuNPs assembled on M13 phage template after 1 day reaction a) DLS histograms showing the size of 9 nm AuNPs, M13 phage and M13-templated gold assemblies. b) UV-Vis spectra of 9 nm AuNPs in colloidal solution (solid line) and self-assembled on M13 phage template (dashed line). The inset shows the ~2 nm red shift in the SPR band due to the assembly of AuNPs on phage template. c) TEM image of 9 nm AuNPs assembled on M13 phage d) High magnification TEM image of 9 nm AuNPs assembled on M13 phage stained with uranyl acetate (0.5%).	38
Figure 2.3.8 DLS histograms for volume based size analysis of M13 phage-13 nm AuNPs solutions in a) 10 mM and b) 25 mM phosphate buffers. DLS histograms of each sample solution were recorded for a 5 day period.....	39
Figure 2.3.9 Characterization of 13 nm AuNPs assembled on M13 phage template after 1 day reaction a) DLS histograms showing the size of 13 nm AuNPs, M13 phage and M13-templated gold assemblies. b) UV-Vis spectra of 13 nm colloidal AuNPs (solid line) and self-assembled on M13 phage template (dashed line). The inset shows the ~3 nm red shift in the SPR band from 525 nm to 528 nm due to the assembly of AuNPs on phage template. c) TEM image of 13 nm AuNPs assembled on M13 phage d) High magnification TEM image of 13 nm AuNPs assembled on M13 phage.	40
Figure 2.3.10 ELISA plate showing the color development due to the binding of integrin to RGD bearing M13 phage-templated gold assemblies. The wells in the first line of ELISA plate contain the samples which are prepared using 3 nm AuNPs whereas the samples in the second line and the third line are composed of 9 nm and 13 nm AuNPs, respectively.	41
Figure 2.3.11 Reactivity of RGD bearing M13 phage-templated Au assemblies and colloidal AuNPs with human integrin protein.....	41
Figure 3.1.1 Structure of T4 Bacteriophage (a) Schematic representation of T4 phage virion (b) Model of proposed T4 head structure (adapted from [214]).	44
Figure 3.3.1 Schematic presentation of pRH plasmid, mutant T4-Z1 and recombinant T4 phage (T4-Z1-SOC-insert).	54
Figure 3.3.2 Detection of the insertion of gold binding sequence fused Soc gene into pRH plasmid by PCR. (a) Marker, molecular size standard; lane 1, PCR product of AYSSGAPMPPF inserted into C-terminal of Soc gene (288 bp); lane 2, PCR product of AYSSGAPMPPF inserted into N-terminal of Soc gene (288 bp) (b) Marker, molecular size standard; lane 1, PCR product of VSGSSPDS inserted into C-terminal of Soc gene	

(276 bp); lane 2, PCR product of VSGSSPDS inserted into N-terminal of Soc gene (276 bp) (c) Marker, molecular size standard; lane 1, PCR product of cysteine inserted into C-terminal of Soc gene (255 bp); lane 2, PCR product of cysteine inserted into N-terminal of Soc gene (255 bp). 54

Figure 3.3.3 Detection of gold binding sequence fused Soc gene insertion into the T4 genome by PCR. (a) Marker, molecular size standard; lane 1-2, PCR product indicating the presence of AYSSGAPMPPF peptide fusion on C-terminal of Soc gene (288 bp); lane 3-4, PCR product indicating the presence of AYSSGAPMPPF peptide fusion on N-terminal of Soc gene (288 bp) (b) Marker, molecular size standard; lane 1, PCR product indicating the presence of VSGSSPDS peptide fusion on C-terminal of Soc gene (276 bp); lane 2, PCR product indicating the presence of VSGSSPDS peptide fusion on N-terminal of Soc gene (276 bp) (c) Marker, molecular size standard; lane 1, PCR product indicating the presence of cysteine fusion on C-terminal of Soc gene (255 bp); lane 2, PCR product indicating the presence of cysteine fusion on N-terminal of Soc gene (255 bp). 55

Figure 3.3.4 Size-exclusion chromatography (SEC) elution profile of T4 phage sample. Elution patterns corresponding to protein content (indicated in gray) and phage content (indicated in orange) of T4 phage solution. 56

Figure 3.3.5 Schematic of T4 phage capsid structure showing the disposition of C- and N-termini of Soc protein. 57

Figure 3.3.6 DLS measurements of reaction solutions including 3-nm AuNPs and Cys-N phage template. DLS histograms for volume-based size analysis of Cys-N phage–3 nm AuNP solutions in a) 50 mM, b) 100 mM, c) 150 mM, and d) 200 mM phosphate buffers. DLS histograms of each sample solution were recorded for a 5 day period. 58

Figure 3.3.7 Characterization of 3-nm AuNPs self-assembled on Cys-N template after 2 days reaction. a) DLS histograms showing the size of 3 nm AuNPs, Cys-N phage and Cys-N-templated gold assemblies. b) UV-Vis spectra of 3 nm colloidal AuNPs (solid line) and self-assembled on Cys-N phage template (dashed line). c) TEM image of wild type T4 phage stained with uranyl acetate (2%) d) TEM image of 3 nm AuNPs assembled on Cys-N phage stained with uranyl acetate (2%). 59

Figure 3.3.8 DLS histograms for volume-based size analysis of Cys-N phage-9 nm AuNP solutions in a) 25 mM, b) 50 mM, and c) 100 mM phosphate buffers. DLS histograms of each sample solution were recorded for a 5 day period. 60

Figure 3.3.9 Characterization of 9-nm AuNPs self-assembled on Cys-N template after 2 days reaction. a) DLS histograms showing the size of 9 nm AuNPs, Cys-N phage and Cys-N-templated gold assemblies. b)

UV-Vis spectra of 9 nm colloidal AuNPs (solid line) and self-assembled on Cys-N phage template (dashed line). c-d) TEM image of 9 nm AuNPs assembled on Cys-N phage. 62

Figure 3.3.10 DLS histograms for volume-based size analysis of Cys-N phage-13 nm AuNPs solutions in a) 25 mM and b) 50 mM phosphate buffers. DLS histograms of each sample solution were recorded for a 5 day period. 63

Figure 3.3.11 Characterization of 13-nm AuNPs self-assembled on Cys-N template after 2 days reaction. a) DLS histograms showing the size of 13-nm AuNPs, Cys-N phage and Cys-N-templated gold assemblies. b) UV-Vis spectra of 13-nm colloidal AuNPs (solid line) and self-assembled on Cys-N phage template (dashed line). c-d) TEM images of 13 nm AuNPs assembled on Cys-N phage..... 64

Figure 3.3.12 Characterization of 3-nm AuNPs self-assembled on Cys-C template. a) DLS histograms for volume based size analysis of Cys-C phage–3-nm AuNP solutions in 200 mM phosphate buffer. DLS histograms were recorded for a 5 day period. b) DLS histograms showing the size of 3 nm AuNPs, Cys-C phage and Cys-C-templated gold assemblies after 2 days reaction. c) UV-Vis spectra of 3-nm colloidal AuNPs (solid line) and self-assembled on Cys-C phage template (dashed line) after 2 days reaction. d) TEM image of 3 nm AuNPs assembled on Cys-C phage..... 65

Figure 3.3.13 Characterization of 9 nm AuNPs self-assembled on Cys-C template. a) DLS histograms for volume based size analysis of Cys-C phage–9 nm AuNPs solutions in 50 mM phosphate buffer. DLS histograms were recorded for a 5 day period. b) DLS histograms showing the size of 9 nm AuNPs, Cys-C phage and Cys-C-templated gold assemblies after 2 days reaction. c) UV-Vis spectra of 9 nm colloidal AuNPs (solid line) and self-assembled on Cys-C phage template (dashed line) after 2 days reaction. d) TEM image of 9 nm AuNPs assembled on Cys-C phage..... 66

Figure 3.3.14 Characterization of 13-nm AuNPs self-assembled on Cys-C template. a) DLS histograms for volume based size analysis of Cys-C phage–13-nm AuNP solutions in 25 mM phosphate buffer. DLS histograms were recorded for a 5 day period. b) DLS histograms showing the size of 13-nm AuNPs, Cys-C phage and Cys-C-templated gold assemblies after 2 days reaction. c) UV-Vis spectra of 13-nm colloidal AuNPs (solid line) and self-assembled on Cys-C phage template (dashed line) after 2 days reaction. d) TEM image of 13 nm AuNPs assembled on Cys-C phage..... 67

Figure 3.3.15 Characterization of 3 nm AuNPs self-assembled on A3-N template. a) DLS histograms showing the size of 3-nm AuNPs, A3-N phage and A3-N-templated gold assemblies after 2 days reaction. b) UV-Vis spectra of 3 nm colloidal AuNPs (solid line) and self-assembled on A3-N phage template (dashed line) after 2 days reaction. 69

Figure 3.3.16 Characterization of 3-nm AuNPs self-assembled on A3-C template. a) DLS histograms showing the size of 3 nm AuNPs, A3-C phage and A3-C-templated gold assemblies after 2 days reaction. b) UV-Vis spectra of 3 nm colloidal AuNPs (solid line) and self-assembled on A3-C phage template (dashed line) after 2 days reaction. 69

Figure 3.3.17 Characterization of 9-nm AuNPs self-assembled on A3-N template. a) DLS histograms showing the size of 9-nm AuNPs, A3-N phage and A3-N-templated gold assemblies after 2 days reaction. b) UV-Vis spectra of 9-nm colloidal AuNPs (solid line) and self-assembled on A3-N phage template (dashed line) after 2 days reaction. 70

Figure 3.3.18 Characterization of 9-nm AuNPs self-assembled on A3-C template. a) DLS histograms showing the size of 9-nm AuNPs, A3-C phage and A3-C-templated gold assemblies after 2 days reaction. b) UV-Vis spectra of 9-nm colloidal AuNPs (solid line) and self-assembled on A3-C phage template (dashed line) after 2 days reaction. 70

Figure 3.3.19 Characterization of 13-nm AuNPs self-assembled on A3-N template. a) DLS histograms showing the size of 13-nm AuNPs, A3-N phage and A3-N-templated gold assemblies after 2 days reaction. b) UV-Vis spectra of 13-nm colloidal AuNPs(solid line) and self-assembled on A3-N phage template (dashed line) after 2 days reaction. 71

Figure 3.3.20 Characterization of 13-nm AuNPs self-assembled on A3-C template. a) DLS histograms showing the size of 13 nm AuNPs, A3-C phage and A3-C-templated gold assemblies after 2 days reaction. b) UV-Vis spectra of 13 nm colloidal AuNPs (solid line) and self-assembled on A3-C phage template (dashed line) after 2 days reaction. 71

Figure 3.3.21 Characterization of 3-nm AuNPs assembled on GB-N template. a) DLS histograms showing the size of 3-nm AuNPs, GB-N phage and GB-N-templated gold assemblies after 2 days reaction. b) UV-Vis spectra of 3-nm colloidal AuNPs (solid line) and self-assembled on GB-N phage template (dashed line) after a 2-day reaction..... 72

Figure 3.3.22 Characterization of 3-nm AuNPs self-assembled on GB-C template. a) DLS histograms showing the size of 3-nm AuNPs, GB-C phage and GB-C-templated gold assemblies after 2 days reaction. b) UV-Vis spectra of 3-nm colloidal AuNPs (solid line) and self-assembled on GB-C phage template (dashed line) after 2 days reaction. 73

Figure 3.3.23 Characterization of 9 nm AuNPs self-assembled on GB-N template. a) DLS histograms showing the size of 9 nm AuNPs, GB-N phage and GB-N-templated gold assemblies after 2 days reaction. b) UV-Vis spectra of 3 nm colloidal AuNPs (solid line) and self-assembled on GB-N phage template (dashed line) after 2 days reaction. 73

Figure 3.3.24 Characterization of 9 nm AuNPs self-assembled on GB-C template. a) DLS histograms showing the size of 9 nm AuNPs, GB-C phage and GB-C-templated AuNP assemblies after 2 days reaction. b) UV-Vis spectra of 3 nm colloidal AuNPs (solid line) and self-assembled on GB-C phage template (dashed line) after 2 days reaction.	74
Figure 3.3.25 Characterization of 13 nm AuNPs self-assembled on GB-N template. a) DLS histograms showing the size of 13 nm AuNPs, GB-N phage and GB-N-templated AuNP assemblies after 2 days reaction. b) UV-Vis spectra of 3 nm colloidal AuNPs (solid line) and self-assembled on GB-N phage template (dashed line) after 2 days reaction.	74
Figure 3.3.26 Characterization of 13 nm AuNPs self-assembled on GB-C template. a) DLS histograms showing the size of 13 nm AuNPs, GB-C phage and GB-C-templated AuNP assemblies after 2 days reaction. b) UV-Vis spectra of 3 nm colloidal AuNPs (solid line) and self-assembled on GB-C phage template (dashed line) after 2 days reaction.	75
Figure 4.3.1 Schematic representation of sample preparation and SERS signal detection.	88
Figure 4.3.2 a) Representative histogram showing the SERS intensity distribution of 13 nm AuNPs assembled on M13 phage template. b) Corresponding SERS map of M13-templated Au assemblies used to plot the histogram. c) The SERS spectrums representing the background of the SERS map without hot spots (I) and the region of M13-templated Au assemblies with hot spots (II).	88
Figure 4.3.3 a) Representative Raman spectra of (bulk) BSPP (20x), and SERS spectra of BSPP adsorbed on 3–13 nm AuNPs (cast on microscope slide). b) Representative SERS spectra of M13-templated AuNP assemblies in the absence and presence of <i>E.coli</i> cell.....	89
Figure 4.3.4 Histogram showing the SERS intensity distribution of 13 nm AuNPs assembled on M13 in the presence (black column) and in the absence of <i>E.coli</i> cell (red column).....	91
Figure 4.3.5 a) Representative SERS spectra of AuNPs assembled on Cys-N phage in the absence and presence of <i>E.coli</i> cell. b) Representative SERS spectra of AuNPs assembled on Cys-C phage in the absence and presence of <i>E.coli</i> cell.....	92
Figure 4.3.6 Representative distribution of SERS signal intensities of 13 nm AuNPs assembled on Cys-N (black) and Cys-C (red) templates. In each box, the top of the rectangle indicates the third quartile, a horizontal line near the middle of the rectangle indicates the median, and the bottom of the rectangle indicates the first quartile. The mean values and maximum values are represented by squares (□) and lines (–) on the top, respectively. (*P<0.05).	93
Figure 4.3.7 a) Schematic of T4 phage capsid structure showing the disposition of C- (red dot) and N-termini (green dot) of Soc protein (drawn in blue). The distance between the centers of two Soc trimeric	

junctions (~8 nm) is shown in yellow. b) Representative scheme showing the disposition of AuNPs centered on the Soc trimeric junctions. c) Representative image showing the disposition of AuNPs centered on the Soc dimeric junctions. 94

Figure 4.3.8 Representative distribution of SERS signal intensities of 13 nm AuNPs assembled on Cys-N (red), Cys-C (green), and M13 (blue) templates. In each box, the top of the rectangle indicates the third quartile, a horizontal line near the middle of the rectangle indicates the median, and the bottom of the rectangle indicates the first quartile. The mean values and maximum values are represented by squares (□) and lines (–) on top of the rectangles, respectively. (*P<0.05). 95

Figure 4.3.9 Representative SERS spectra of AuNPs assembled on A3-N phage (a), A3-C phage (b), GB-N phage (c), and GB-C phage (d). 96

Figure 4.3.10 Representative SERS spectra of M13-templated AuNP assemblies at different laser powers demonstrating the effect of graphitization within the plasmonic hotspots. 98

Figure 4.3.11 Representative distribution of SERS signal intensities recorded at high laser power (7.72 mW) and low laser power (1.75 mW) for 13 nm AuNPs assembled on M13 phage. In each box, the top of the rectangle indicates the third quartile, a horizontal line near the middle of the rectangle indicates the median, and the bottom of the rectangle indicates the first quartile. The mean values and maximum values are represented by squares (□) and lines (–) on the top, respectively. (*P<0.05). 98

Figure 5.3.1 a) Representative scheme of droplet casting of phage-templated AuNP assemblies on glass slide (I), sample drying (II) and instrument set-up employed to acquire the images of dried samples (III). b) Original image of 13 nm AuNPs assembled on M13 phage and corresponding histogram representing 2PEF signal intensity distribution. c) Processed image of 13 nm AuNPs assembled on M13 phage and corresponding histogram representing 2PEF signal intensity distribution..... 108

Figure 5.3.2 Representative 2PEF signal distribution histograms of isolated AuNPs and M13-templated AuNP assemblies with diameter of a) 3 nm, b) 9 nm, and c) 13 nm. d) The box chart plotted to compare the 2PEF signal intensities of isolated AuNPs with the 2PEF signal intensities of M13-templated AuNPs assemblies. In each box, the horizontal line on the top indicates the third quartile, a horizontal line near the middle indicates the median, and the horizontal line at the bottom indicates the first quartile. The blue and red diamonds overlapping with the boxes represent the entire data of the samples. The numerical values below each box indicate the mean value of the data set. (*P<0.05). 110

Figure 5.3.3 a) Representative 2PEF signal distribution histograms of M13-templated AuNP assemblies in the presence of *E.coli* cells. b) The box chart plotted to compare the 2PEF signal intensities of M13-templated AuNPs assemblies in the presence of *E.coli* cells. In each box, the horizontal line on the top

indicates the third quartile, a horizontal line near the middle indicates the median, and the horizontal line at the bottom indicates the first quartile. The black diamonds overlapping with the boxes represent the entire data of the samples. The numerical values below each box indicate the mean value of the data set. (*P<0.05). 111

Figure 5.3.4 The box chart plotted to compare the 2PEF signal intensities of Cys-C-templated AuNPs assemblies in the absence and in the presence of *E.coli* cells. In each box, the horizontal line on top indicates the third quartile, a horizontal line near the middle indicates the median, and the horizontal line at the bottom indicates the first quartile. The black and red diamonds overlapping with the boxes represent the entire data of the samples. The numerical values below each box indicate the mean value of the data set. (*P<0.05). 113

Figure 5.3.5 The box chart plotted to compare the 2PEF signal intensities of Cys-N-templated AuNPs assemblies in the absence and in the presence of *E.coli* cells. In each box, the horizontal line on top indicates the third quartile, a horizontal line near the middle indicates the median, and the horizontal line at the bottom indicates the first quartile. The black and red diamonds overlapping with the boxes represent the entire data of the samples. The numerical values below each box indicate the mean value of the data set. (*P<0.05). 114

Figure 5.3.6 The box chart plotted to compare the 2PEF signal intensities of AuNPs assembled on Cys-N, Cys-C and M13 phages. In each box, the horizontal line on top indicates the third quartile, a horizontal line near the middle indicates the median, and the horizontal line at the bottom indicates the first quartile. The red, green and blue diamonds overlapping with the boxes represent the entire data of the samples. The numerical values below each box indicate the mean value of the data set. (*P<0.05). 115

1 INTRODUCTION

1.1 Problematic

Recent advances in nanotechnology, particularly in methods of nanofabrication, have enabled the design of novel materials with enhanced properties, and “plasmonics” has been one of the growing fields driven by these developments. Plasmonics is a field that studies light–metal interactions and has attracted great attention due to its potential technological applications, ranging from energy to medicine [1]. The light–metal interactions arise from the capability of electromagnetic fields to induce coherent oscillations of the free electrons on metallic surfaces. Although the electromagnetic field can be propagated by the oscillation of electrons over a broad range of frequencies, a strong resonance is observed at a specific frequency, which is called the surface plasmon resonance (SPR) [2]. For instance, at the SPR frequency, coupling of the incident light to the electrons of the metal results in a strong local electric field enhancement at the nanoparticle’s surface as well as enhanced light absorption and scattering by the nanoparticle [3]. For metallic nanoparticles with sizes smaller than the wavelength of the incident light, optical absorption becomes dominant whereas it is accompanied by a strong optical scattering for larger particles [37]. Therefore, size is an important parameter that influences the optical properties of metals. Shape and composition are other factors that affect the optical properties of metals, and all three parameters can be engineered to fabricate metallic nanostructures with desired features for the application of interest [38].

SPR-enhanced optical properties have enabled the employment of metallic nanostructures in different applications. For instance, enhanced absorption and scattering properties make metals alternative optical labels for applications such as sensing and imaging [4, 5]. Unlike fluorophores, which are another group of optical labels, metallic nanoparticles do not photobleach or ‘blink’, and thus become intense and stable alternatives [6]. Moreover, by converting the energy of light into thermal energy, the metal nanoparticles can generate heat to destroy e.g., cancer cells for therapeutic interventions in medicine [7]. On the other hand, local electric field enhancement opens up other possibilities for the use of metallic nanostructures. The energy confined in small volumes around metallic nanoparticles provides a platform for enhancing the electronic transitions of optical absorbers or emitters placed in close proximity. Several optical processes such as surface enhanced Raman scattering (SERS), plasmon enhanced fluorescence (PEF), two-photon excited fluorescence (2PEF), and second harmonic generation

(SHG) can be enhanced in the spectral region around the SPR frequency and offer sensing platforms with high sensitivity [8-11]. In addition, the catalytic activity of certain enzymes used in biofuel cells can also be enhanced in the presence of enhanced electromagnetic field which will improve the performance of the fuel cell [12].

Although the SPR phenomena exist for many metals, surface plasmon studies are mostly carried out with gold nanoparticles (AuNPs). There are several factors motivating the use of gold. First of all, gold forms air-stable colloids that do not oxidize. Second, its SPR frequency lies in the visible part of the spectrum. Hence AuNPs display strong color that is visible to naked eye, making them interesting as optical labels. Third, they can be easily synthesized in a wide range of sizes and shapes, which enables control of their optical properties [2]. Fourth, their surface can be easily modified with amino and thiol groups for the selective binding and detection of molecules. Lastly, they exhibit excellent biocompatibility that is critical for biomedical applications [13]. In this regard, AuNPs have been extensively studied for their SPR-enhanced optical properties and with the recent advances in particle synthesis and fabrication techniques, interesting new optical nanostructures have been formed.

As previously mentioned, the size of AuNPs is an important parameter that significantly affects their plasmonic properties. The SPR band becomes red-shifted for the particles with larger size allowing one to choose the size of AuNPs that matches well with the wavelength of light intended for the application [14]. The shape of AuNPs also affects the SPR band whereas an increase in the edges or sharpness of the particles results in a red-shift. Different gold nanoparticles with various shapes such as triangles, cubes, nanorods, nanoshells, and nanostars have been synthesized to create structures with SPR in the near infrared region [15-17]. In addition to the shift in the SPR band, non-spherical NPs attract great attention due to the formation of "hot spot" with enhanced electromagnetic field at the tips or edges of these structures. Enhanced electric field makes these nanostructures favorable for surface enhanced spectroscopies [18]. Hot spots can be also produced by placing two nanoparticles in close proximity to one another, within their local field decay lengths. In this case, plasmon oscillations of two particles will couple and result in an enhanced local field due to the ability of focusing light at the inter-particle junctions [19]. The enhancement created by plasmon coupling depends on the size of AuNPs and the inter-particle distance [20]. Extraordinarily large enhancements, which are not possible to obtain with individual non-spherical AuNPs, can be produced by tailoring these parameters [21]. However, it is challenging to fabricate reproducible structures over a sufficiently large area to make them practical for real applications.

Several techniques have been developed to achieve control over the size and shape of nanostructures. Generally, plasmonic nanostructures are fabricated on planar substrates by top-down approaches. Lithographic techniques such as electron beam lithography and focused beam lithography have been the most popular strategies as they provide good reproducibility and large scale uniformity. In these techniques, a focused beam is scanned to draw custom pattern on a surface, which enables precise control on the size, shape, and inter-particle spacing of nanostructures with sub-10 nm resolution [39, 40]. Nanoimprint lithography is another technique offering high precision while the patterns of nanostructures are created by mechanical deformation of a polymeric material [41]. However, these techniques are limited by high production costs and speed [1]. Therefore, alternative cost-effective lithographic methods combining bottom-up approaches with top-down approaches have been proposed. Colloidal lithography is one of these methods as it can fabricate high density plasmonic arrays by depositing metal films on the surface of a colloidal monolayer. In this method, polymer nanospheres are self-assembled into a close-packed pattern to form a mask where a nanostructure of small islands is formed within the gaps between nanospheres upon deposition of metal film over the mask with a certain thickness [42]. Despite the cost-effective production, colloidal lithography strategies suffer from limited resolution and moderate control on the geometries and fine features [43]. Furthermore, all the aforementioned lithographic techniques have a common drawback that originates from their ability to form only planar thin-film structures [44]. Fabrication of complex 3D structures with better optical enhancement is challenging for these techniques.

Therefore, a need exists for techniques that enable the production of advanced, complex plasmonic nanostructures with high resolution, good reproducibility, and in a simple cost-effective manner.

1.2 Template-assisted production of plasmonic nanostructures

The self-assembly of basic building blocks and their use as template material for the fabrication of highly ordered nanostructures has emerged as an alternative bottom-up approach offering high precision and high resolution. In this approach, a template material serves as a host for structurally-controlled assembly of nanoparticles. The most common template materials are chemically/topologically patterned surfaces and organic building blocks, such as block copolymer systems [45, 46]. However, these materials are still far from offering satisfactory production routes. While the chemically-topologically patterned surfaces need expensive and time-consuming top-down fabrication techniques, the block copolymers suffer from limited control over the formation of stable microdomains with desired structure [47, 48]. As

such, biological materials emerge as promising alternative templates. The bottom-up synthesis of nanostructures on biological templates is called “biotemplating” and is directed by covalent/noncovalent interactions between biological and inorganic materials, as well as molecular recognition processes [49]. Biological materials provide a template with a specific pattern onto which one can assemble organic/inorganic materials. Furthermore, in some cases, this template can be employed to induce the nucleation of inorganic structures with specific patterns [50].

Biotemplating becomes more advantageous compared to other fabrication strategies for several reasons. First of all, biological materials available in the nature offer a huge structural diversity for fabricating nanostructures, with ability to create 3D architectures of higher complexity than is possible with conventional top-down fabrication routes [51, 52]. Moreover, biological templates are cost-effective materials, which reduces fabrication costs. Compared to serial nanofabrication techniques of the top-down approach, biological templates enable parallel fabrication and become time-effective [53].

A wide range of biological materials, ranging from biological entities (bacteria, diatoms, and virus) to designed biological building blocks (peptides, lipids and DNA), have been used as biotemplates to create highly-ordered nanostructures [54-56]. DNA and viruses have been the template materials most extensively studied.

DNA (deoxyribonucleic acid) is a molecule that carries the genetic information of nature. It is composed of two complementary strands that hybridize to form double-stranded DNA through hydrogen-bonded base pairs (adenine (A)–thymine (T) and guanine (G)–cytosine (C)) [57]. This simple complementary base-pairing mechanism is used to fabricate materials made entirely of DNA with predictable and well-defined dimensions. The self-assembly properties of DNA allow predictive fabrication of 1D, 2D, or 3D hierarchical structures with different shapes and complexity [58, 59]. Besides that, molecular recognition properties can be introduced to DNA templates by chemical modifications, and used to direct the ordered assembly of inorganic materials such as single-walled carbon nanotubes (SWNT), gold, silver, and semiconductor nanoparticles on DNA scaffolds to design functional nanostructures [60-62]. It should be noted that the most important feature of DNA scaffolds is the exceptional control over the geometrical assembly of nanoparticles with tunable inter-particle spacing. Indeed, several reports have shown that self-assembly of nanoparticles on DNA templates can be accomplished over distances of micrometers [63]. Nevertheless, there are several drawbacks with respect to the fabrication of nanostructures with DNA scaffolds. The production scales achieved with DNA templates are not efficient for real applications, requiring a controlled organization over larger areas [49].

Moreover, the high cost of synthetic DNA and high error rate of self-assembly still remain two main drawbacks of this approach [64]. In addition, the temperature sensitivity of DNA material may be problematic for certain applications, such as surface enhanced spectroscopy, which involves temperature increase [65]. Also, the conjugation of biomolecules to DNA scaffolds with the correct orientation and placing is another challenge that remains to be resolved. For applications relying on local electric field enhancements, it is critical to place the molecule of interest in hot spots where the enhanced field is formed. That's why, biotemplated nanostructures must be a good template for other 'probe' molecules, in addition to their good plasmonic properties [66]. In this regard, viruses have been studied as biotemplate material as they offer great diversity of structure and size for fabrication of cost-effective, stable, and precise nanostructures.

From a material point of view, viruses can be considered as protein-based supramolecular assemblies composed of multiple copies of coat proteins assembled into a shell structure with different shapes and sizes, ranging from tens to hundreds of nanometers. The protein outer shell, so-called capsid, encapsulates the genomic material that contains all essential genes to replicate within a host [67]. The primary function of the capsid is to protect the genomic material and this feature makes viruses stable under conditions such as extreme temperature and pH [68]. However, some viruses can be also produced without genetic material as empty self-assembled capsids. These particles are called virus-like particles and demonstrate the same stability as the original viruses [69]. The lack of genetic material makes virus-like particles replication deficient, thus they can be considered less hazardous for human cells [70]. Indeed, viruses do not have their own metabolism, and thus they use the metabolic machinery of a living host cell for their replication, making them non-pathogenic for non-host cells [71]. A particular quality of viruses is that they can be modified to display foreign peptides on their coat proteins by changing the nucleic acid sequence of the viral genome. [72]. Once this modification is achieved, new virus particles displaying peptide sequences with specific functions can be produced at any time in a host cell culture. The surface coat proteins can also be modified through conjugation chemistry [73].

Although animal viruses are widely recognized as a delivery vehicle, or 'vector', for gene therapy, their use as building block is limited given safety. In contrast, plant and bacteria viruses have received more attention as scaffolds in the material sciences. The most studied plant viruses include tobacco mosaic virus (TMV), cowpea chlorotic mottle virus (CCMV), and cowpea mosaic virus (CMV) whereas the bacteriophages, in particular M13 phage, are most extensively used bacterial viruses in material applications [22]. In comparison to conventional synthetic materials, viruses are attractive building blocks

for the fabrication of nanostructures. Viruses have precise, nanoscale, uniform structures and dimensions that are difficult to replicate using standard synthetic and/or top-down methods [23]. In addition, the surface properties of the viruses can be controlled using chemical and genetic approaches without destroying their structural integrity. This feature enables spatial control on the position of functional moieties on the virus surface [24]. The most interesting property of viruses, in terms of material synthesis, is that viruses can be produced in large quantities by infecting their host cells, and then can be purified inexpensively on a large scale. These are critical characteristics required for a material intended to be used as a building block for nanomaterial fabrication.

1.3 Phage-templated strategies for fabrication of plasmonic nanostructures

Bacteriophage (phage; i.e., viruses that infect bacteria) particles have attracted significant attention as building blocks for the assembly of hierarchically-organized nanostructures. Their relatively simple structures compared to prokaryotic and eukaryotic cells, as well as easy growth and environmentally-friendly synthesis, have made phage particles a popular option for research on biologically-inspired material assembly [74, 75].

Amongst all phage types, M13 phage has been the most widely used building block for several important reasons. First of all, M13 phage exhibits liquid-crystalline behavior in solution and can thus be self-assembled into well-ordered two- and three-dimensional structures. The liquid-crystalline structure of M13 arises from its long, rod-like shape and unique monodisperse characteristics. Like other liquid crystals of rod-like molecules, M13 phage exhibits the following phase sequence with increasing phage concentration: isotropic, nematic, and smectic (Figure 1.3.1). At low concentration, M13 has an isotropic phase arrangement where all phage particles are disordered and are oriented in random directions. Phage solutions with higher concentrations form a “nematic phase” with all phage aligned along one particular axis. The further increase in phage concentration results in more ordered phases, which are called smectic phases. In the “smectic A phase”, phage are organized into one-phage-length thick liquid-like layers of aligned phages that are stacked one on top of each other. The phage particles in this orientation begin to intertwine with each other along the perpendicular axis of the layers. This interaction creates helicity and leads to the formation of a “smectic C phase”.

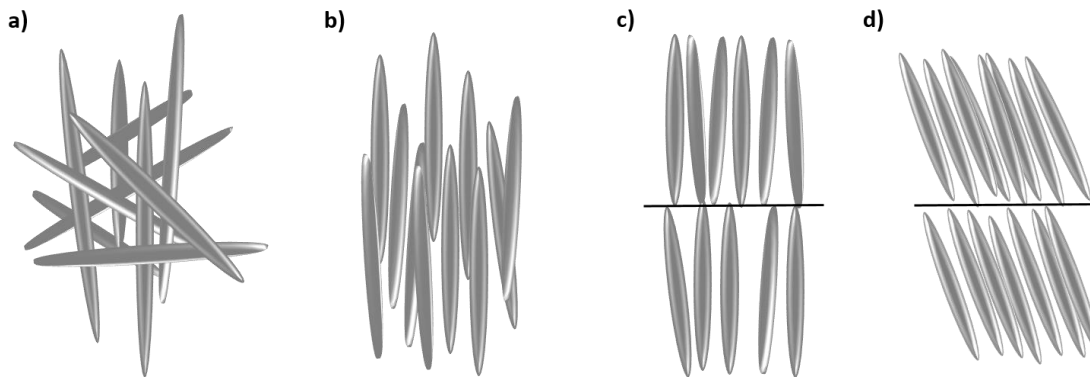


Figure 1.3.1 Schematic structures of the liquid-crystalline phases of M13 bacteriophages a) Isotropic, b) nematic, c) smectic A, and d) smectic C phases.

Although tobacco mosaic virus (TMV) was the first model system used to study the liquid crystalline properties of rod-shaped molecules, fd and M13 filamentous phages, which have identical structures, have been also used as model platforms [76]. In comparison to other synthetic rod-like colloidal particles such as polymers, viruses are unimolecular (no size distribution) thus enabling quantitative comparison between experiments and theory and consequently advancing the fundamental understanding of colloidal liquid crystals [77]. Recently, filamentous phages have substituted TMV and have become the most popular model systems because of the time-consuming nature of plant virus preparation, as well as the difficulty in their genetic modifications. Moreover, the length of filamentous phages (ca. micron) enables the visualization of single molecules in real time by optical microscopy, which is not possible for smaller systems. Visualization of the phase behavior of phage particles has provided important information about the dynamics of nematic and smectic phases of colloidal liquid crystals and allowed the description of diffusion processes without any assumption on these systems [74, 78-82]. The extensive data available on the liquid-crystalline structure of M13 phage solutions has led researchers to investigate the feasibility of using the latter for the production of one dimensional micro- and nano-sized diameter fibers. Inspired by nature, a process was developed that mimics the spinning process of spider silk, resulting in continuous fibers from a liquid crystalline proteins [83]. These results demonstrate that M13 phage can template continuous fiber formation over large length scales, which can find application in the synthesis of novel membrane materials.

In addition to its liquid-crystalline behavior, the ease of modification of M13, either chemically or genetically via phage display, enables the introduction of specific functional groups on the phage's surface. This can be exploited to use M13 as a building block in a variety of applications. Chemical modification can be achieved on three different reactive groups of M13 coat proteins: (i) the amino groups of lysyl residues or the N-terminus, (ii) the carboxylic acid groups of aspartyl or glutamyl residues, and (iii)

the phenol group of tyrosyl residues. The modification of all of these residues has been reported, employing different chemo-selective reactions. This has enabled the modification of the phage surface with various molecules. Amongst all these reactive groups, the N-terminus and the Lys-8 residue of p8 coat protein have significantly higher reactivity than other nucleophilic groups, and can be labeled at a higher level compared to carboxylic acid and phenol groups. Because of this, amino groups have been the most frequently-modified group on M13 surface [84, 85]. For instance, aniline molecules were conjugated to M13 phage through derivatization of lysyl residues and resulted in conductive polyaniline-M13 composite nanowires, which could be easily spin-coated into thin films [86]. Alternatively, phage display technology has emerged as a tool to change the liquid crystalline properties of M13 phage, which is dependent on phage length and its corresponding DNA size [87-90].

The convenient modification of the phage surface has enabled the study of the liquid-crystalline properties of M13 phage and provided valuable insight into M13-based thin films. In this regard, the display of streptavidin-binding peptides on p3 minor coat protein has enabled the conjugation of streptavidin-labelled materials such as AuNPs, fluorescein, and phycoerythrin to M13 surface. These modifications enabled the easy visualization of one-micrometer-long periodic long-range ordering of phage films [91]. These observations are attractive in terms of showing the possibility of forming complex structures with the help of M13 phage scaffolds.

Phage display technology can be also employed to identify peptide sequences that bind to inorganic substrates. This has motivated the use of M13 phage as a building block for the design of highly-ordered functional structures. Inspiration for such work came from reports showing that random peptide sequences displayed on the outer surface of *E.coli* could recognize and specifically bind to metal/metal oxide surfaces (e.g., gold, iron oxide, and chromium) [92, 93]. The first application of phage display libraries to evolve peptide sequences binding to inorganic substrates was performed for a range of semiconductor surfaces with the motivation of directing nanoparticles to specific locations on a semiconductor structures for the fabrication of complex, sophisticated electronic materials [94]. In this report, several peptide sequences selective for the crystal composition (binding to GaAs but not to Si) and crystalline face (binding to (100) GaAs, but not to arsenic-rich (111) GaAs) were identified. This achievement stimulated the research into the selection of material-binding peptides, and several peptide sequences with affinity towards different materials were identified (e.g. platinum, palladium, titanium, silicon, silver, gold, zinc sulfide, cadmium sulfide, graphite, calcite, indium phosphide, chlorine-doped polypyrrole (PPyCl), and carbon nanotubes) [95-109].

Phage display selected peptides with material-recognition properties can be also applied to direct the mineralization of nanomaterials. This approach has been inspired by the biomineralization of materials in nature by living organisms. Indeed, several biominerals are formed in a biologically-templated manner under mild conditions, including calcium phosphate minerals in teeth, bone, as well as silica in sea sponges. The interest in biomineralization has recently grown as it offers a greener and cheaper alternative to inorganic synthesis of materials, which usually requires high temperatures and harsh chemical reagents [110]. M13 phage was used to select several peptide sequences capable of recognition and nucleation of different materials such as zinc sulfide (ZnS), cadmium sulfide (CdS) nanocrystals, iridium oxide (IrO₂), cobalt platinum (CoPt), and iron platinum (FePt) [111-115].

The organization of individual building blocks over large length scales with the simultaneous ability to control the chemical functionality is one of the main challenges in the fabrication of self-assembled thin films. The construction of M13-based thin films with varying thickness over large areas can be achieved by applying the electrostatic layer-by-layer (LBL) assembly technique. This process exploits negatively- and positively-charged polyelectrolytes to form an ionically-crosslinked network in which M13 phage particles can be deposited to form an ordered monolayer structure. The ordering of the phage particles on the surface results from the competition between the negatively charged polyelectrolyte and M13 phage to bind to the positively charged polyelectrolyte. As the electrostatic interaction between the complementary polyelectrolytes is stronger, phage particles are forced to the surface and form a close-packed monolayer. The ability to introduce material-recognition and binding properties to the phage surface enables the assembly of dense, highly ordered hybrid phage monolayers on thin films. In this regard, M13 phage was employed to create cobalt nanowires as well as arrays of AuNPs along the phage scaffold on top of a thin LBL film. Densely-packed GaN nanowire films were also formed using similar approach [116]. The LBL assembly technique has not only been used to form thin films, but has also been employed to fabricate nanoporous networks [117]. Titania films with nanoporous structures were fabricated on M13-based films. Moreover, it was demonstrated that AuNPs could be incorporated into titania film structures during the assembly process of phage films through gold binding motifs displayed on major coat protein of M13. This allows the design of functional porous thin films with enhanced electric field and light absorption for photovoltaic devices.

M13-templated nanostructures have been successfully employed in various applications and the fabrication of electro-catalysts based on M13 phage-templated gold and platinum nanowires has been one of them [118]. Gold and platinum nanoparticles nucleated on M13 major coat protein were used to

prepare electrodes by dropping phage-templated nanoparticle arrays onto a silicon wafer. The electrocatalytic activity of resulting electrodes were evaluated for methanol oxidation, and higher catalytic activity was observed in comparison to the electrodes prepared with only gold and platinum nanoparticles, most probably due to their 3D structures.

The fabrication of batteries has been another application area for M13-based nanostructures, offering green solutions for the improvement of the performance of current batteries, in terms of fabricating smaller and more flexible materials with controlled nanostructures. In several reports, M13-templated nucleation of nanoparticles has been employed as an approach to synthesize and assemble nanowire electrodes to improve the capacity of lithium batteries. This approach has been successfully applied for M13-templated synthesis of cobalt oxide (Co_3O_4) nanowires as negative electrode material for lithium-ion batteries [119]. Using a phage template, it was possible to fabricate Co_3O_4 nanowires at room temperature with properties comparable to those of particles fabricated at temperatures above 500 °C. Phage display technology offers a high level of control on the arrangement of different nanomaterials on phage surface. Indeed, gold nanoparticles could be introduced onto Co_3O_4 nanowires with uniform distribution by displaying an additional peptide sequence on the major coat protein that was specific to gold [120]. This provided an enhancement in the electrochemical properties of the nanowires through the cooperative contribution of Co_3O_4 and gold materials. The combination of the LBL assembly technique with phage-templated Co_3O_4 nanowire synthesis allowed the generation of self-assembled micro-battery electrodes due to the ability of M13 to assemble on top of the polyelectrolytes [121]. M13 phage templates have been also used to synthesize amorphous anhydrous iron phosphate ($\alpha\text{-FePO}_4$) on silver nanoparticles, uniformly distributed along the phage surface as cathode material for lithium-ion batteries [122]. Due to the small size of the produced $\alpha\text{-FePO}_4$ nanoparticles, which were 10–20 nm in diameter, better electrical contact between the active materials was obtained and the electronic conductivity in the cathode material was increased. In order to improve battery performance further, single-walled carbon nanotubes (SWNTs) were incorporated into the phage-templated nanowires by displaying SWNT-specific peptide sequence on p3 minor coat protein. Incorporation of SWNTs with high conductivity and high aspect ratios resulted in a percolation network with better electronic conductivity. The specificity of M13 phage to SWNTs prevented their aggregation via strong binding interactions, leading to a percolation network due to better particle dispersion. Besides Co_3O_4 and $\alpha\text{-FePO}_4$ nanowires, M13 phage has been used to synthesize pure silver nanowires and silver-gold alloy nanowires [123].

The use of M13 phage for the identification of peptide sequences with specific affinity towards cells, tumors, and organs, has inspired researchers to consider M13 phage as a targeting probe/nanocarrier in medicine. Genetically-modified M13 phage displaying target-specific peptides as well as inorganic binding moieties have been used as building blocks for self-assembled nanostructures for disease diagnosis and treatment. In addition to high selectivity, the ability of filamentous phage to penetrate the central nervous system, which is difficult due to the relatively impermeability of blood-brain-barrier, makes M13 a promising delivery platform for a broad range of biomedical applications [124]. In this manner, several M13-templated probes have been designed for the diagnosis of prostate cancer based on different detection techniques including: SWNT-guided fluorescence imaging and magnetic resonance imaging (using iron oxides nanoparticles) [125, 126].

Self-assembly of drug-loaded liposomes on M13 phage has been another approach using M13 phage templates as a nanocarrier [127]. Liposomes loaded with zinc phthalocyanine (ZnPc), which is a potential photosensitizer for photodynamic therapy (PDT), assembled on M13 phage to fabricate a nanocarrier for drug delivery. Phage-templated drug-loaded liposomes displayed enhanced singlet oxygen generation efficiency and were able to internalize in breast cancer cells. These two properties make the phage-liposome complex a promising tool for targeted drug delivery, as their cancer cell-targeting ability could be introduced by displaying cell-specific peptides on the tip proteins of phage. Moreover, the phage template stabilized the liposomes in biological media against flocculation and assisted the delivery of the content loaded inside the liposome to specific targets.

The M13-templated self-assembly of AuNPs (~44 nm diameter) was also studied as an approach to form phage-gold networks as optical probes for biomedical applications [29]. Due to the enhanced plasmonic properties of AuNPs aggregated on phage template, gold-phage networks could be employed as SERS- and fluorescence-based labels to detect cancer cells.

1.4 Overview of this thesis

The self-assembly of AuNPs on viral templates has been reported in the literature. Several types of viruses including M13 phage, T7 phage, Cowpea Mosaic Virus (CPMV), Cowpea Chlorotic Mottle Virus (CCMV), Chilo Iridescent Virus (CIV), Tobacco Mosaic Virus (TMV), and TMV coat protein disks have been employed as template material for the fabrication of plasmonic nanostructures, with or without surface modifications [26, 33, 128-132]. In comparison to these templates, T4 phage offers another unique

template material with its characteristic size, shape, and coat protein organization that has never been used as scaffold for the attachment of AuNPs. In addition, the previously-published reports mainly demonstrate the synthesis routes of virus-templated nanostructures and their performance in intended applications, exploring only a few of the available design parameters available. The effect of AuNP size on the plasmonic properties of these assemblies, in particular for surface enhanced spectroscopy, has not yet been investigated. Indeed, the aforementioned studies typically only examined one size of AuNP, which is most suitable for the application of interest. However, the size of AuNPs can be critical in certain cases, such as *in vitro* and *in vivo* biomedical applications. In fact, the size of nanomaterials has significant effect on their distribution and clearance in the body, which should be considered in choosing the right particle size for the application. The U.S. Food and Drug Administration (FDA) has required that all agents injected into the human body be completely cleared in a reasonable amount of time [133]. The clearance of nanoparticles smaller than the kidney filtration threshold (~5.5 nm) is achieved through the urinary system whereas larger nanoparticles up to 100–150 nm in diameter are taken up by phagocytic cells in the blood, liver, spleen, and bone marrow. Chronic toxicity related to long retention times of nanoparticles in these tissues is the challenge of mononuclear phagocyte system clearance [134, 135]. On the other hand, kidney filtration is a desirable pathway for the clearance of NPs since the particles can be rapidly eliminated from the body without potential health hazards resulting from long term accumulation and decomposition of NPs in the body [136]. In this manner, studying the influence of AuNP size as a variable parameter can provide valuable information about the enhancements that can be achieved within the plasmonic assemblies and the limits of particle size that can help to obtain these achievements.

In the present thesis, two bacteriophage templates, M13 and T4, were examined as biological templates to create well-defined assemblies of very small AuNPs (3–13 nm). These phage were selected because of their considerably different geometries (filamentous vs icosahedral for M13 and T4, respectively), which will allow us to investigate both the effect of short-range and longer-range ordering of the AuNPs on plasmonic properties. Because of the paucity of data on the assembly of very small (<13 nm) AuNPs on bacteriophage, several gold-binding motifs were explored and, for T4, the relative disposition of these motifs on the phage surface was also varied. In Chapters 2 and 3, the genetic engineering of the phage is presented, and protocols for the assembly of 3, 9, and 13-nm AuNPs are established. In Chapters 4 and 5, the plasmonic properties of the phage–AuNP assemblies are examined by surface-enhanced Raman scattering and two-photon excitation fluorescence microscopy. Overall, this thesis contributes to a better understanding on the opportunities and limitations relevant to the use of these plasmonic assemblies as imaging contrast agents.

1.5 Structure of this thesis

This thesis is divided into 6 different Chapters organized as follows:

In **Chapter 1**, the topic of the thesis, the ‘design of plasmonic nanostructures by self-assembly approaches’, is introduced. Considering the breadth of this area of research, current developments and the most common strategies in the field are overviewed. Additional emphasis is placed on phage-assisted self-assembly of nanomaterials, a topic of particular interest for the scientific content of this thesis.

Chapter 2 provides a brief literature review specific to the M13 phage display platform and M13-based materials. Thereafter, the experimental details for the engineering of M13 phage so that it can be used as template for AuNPs self-assembly are reported, as well as the characterization of the resulting AuNP–M13 assemblies is provided.

Chapter 3 provides a literature review specific to the T4 phage display platform. Thereafter, the experimental details for the engineering of T4 phage so that it can be used as template for AuNP self-assembly are reported, as well as the characterization of the resulting AuNP–T4 assemblies is provided.

Chapter 4 presents the performance of AuNP–phage assemblies in surface enhanced Raman scattering (SERS) microscopy. Sample preparation, measurements, and discussion of the obtained results are described in detail. The two phage templates, M13 and T4, are compared in terms of the SERS-enhancement they achieve. The effect of AuNP size and other parameters on SERS enhancement is also discussed.

Chapter 5 presents the performance of AuNP–phage assemblies in two-photon excited fluorescence (2PEF). This Chapter covers all aspects of sample preparation, measurements, and discussion of results. The effect of AuNP size and phage template on observed enhancements is discussed.

Chapter 6 presents the most significant contribution of this thesis to the field, as well as the major limitations of this work. Both are framed with possible future directions that can be explored.

Annex. Following the main body of thesis, an appendix provides additional data related to the scientific content of certain chapters.

2 M13 PHAGE-TEMPLATED AuNP ASSEMBLIES

2.1 Introduction

2.1.1 Structure and Characteristics of M13 Bacteriophage

M13 is a filamentous bacteriophage that specifically infects *Escherichia coli* bacteria. Due to its relative simplicity, the structure of the M13 virion has been extensively studied and is very well known. M13 is 65 Å in diameter and its length is dependent on the size of enclosed genome (9300 Å in the case of the wild-type phage). The flexible filament contains a circular, 6407-base, single-stranded DNA genome coated with 2700 copies of the major coat protein, p8 (Figure 2.1.1a). The major coat proteins form a tube around phage DNA, in an overlapping helical array (Figure 2.1.1b). The N-terminus of the p8 protein is located at the outside of the phage coat while the C-terminus interacts with the DNA in the inside. The hydrophobic domain located in the central part of p8 protein stabilizes the viral particle by interlocking the coat protein with its neighboring coat proteins. Additionally, the four minor coat proteins are present at 5 copies per particle: p7 and p9 compromise one end of the particle while the other end contains p3 and p6. P3 is the largest and most complex coat protein and is responsible for the host cell recognition and infection. It contains three distinct domains: domain N1 on N-terminus of p3 initiates translocation of the viral DNA into *E. coli* after binding of domain N2 to the F pilus on *E. coli* surface, and the C-terminal domain is responsible for the integration of p3 into the phage coat (Figure 2.1.1c) [137-139].

M13 phage engages in a chronic infection life cycle where the propagated phage particles are slowly released from the host cell by secretion through the outer membrane, thereby avoiding bacterial lysis. Phage infection starts with the attachment of p3 protein to the F pilus of bacteria. The genome of the phage enters the cell and is then converted to double-stranded DNA. Afterwards, the synthesis of all M13 phage proteins starts and the double-stranded DNA is amplified in a process involving p2 and p10 proteins to produce plus-strand copies of the phage DNA. Protein p5 coats the amplified DNA molecules, while the coat proteins p8, p7, p9, p6, and p3 are inserted into the inner bacterial membrane (IM). A small uncovered hairpin of single-stranded DNA is captured by a complex of integral membrane proteins p1, p4 and p9. This complex is described as the 'membrane pore', from where the phage is assembled and extruded from the bacterium. As the release of mature M13 virions occurs right after the phage assembly,

the virions do not accumulate inside the bacteria and the infected cells continue to grow, though at a reduced rate [138, 140-143].

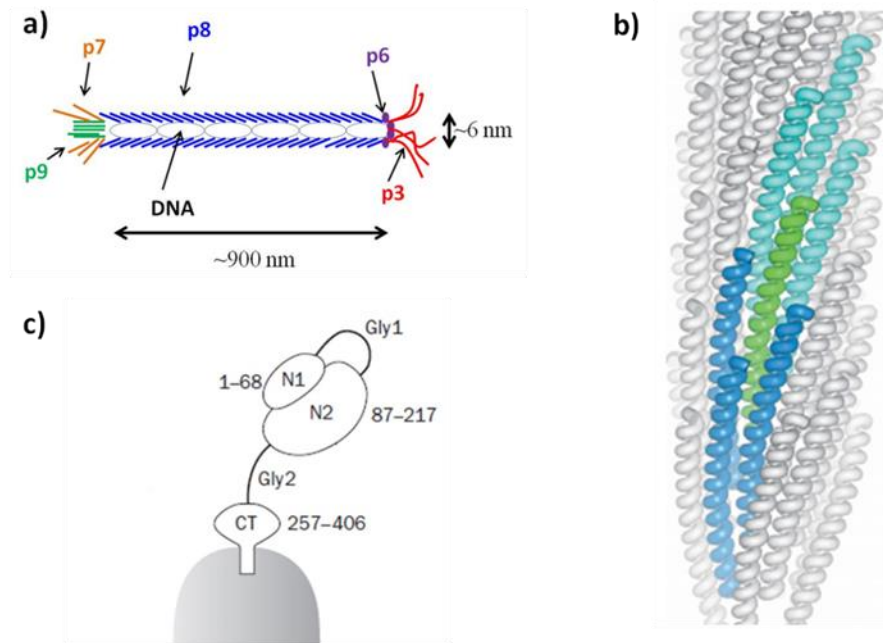


Figure 2.1.1 Structure of M13 bacteriophage (a) Schematic representation of M13 phage virion showing the single-stranded DNA core surrounded by 5 coat proteins; p8, p3, p6, p7 and p9 (b) Repeating array of major coat protein (p8) represented as ribbon. Reproduced with permission from [144] (c) Domain structure of p3 protein. Three domains of p3 are presented as N1, N2 (N terminal domains) and CT (C terminal domain) which are separated by glycine rich linker sequences (Gly1 and Gly2). Numbers refer to the residues in mature protein sequence. Adapted from [145].

2.1.2 M13 Phage Display Platform

M13 has been the most widely used phage display platform since the invention of phage display in 1985 by George P. Smith [146, 147]. The relative simplicity of its structure has made M13 phage an extremely useful model to study macromolecular structure and interactions. Combinatorial libraries of polypeptides fused to phage coat proteins provide a valuable platform for screening binding candidates against several targets as well as studying structure–function relations of proteins [137].

In phage display, the genome of M13 phage is easily manipulated by inserting a DNA sequence into a gene encoding phage coat protein. Generally, highly diverse combinatorial peptide libraries are displayed as fusions of short peptide sequences (8–12 amino acids) to the coat proteins of M13 phage. Any modification of the phage genome is reflected in a corresponding modification in the coat proteins of the phage, which provides a link between the phenotype of the phage and its genotype. Selection of

the best peptide binding sequence for a given target material is performed through an enrichment process called “biopanning”. Initially, the phage particles are allowed to bind to the target. After washing away the non-bound phage, the bound ones displaying binding sequences are eluted, and amplified through host bacterial infection. This man-made evolutionary process to select the best binding peptide sequence is repeated several times (‘rounds’) for enrichment. Finally the selected binding peptides are identified by DNA analysis of the phage genome [148-150]. Phage display technology has been extensively used to identify specific binding peptides for many biological molecules including toxins, bacteria, organs, and tumor associated antigens [151-154]. Although all five coat proteins have been used to display foreign proteins, the most common approach is to fuse the foreign sequences to the N-terminus of p3 and p8 coat proteins [155-157].

There are three different strategies for the display of proteins as fusions to p3 and p8 coat proteins, which are categorized as phage, phagemid, and hybrid systems. In the phage system, the gene encoding the foreign protein is directly inserted into the phage genome and results in fusion proteins displayed on every copy of chosen coat protein. As a general rule, larger proteins are more efficiently displayed on the p3 protein, and the p8 protein is limited to displaying short peptide sequences with 6–8 amino acids. However, even the p3 protein is limited in what it can display, and proteins larger than 50 amino acids typically cannot be displayed on all 5 copies. In this manner, it can be necessary to decrease the copy number of fusion proteins to efficiently display them on desired coat protein. The phagemid system is used to overcome this limitation by introducing a phagemid as special helping display vector. A phagemid is a plasmid carrying the viral gene encoding the fusion coat protein, phage origin of replication, and a phage packaging signal. The genes required for phage assembly including the wild type coat protein is provided by packaging defective helper phage. Upon coinfection of bacteria by phagemid and helper phage, wild-type proteins and fusion coat proteins are synthesized and preferentially assembled around the phagemid DNA, which has lower copy number than helper phage DNA. This results in hybrid phages displaying only a few copies of the fusion coat protein. The hybrid system was also invented with a similar motivation to the phagemid system: to enable the display of large protein sequences on phage surface. However, unlike the phagemid system, it only employs the phage genome which carries both the gene encoding wild type coat protein and the gene encoding fusion protein. Smith defined these three systems by using the terms “3”, “3+3” and “33” respectively (Figure 2.1.2). Number “3” indicates p3 coat protein where the formats “8”, “8+8” and “88” are used for phage display on p8 coat protein [138, 158-160].

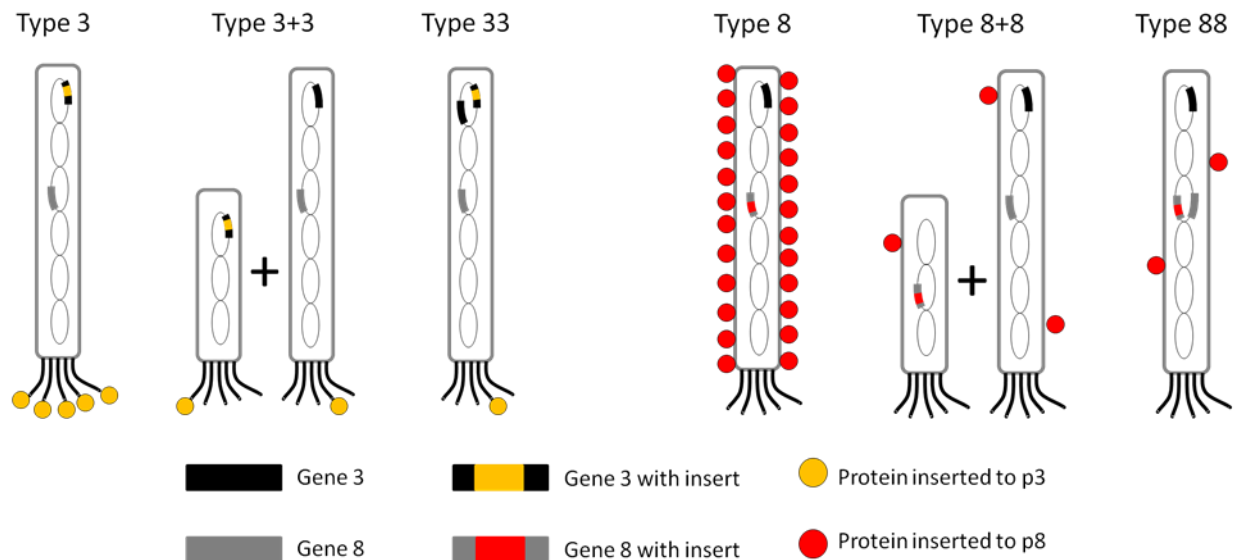


Figure 2.1.2 Classification of phage display systemsIn phage system (type 3), fusion of insert gene into gene 3 results in fusion proteins on all copies of p3 coat protein. In phagemid system (type 3+3), gene 3 inserted with fusion gene is carried on a phagemid and wild type gene 3 is provided by helper phage. Phage display using phagemid system results in hybrid phages displaying only few copies of fusion coat proteins. In hybrid system (type 33), the phage genome contains two copies of gene 3, one with an insert and one without. As in phagemid system, it also results in hybrid phages displaying few copies of fusion coat proteins. Type 8, 8+8 and 88 are the corresponding types for inserts in gene 8. Adapted from [160].

2.1.3 M13-templated self-assembly of AuNPs

The self-assembly of AuNPs on the surface of M13 phage has been explored to design functional materials for several applications including battery electrodes, fuel cells, catalysts, and sensors [120, 161-165]. The incorporation of gold onto the phage-templated nanostructures in a well-controlled manner has been accomplished by precisely modifying phage surfaces and has typically resulted in improved material performance in the aforementioned applications.

In order to incorporate gold materials onto M13 phage, their surface can be modified either chemically or genetically to introduce desired functionalities. For chemical modification, the amino groups of lysine residues on p8 major coat protein have been used to introduce thiol groups [118, 166]. Due to the well-known affinity of thiol groups to gold, modified M13 phage exhibited increased interaction with the Au atoms and served as template to nucleate and grow AuNPs in the presence of a reducing agent, NaBH₄. The advantage of using thiol groups in AuNP nucleation is that other metals having affinity to thiol groups such as platinum and silver can also be nucleated using same phage template. Rather than directly conjugating AuNP to phage surface, DNA strands can be used to modify phage coat proteins for the

attachment of DNA-labelled AuNPs through DNA sequence complementary [167]. As an alternative approach, DNA strands can be modified with maleimide groups and conjugation to the phage surface achieved through thiol groups introduced to the lysine residues of phage coat proteins using e.g., N-succinimidyl 3-[2-pyridyldithio]-propionate [168]. Moreover, it is not always necessary to modify the phage surface for self-assembly, as the 'natural' amino acid residues on the phage coat proteins can be directly used for particle attachment. For instance, the AuNPs bearing carboxylic acids on their surface have been conjugated to the amine groups of M13 through carbodiimide coupling reaction using 1-ethyl-3-(3-dimethylaminopropyl) carbodiimide hydrochloride (EDC) and N-hydroxysuccinimide (NHS) [112, 169].

The genetic engineering of M13 coat proteins to display gold-binding peptide sequences has been the most popular approach to self-assemble AuNPs. Several peptide sequences with affinity to gold materials have been identified by phage display and have been employed for this purpose. While some of these peptide sequences exhibit only gold binding affinity (e.g., VSGSSPDS, LKAHLPPSRLPS, TLLVIRGLPGAC) [120, 170, 171], some also possess the ability to reduce gold (e.g., NPSSLFRYLPSD (named AG4 peptide), AYSSGAPPMPFF (named A3 peptide), TGTSVLIATPYV) [172-174]. The gold-binding and gold-reducing mechanisms of these peptides have been investigated by researchers and some common features within their sequences have been observed. Regarding their gold-binding affinity, amino acids with sulfur atoms such as cysteine and methionine are known as strong gold binders. Consequently, peptides having these amino acids show strong gold-binding affinity. Histidine and tryptophan are other amino acids with good gold binding affinity due to the presence of nitrogen heterocycles, whereas the amino acids with aromatic residues such as tyrosine and phenylalanine are also known as good gold binders because of the anchoring effect of the aromatic ring structure to the surface of gold. In addition, amino acids with hydroxyl groups (serine and threonine) and hydrophobic amino acids (e.g. alanine, valine, leucine, proline, glycine) are also important for interacting with gold surfaces, and enhance the gold-affinity of the peptides [170, 171, 175, 176]. In the case of peptide-mediated reduction and growth of AuNPs, weak gold-binding amino acids become more beneficial given that strong binders (e.g. cysteine, histidine, and methionine) can strongly complex gold ions, which prevents the further reduction of precursor Au(III) ions to Au(0) atoms. Some studies suggest that peptide sequences with intermediate binding affinity to gold *ions* and gold *surfaces*, particularly positively charged peptides, can bring the chloroaurate ions closer to the reduction sites without excessive chelation, and enable the reduction of AuNPs [177]. Tyrosine is an amino acid that is involved in many gold-reducing peptide sequences and known as a good gold-reducer. This reducing ability is explained by the reduction of tyrosine side-chain to

phenoxide, which occurs during the electron-transfer to soluble gold ions (AuCl_4) [178]. Although these identified peptide sequences have the ability to reduce gold ions by themselves, the formation of AuNPs is usually performed with a reducing agent such as NaBH_4 and HEPES to increase the reaction rate for gold nucleation. HEPES (4-(2-hydroxyethyl)piperazine-1-ethanesulfonic acid) is one of Good's buffer that is widely used in biological research and it has ability to reduce Au(III) through the generation of a nitrogen-centered cationic free-radical from the piperzaine ring [179, 180]. This reducing agent can rapidly reduce Au(III) ions to Au(0) atoms, and the fast nucleation of AuNPs results in nanoparticles with narrow size distributions while the gold-binding peptides lead to larger particles by binding to free Au(0) atoms and reducing the number of critical nuclei. As a consequence, gold-reducing peptides are mostly considered as synthetic additives providing a great control on growth of AuNPs with the ability of determining their size and shape [174]. For this reason, AuNP formation on phage templates is usually performed using a reducing agent (e.g. NaBH_4) to induce rapid gold nucleation, whereas the gold-binding peptides displayed on M13 surface serve as a nucleation site for controlled particle growth [171]. It is worth mentioning that NaBH_4 is a reasonably harsh chemical and any residue present after synthesis is not acceptable for biomedical applications. Therefore, HEPES buffer can be the choice of reducing agent if the produced particles are intended to be used for biomedical research.

In addition to phage display-selected gold-binding peptides, custom designed peptide sequences have also been employed to assemble AuNPs on M13 phage. For instance, a cysteine-rich peptide was successfully-employed to assemble gold-coated magnetic nanoparticles on the p8 major coat protein of M13 [181]. The regulation of electrostatic interactions between gold materials and phage particles was also used as a strategy to induce phage-gold complex formation. Engineering of M13 phage to display four arginyl residues enhanced the interaction of phage with anionic AuNPs due to the positively charged side groups of arginine and resulted in self-assembly of gold on phage [182]. In a similar way, cationic AuNPs were self-assembled on M13 phage engineered to display four glutamyl residues making the net charge of phage more negative [116].

In this chapter, M13 phage is employed as a biological template to generate AuNP–M13 assemblies. Initially, the engineering of M13 phage to display gold-binding moieties will be presented, and will be followed by the description of the methods used for optimization of AuNP assembly on the designed phage templates. Regarding nomenclature, it is noteworthy to mention that in this work AuNPs self-assembled on phage templates are termed “phage-templated AuNP assemblies”, in order to distinguish them from random aggregates of AuNPs formed in the reaction solutions.

2.2 Materials and Methodology

2.2.1 Materials

All chemicals were obtained from Bioshop (Ontario, Canada) unless otherwise noted. They were of the highest grade available and were used as received without further purification. All aqueous solutions were prepared with deionized distilled water obtained from a Milli-Q water purifying system (18 MΩ/cm).

2.2.2 Engineering of M13 Phage Template

2.2.2.1 p3 Cloning of RGD Bearing Peptides

In order to target over-expressed integrin receptors on cancer cells, peptide sequence containing **R** (Arginine)-**G** (Glycine)-**D** (Aspartic acid) motif (**GRGDSP**) was displayed on p3 minor coat protein of M13 phage.

The display of RGD peptides on p3 protein was accomplished using Ph.D. Peptide Display Cloning System (New England Biolabs Inc., Ontario). Oligonucleotides including the RGD sequences (Table 2.1; synthesized by IDT, Integrated DNA Technologies, Inc.) were annealed to the extension primer (Table 2.1) and then extended as a duplex using Klenow fragment (New England Biolabs, Ontario). The extended duplex and M12KE vector were digested with Acc65I and EagI restriction enzymes (New England Biolabs, Ontario) according to the instructions of the manufacturer, and then digestion products were gel purified. The extended duplex was purified on an 8% nondenaturing polyacrylamide gel [25] and extracted from the gel using a QIAEX II Gel Extraction Kit (QIAGEN, Ontario). The digested M13KE vector was agarose-gel purified with QIAquick Gel Extraction Kit (QIAGEN, Ontario). The purified vector and DNA duplex were ligated using T4 DNA ligase (New England Biolabs, Ontario) at 16 °C overnight and the ligation mix was transformed into XL10-Gold ultracompetent cells (Agilent, ON). After overnight incubation of the transformed cells on LB/IPTG/X-gal plates (LB agar; IPTG, isopropyl-β-D-thiogalactoside; X-gal, 5-bromo-4-chloro-3-indolyl-β-D-galactoside) at 37 °C, blue plaques were picked and analyzed for the presence of the insert. PCR analysis was performed by amplification of the M13KE DNA region, which includes the insert using designed primer sequences (Table 2.2.1). Positive phage plaques were sent to *the Plate-forme d'Analyses Génomiques* (Université Laval) for sequence analysis.

Oligonucleotide	Sequence (5' - 3')
M13KE Forward	TGT ACC GTA ACA CTG AGT TTC
M13KE Reverse	ATT CAC CTC GAA AGC AAG CTG A
<u>GRGDSP</u>	CAT GTT TCG GCC GAG CCG CCG CCC GGG CTG TCA CCA CGG CCA GAG TGA GAA TAG AAA GGT ACC CGG G
Extension Primer	CAT GCC CGG GTA CCT TTC TAT TCT C

Table 2.2.1 Oligonucleotide sequences for M13 phage p3 cloning.

2.2.2.2 Propagation and Purification of Recombinant M13 Phages

Phage propagation was performed using the *E. coli* host strain ER2738 recommended by the manufacturer of the M13KE vector system, New England Biolabs. A glycerol culture of ER2738 was streaked onto a LB agar plate supplemented with tetracycline (10 µg/mL) and incubated at 37 °C overnight. A ER2738 culture for infection was grown by inoculating 5 mL LB broth with a single colony from the plate and incubating overnight with shaking at 200 rpm at 37 °C. The next day, the culture was diluted 1:100 in 20 mL LB broth and after infection with phage stock, it was incubated with shaking at 200 rpm at 37 °C for 5 hours. The recovery of the phage from the culture was achieved by PEG precipitation. For this purpose, the culture was centrifuged at 12,000 x *g* for 10 minutes at 4 °C and 1/6 volume of 20% polyethylene glycol (PEG-8000)/2.5 M NaCl solution was added to the supernatant. The mixture was kept in the fridge overnight and the phage was collected as a pellet by centrifugation at 12,000 x *g* for 15 minutes at 4 °C. The phage pellet was resuspended in 1 mL of TBS buffer (50 mM Tris-HCl, pH 7.5 and 150 mM NaCl) and centrifuged at 14,000 rpm, 4 °C for 5 minutes. Phage in the supernatant were re-precipitated with 1/6 volume of 20% PEG/2.5 M NaCl solution by incubating 1 hour on ice and performing a final centrifugation at 14,000 rpm, 4 °C for 10 minutes. The pellet was resuspended in TBS buffer and stored at 4 °C as phage stock.

The double-layer agar plate method was used for titration of recombinant M13 phage stocks. An overnight ER2738 culture that was grown from a single colony was diluted 1:100 in LB broth and incubated with shaking at 200 rpm at 37 °C. After 5 hours of incubation, 200 µL of ER2738 culture and 10 µL of serial dilutions of phage sample were mixed in 3 mL of LB top agar and poured onto LB/IPTG/X-gal plates. The blue plaques formed during the overnight incubation were counted to calculate the phage titer.

2.2.2.3 p8 Cloning of Gold Binding Peptide

Recombinant M13 phage, named M13-L, displaying linear GRGDSP peptide on the p3 minor coat protein was engineered to display a VSGSSPDS gold binding peptide on the major coat protein p8. The insert was positioned at the N-terminus of the wild type p8 protein by creating a PstI restriction site (CTGCAG) in this region. This was achieved by mutation of the nucleic acid base at position 1372 of M13-L plasmid from T to A. The existing PstI site of M13-L plasmid at position 6245 was deleted by mutating A to T at position 6249, as well. The site-directed mutagenesis at these positions was accomplished by using QuikChange Lightning Multi Site-Directed Mutagenesis Kit (QIAGEN, Ontario). The phage DNA for mutagenesis was prepared by propagating M13-L phage as explained in the previous section. After propagation, the phage particles were collected by centrifugation and dsDNA inside the pellet was purified using QIAprep Spin Miniprep Kit (QIAGEN, Ontario). For mutagenesis, purified dsDNA was amplified using designed primer sequences (IDT, Integrated DNA Technologies, Inc.) (Table 2.2.2) and mutant strands were synthesized.

Oligonucleotide	Sequence (5'- 3')
Primer for Mutation at 1372	GCT GTC TTT CGC TGC AGA GGG TGA CGA TCC
Forward Primer for Verification of Mutation 1372	TTC TTA AAC AGC TTG ATA CCG ATA G
Reverse Primer for Verification of Mutation 1372	TGT TTC GCG CTT GGT ATA ATC G
Primer for Mutation at 6249	GCT TGC ATG CCT GCT GGT CCT CGA ATT CAC
Forward Primer for Verification of Mutation 6249	GCC ATT CGC CAT TCA GGC TG
Reverse Primer for Verification of Mutation 6249	TGA GTT AGC TCA CTC ATT AGG CAC
Forward Primer for p8 Cloning	CCT CTG CAG CGA AAG ACA GCA TCG G
Reverse Primer for p8 Cloning	ATA TAT CTG CAG TGT CGG GTA GTA GTC CGG ATT CGG ATC CCG CAA AAG CGG CCT TTA ACT CCC
Forward Primer for Verification of p8 Insert	TTC TTA AAC AGC TTG ATA CCG ATA G
Reverse Primer for Verification of p8 Insert	TGT TTC GCG CTT GGT ATA ATC G

Table 2.2.2 Oligonucleotide sequences for M13 phage p8 cloning.

After the reaction, the parent DNA template was digested with DpnI endonuclease at 37 °C for 5 minutes. The remaining mutated ssDNA was transformed into XL10-Gold ultracompetent cells and

incubated overnight at 37 °C on LB/IPTG/X-gal plates. The mutant closed circle ssDNA was converted into duplex form *in vivo* and propagated as phage. Following the incubation, the blue plaques on LB/IPTG/X-gal plates including mutated phage DNA were picked up and propagated as previously described. The mutated regions of propagated phage DNA were amplified by PCR using the designed primer sequences (IDT, Integrated DNA Technologies, Inc.) (Table 2.2.2) and sent to the *Plate-forme d'Analyses Génomiques* (Université Laval) for DNA sequence analysis.

The gold-binding peptide was inserted into modified M13-L phage using a PstI restriction site. The insert was positioned between the first and the fifth amino acids of the p8 protein by replacing residues 2–4 from (Alanine¹ - Glutamic acid² - Glycine³ - Aspartic acid⁴ - Aspartic acid⁵) to (Alanine¹ – insert - Aspartic acid⁵). Two primer sequences were designed: a forward primer including the insert sequence and a reverse primer to linearize the vector (Table 2.2.2). M13-L phage with an engineered PstI restriction site was propagated according to the protocol in previous section and viral DNA was purified using QIAprep Spin Miniprep Kit (QIAGEN, Ontario). To incorporate the insert, PCR was performed using Phusion® High-Fidelity DNA Polymerase (New England Biolab, Ontario), the two primers, and the mutated M13-L plasmid as DNA template according to the manufacturer's instructions (New England Biolab, Ontario). The obtained product was gel purified (1% agarose in TAE buffer, 45 minutes, 80 mV), extracted using QIAEX II Gel Extraction Kit (QIAGEN, Ontario), digested with PstI enzyme (New England Biolabs, Ontario) at 37 °C overnight and recircularized with T4 DNA Ligase (New England Biolabs, Ontario) by incubating overnight at 16 °C. The ligation mixture was transformed into XL10-Gold ultracompetent cells (Agilent, Ontario) and incubated on LB/IPTG/X-gal plates at 37 °C overnight. The blue plaques were picked up and their plasmids were amplified as previously described. After purification with QIAprep Spin Miniprep Kit (QIAGEN, Ontario), DNA samples were sent to the *Plate-forme d'Analyses Génomiques* of Laval University for DNA sequencing.

2.2.3 Synthesis and Characterization of AuNPs

2.2.3.1 Preparation of 9 nm AuNPs

AuNPs with 9-nm diameter (5.7×10^{12} particle/mL) were purchased from Ted Pella Inc. (CA, USA) and passivated with BSPP (bis(p-sulfonatophenyl)phenylphosphine) before their use. For passivation, BSPP was added to 100 mL of gold nanoparticle solution to a concentration of 1 mg/mL. After overnight incubation in the dark, the gold nanoparticles were spin concentrated with Amicon ultra-15 centrifugal filter units (molecular weight cut-off, MWCO; 30kDa, EMD Millipore, Canada) and desalted using a BSPP

solution as follows. The desalting procedure was carried out by spin concentrating the nanoparticle solution and rediluting to 5 mL with a 1 mg/mL BSPP solution in water. This was repeated six times to ensure complete removal of sodium citrate. The final volume of the solution was adjusted to 10 mL (5.7×10^{13} particle/mL) with 1 mg/mL BSPP solution in water and it was stored in the fridge by covering the container in aluminum foil to minimize exposure to light.

2.2.3.2 Synthesis of 3 nm AuNPs

AuNPs were synthesized according to the protocol of Zahr and Blum [26]. A tetrachloroauric acid (HAuCl₄) (Sigma Aldrich, Canada) solution (2.5×10^{-4} M) was prepared in 20 mL of deionized water and mixed with 10 μ L of 0.5 M sodium citrate solution. The solution was reduced by adding 600 μ L of 0.1 M of sodium borohydride in water with vigorous stirring and stored overnight in the dark for AuNP formation. In order to passivate the synthesized particles, BSPP was added to the solution to a concentration of 1 mg/mL. After overnight incubation in the dark, AuNPs were desalted according to the protocol used for 9 nm AuNPs. Lastly, the solution was centrifuged at 10,000 x g for 35 minutes to remove larger particles from the sample and the volume of the solution was adjusted to 2 mL with BSPP solution (1 mg/mL in water). The number of AuNPs in stock solution (2.8×10^{15} particle/mL) was estimated by using the equation based on the weight of HAuCl₄ used in the synthesis [27].

2.2.3.3 Synthesis of 13 nm AuNPs

Modified Turkevich method was used to synthesize 13 nm AuNPs [28]. Sodium citrate was dissolved in 150 mL water at a concentration of 2.2 mM and the solution was heated under reflux to near boiling. Tetrachloroauric acid (HAuCl₄) was added to the solution at a final concentration of 2.5×10^{-4} M and the temperature was kept constant until the solution turned red signifying the formation of the AuNPs. The synthesized AuNPs were passivated with BSPP (concentration) and desalted as 3 nm and 9 nm AuNPs using same protocol. The final volume of the AuNP solution was adjusted to 15 mL and stored in the fridge. The number of AuNPs in stock solution (3×10^{13} particle/mL) was estimated by using the equation based on the weight of HAuCl₄ used in the synthesis [27].

2.2.3.4 Characterization of Optical Properties by Ultraviolet and Visible (UV-Vis) Absorption Spectroscopy

AuNPs have optical properties resulting from the collective oscillation of free electrons, which are excited by the oscillating electromagnetic field of the light. This electron oscillation around the particle's surface causes a charge separation, forming a dipole oscillation along the direction of the electric field of

the light. The amplitude of the oscillation reaches its maximum at a specific frequency, called surface plasmon resonance (SPR), and induces a strong absorption of the incident light in the visible region that can be measured using a UV–Vis absorption spectrometer [14, 183, 184]. The extinction spectrum, generated by SPR, depends on the electron charge density of the particles and is affected by factors such as particle size, shape, structure, composition, and aggregation level. Therefore, it is possible to characterize AuNPs using UV-Vis spectroscopy, which allows estimation of AuNP-size, concentration, aggregation state, and surface functionalization [14, 185-187].

In this manner, UV-Vis spectroscopy was employed to determine the size of the synthesized AuNPs. The UV-Vis absorption spectra of samples were obtained with Cary-1E UV-Vis spectrophotometer (Varian Inc.) in the wavelength range of 400–1000 nm. The position of the SPR band which depends on the size of particles was used for characterization of the AuNPs. The measurements were carried out using methacrylate (PMMA) disposable cuvettes (BRANDTECH® Scientific Inc.) with 10 mm optical path.

2.2.3.5 Characterization by Transmission Electron Microscopy (TEM)

TEM is the most widely used characterization technique for nanomaterials and can offer direct image and chemical information of the samples. In addition to providing information on size, size distribution, and shape of the materials, the high resolution provided at atomic scale makes TEM a powerful technique in obtaining detailed information about its crystal structure and morphology [188].

In TEM, a high-energy electron beam (80–300 keV) is transmitted through a very thin layer of the sample. An electron emission source is used to produce the electrons into a focused beam and accelerated towards the specimen at a given beam energy. The electron beam is tightly focused using electromagnetic condenser lenses and reaches the specimen. A fraction of the incident electrons interacts with the sample and is scattered while some electrons are transmitted with little change in energy or direction. After passing through the specimen, additional electromagnetic condenser lenses are employed to refocus the electron and project it onto a screen to generate the image. Depending on the way of addressing the specimen, there are two modes of TEM: conventional TEM (CTEM) and scanning TEM (STEM). CTEM is a wide-beam technique where the electron beam floods the whole area of interest, and then the electrons scattered and transmitted from the sample are focused by a series of electromagnetic lenses. In the case of STEM, a fine focused beam is formed by a probe-forming lens before the specimen and addresses each pixel of the sample to form a sequential image as the probe is scanned across the specimen. [189, 190]. The energy-dispersive X-ray spectroscopy (EDS) and electron energy loss spectroscopy (EELS) are the

complementary tools used for analysis of the chemical composition and the electronic structure of the sample in TEM. While EDS relies on the counting of X-rays emitted from the specimen as a function of the photon energy, EELS analyzes the direct energy losses of transmitted electrons [191].

The morphology and size distribution of the synthesized AuNPs were analyzed using TEM (JEM-2100F, JEOL Inc., USA) at 200 kV at École Polytechnique de Montréal. For measurements, 10 μ L of the sample was deposited onto copper TEM grids (SOQUELEC Ltd., QC) stabilized with evaporated carbon film (3–4 nm thickness) and allowed to dry in air. The size distribution analysis was performed using ImageJ software.

2.2.4 Self-Assembly of AuNPs on M13 Phage template

2.2.4.1 Assembly of AuNPs on M13 phage

As the M13 phage was already PEG-purified after its propagation, it was directly used by diluting in reaction solution at a concentration of 10^9 PFU/mL.

The self-assembly of 3, 9, and 13 nm AuNPs on M13 phage templates was performed in 1 mL of phosphate buffer (PB) (pH 7.0) including 10 μ L of purified phage solution (10^{11} PFU/mL in TBS) and 100 μ L of nanoparticle stock solution. Optimization of the self-assembly process was performed for each AuNP size by studying the effect of reaction time and the ionic strength of reaction solutions. In order to optimize the time, reaction solutions were incubated on an orbital shaker at room temperature in the dark up to 5 days. The effect of the ionic strength of reaction buffer was studied in a range of 10 mM and 100 mM. Nanoparticle controls were prepared using same concentrations of AuNPs and replacing the phage template solutions with buffer of the same pH and ionic strength as the reaction solutions.

2.2.4.2 UV-Vis Absorption Spectroscopy

Assembly of AuNPs on the phage templates formed assemblies. Depending on the inter-particle distance, the surface plasmons of the particles can combine, which results in a red shift and broadening of the surface plasmon band [192]. This inter-particle plasmon coupling of the AuNPs on the phage templates can be detected in solution using UV-Vis spectroscopy as an SPR band with a different extinction spectrum compared to that of the isolated AuNPs in solution.

The growth of assemblies was tracked during the reaction using a Cary-1E UV-Vis spectrophotometer (Varian Inc.). Kinetic data of the assembly process was collected by recording UV-Vis

spectrum in the 400–1000 nm region during a period of up to five days. Nanoparticle controls were also characterized by recording their UV-Vis spectrum in the 400–1000 nm region over a period of five days.

2.2.4.3 TEM

The assembly of AuNPs on phage templates was visualized by TEM after 2 days of incubation. For TEM observation, 10 μL of the reaction solution was deposited onto copper TEM grids (SOQUELEC Ltd.) stabilized with evaporated carbon film (3–4 nm thickness) and allowed to sit for 5 minutes. Using a wedge of filter paper, the solution was wicked away from the grid. Immediately, 10 μL of staining solution (0.5% uranyl acetate (Canemco Inc., QC) in water) was applied to the grid for 10 seconds and the stain solution was wicked away by a wedge of filter paper. Lastly, the TEM grid was quickly dried with a hair drier and stored in a grid box. Images were collected using a JEM-2100F model TEM (JEOL Inc., USA) at 200 kV. Because a uranyl acetate solution was used to negatively stain the phage particles, both AuNPs and phage particles could be observed in the images.

2.2.4.4 DLS

Dynamic light scattering (DLS) is a versatile and useful technique to determine the average particle size and size distributions of nanoparticles in liquids. The technique is based on the constant movement of colloidal particles in a liquid due to Brownian motion. In Brownian motion, the particles randomly move due to the multiple collisions they encounter with solvent molecules surrounding the particles. DLS measurements are performed by illuminating the particles with a laser and analyzing the intensity of light scattered with time, at a given scattering angle. The light scattered from the particles can either interfere constructively (light regions) or destructively (dark regions) forming set of speckle patterns on the surface of a detector and its intensity at any particular point changes by time due to Brownian motion of the particles. This fluctuation in the intensity of scattered light is measured and used to calculate the size of the particles. This is usually done using an auto-correlator, which allows rapid real-time calculation of the scattered intensity time correlation function and measures the diffusion coefficient of the particle (D). For spherical particles in a dilute dispersion, the average hydrodynamic radius of the particles (R) is then calculated from D using the Stokes–Einstein relationship (eq. 2.1).

$$D = k_B T / 6\pi\eta R \quad (2.1)$$

where k_B is Boltzmann's constant, T is the absolute temperature, and η is the viscosity of the suspending medium [193-196].

DLS measurements were performed to determine the assembly of AuNPs on phage templates. The change in the size of phage templates upon binding of the AuNPs and the change in total size distribution of the reaction solution were observed during a period of 5 days. The measurements were conducted using Zetasizer Nano S90 DLS system (Malvern Instruments Ltd, UK). The samples were held at 25 °C by a sample holder and the measurements were determined from 8 runs, 8 seconds each. Each sample was analyzed in triplicate and all DLS data were analyzed using Malvern Zetasizer 7.11 software. All reported mean particle hydrodynamic diameters (DH) were calculated from volume based particle size distributions.

2.2.4.5 Assessment of Integrin Binding Affinity of M13-templated Gold Assemblies

Phage ELISA (Enzyme-Linked ImmunoSorbent Assay) was performed to determine the integrin affinity of RGD bearing M13-templated gold assemblies. In this assay, the wells of a microplate were coated with 200 μ L of human integrin alpha V beta 1 heterodimer protein (Acrobiosystems Inc., Newark, US) dissolved in phosphate-buffered saline (PBS; 137 mM NaCl, 2.7 mM KCl, 4.3 mM Na₂HPO₄, 1.47 mM KH₂PO₄, pH 7.4) at a concentration of 14 μ g/mL. After incubating the microplate overnight at 4 °C, the unbound protein was removed and the wells were incubated with 200 μ L of blocking buffer (3% bovine serum albumin (BSA) in PBS) for 2 hours at room temperature. Meanwhile, the phage-templated gold assemblies composed of 3 nm, 9 nm and 13 nm AuNPs and their corresponding control reaction solutions without phage templates were prepared. The samples were diluted with an equal volume of blocking buffer and incubated for 20 min before their addition to the wells. After removal of the blocking buffer, 200 μ L of the diluted samples were added to the integrin-coated wells and incubated for 2 hours at room temperature. The wells were extensively washed with washing buffer (0.05% Tween 20 in PBS) and 200 μ L of horseradish peroxidase conjugated anti-M13 monoclonal antibody (Fisher Scientific, Ontario) in blocking buffer was added to label the bound phages inside the wells. The microplate was incubated for 1 hour at room temperature and unbound anti-M13 antibodies were removed by washing six times with washing buffer. Binding of anti-M13 antibodies to recombinant M13 phages inside the wells was detected by adding 200 μ L of TMB (3,3',5,5'-Tetramethylbenzidine) substrate (Invitrogen Inc.) and recording the enzymatic reaction with absorbance measurements at 450 nm. The enzymatic reaction was stopped after 45 min by adding 100 μ L of stopping reagent (Invitrogen Inc.) and the absorbance measurements were performed using microplate reader (Cytation 5 imaging reader, Biotek, US).

2.3 Results and Discussion

2.3.1 M13 Phage template displaying gold-binding moieties and RGD peptide

Small RGD peptides specifically recognize integrin molecules that are over-expressed on tumor vasculature and tumor cells [197, 198]. Therefore, they have been employed in several applications including targeted delivery of nano carriers (e.g. drugs, nanoparticles) to cancer cells and the construction of support materials for tissue regeneration [199-202]. In this manner, an RGD peptide (GRGDSP) was inserted into p3 minor coat protein for possible future bio-applications of designed M13 templates, and to evaluate the effect of AuNP assembly on the phage on their ability to target specific biomolecules or structures.

In order to design M13 phage templates, initially, RGD peptides were displayed on p3 minor coat protein. Ph.D. Peptide Display Cloning System includes M13KE g3 cloning vector and extension primer. M13KE is a simple M13 derivative in which cloning sites have been introduced at the 5' end of gene 3 (g3) for display of short peptide sequences as N-terminal p3 fusions. Since the vector is a phage, all 5 copies of p3 on the surface of each virion are fused to the cloned peptide. By employing one of tip coat protein of M13, p3, in RGD display, it was aimed to prevent possible interference of AuNPs with integrin binding ability of phage template. The presence of p3 cloning side in M13KE phage, but not other tip coat proteins, made p3 coat protein the best option for RGD display.

Successful insertions into M13KE resulted in M13 phage particles with gene products of RGD peptide sequences. These phage particles formed blue plaques after their overnight amplification in XL10-Gold ultracompetent cells. Analysis of phage plaques was performed by PCR amplification whereas specific primer sets were designed to amplify the region including the gene encoding RGD peptide fused p3 protein. PCR amplification of phage samples resulted in a product with the size of 327 bp and corresponding fragments were detected on agarose gel (Figure 2.3.1). PCR amplification of some blue plaques resulted in PCR products with the size of 300 bp. These are the phage particles formed from M13KE vector without the inserts of RGD peptides which occurs when M13KE DNA is ligated and closed without taking any insert. The presence of the inserts was also confirmed by DNA sequencing.

The last step in M13 phage template design was display of gold-binding peptide (VSGSSPDS) on p8 major coat protein which provided a platform for self-assembly of AuNPs with close proximity due to the high copy number (2700). Recombinant M13 phage displaying RGD peptide on p3, named M13-L, was

used as template DNA. VSGSPDS peptide was inserted into created PstI restriction site and was confirmed by DNA sequence analysis.

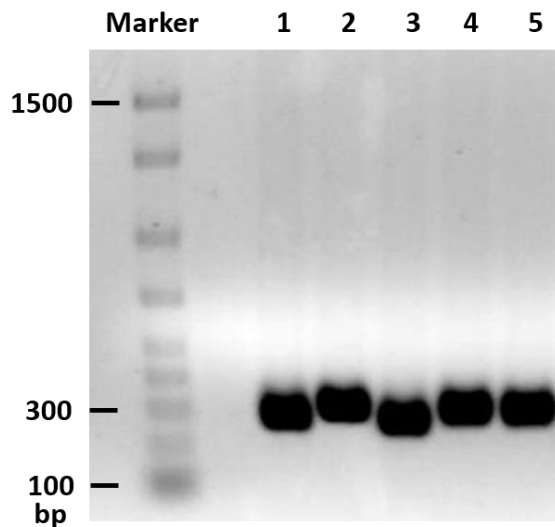


Figure 2.3.1 Detection of RGD peptide insertions in M13KE cloning vector by PCR. Marker, molecular size standard; lane 1-3, PCR product of M13KE phage (300 bp); lane 2-4-5, PCR product indicating the presence of linear GRGDSP peptide fusion in M13KE phage (327 bp).

2.3.2 BSPP-passivated AuNPs

All AuNPs prepared for this work were characterized by UV-Vis absorption spectroscopy and TEM imaging. Characterization was performed after BSPP-passivation of nanoparticles. BSPP is a negatively charged phosphine ligand used for stabilization of AuNPs [203, 204]. Although it is a strong ligand that increases AuNPs stability, moderate affinity between gold and BSPP molecules enables replacement of BSPP with other molecules for further modifications of the AuNP surface. As the final goal of the project was self-assembly of AuNPs on phage templates, high stability of particles at reaction conditions was intended and BSPP was employed as a stabilization agent to avoid aggregation.

Size distribution analysis of TEM images demonstrated that the synthesis of AuNPs resulted in 3 and 13 nm particles (Figure 2.3.2a and Figure 2.3.2c). AuNPs purchased from Tedpella Inc. were also characterized by TEM and possessed ~9 nm diameters (Figure 2.3.2b).

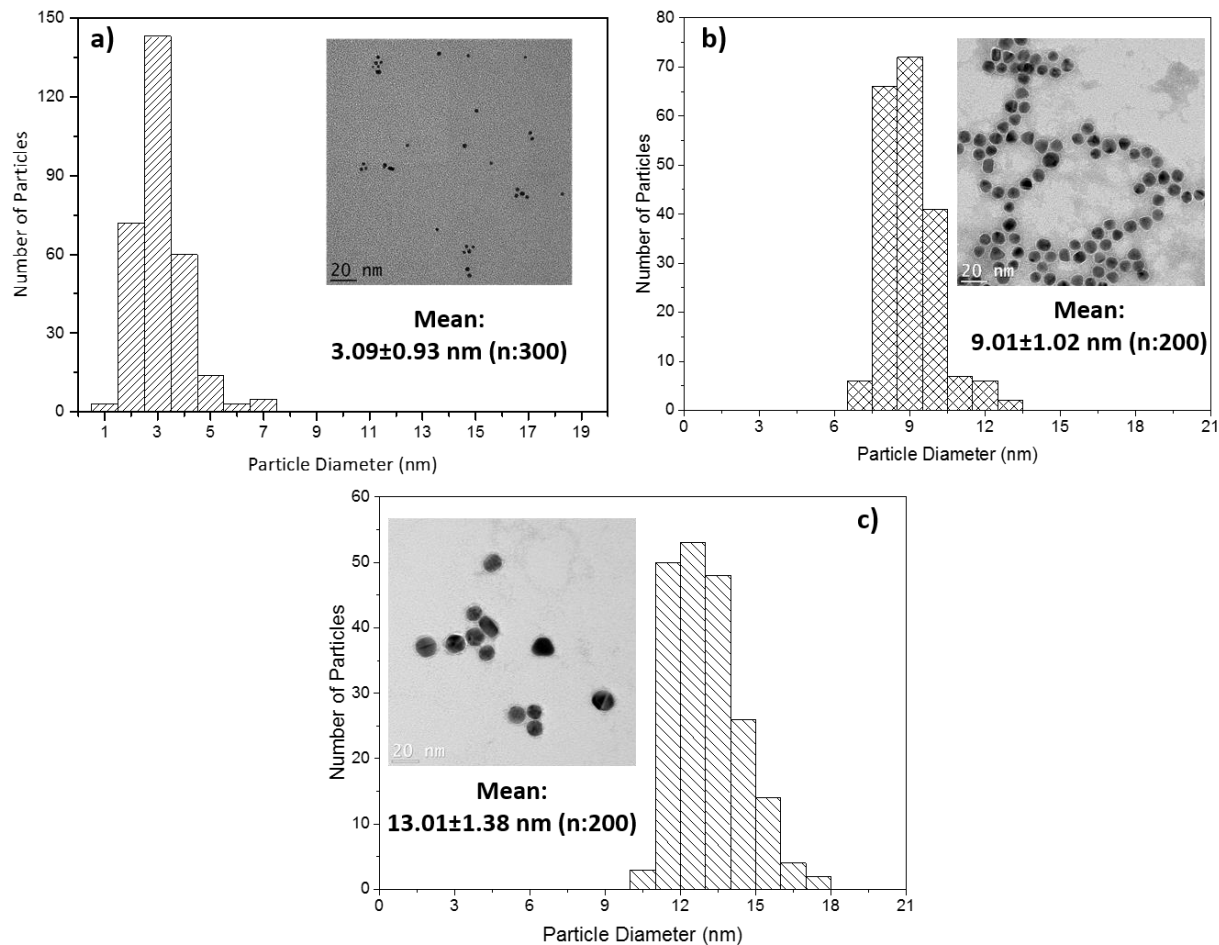


Figure 2.3.2 TEM images and corresponding size distribution histograms of BSPP-passivated AuNPs.

UV-Vis absorption spectra of colloidal AuNPs were also recorded and size information extracted from SPR peak position was in agreement with the measured particle diameters obtained by TEM (Figure 2.3.3). The SPR band of AuNPs, which is around 520 nm, is affected by particle size as the plasmon wavelength maximum shifts to the longer wavelengths with increasing particle size [14]. Similar trend was also observed in our measurement; the smallest plasmon wavelength maximum was recorded for 3 nm AuNPs whereas 13 nm AuNPs had the highest value.

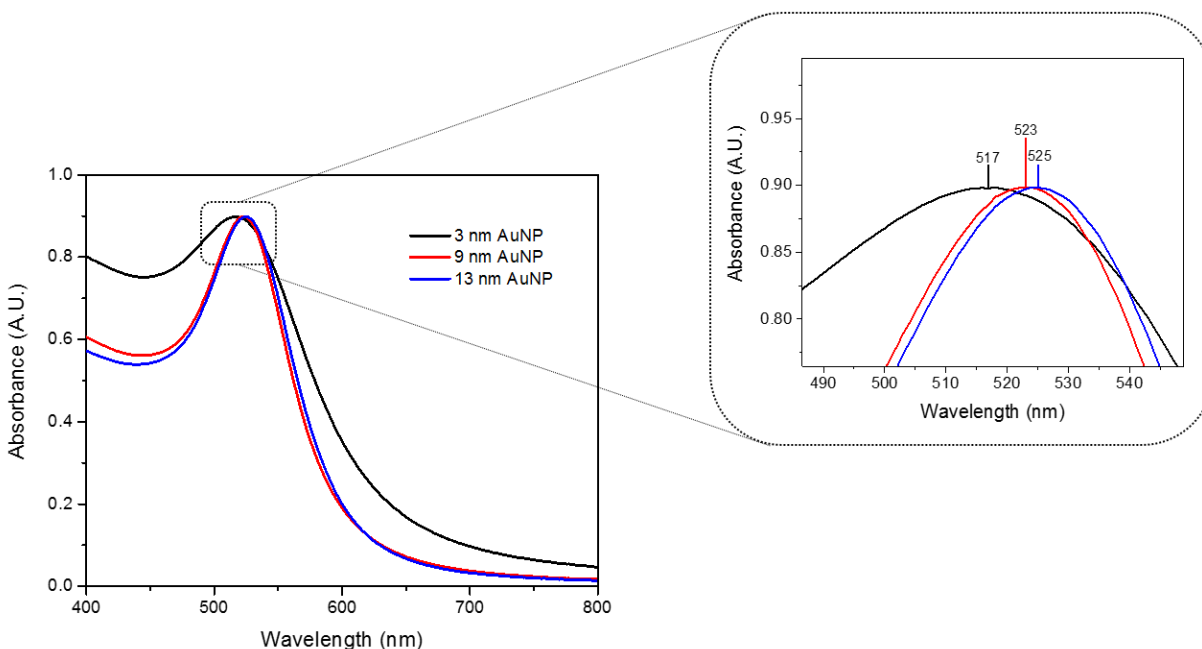


Figure 2.3.3 UV-Vis absorption spectra of BSPP-passivated AuNPs with diameters of 3 nm (black line), 9 nm (red line) and 13 nm (blue line).

2.3.3 Self-assembly of AuNPs on M13 Phage Template

Optimization of AuNP self-assembly on M13 phage template was initially performed for 3 nm AuNPs. The gold-binding peptides displayed on M13 were responsible for mediating the interaction of AuNPs with phage template and controlling their locations on M13 surface. However, both AuNPs and M13 phage were negatively charged and it was crucial to overcome the repulsive forces between them for a successful assembly process [26, 205]. For this purpose, the ionic strength of the reaction solution was optimized to find the best electrolyte concentration to minimize the repulsion between the particles. Electrolyte concentration plays an important role in reducing the repulsive forces by shielding the negative charge of the molecules, as well as AuNPs, and enables the interaction between them [206, 207]. The assembly of AuNPs on M13 templates was tracked in different buffer solutions by DLS (Figure 2.6). It was observed that the interaction between AuNPs and phage template in 5 mM PB was too weak, given that a 2-day reaction resulted in the formation of two main populations corresponding to isolated AuNPs (~ 26 nm) and AuNPs partially assembled on M13 template (~ 93 nm) (Figure 2.3.4a). This was due to the fact that the electrolyte concentration was too low to reduce the repulsive forces between the particles. It is worth mentioning that the size of isolated AuNPs in the reaction solution was higher than its expected value. There are several possible explanations for this size difference. First of all, the diameter of AuNPs

(3 nm) was too small to be correctly detected by DLS system used in this work. Additionally, the reduced repulsion between AuNPs in these solution conditions could induce partial formation of small gold aggregates with higher size.

It is important to mention that the use of DLS in this study allowed us to observe the assembly process in the presence of unbound AuNPs, which were present in excess, because AuNPs scatter light more efficiently than phage particles [208]. At low ionic strengths, AuNPs did not interact with phage particles as they were still maintaining in colloidal form with their typical hydrodynamic diameter. Once AuNPs were assembled on phage template, they formed clusters larger than the isolated colloidal gold and they were distinguished by their scattering peak being shifted toward larger diameters [209]. Therefore, the second population observed in the DLS histogram suggested the assembly of AuNPs on M13. The size of the population was higher than the size of the original M13 phage measured with the same DLS system (~ 70 nm). As a result of the presumed AuNP assembly, the diameter of the assembly increased from ~ 70 nm to ~ 93 nm [126]. However the ionic strength was not high enough for a strong phage–gold interaction, as the overall number of the M13-templated gold assemblies was very low compared to free AuNPs in the solution. As the reaction was taking place, after 2 days of reaction, the population belonging to isolated AuNPs disappeared, resulting in the formation of new populations (~ 67 nm and ~ 78 nm) which were smaller than the previous M13-templated AuNP assemblies (~ 93 nm). The difference in size of the assemblies formed during the reaction might be due to the flexibility of the phage structure made of protein coat and DNA material inside. Depending on the position of phage particles in solution, it could be possible to observe different sized assemblies. Although the majority of AuNPs assembled on phage template after 3 days, a third population (~ 5300 nm) was also formed in the solution. The formation of large random phage–AuNP aggregates was the result of the instability of AuNPs, making reaction times longer than 2 days unfavorable.

The self-assembly of AuNPs in 10 mM PB showed a different trend as there was no population corresponding to the unbound AuNPs at the beginning of the reaction, indicating stronger gold–phage interactions (Figure 2.3.4b). The main population consisted of M13–AuNP assemblies with sizes ranging from ~ 61 nm to ~ 87 nm. As observed with 5 mM PB, extended reaction times induced the formation of large phage–AuNP aggregates (~ 5030 nm).

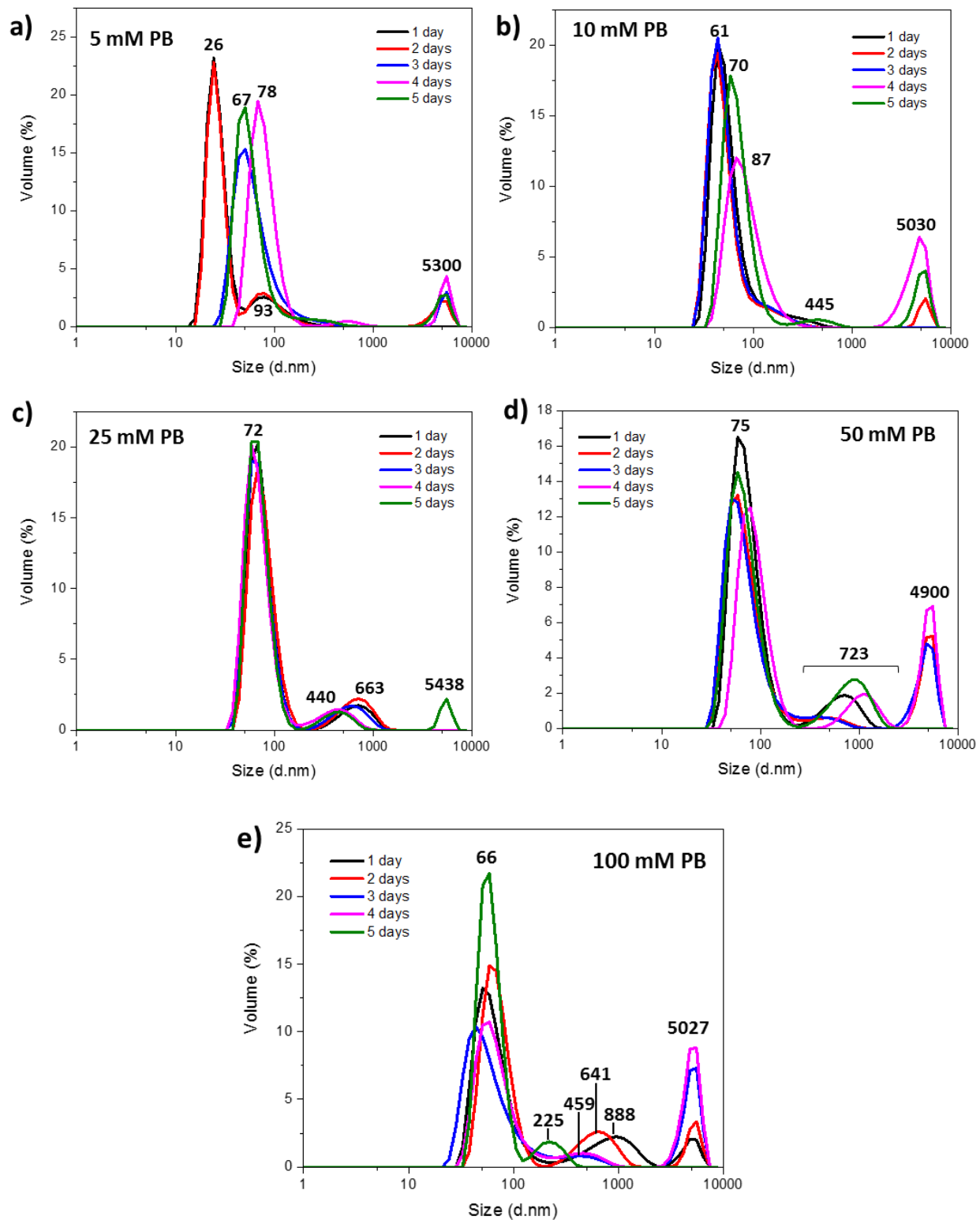


Figure 2.3.4 DLS histograms for volume based size analysis of M13 phage-3 nm AuNP solutions in a) 5 mM, b) 10 mM, c) 25 mM, d) 50 mM and e) 100 mM phosphate buffers. DLS histograms of each sample solution were recorded for a 5 day period.

Increasing the ionic strength of the reaction solution up to 25 mM enhanced the interactions between phage and AuNPs. M13–AuNP assemblies formed quickly and kept their stability for a longer period (Figure 2.3.4c). Large phage–AuNP aggregates were observed only after five days. During the first 4 days, the size of two main populations remained almost unchanged (~ 72 nm; ~ 440 – ~ 663 nm). Unlike 5 mM and 10 mM PB, a new population with an average size between ~ 440 – 663 nm was formed. This new population can be explained by a better coverage of phage surface with AuNPs. AuNPs assembled along the length of M13 phage would result in a AuNP assembly with the size of phage length which is ~ 900 nm.

Further increase in ionic strength up to 50–100 mM did not change the size of the observed main populations, which were ~ 75 nm (Figure 2.6d) and ~ 66 nm (Figure 2.3.4e). However, the increase in the electrolyte concentration made AuNPs more unstable and induced the formation of large phage–AuNP aggregates immediately at the onset of the reaction. Similar to the phage–AuNP interaction in 25 mM PB, a second population with a size close to phage length was also observed in reaction solutions with higher ionic strengths. However, the size of this population in 100 mM reaction solution decreased from ~ 888 nm to ~ 225 nm by time. This was another indication of AuNPs instability under these reaction condition. M13–AuNP assemblies evolved into larger aggregates with time as AuNPs became unstable.

DLS measurements have demonstrated that the self-assembly of 3 nm AuNPs on M13 phage could be achieved in a controlled manner in 25 mM phosphate buffer. A reaction time of one day resulted in the formation of M13–AuNP assemblies. In order to demonstrate the change in size of phage template upon self-assembly of AuNPs, the DLS histograms of AuNPs, M13 template and M13-templated AuNPs were plotted in the same graph. As shown in Figure 2.3.5a, the size of M13 phage (~ 70 nm) increased upon binding of AuNPs. While the size of the first population in the DLS histogram slightly increased (from ~ 70 nm to ~ 72 nm), the increase in volume of the second population (~ 663) was more significant (from 2% to 15%). UV-Vis spectroscopy was employed to study the effect of the assembly process on the plasmonic properties of AuNPs. It was interesting to observe that the assembly of AuNPs on M13 phage did not produce a marked shift or broadening in their SPR band (Figure 2.3.5b). Plasmon coupling between adjacent metal nanoparticles is observed under special conditions where the distance between AuNPs (D) is less than the average particle diameter ($2r$) [29]. The inter-particle distance (D) between AuNPs assembled on M13 phage was analyzed using the images recorded by TEM (Figure 2.3.5d). By averaging 200 measurements, D value was calculated 3.26 ± 1.16 nm. The obtained D value, larger than 3 nm, was

also an indication of large inter-particle distance which prevented the plasmon coupling between AuNPs. Therefore, the position of the SPR band was preserved.

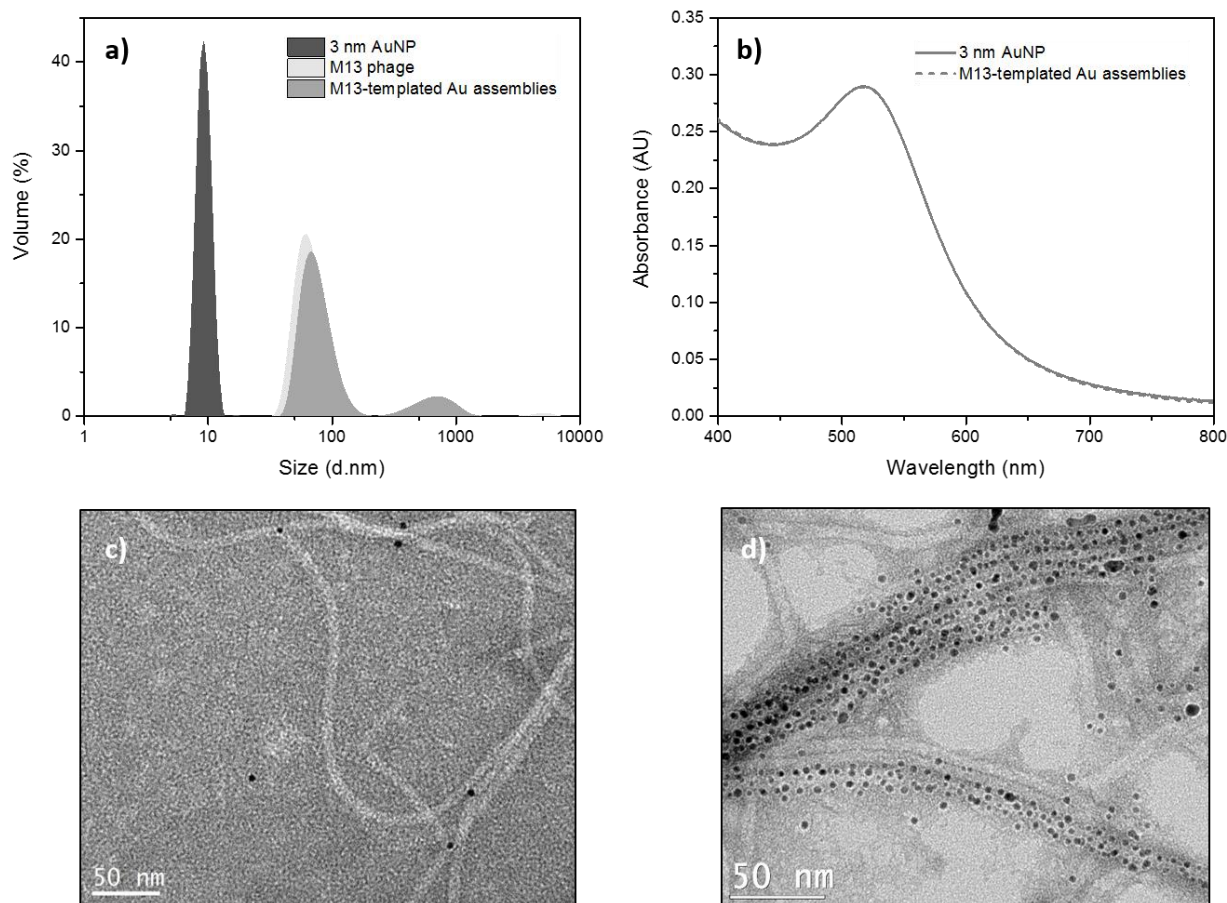


Figure 2.3.5 Characterization of 3 nm AuNPs self-assembled on M13 phage template after 1 day reaction a) DLS histograms showing the size of 3 nm AuNPs, M13 phage and M13-templated gold assemblies. b) UV-Vis spectra of 3 nm AuNPs in colloidal solution (solid line) and self-assembled on M13 phage template (dashed line). c) TEM image of M13 phage stained with uranyl acetate (2%) d) TEM image of 3 nm AuNPs assembled on M13 phage stained with uranyl acetate (2%).

The self-assembly of 9-nm AuNPs on M13 phage was optimized in a similar way to above. In previous experiments performed with 3 nm AuNPs, it was observed that low ionic strength reaction solutions (5 mM and 10 mM PB) were not favorable for the formation of M13-templated gold assemblies, due to the low electrolyte concentrations. In the case of reaction solutions with ionic strength higher than 25 mM, the electrolyte concentrations were too high to maintain sufficient stability of AuNPs for the formation of stable assemblies. Therefore, the effect of ionic strength on assembly of 9 nm AuNPs was investigated by performing phage-gold binding reactions in 10 mM and 25 mM phosphate buffers (Figure 2.3.6).

As observed for 3 nm AuNPs, the interaction of 9 nm AuNPs with phage templates in 10 mM PB was also very weak and did not result in the formation of an assembly. Over a 5-day period, the main population had a size of ~ 22.4 nm corresponding to the size of colloidal 9 nm AuNPs in the reaction solution (Figure 2.3.6a). Nevertheless, the formation of phage–AuNP assemblies (~ 257 nm) was observed after 3 days of reaction. However, the main AuNPs, representing a volume higher than 90% in the reaction solution. Large phage–AuNP aggregates (~ 4930 nm) were also observed after the first 3 days of reaction. As expected, the interactions of 9 nm AuNPs with phage templates in 25 mM PB was stronger and M13–AuNP assemblies dominated the reaction solution with populations having the size of ~ 704 nm and ~ 1100 nm (Figure 2.3.6b). The populations with smaller size (46 nm, 100 nm and 200 nm) can be explained as being random small AuNP aggregates and incomplete AuNP coverage on the phage templates.

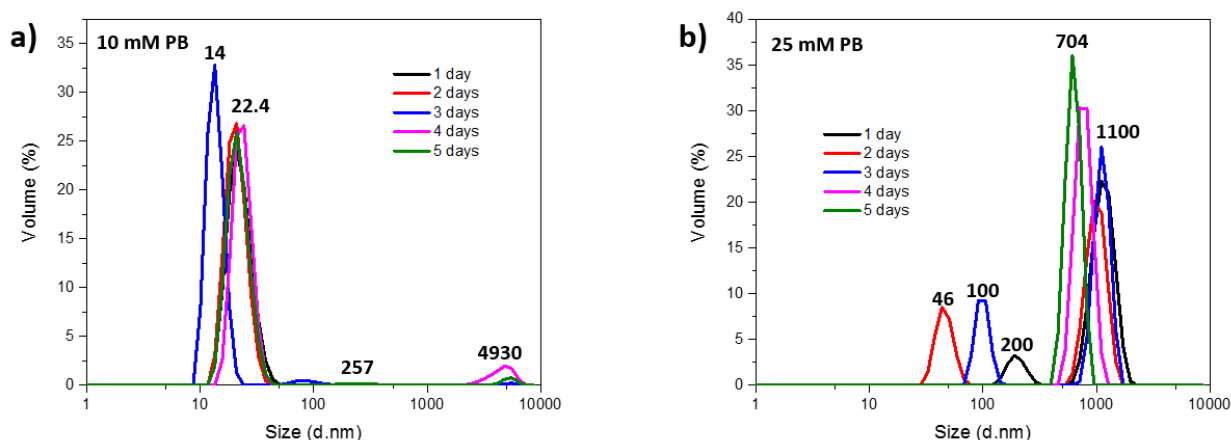


Figure 2.3.6 DLS histograms for volume based size analysis of M13 phage-9 nm AuNPs solutions in a) 10 mM and b) 25 mM phosphate buffers. DLS histograms of each sample solution were recorded for a 5 day period.

Analysis of the size distribution histograms belonging to 9 nm AuNPs, M13 phage and M13–AuNP assemblies clearly showed the change in the size of phage template as well as AuNPs due to the self-assembly of AuNPs (Figure 2.3.7a). While the peak of colloidal AuNPs disappeared, phage–AuNP assemblies became visible with the formation of a peak at ~ 1008 nm which was the approximate length of M13. The peak centered at ~ 70 nm can be assigned to the phage template partially covered with AuNPs. Characterization of M13–AuNP assemblies by UV-Vis spectroscopy also confirmed the self-assembly of AuNPs on M13. Due to the assembly of AuNPs on the phage surface, a red shift (~ 2 nm) and broadening of the SPR band occurred (Figure 2.3.7b). TEM images were used to calculate the inter-particle distance between AuNPs assembled on M13 phage. Compared to self-assembly of 3 nm AuNPs, assembly of 9 nm AuNPs along the length of M13 resulted in a system with inter-particle distance of 6.34 ± 2.05 (n = 200), which was shorter than the diameter of the AuNPs. This value was sufficiently short and created a

coupling in plasmon oscillations of AuNPs assembled on phage template. The broadening in the SPR band of AuNPs upon their assembly on virus templates was also observed by other groups. For instance, the assembly of AuNPs on Tobacco Mosaic Virus coat was defined by the formation of new peaks in the 530–600 nm region of UV-Vis spectrum [26]. TEM images of the binding solutions after 1 day reaction also confirmed the self-assembly of AuNPs (Figure 2.3.7c and Figure 2.3.7d).

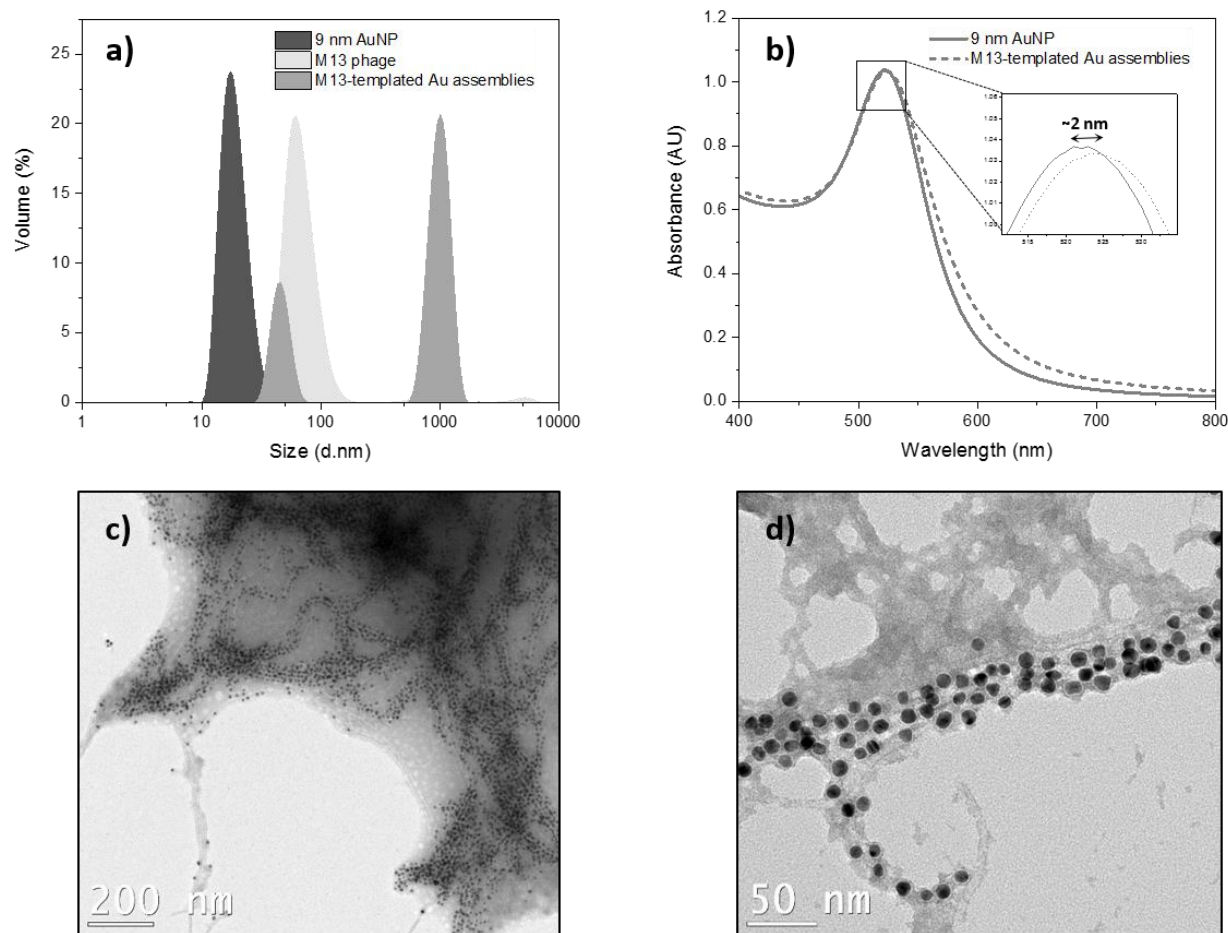


Figure 2.3.7 Characterization of 9 nm AuNPs assembled on M13 phage template after 1 day reaction a) DLS histograms showing the size of 9 nm AuNPs, M13 phage and M13-templated gold assemblies. b) UV-Vis spectra of 9 nm AuNPs in colloidal solution (solid line) and self-assembled on M13 phage template (dashed line). The inset shows the ~ 2 nm red shift in the SPR band due to the assembly of AuNPs on phage template. c) TEM image of 9 nm AuNPs assembled on M13 phage d) High magnification TEM image of 9 nm AuNPs assembled on M13 phage stained with uranyl acetate (0.5%).

The effect of ionic strength on self-assembly of 13 nm AuNPs on M13 phage was also studied by performing the phage–AuNP binding reactions in 10 mM and 25 mM PB. As previously observed for 3 nm and 9 nm AuNPs, 10 mM PB did not provide sufficient electrolyte amount to shield the negative charges of particles and consequently, AuNPs could not deposit on phage surface. DLS histograms of phage–AuNP

binding reactions at 10 mM PB mainly composed of the populations belonging to colloidal AuNPs with the size of ~23 nm (Figure 2.3.8a). Increase of the ionic strength to 25 mM favored interactions between phage and AuNPs and resulted in assembly of AuNPs on M13 surface. Formation of M13–AuNP assemblies was observed by the presence of main population peak with the size of ~957 nm (Figure 2.3.8b). Although the AuNP assemblies were formed in the first day of the binding reaction, the populations of small AuNP aggregates and phage templates partially covered with AuNPs (64 nm, 98 nm and 180 nm) were also observed during the first three days of reaction.

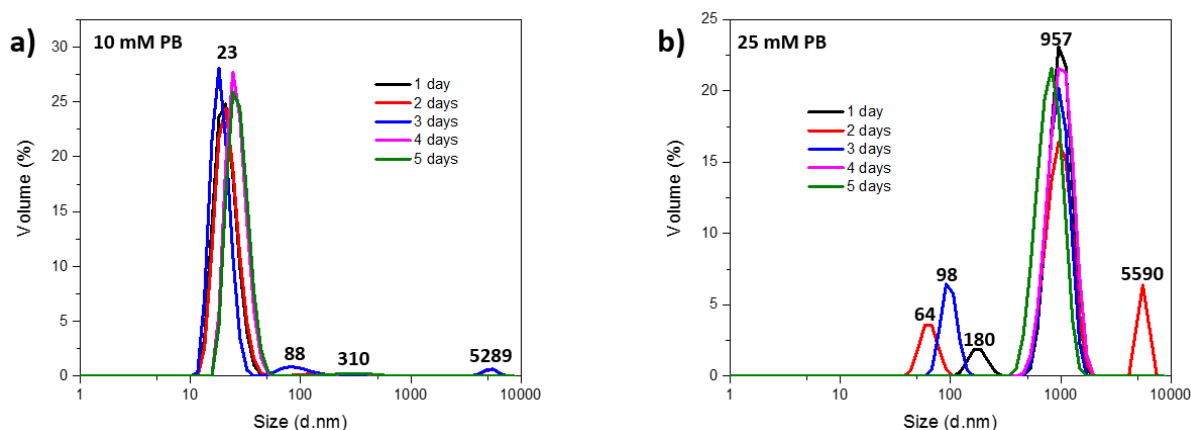


Figure 2.3.8 DLS histograms for volume based size analysis of M13 phage-13 nm AuNPs solutions in a) 10 mM and b) 25 mM phosphate buffers. DLS histograms of each sample solution were recorded for a 5 day period.

The size distribution histogram of M13–AuNP assemblies made of 13 nm AuNPs showed distinguishing features in comparison to the isolated AuNPs and M13 phage template (Figure 2.3.9a). The main populations dominating the histograms of colloidal AuNPs (~21 nm) and M13 phage template (~70 nm) were replaced by the population representing M13–AuNP assemblies. Besides this main population, there were other populations of large phage–AuNP aggregates and M13 phage partially covered with AuNPs. The change in absorbance spectrum of colloidal AuNPs was also observed for 13 nm AuNPs upon their assembly on M13 phage surface (Figure 2.3.9b). The inter-particle distance between 13 nm AuNPs assembled on M13 phage was calculated 3.17 ± 2 nm ($n = 200$) which resulted in a collective surface plasmon resonance on phage surface. The red shift (~3 nm) in the SPR band was close to the value observed for the clusters formed with 9 nm AuNPs (~2 nm). TEM images of the binding solutions after 1 day reaction also confirmed the self-assembly of AuNPs (Figure 2.3.9c and Figure 2.3.9d).

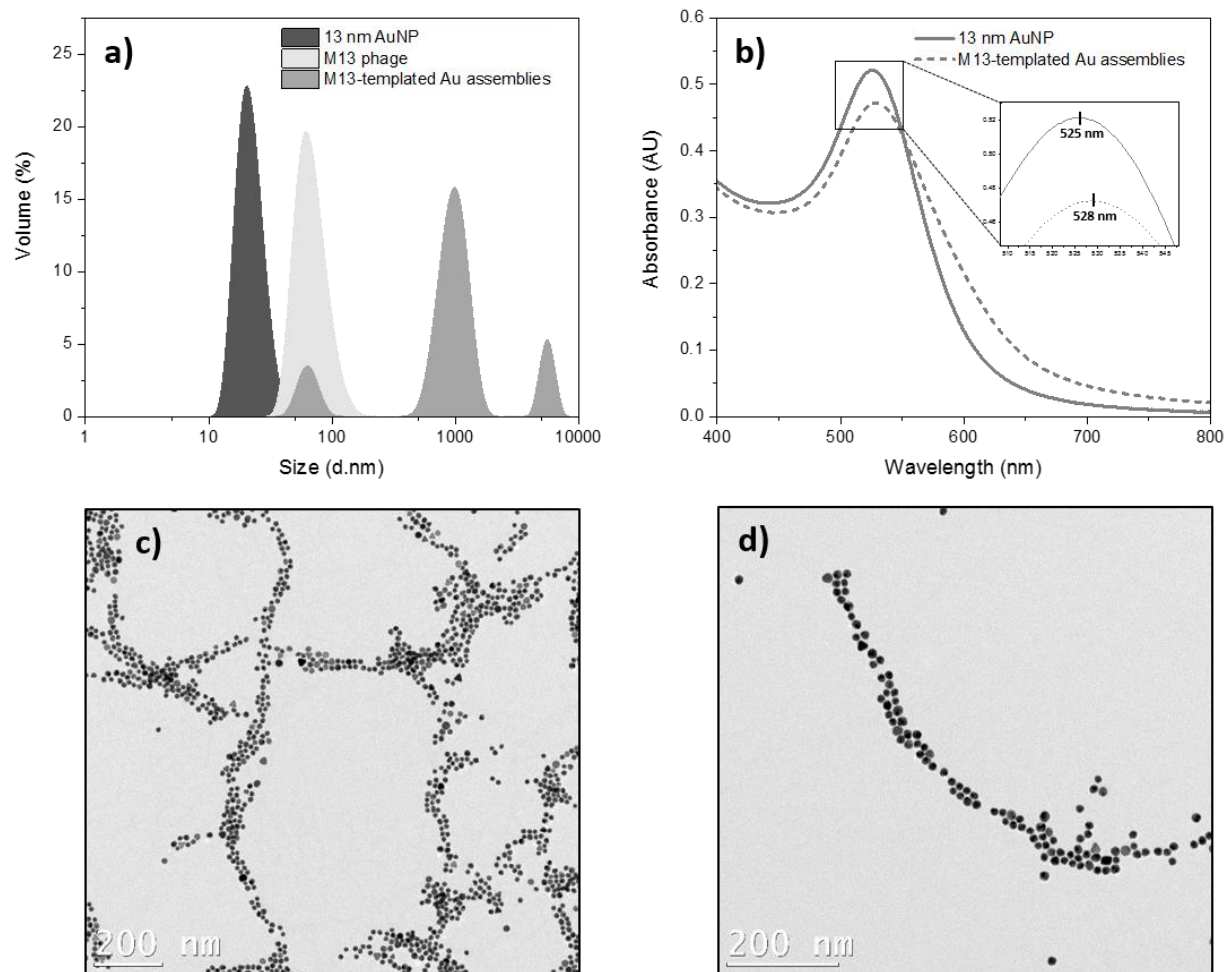


Figure 2.3.9 Characterization of 13 nm AuNPs assembled on M13 phage template after 1 day reaction a) DLS histograms showing the size of 13 nm AuNPs, M13 phage and M13-templated gold assemblies. b) UV-Vis spectra of 13 nm colloidal AuNPs (solid line) and self-assembled on M13 phage template (dashed line). The inset shows the ~3 nm red shift in the SPR band from 525 nm to 528 nm due to the assembly of AuNPs on phage template. c) TEM image of 13 nm AuNPs assembled on M13 phage d) High magnification TEM image of 13 nm AuNPs assembled on M13 phage.

2.3.4 Integrin Targeting Ability of RGD peptide on M13-templated Gold Assemblies

Display of RGD peptide on M13 phage and its functionality in the presence of assembled AuNPs were probed by ELISA, which was performed using integrin-coated microplate wells. Attachment of M13–AuNP assemblies to the integrin protein via its RGD peptide was detected using an anti-M13–HRP secondary antibody. The level of labeling was determined by adding HRP substrates which were peroxide and TMB. In the presence of peroxide, TMB was oxidized and converted into a product with blue color. As

seen in Figure 2.3.10, formation of blue color was observed in all wells containing M13–AuNP assemblies. On the other hand, the wells incubated with only AuNPs did not show any color formation.

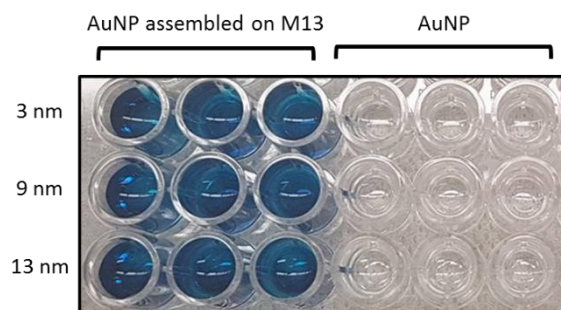


Figure 2.3.10 ELISA plate showing the color development due to the binding of integrin to RGD bearing M13 phage–templated gold assemblies. The wells in the first line of ELISA plate contain the samples which are prepared using 3 nm AuNPs whereas the samples in the second line and the third line are composed of 9 nm and 13 nm AuNPs, respectively.

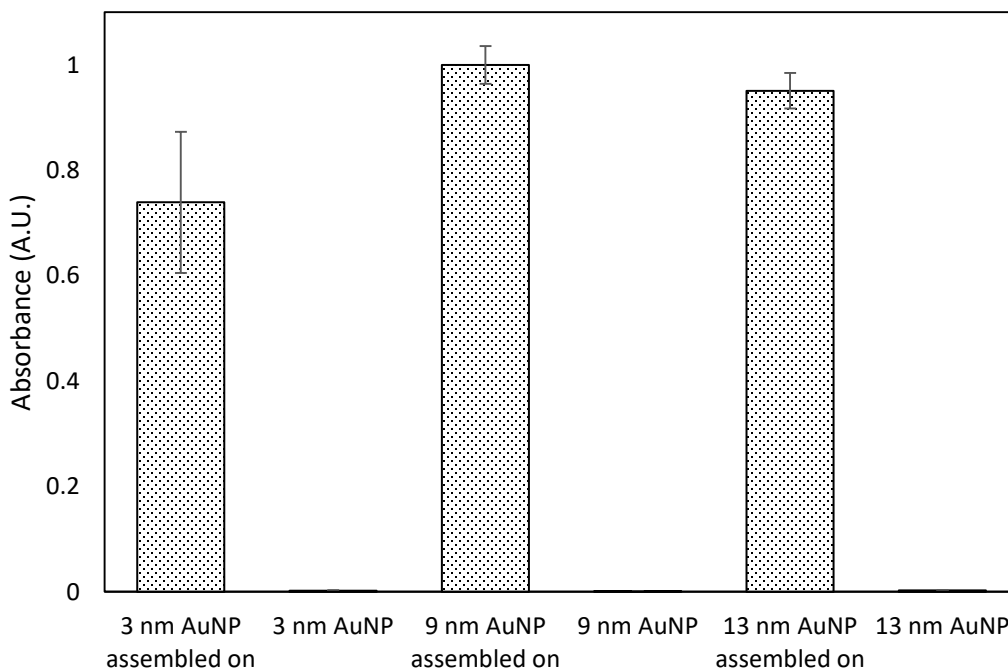


Figure 2.3.11 Reactivity of RGD bearing M13 phage–templated Au assemblies and colloidal AuNPs with human integrin protein.

The absorbance values of the samples in each well were plotted as seen in Figure 2.3.11. As a conclusion, the results of ELISA showed that AuNPs assembly along the p8 major coat protein of M13 phage did not sterically interfere with the specific binding ability of RGD peptide to integrin protein. As a result, M13–AuNP assemblies were able to recognize and bind to the integrin protein inside the wells.

2.4 Conclusion

In this chapter, M13 phage was used as a template to assemble AuNPs into well-defined three dimensional structures. Display of RGD peptide on p3 of M13 phage was intended for possible future applications of phage–AuNP assemblies as contrast agent in diagnosis of cancer, and was confirmed by PCR analysis and DNA sequencing. In a similar way, insertion of the Au-binding peptide sequence (VSGSSPDS) into p8 major coat protein was also confirmed by DNA sequencing. AuNPs of three different sizes (ca. 3, 9, and 13 nm) were assembled onto the resulting biotemplate to generate M13–AuNP assemblies.

The relative rate of assembly of AuNP on M13 versus the self-aggregation of the AuNPs was found to be crucial for preparing the assemblies, and could be controlled via the ionic strength of the incubation medium. Optimal conditions were observed at ionic strengths slightly lower than that causing AuNP self-aggregation [130]. Lower ionic strength buffers did not result in formation of M13–AuNP assemblies.

Finally, an immunoassay was performed to assess the functionality of RGD peptide within the assemblies. It was shown that M13–AuNP assemblies were able to recognize and bind to the integrin molecules through the RGD peptide displayed on p3 protein, despite the presence of AuNPs. This feature will make plasmonic M13-templated nanostructures promising platforms for developing imaging contrast agents or therapeutic entities.

3 T4 PHAGE-TEMPLATED AuNP ASSEMBLIES

3.1 Introduction

3.1.1 Structure and Characteristics of T4 Bacteriophage

T4 phage is a double-stranded DNA virus that is known to be one of the largest viruses to infect bacteria. It belongs to the Myoviridae family and infects *Escherichia coli* and the closely related *Shigella*. Like other members of Myoviridae family, T4 has a prolate icosahedral head, a collar with whiskers, and a contractile tail terminating in a baseplate that is attached to six long tail fibers (Figure 3.1.1a). While the fibers recognize the host cell surface and attach to the bacterium during the infection, the baseplate binds to the specific surface receptors and degrades the bacterial wall with the help of its enzymes. This process enables introduction of DNA into the cell. The virion consists of several components including DNA, proteins, and a few non-protein constituents such as polyamines associated with DNA (putrescine, spermidine, cadaverine), ATP and Ca²⁺ associated with the tail sheath, and dihydroxyteroylhexaglutamate associated with the baseplate [210].

The DNA of T4 phage is tightly packed inside the protein capsid, which has precise dimensions: a length of 120 nm and a width of 86 nm. The capsid is built with three essential proteins: the major capsid protein, gene product gp23* (49 kDa; 930 copies; * represents cleaved form), the vertex protein gp24* (47 kDa; 55 copies), and the portal protein gp20 (61 kDa; 12 copies) (Figure 3.1.1b). Additionally, there are two outer capsid proteins, the highly antigenic outer capsid protein (Hoc, 39.1 kDa, 155 copies), and the small outer capsid protein (Soc, 9.7 kDa, 810 copies), which are nonessential and bind to the surface of the capsid after its assembly is complete. The Hoc protein occupies the center of the gp23 capsomers and is present in up to 155 copies per capsid particle. The rod-like Soc proteins bind to the capsid surface between the gp23* capsomers (up to 810 copies per capsid) and form a nearly continuous mesh on the surface encircling the gp23* hexamers. Interaction of a Soc protein with two gp23* proteins of adjacent capsomers, as well as trimerization of Soc proteins through C-terminal interactions, stabilize the gp23* hexameric capsomers. Although Soc protein is not essential, the assembly of Soc proteins on the surface of the T4 capsid provides great stability and makes the phage survive under unfavorable conditions such as extreme pH (pH 11), extreme temperature (60 °C), osmotic shock, and the presence of denaturing agents. Nevertheless, deletion of either one or both *Hoc* and *Soc* genes does not affect phage viability or infectivity under standard laboratory conditions [211-213].

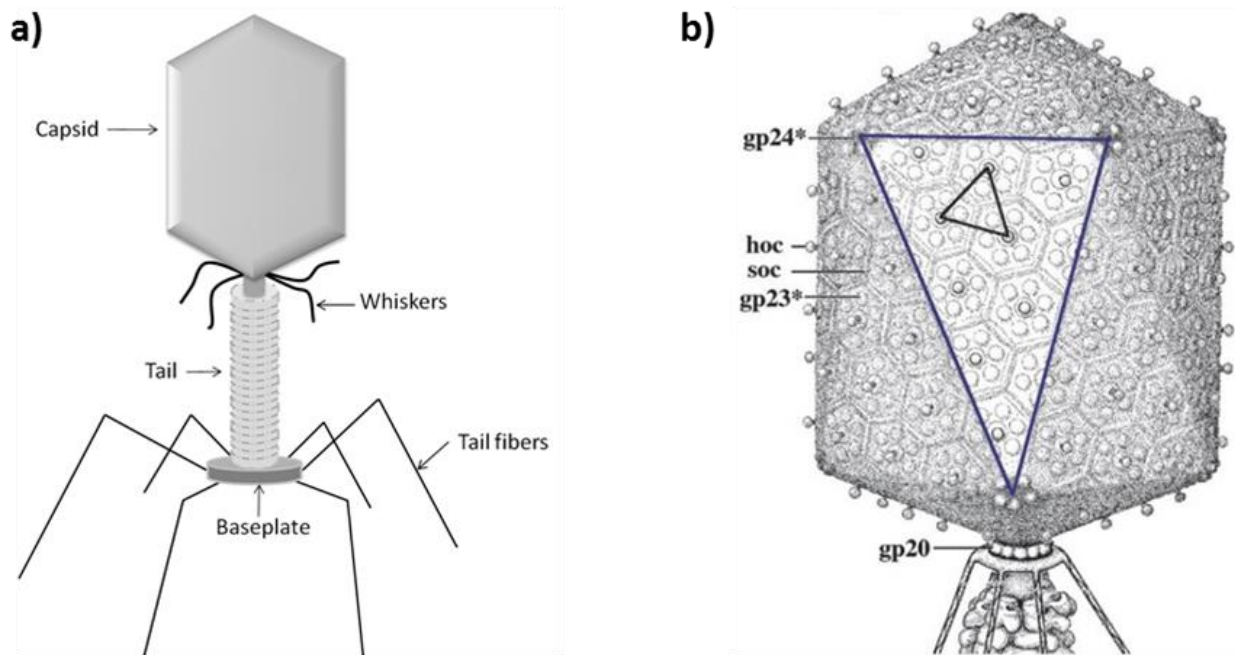


Figure 3.1.1 Structure of T4 Bacteriophage (a) Schematic representation of T4 phage virion (b) Model of proposed T4 head structure (adapted from [214]).

3.1.2 T4 Phage Display Platform

The display of fusion peptides/proteins on T4 phage has recently emerged as a promising tool to overcome the limitations of phage display platforms employing filamentous phages. For instance, one of the drawbacks of filamentous phage display is the limited size of the peptides displayed on the major coat protein (6–10 amino acid residues). Larger polypeptides can only be displayed on minor coat proteins but at very low copy numbers. Moreover, during phage amplification, synthesized coat proteins are inserted into the inner cell membrane where virion assembly and export occur. Due to the membrane-mediated nature of this process, fusion proteins that cannot cross the cell membrane will not be displayed on the phage surface. The secretion system of *E. coli* may also prevent the display of some peptides that are toxic to bacteria and also create the problem of correct folding of the displayed protein [215-218]. However, T4 phage uses a lytic life cycle for reproduction in which phage assembly takes place inside the infected cell and, afterwards, progeny phages are released by cell lysis. This feature of T4 enables the display of a broader range of proteins with different size, structure, and biological functions that may not be possible with filamentous phage display [210, 219].

In T4 phage display, decorative outer capsid proteins, Soc and Hoc, are used for the fusion of foreign proteins. As either Soc or Hoc sites can be used, it has also been shown that higher copy numbers of fusions on the phage surface can be achieved by display on both sites (Soc and Hoc) [71, 220]. Foreign proteins can be displayed on T4 phage by *in vivo* and *in vitro* approaches. The *in vivo* approach can be performed in different ways and one of them is based on the integration of a modified *Soc* gene into a *Soc* deleted T4 genome through a modified positive selection plasmid (pRH). In a pRH plasmid, the *Soc* gene is flanked on its 5' side by a 3' portion of the T4 lysozyme gene (*e'*), and on its 3' side by a 5' part of another T4 gene (*denV'*), which allows homologous recombination between the phage and the plasmid. Integration of the *Soc* fusion gene into the T4 genome allows the expression and *in vivo* binding of fusion proteins to the phage capsid [217]. Alternatively, Soc and Hoc fusion proteins can be incorporated to the phage capsid through a natural assembly process in host bacteria expressing the fusion proteins from a designed expression vector. Upon infection of bacteria with T4 phage strains having defective *Soc* or *Hoc* genes, fusion proteins are expressed and assembled onto the phage capsid [221, 222].

Although *in vivo* approaches have been widely used to display different proteins on the surface of T4 phage, they are limited to the display of a single component such as a peptide, domain, or protein. Limitations in displaying multiple components and large domains arise from the fact that the expression and assembly of the foreign proteins occur during phage infection. This lytic phage cycle leads to problems such as loss of critical epitopes due to nonspecific proteolysis, low and variable copy number of displayed proteins due to the variations in intracellular expression, structural heterogeneity due to aggregation of the expressed proteins, insolubility, and improper folding [217, 223, 224]. Thus, an *in vitro* approach has been developed to overcome these drawbacks for efficient and controlled display of large proteins on the phage surface. In this approach, foreign proteins fused to Soc and Hoc proteins are overexpressed in bacteria and purified. The high affinity interactions between Hoc/Soc proteins and the phage capsid enable *in vitro* assembly of purified proteins on *Hoc*- and *Soc*-defective phage, which is performed by simply mixing the components. Therefore, the *in vitro* approach results in a phenotype no longer connected to the genotype of the engineered phage in contrast to the *in vivo* approach. An attractive feature of the *in vitro* approach is that the expression of Hoc/Soc fusion proteins is not restricted to *E. coli* or a specific host, thus any expression system can be used for production of fusions. Consequently, functionally well-characterized and conformationally-homogenous fusion proteins are produced and displayed on phage capsids. Additionally, the copy number of displayed proteins can be controlled by changing the ratio of protein to capsid binding sites. It is worthy to note that the *in vitro* approach also allows customized engineering of T4 phage to display multiple proteins on the same capsid [225-227].

3.1.3 Self-assembly of T4 phage surface with organic/inorganic materials

The ability of introducing large protein fragments on Hoc and Soc proteins makes T4 phage a promising candidate for vaccine design. It has been already shown that the antigens specific for *Yersinia pestis* (the etiologic agent of plague), swine fever, anthrax and HIV (Human Immunodeficiency Virus) were successfully displayed on T4 phage and induced high antibody production [212, 220, 228, 229]. Lately, it has been demonstrated that T4 phage particles displaying anthrax protective antigens can be employed as a nanocarrier to assemble liposomes for the development of inexpensive vaccine formulations [230]. Liposomes containing monophosphoryl lipid A (MPLA) is an active adjuvant used in human phase I trials. Attachment of MPLA-containing liposomes onto the phage surface is achieved through the affinity of T4 receptor proteins to the glucosyl groups incorporated into the liposome structure in their glucosyl ceramide form. The high copy numbers of antigens displayed on phage surface make the resulting vaccine formulation more favorable than the existing platforms employing simple mixing of antigens with liposomes. In addition to ease of production, they are also efficient in inducing high titers of antigen specific antibodies.

As it was shown in vaccine design, the large surface area and high copy numbers of Hoc/Soc proteins enable the decoration of T4 phage's surface with a large copy number of functional molecules. Labelling of T4's surface with fluorescence dyes (Cy3 and Alexa Fluor 546) is another approach enabling their use as a molecular probe for cell imaging and flow cytometry applications. More than 1.9×10^4 dyes can be incorporated onto the phage capsid through the amine groups and, their attachment to phage coat proteins results in an enhancement of fluorescence [231]. This property may be interesting for their use as imaging contrast agents.

Magnetic particles are another group of material that have been assembled on T4 [232]. T4 phage has been widely used for detection of bacteria in biosensor applications, as a natural recognition probe of *E.coli* cells. Magnetic separation is an important step in biosensor design to concentrate the sample for improved detection limits. T4 phage particles have also been conjugated with magnetic particles to enable magnetic manipulation of samples. The conjugation of magnetic particles to T4 is typically achieved through the covalent attachment via the carboxyl or amino groups of phage coat proteins. Magnetically-labelled phage particles have been used to capture bacteria for sample concentration, as well as for the separation of impurities in the sample solution before the detection. After capturing the bacteria, samples can be detected by using several sensing platforms, such as electrochemical impedance spectroscopy or

flow cytometry [233]. It has been shown that magnetic manipulation of the sample improved the detection system by one order of magnitude, in terms of sensitivity and the ability to detect bacteria in complex media [234].

In addition to the chemical conjugation of materials onto T4, the capsid can be also used as a bioscaffold to synthesize metal nanoparticles. The formation of 3D nanostructures on the phage capsid is performed in two steps; 1) T4 particles are initially incubated in the solution of metal salts and 2) metal ions that interact with phage coat proteins are reduced by dimethylaminoborane [235]. Although this approach has been applied to synthesize different phage-templated metal nanostructures (e.g. gold, platinum, rhodium, cobalt, iron, palladium, and nickel), the mechanism of metal nanoparticle formation on phage coat protein is not known [236]. It has been suggested that the side-chains of the surface-exposed amino acids on coat proteins interact with the metal ions and mediate the nucleation and organization of the nanoparticles on T4 capsid [237].

In this chapter, T4 is employed as a biotemplate for the assembly of AuNPs for the generation of T4–AuNP assemblies. Initially, engineering of T4 phage to display gold-binding moieties will be presented, and will be followed by the description of the methods used for the optimization of AuNP self-assembly on designed phage templates.

3.2 Materials and Methodology

3.2.1 Materials

Bacteriophage T4 (HER27) and its host *Escherichia coli* B (HER1024) were obtained from the Felix d'Herelle Reference Center for Bacterial Viruses (Université Laval, Quebec). Bacteriophage T4-Z was kindly provided by Prof. Lindsay Black (University of Maryland, Baltimore). *Escherichia coli* strain HB101 competent cells were obtained from Promega (Madison, WI). All chemicals were obtained from Bioshop (Ontario, Canada) unless otherwise noted. They were of the highest grade available and were used as received without further purification. All aqueous solutions were prepared with deionized distilled water obtained from a Milli-Q water purifying system (18 M Ω /cm).

3.2.2 Engineering of T4 Phage Templates

3.2.2.1 Preparation of Bacterial Strains and Bacteriophages

Bacterial stock cultures were maintained in 35% glycerol and were kept at $-80\text{ }^{\circ}\text{C}$. To prepare fresh bacterial cultures, an inoculum from frozen glycerol stock was streaked onto a Luria Bertani (LB) (Miller) agar plate and incubated at $37\text{ }^{\circ}\text{C}$ overnight. A single colony from the plate was inoculated into 10 mL of LB broth (Miller) and incubated overnight at $37\text{ }^{\circ}\text{C}$ with shaking at 200 rpm. Transformed bacteria carrying recombinant pRH plasmids were cultured in LB broth/agar supplemented with $100\text{ }\mu\text{g}/\text{mL}$ of ampicillin. The viable bacteria number was calculated by preparing serial dilutions of culture and plating on LB agar plates. After overnight incubation, the colonies formed on agar plates were counted to calculate bacteria concentration as colony forming units (CFU).

The propagation of T4 phage was performed by the standard double-layer agar plate method [238]. In the case of wild-type and recombinant phage, $200\text{ }\mu\text{L}$ of overnight culture of *Escherichia coli* B and $100\text{ }\mu\text{L}$ of stock phage solution were mixed in 3 mL of soft agar (7 g/L of bacteriological agar (Fischer BioReagents) in LB broth). The mixture was poured over LB agar plates and allowed to harden to form a thin layer and incubated. After overnight incubation at $37\text{ }^{\circ}\text{C}$, the soft agar layer was scraped into a centrifuge tube containing 10 mL λ buffer (100 mM NaCl, 8 mM $\text{MgSO}_4\cdot 7\text{H}_2\text{O}$, 50 mM Tris-HCl (pH 7.5), and 0.002% (w/v) gelatin). The bacteria–phage–agar suspension was treated with a few drops of chloroform to release any progeny phages that might still have been in the host cells, and to prevent adsorption of phage to bacteria or bacterial debris. The suspension was centrifuged for 15 minutes at 5000 rpm (Thermo Scientific, Sorvall ST 8R) to remove agar and cell debris, then the supernatant was withdrawn and filtered through $0.2\text{ }\mu\text{m}$ pore size Millex-GV sterile syringe filters (EMD Millipore Ltd., Ontario). The phage lysates were stored at $4\text{ }^{\circ}\text{C}$. Enumeration of phage particles was also performed by double-layer agar plate method where serial dilutions of phage samples in λ buffer were mixed with overnight bacterial culture. The plaques formed on overnight incubated plates were counted to calculate phage titer in plaque forming units (PFU).

T4-Z phage is a lysozyme-deletion mutant of T4 phage and the protocol for phage propagation and titration was modified accordingly. In this manner, LB medium was replaced with Citrate medium (CM) (10 g tryptone; 5 g NaCl; 50 mL Tris pH 8.0, 1 M; 10 mL 25% sodium citrate in 1 L water) supplemented with chicken egg white lysozyme (EWL) (Fluka Analytical, US). Citrate bottom agar and soft agar included 15 g/L and 7 g/L agar, respectively. Citrate soft agar (2.5 mL) was mixed with $200\text{ }\mu\text{L}$ of overnight culture

of *Escherichia coli* B, 100 µL of stock phage solution and 500 µg of EWL, and then plated on citrate agar plates. After overnight incubation at 37 °C, the plates were exposed to chloroform vapors by adding 1 mL of chloroform to the top of the petri plate and leaving the inverted plate at room temperature for 15 minutes. The soft agar layer was scraped into a centrifuge tube containing 10 mL λ buffer and the suspension was centrifuged for 15 minutes at 5000 rpm (Thermo Scientific, Sorvall ST 8R), then the supernatant was withdrawn and filtered through 0.2 µm pore size Millex-GV sterile syringe filters (EMD Millipore Ltd., Ontario). The phage lysates were stored at 4 °C. Titration of T4-Z phage samples were performed by double-layer agar plate method where serial dilutions of phage samples in λ buffer and overnight bacterial culture were mixed in CM top agar supplemented with 500 µg of EWL.

3.2.2.2 Construction of T4-Soc Integration Vector, pRH

The integration vectors were constructed using a pRH plasmid kindly provided by Prof. Lindsay Black (University of Maryland, Baltimore) and DNA fragments of *Soc* derivatives. In order to construct *Soc* derivatives, the genes encoding gold-binding peptides were inserted into the *Soc* gene of wild type T4 phage by PCR-based side-directed mutagenesis. In this reaction, wild type T4 phage was used as DNA template and its *Soc* gene was amplified using a set of designed primers including gold binding peptide sequences (Table 3.2.1). All PCR assays were performed in Biometra TGradient Thermocycler using 1 µL of DNA template in 50 µL of PCR mixture. Final concentrations of PCR reagents were 1 × PCR buffer, 2 mM MgCl₂, 200 µM deoxynucleoside triphosphate mix, 250 µM each of forward and reverse oligonucleotide primers (IDT, Integrated DNA Technologies, Inc.), and 2.5 units of Taq Plus DNA polymerase. PCR was performed according to the manufacturer's instructions. The success of PCR was evaluated by agarose gel electrophoresis. PCR fragments were separated in 1% agarose gel prepared in 1 × Tris acetate EDTA (TAE) buffer (4.84 g/L Tris, 1.14 mL/L acetic acid, and 2 mL EDTA (0.5 M. pH 8.0)) at 100 volts using a gel electrophoresis unit (Bio-Rad, ON, CA). After running the gel for 45 min, DNA molecules were visualized under UV light with the help of safe T stain (Bioshop, CA) added into agarose gel during preparation. Amplified DNA fragments belonging to *Soc* derivatives were purified using spin columns (QIAGEN, Ontario).

Insert	Type of Fusion	Primers	Sequence (5' - 3')
GSGSC	C- Terminal	SOC-Cys FWD	TAC ATA TGG CTA GTA CTC GCG GTT ATG
		SOC-Cys REV	AAT TGA ATT CGA TTA GCA GCT GCC GCT GCC ACC AGT TAC TTT CCA CAA ATC
CGSGS	N- Terminal	Cys-SOC FWD	TAC ATA TGT GCG GCA GCG GCA GCG CTA GTA CTC GCG GTT ATG
		Cys-SOC REV	AAT TGA ATT CGA TTA ACC AGT TAC TTT CCA CAA ATC TTC ATT
GSGSVSGSSPDS	C- Terminal	SOC-GB2 FWD	TAC ATA TGG CTA GTA CTC GCG GTT ATG
		SOC-GB2 REV	AAT TGA ATT CGA TTA GCT ATC CGG GCT GCT GCC GCT CAC GCT GCC GCT GCC ACC AGT TAC TTT CCA CAA ATC
VSGSSPDSGSGS	N- Terminal	GB2-SOC FWD	TAC ATA TGG TGA GCG GCA GCA GCC CGG ATA GCG GCA GCG GCA GCG CTA GTA CTC GCG GTT ATG
		GB2-SOC REV	AAT TGA ATT CGA TTA ACC AGT TAC TTT CCA CAA ATC TTC ATT
GSGSAYSSGAPPMPPF	C- Terminal	SOC-A3 FWD	TAC ATA TGG CTA GTA CTC GCG GTT ATG
		SOC-A3 REV	AAT TGA ATT CGA TTA AAA CGG CGG CAT CGG CGG GGC GCC GCT GCT ATA GGC GCT GCC GCT GCC ACC AGT TAC TTT CCA CAA ATC
AYSSGAPPMPPFGSGS	N- Terminal	A3-SOC FWD	TAC ATA TGG CCT ATA GCA GCG GCG CCC CGC CGA TGC CGC CGT TTG GCA GCG GCA GCG CTA GTA CTC GCG GTT ATG
		A3-SOC REV	AAT TGA ATT CGA TTA ACC AGT TAC TTT CCA CAA ATC TTC ATT

Table 3.2.1 Primer sequences for T4 phage display of gold binding peptides.

Amplification of the pRH plasmid was performed in LB broth by overnight culturing of *E.coli* cells harboring plasmid DNA. The cell pellet was collected by centrifugation at 5000 rpm for 15 min and plasmid DNA inside the cells was purified by using a QIAprep Spin Miniprep Kit (QIAGEN, Ontario). Before ligation of *Soc* derivatives into the pRH plasmid, the amplified gene products were digested through the restriction sites (EcoRI and NdeI), which were inserted into the *Soc* gene by PCR. All digestions were achieved with the help of restriction enzymes EcoRI and NdeI, following the manufacturer's instructions (New England Biolabs, Ontario). Plasmid DNA was also digested through the same restriction sites and gel purified using QIAquick Gel Extraction Kit (QIAGEN, Ontario). The digested *Soc* derivatives were ligated into the pRH plasmid using a Quick Ligation Kit (New England Biolabs, Ontario), and the ligation mix was transformed into *E. coli* HB101 competent cells (Promega, Madison, WI). The transformed cells were selected on LB

agars containing 100 µg/mL ampicillin. The success of transformation was confirmed by PCR analysis and DNA sequencing at the *Plate-forme d'Analyses Génomiques* (Université Laval).

3.2.2.3 Homologous Recombination

After confirmation by sequence analysis, the positive clones were infected with T4-Z mutant phages to reintegrate the *Soc* gene including the gold-binding peptide sequence into the phage genome. According to the procedure described by Ren et al. (1996), *E. coli* HB101 cells transformed with pRH-*Soc* derivatives were grown in citrate medium (CM) containing 100 µg/mL ampicillin up to a concentration of 10⁸ CFU/mL. This bacterial culture (20 mL) was infected with T4-Z phage at a multiplicity of infection (MOI) of 1. After incubating for 5 hours at 37 °C, the infected bacteria were concentrated by centrifugation at 3,200 × *g* for 15 minutes and suspended in LB broth. Chloroform was added to the suspension to release any progeny phages inside the bacteria, and cell debris were removed by centrifugation at 10,000 rpm for 5 minutes. The supernatant, after centrifugation at 20,000 × *g* for one hour for antibiotic wash, was spread on a CM plate (11 g/L of bacteriological agar (Fisher BioReagents) in CM broth) containing *E. coli* B in CM top agar without lysozyme. Single plaques were isolated and integrants were confirmed by PCR.

3.2.3 Self-Assembly of AuNPs on T4 Phage templates

3.2.3.1 Purification of T4 Phage Templates

Prepared T4 phage stocks were purified by gel filtration with Superose™ 6 prep grade (GE Healthcare Biosciences, QC). The phage stocks were concentrated by centrifugation at 20,000 × *g* for 90 minutes and the collected phage pellets were re-suspended in 1 mL of λ buffer. The medium was packed in a C 16/40 column (GE Healthcare Biosciences, QC) and initially washed with distilled water. After equilibration of the column with PBS, the concentrated phage sample was loaded to the column and the sample elution was performed by running PBS at a constant flow rate adjusted by peristaltic pump. The fractions were collected in 5 mL volumes and analyzed for protein and phage content. A UV-Vis spectrometer was employed for protein analysis where the absorbance of fractions was recorded at 280 nm. The phage concentration was determined by titration of the fractions, which was performed by double-layer agar plate method as previously described. The fraction with highest phage concentration was spin concentrated with Amicon ultra-15 centrifugal filter units (MWCO; 30 kDa, EMD Millipore,

Canada) and washed 3 times using 0.1 M phosphate buffer (pH was adjusted to 7.0 by mixing 0.1 M NaH_2PO_4 with 0.1 M Na_2HPO_4). The final volume of the sample was adjusted to 500 μL and the sample was stored at 4 °C after titrating.

3.2.3.2 Assembly of AuNPs on T4 Phage

The self-assembly of 3, 9, and 13 nm AuNPs on T4 phage templates was performed in 1 mL of phosphate buffer (PB) (pH 7.0) including 100 μL of purified phage solution (10^{10} PFU/mL in TBS) and 100 μL of nanoparticle stock solution. Optimization of the self-assembly process was performed for each AuNP size by studying the effect of reaction time and the ionic strength of reaction solutions. In order to optimize the time, reaction solutions were incubated on an orbital shaker at room temperature in the dark up to 5 days. The effect of the ionic strength of reaction buffer was studied in a range of 25 mM and 200 mM. The samples were kept in a closed box to minimize exposure to the light. Nanoparticle controls were prepared using the same concentrations of AuNPs and replacing the phage template solutions with buffer of the same pH and ionic strength as the reaction solutions.

3.2.3.3 UV-Vis Absorption Spectroscopy

The growth of assemblies was tracked during the reaction using a Cary-1E UV-Vis spectrophotometer (Varian Inc.). Kinetic data of the assembly process was collected by recording UV-Vis spectra in the 400–1000 nm region with time, during a period of up to four days. Nanoparticle controls were also characterized by recording their UV-Vis spectra in the 400–1000 nm region over a period of four days.

3.2.3.4 TEM

The assembly of AuNPs on phage templates was visualized by TEM after 2 days of incubation. For TEM observation, 5 μL of the reaction solution was deposited onto copper TEM grids (SOQUELEC Ltd.) stabilized with evaporated carbon film (3–4 nm thickness) and allowed to sit for 5 minutes. Using a wedge of filter paper, the solution was wicked away from the grid. Immediately, 5 μL of staining solution (0.5% uranyl acetate (Canemco Inc., QC) in water) was applied to the grid for 10 seconds and the stain solution was wicked away with a wedge of filter paper. Finally, the TEM grid was stored in a grid box. Images were collected using a JEM-2100F model TEM (JEOL Inc., USA) at 200 kV. Because a uranyl acetate solution was

used to negatively stain the phage particles, both AuNPs and phage particles could be observed in the images.

3.2.3.5 DLS

The change in the size of phage templates upon binding of the AuNPs and the change in total size distribution of the reaction solution were observed during a period of 4 days. Measurements were conducted using a Zetasizer Nano S90 DLS system (Malvern Instruments Ltd, UK). The samples were held at 25 °C in the sample holder and the measurements were determined from 8 runs, 8 seconds each. Each sample was analyzed in triplicate and all DLS data were analyzed using Malvern Zetasizer 7.11 software. All reported mean particle hydrodynamic diameters (D_H) were calculated from volume-based particle size distributions.

3.3 Results and Discussion

3.3.1 Engineering of T4 phage to display gold binding moieties on Soc protein

In order to construct a T4 phage displaying gold-binding peptides, fusions of *Soc* genes with desired coding sequences were inserted into pRH recombination plasmid as described in Section 3.2.2. *Soc* is a rod-shaped molecule with N- and C-termini that are surface-exposed and present at the edges, whereas the capsid-binding site is located in the middle of the structure. This feature of *Soc* protein enables fusion with protein moieties at both N- and C-termini without disrupting capsid-binding [225]. In these constructs, the *Soc* gene is flanked on its 5' side by a 3' portion of the 'e' (lysozyme) gene of phage T4 and by the strong IPIII promoter to drive *Soc* expression (Figure 3.3.1). At the 3' end of *Soc*, a portion of a downstream T4 gene, *denV*, allows homologous recombination between the phage and the plasmid on either side of the *Soc* gene. T4-Z1 phage is deleted of 9.8 kb (alt, IPIII, and *soc*) and is also a partial deletion mutant for the lysozyme (e) gene. This construct allows 6 kb more DNA to be packed into the T4 head, with easy selection of positive mutants by plating on regular medium not supplemented with lysozyme.

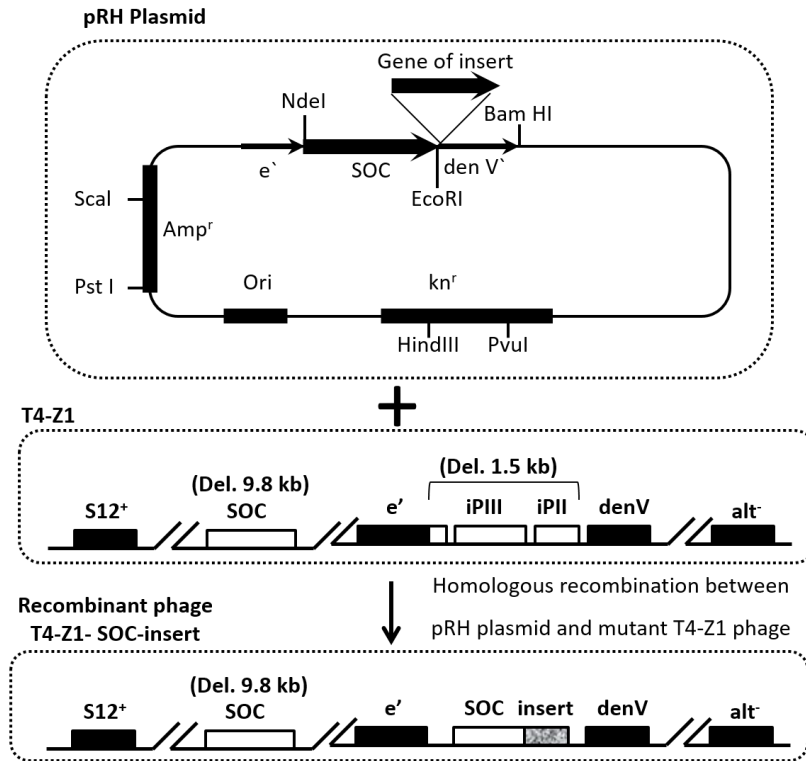


Figure 3.3.1 Schematic presentation of pRH plasmid, mutant T4-Z1 and recombinant T4 phage (T4-Z1-SOC-insert).

After the construction of pRH integration vectors with the genes encoding gold-binding peptide sequences, *E. coli* cells were transformed with these integration vectors and analyzed by PCR. PCR amplification of transformed cells resulted in the products which had the size of corresponding Soc fusions (Figure 3.3.2).

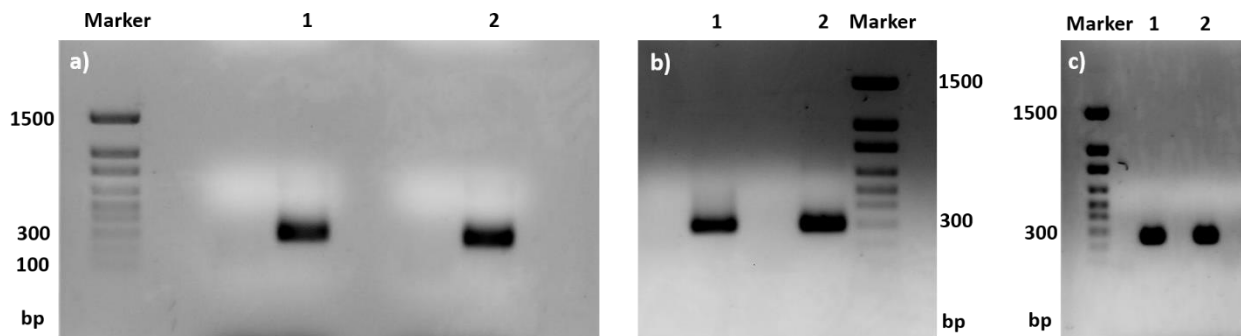


Figure 3.3.2 Detection of the insertion of gold binding sequence fused Soc gene into pRH plasmid by PCR. (a) Marker, molecular size standard; lane 1, PCR product of AYSSGAPMPPF inserted into C-terminal of Soc gene (288 bp); lane 2, PCR product of AYSSGAPMPPF inserted into N-terminal of Soc gene (288 bp) (b) Marker, molecular size standard; lane 1, PCR product of VSGSSPDS inserted into C-terminal of Soc gene (276 bp); lane 2, PCR product of VSGSSPDS inserted into N-terminal of Soc gene (276 bp) (c) Marker, molecular size standard; lane 1, PCR product of cysteine inserted into C-terminal of Soc gene (255 bp); lane 2, PCR product of cysteine inserted into N-terminal of Soc gene (255 bp).

For instance, PCR amplification of the cells carrying the plasmid of AYSSGAPPMPPF peptide sequence resulted in a product with the size of 288 bp indicating the presence of 36 bp gold-binding sequence, 12 bp linker, and 240 bp soc gene. In a similar way, the PCR products of VSGSSPDS peptide and single cysteine (C) sequences had the size of 276 bp and 255 bp, respectively. The presence of Soc fusions were confirmed via DNA sequencing, as well.

Transformed cells were infected with T4-Z1. During phage infection, recombination occurred and Soc fusions were incorporated into the lysozyme and Soc-deficient T4-Z1 phage. As a result of homologous recombination, lysozyme activity of mutant phage was recovered and the produced phage particles were able to propagate without addition of lysozyme into the growth medium. In addition to the recovery of lysozyme activity, PCR amplification was also used to confirm the presence of the region including Soc fusions. The Soc–gold-binding peptide fusions incorporated into the defective phage genome were detected through the corresponding ~300 bp fragments on an agarose gel (Figure 3.3.3).

In the remainder of this thesis, recombinant T4 phages will be named as follows: T4 displaying AYSSGAPPMPPF peptide on the C-terminus of Soc protein, **A3-C phage**; T4 phage displaying AYSSGAPPMPPF peptide on the N-terminus of Soc protein, **A3-N phage**; T4 phage displaying VSGSSPDS peptide on the C-terminus of Soc protein, **GB-C phage**; T4 phage displaying VSGSSPDS peptide on the N-terminus of Soc protein, **GB-N phage**; T4 phage displaying cysteine on the C-terminus of Soc protein, **Cys-C phage**; T4 phage displaying cysteine on the N-terminus of Soc protein, **Cys-N phage**.

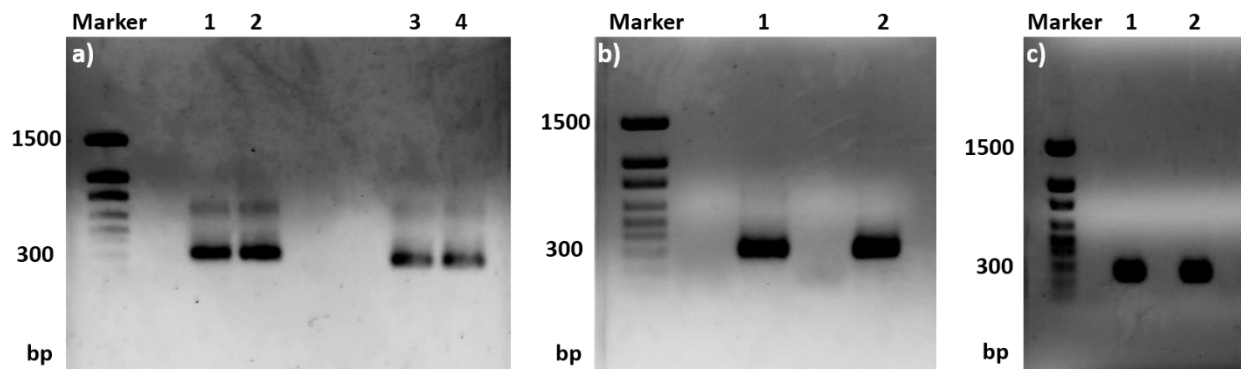


Figure 3.3.3 Detection of gold binding sequence fused Soc gene insertion into the T4 genome by PCR. (a) Marker, molecular size standard; lane 1-2, PCR product indicating the presence of AYSSGAPPMPPF peptide fusion on C-terminal of Soc gene (288 bp); lane 3-4, PCR product indicating the presence of AYSSGAPPMPPF peptide fusion on N-terminal of Soc gene (288 bp) (b) Marker, molecular size standard; lane 1, PCR product indicating the presence of VSGSSPDS peptide fusion on C-terminal of Soc gene (276 bp); lane 2, PCR product indicating the presence of VSGSSPDS peptide fusion on N-terminal of Soc gene (276 bp) (c) Marker, molecular size standard; lane 1, PCR product indicating the presence of cysteine fusion on C-terminal of Soc gene (255 bp); lane 2, PCR product indicating the presence of cysteine fusion on N-terminal of Soc gene (255 bp).

3.3.2 Self-assembly of AuNPs on T4 phage templates

3.3.2.1 Preparation of T4 phage template for self-assembly reaction

The phage stocks used in self-assembly of AuNPs were column-purified in order to remove all cell debris and protein fragments that might interfere with gold-binding. Eluted fractions were analyzed for protein content by UV-vis spectroscopy and the phage content of each fraction was assessed by phage titration. As it was shown in Figure 3.3.4, the fourth 5-mL fraction contained the highest number of phage particles, which was 6×10^9 PFU. Although a significant amount of phage particles ($\sim 10^8$ PFU) were detected in the following fractions, they were excluded because of protein impurities. The protein impurities were eluted after the main phage fraction and were most probably composed of cell debris and large protein aggregates, which were concentrated with phage particles in the preceding centrifugation step. Impurities with comparable size to the phage would remain in the solution and could be carried to the next steps. Following purification, the fourth fraction was spin concentrated to 0.5 mL, and resulted in a phage recovery of $\sim 10\%$. During this concentration step, the buffer of the phage sample, PBS, was exchanged for 100 mM phosphate buffer (pH 7.0).

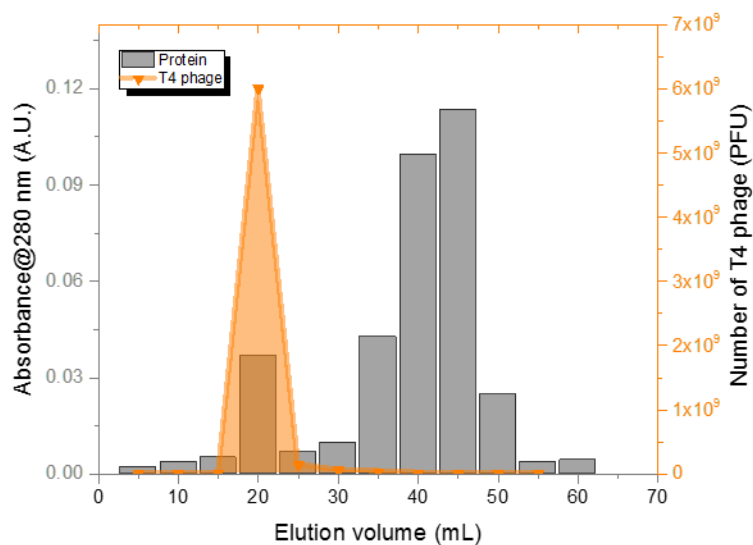


Figure 3.3.4 Size-exclusion chromatography (SEC) elution profile of T4 phage sample. Elution patterns corresponding to protein content (indicated in gray) and phage content (indicated in orange) of T4 phage solution.

3.3.2.2 Assembly of AuNPs on T4 phage template

Similarly to the M13 phage, assembly of AuNPs on T4 phage was challenging owing to the repulsion between the AuNPs and T4 phage templates, which are both negatively-charged [239]. For this

reason, the effect of ionic strength on T4 phage-AuNP binding reaction was also studied, and reaction buffer was optimized accordingly. Conditions for the three different gold-binding moieties (Cysteine; A3 peptide (AYSSGAPPMPFF); GB peptide (VSGSSPDS)) were optimized separately.

Assembly of AuNPs on Cysteine-bearing T4 phage templates

The self-assembly of AuNPs was initially optimized for cysteine-bearing T4 phage templates. As explained previously, cysteine was fused to the N- and C- termini of Soc protein. Depending on the terminus, disposition of the cysteine residues on the phage surface are different. For instance, the C termini of Soc protein face each other at the trimeric junctions, while the N termini form dimeric junctions [225] (Figure 3.3.5). As such, the effect of AuNP disposition on T4 phage could be studied.

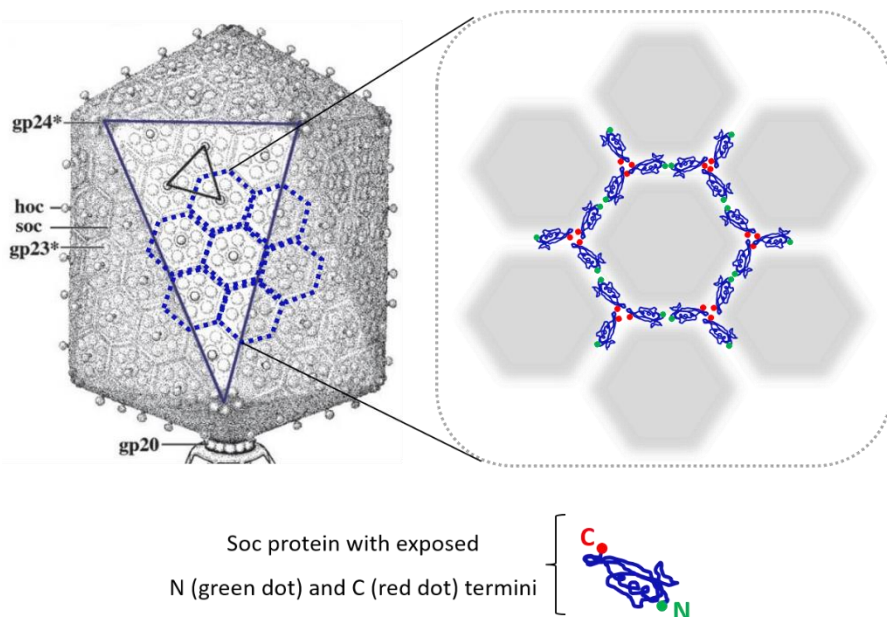


Figure 3.3.5 Schematic of T4 phage capsid structure showing the disposition of C- and N-termini of Soc protein.

Interactions of 3-nm AuNPs with Cys-N phage was studied in phosphate buffers with different ionic strengths ranging between 50 – 200 mM (Figure 3.3.6). During the reactions, two main populations were observed. The smallest population (~20 nm), was related to the formation of small AuNP aggregates. In the reaction solution, AuNPs were present in excess in comparison to the phage templates. This enabled the observation of the unbound AuNPs and their small aggregates in all buffer solutions during the extensive 5-day reaction period.

The second most abundant population had an average size around 100 nm. While the size of this population changed with the ionic strength, its presence was considered an indication of Au assembly on phage template. At low ionic strength buffer (50 mM), the average size of this population was ~122 nm, and increased to ~181 nm in 200 mM phosphate buffer. This increase suggested stronger AuNP–phage interactions at higher ionic strength buffers, due to the reduced repulsive forces between the particles. It was also important to observe that the size of the AuNP–T4 clusters was larger than T4 itself (~126 nm). The average size of the clusters measured in 100 mM phosphate buffer (~145 nm) was in agreement with expectations. However, during extensive incubation in the reaction medium over a 5 days period, the size of this population decreased from 173 nm to 93 nm. This suggests some instability of AuNP–phage interaction under these conditions. On the other hand, the size of the population in 200 mM phosphate buffer was more stable and remained between 151 nm and 204.3 nm during a 5-day period.

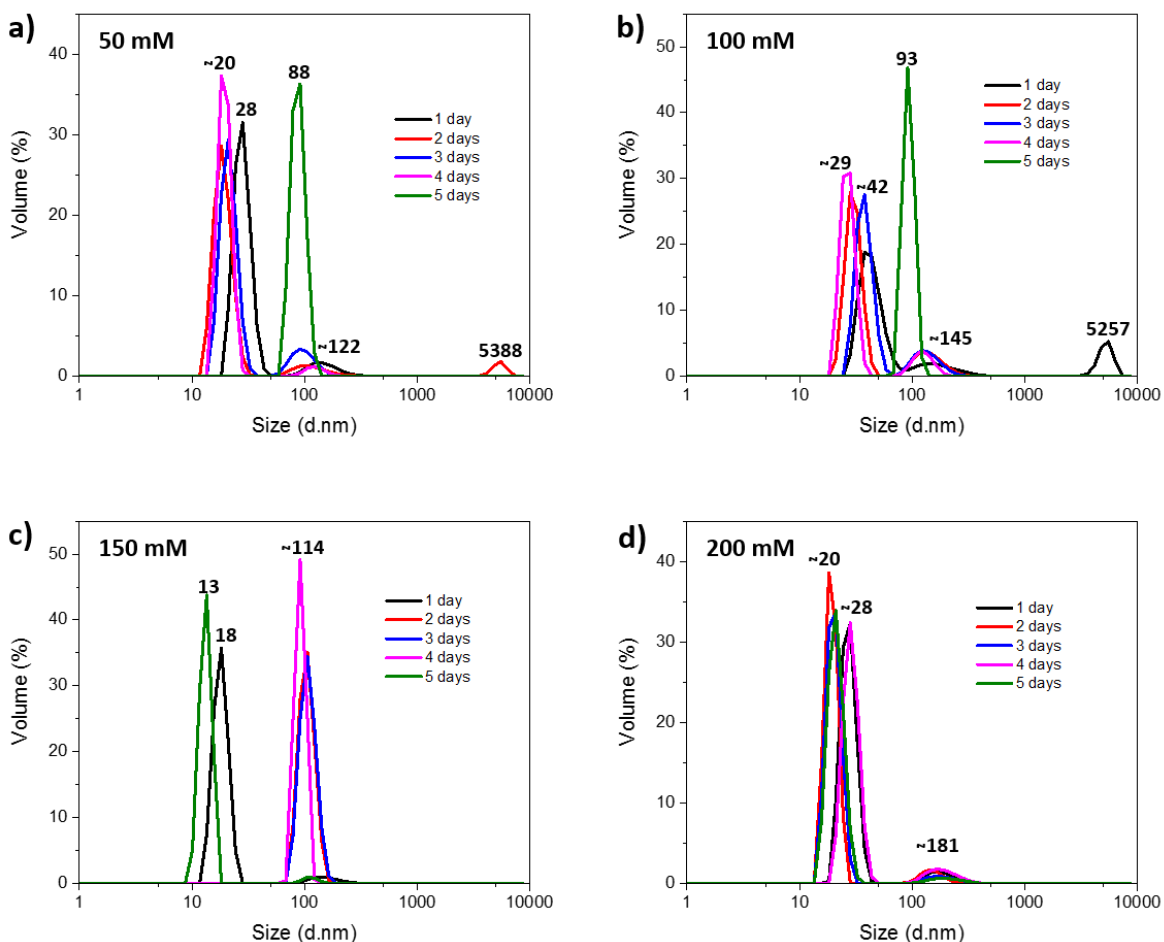


Figure 3.3.6 DLS measurements of reaction solutions including 3-nm AuNPs and Cys-N phage template. DLS histograms for volume-based size analysis of Cys-N phage–3 nm AuNP solutions in a) 50 mM, b) 100 mM, c) 150 mM, and d) 200 mM phosphate buffers. DLS histograms of each sample solution were recorded for a 5 day period.

Although the assembly process appeared complete following the first day of the reaction, with a resulting population size of 179.5 nm, the reaction was allowed to continue until the third day to ensure the maximum coverage of the phage surface with AuNPs. The assembly process was also assessed by UV-Vis spectroscopy by comparing the SPR spectra of a 3-nm colloidal AuNP solution with the SPR spectra of Cys-N–AuNP assemblies (Figure 3.3.7b). It was observed that there was no significant change in the SPR band of the AuNPs after their self-assembly on phage template.

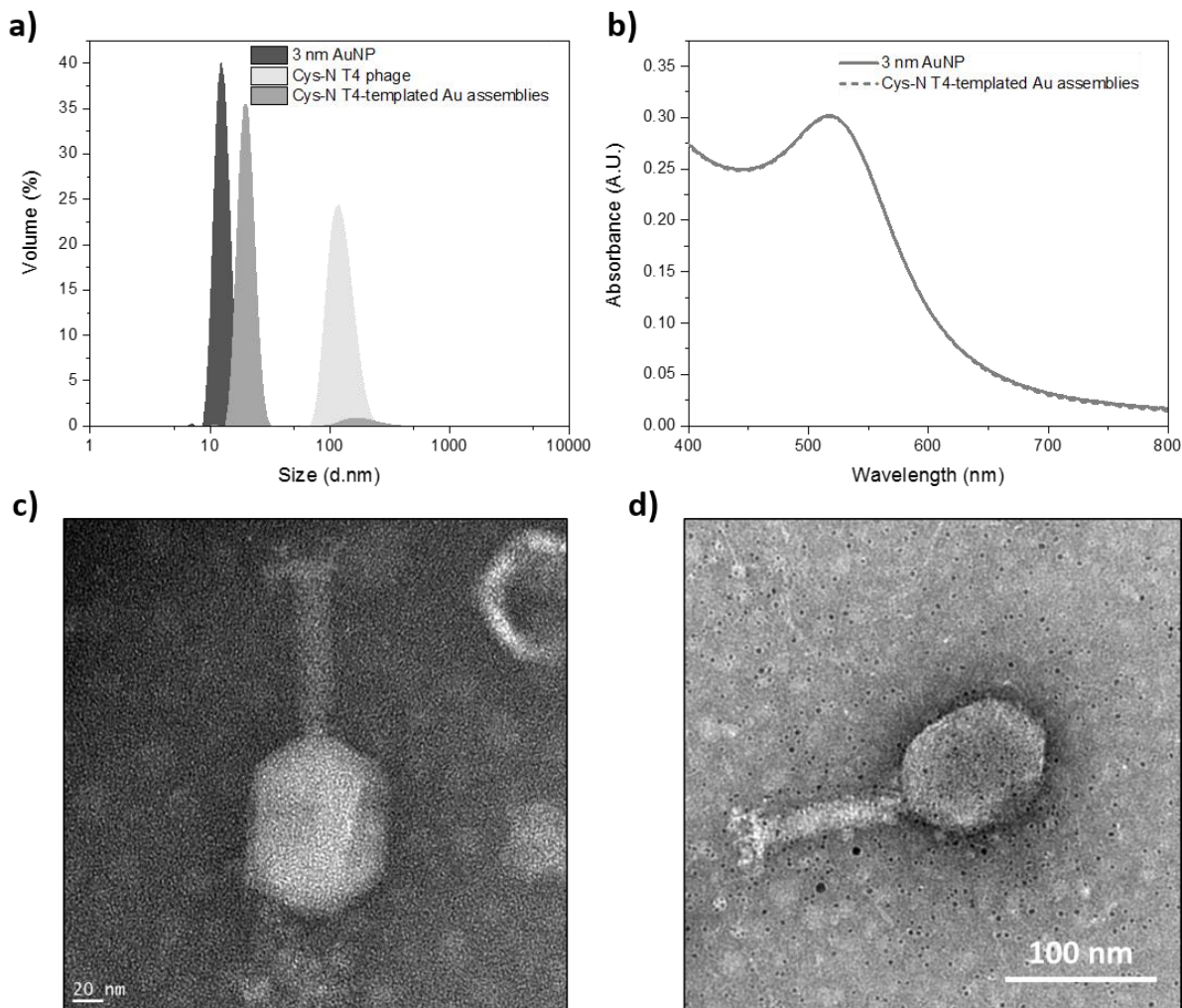


Figure 3.3.7 Characterization of 3-nm AuNPs self-assembled on Cys-N template after 2 days reaction. a) DLS histograms showing the size of 3 nm AuNPs, Cys-N phage and Cys-N-templated gold assemblies. b) UV-Vis spectra of 3 nm colloidal AuNPs (solid line) and self-assembled on Cys-N phage template (dashed line). c) TEM image of wild type T4 phage stained with uranyl acetate (2%) d) TEM image of 3 nm AuNPs assembled on Cys-N phage stained with uranyl acetate (2%).

In order to verify the assembly process, phage–AuNP assemblies were observed by TEM. However, TEM observations mostly produced images with phage particles partially covered with AuNPs or phage particles without any AuNPs attached on them (Figure 3.3.7d). It is important to note that TEM

observations are performed with dry samples under high vacuum. In this regard, the TEM results suggest that dehydration of phage particles during sample preparation might deform the capsid structure, which includes angular positions close to the 5-fold vertices (Figure 3.3.5). Due to the structural changes, the positions of binding moieties on phage capsid might also change and result in disassembly of AuNPs. Despite screening many sample preparation conditions, better TEM results could not be achieved and all T4 phage templates in this work were observed under the same conditions. Consequently, the TEM images observed herein are believed to be representative of the phage–AuNP assemblies in dry state, rather than the actual features of T4–AuNP assemblies in their colloidal state.

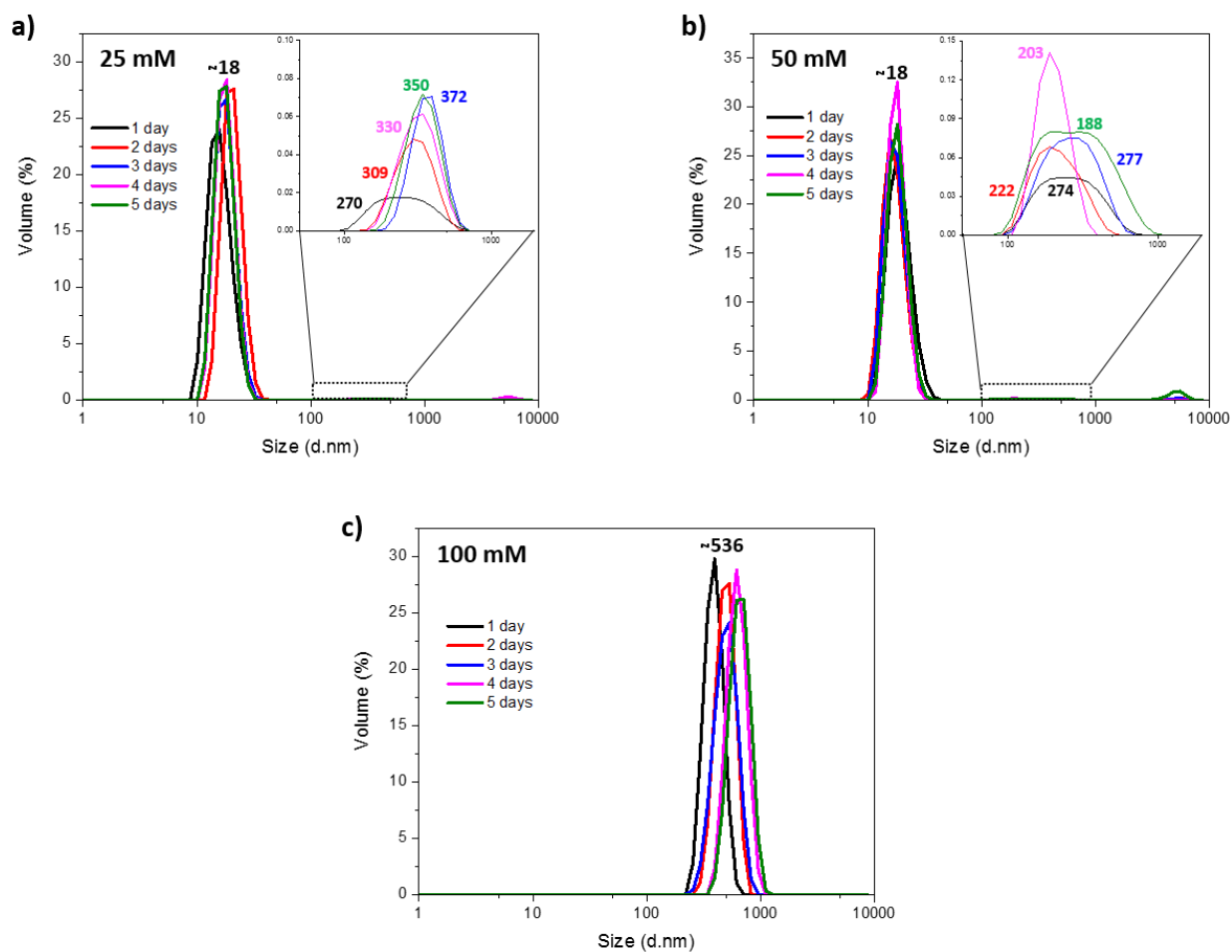


Figure 3.3.8 DLS histograms for volume-based size analysis of Cys-N phage-9 nm AuNP solutions in a) 25 mM, b) 50 mM, and c) 100 mM phosphate buffers. DLS histograms of each sample solution were recorded for a 5 day period.

The self-assembly of 9-nm AuNPs on Cys-N phage was studied in PB with molarity ranging from 25 mM to 100 mM. Stability of AuNPs in reaction solutions was crucial for the assembly process.

Therefore, the reaction solutions with molarity higher than 100 mM were eliminated as they generated black macroscopic precipitates in the solutions upon mixing phage templates with AuNPs. For reactions buffers containing 25 mM and 50 mM phosphate, two distinct populations were observed (Figure 3.3.8a and 3.3.8b). While the first population (~18 nm) was assigned to the colloidal AuNPs that were in excess in the reaction solutions, the second population was an indication of self-assembly of AuNPs on the phage templates. The size of the second population in 25 mM phosphate buffer increased with time from 270 to 350 nm during a 5 day period. On the other hand, the size of the second population in 50 mM phosphate buffer was smaller and varied between 188 and 277 nm. As the AuNPs were stable in both 25 mM and 50 mM reaction solutions, the assembly process was more controlled compared to the reaction conducted at higher ionic strength.

The Interaction of 9-nm AuNPs with Cys-N phage in 100 mM phosphate buffer resulted in the formation of a single population with an average size of 536 nm (Figure 3.3.8c). This was the result of strong AuNP–AuNP and phage–AuNP interactions. DLS histograms of control reaction solutions including only 9-nm AuNPs demonstrated the instability of the particles under similar conditions (Appendix 1). In addition to the peak of colloidal isolated AuNPs at ~20 nm, interactions of AuNPs in 100 mM PB resulted in a second peak with a higher size (~180 nm). Due to the instability of AuNPs, as well as the strong interactions between the AuNPs and phage particles, we only observed phage–AuNP aggregates with a size of ~536 nm, which is much larger than phage template (~126 nm).

Since the interactions of AuNPs with phage templates were expected to be stronger in 50 mM reaction solution, the assembly of AuNPs on templates was also expected to be more stable. Thus, 50 mM phosphate buffer was chosen as the reaction solution for the self-assembly of 9-nm AuNPs on Cys-N phage. Although the presence of the peak centered at 274 nm after 1 day demonstrated the formation of phage–AuNP assemblies, the reaction time was extended to 2 day, to ensure maximal coverage of the phage capsid with AuNPs. Beyond 2 days in 50 mM phosphate buffer, the AuNPs became unstable and formed aggregates (Appendix A). Consequently, phage–AuNP binding reactions were performed over a 2 days period. Because of the excess AuNPs in the reactions solutions, DLS histograms were re-plotted for intensity-based size analysis. As shown in Figure 3.3.9a, conjugation of 9-nm AuNPs onto Cys-N phage surface resulted in an increase in the size of phage template from 126 nm to 277 nm. The UV-Vis spectrum of an 9-nm AuNP solution was also different than that of the Cys-N–AuNP assemblies (Figure 3.3.9b). The changes in UV-Vis spectrum corresponded to a slight broadening and red shift (~1 nm) of the SPR band. TEM images were not totally in agreement with DLS and UV-Vis spectroscopy results. The phage particles

in TEM images were partially covered with AuNPs which were abundant on the edge of capsids (Figure 3.3.9c/d). Most probably, the binding positions on the edge of capsid were still available to attach AuNPs whereas the binding moieties on equatorial region of capsid were deformed and resulted in disassembly during sample preparation.

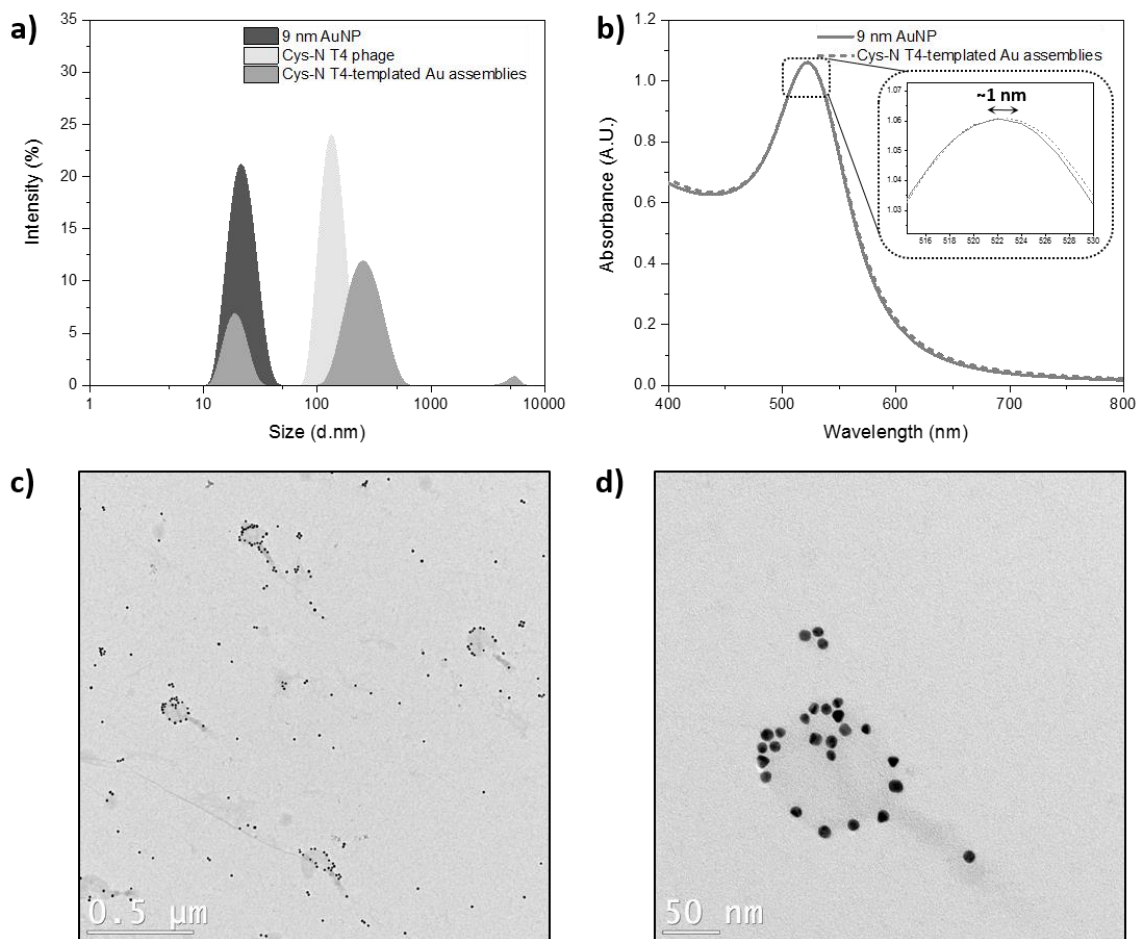


Figure 3.3.9 Characterization of 9-nm AuNPs self-assembled on Cys-N template after 2 days reaction. a) DLS histograms showing the size of 9 nm AuNPs, Cys-N phage and Cys-N-templated gold assemblies. b) UV-Vis spectra of 9 nm colloidal AuNPs (solid line) and self-assembled on Cys-N phage template (dashed line). c-d) TEM image of 9 nm AuNPs assembled on Cys-N phage.

Similarly to 3-nm and 9-nm AuNPs, the interactions of 13-nm AuNPs with Cys-N phage template was studied in reaction solutions with different ionic strengths in order to optimize the assembly process. In general, the stability of 13-nm AuNPs in high ionic strength buffers was worse than that of the other AuNPs. Unlike 3-nm and 9-nm AuNPs, black precipitates were observed in reaction solutions prepared with 100 mM phosphate buffer. Therefore, the assembly of 13-nm AuNPs on Cys-N phage was limited to 25 mM and 50 mM phosphate buffers. As expected, the binding reaction resulted in formation of two

distinct populations. The first population (~20 nm and ~16 nm) was attributed to the colloidal AuNPs whereas the second population belonged to the phage-templated Au assemblies. In both 25 mM and 50 mM reaction solutions, the size of the second population increased with time. It was observed that the size of the second population in 25 mM reaction solution was 282 nm on the first day and increased to 454 nm by the fifth day of the reaction (Figure 3.3.10a). In case of 50 mM reaction solution, the size of the second population measured in the first and fifth days of reaction were 138 nm and 349 nm, respectively (Figure 3.3.10b). However, the AuNPs in 50 mM phosphate buffer were not stable enough for the assembly process. DLS histograms of 13-nm AuNPs in 50 mM phosphate buffer showed the formation of aggregates even in the first day (Appendix A). Consequently, assembly of 13-nm AuNPs on Cys-N phage was performed in 25 mM phosphate buffer.

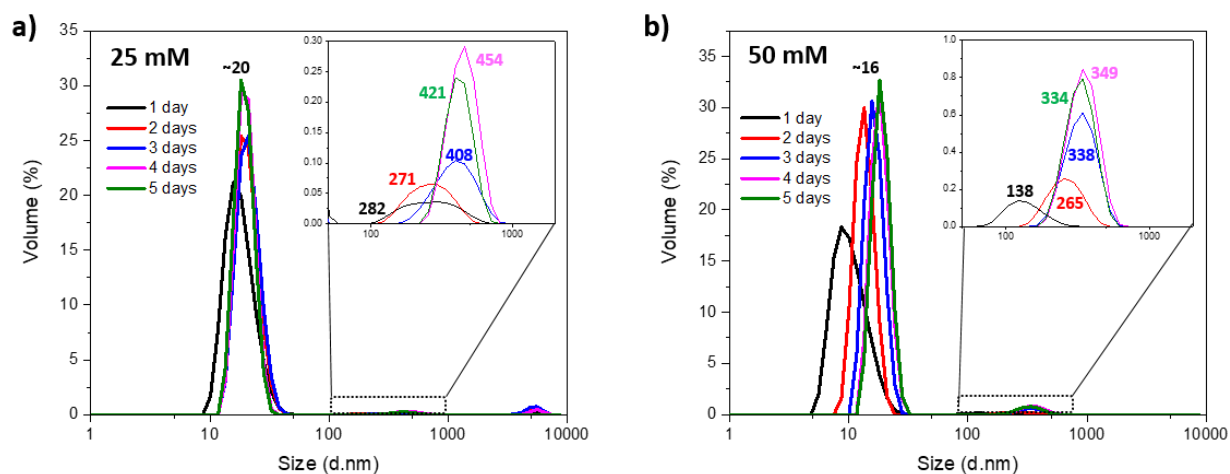


Figure 3.3.10 DLS histograms for volume-based size analysis of Cys-N phage-13 nm AuNPs solutions in a) 25 mM and b) 50 mM phosphate buffers. DLS histograms of each sample solution were recorded for a 5 day period.

In order to maintain the stability of the reaction solution and to avoid the formation of random aggregates, the assembly of AuNPs on phage template was followed for a 2-day period, during which time the AuNPs were stable. Intensity-based size analysis of the reaction solution showed the formation of a new population with a size higher than both the colloidal AuNPs and phage templates (Figure 3.3.11a). Self-assembly of AuNPs in 25 mM reaction solution was also demonstrated by UV-Vis spectroscopy (Figure 3.3.11b). Formation of phage–AuNP assemblies generated a red shift (~2 nm) and broadening in the SPR band, compared to a solution of 13-nm AuNPs. However, TEM observations did not result in phage particles covered with AuNPs (Figure 3.3.11c/d). The damage to the phage capsid structure was clear with observation of black color inside the capsid. Due to the destruction of surface proteins, DNA got out of

capsid letting the staining solution get inside and stain the capsid in black. Few numbers of AuNPs observed on phage capsid might be the particles remaining on the capsid after the damage.

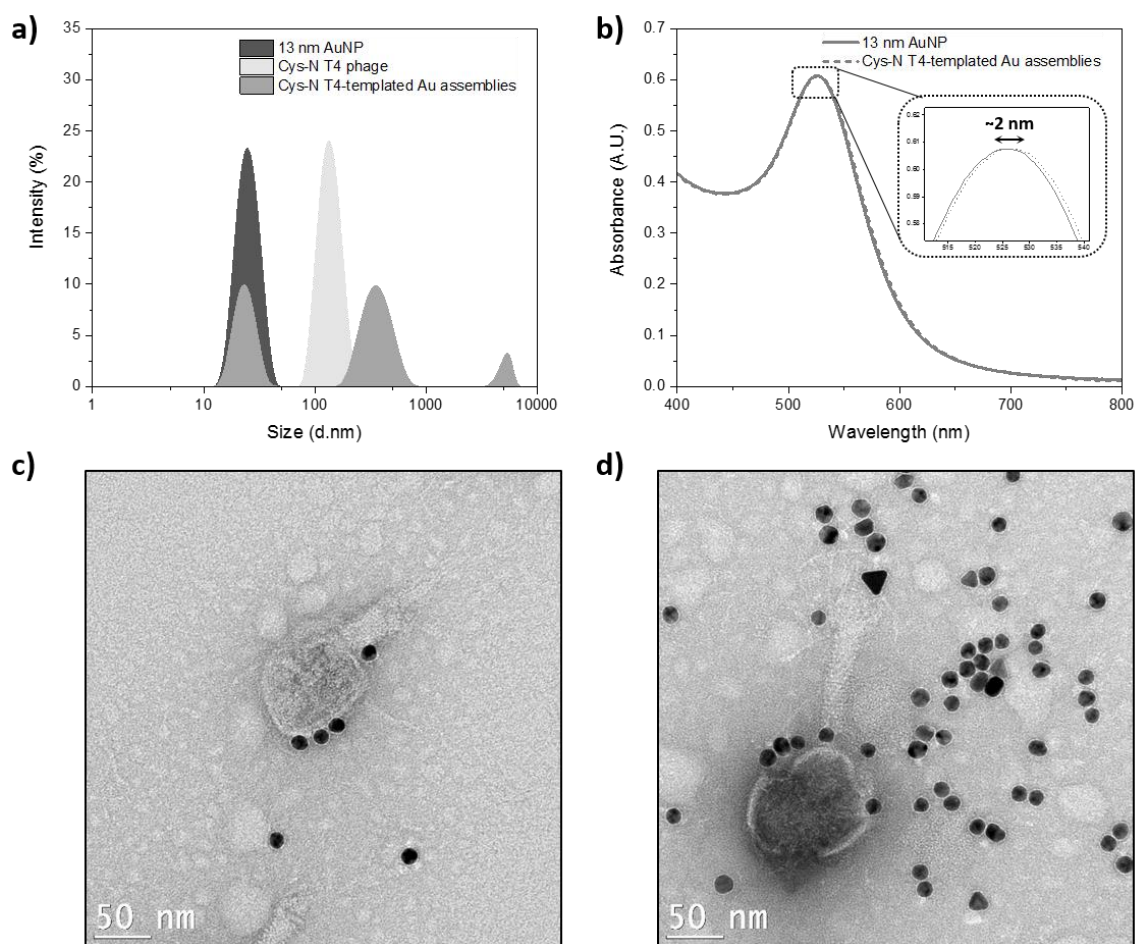


Figure 3.3.11 Characterization of 13-nm AuNPs self-assembled on Cys-N template after 2 days reaction. a) DLS histograms showing the size of 13-nm AuNPs, Cys-N phage and Cys-N-templated gold assemblies. b) UV-Vis spectra of 13-nm colloidal AuNPs (solid line) and self-assembled on Cys-N phage template (dashed line). c-d) TEM images of 13 nm AuNPs assembled on Cys-N phage.

The self-assembly of AuNPs on Cys-C phage was also optimized in a similar way performed for Cys-N phage. For brevity, only the optimized reaction conditions will be presented. The DLS histograms of the reaction solutions with different ionic strengths were provided in Appendix A. The interactions of 13-nm AuNPs with Cys-C phage in reaction solutions with different ionic strengths was identical to that observed for Cys-N phage. The assembly process was performed in the reaction solution composed of 200 mM phosphate buffer created the highest volume for the population corresponding to the phage-templated Au assemblies (Figure 3.3.12a). The size of the population was ~169 nm whereas its relative proportion was ~30% in volume-based distribution. The analysis of the UV-Vis spectrum belonging to Cys-C–AuNP assemblies revealed no change in the SPR band compared to isolated AuNPs (Figure 3.3.12b). In

contrast to Cys-N phage, 3 nm AuNPs assembled on Cys-C could be observed by TEM (Figure 3.3.12d). Deformation in capsid structure of Cys-C phage templates was remarkable, however it was relatively low in comparison to Cys-N–AuNP assemblies and enabled the observation of AuNPs assembled on Cys-C templates. The inter-particle distance between AuNPs assembled on Cys-C phage was determined 3.05 ± 0.98 nm by averaging 200 measurements. An inter-particle distance close to the diameter of AuNP (3 nm) might explain the preserved position of SPR band in phage–AuNP assemblies whereas the inter-particle distance larger than the particle diameter would prevent the plasmon coupling between AuNPs.

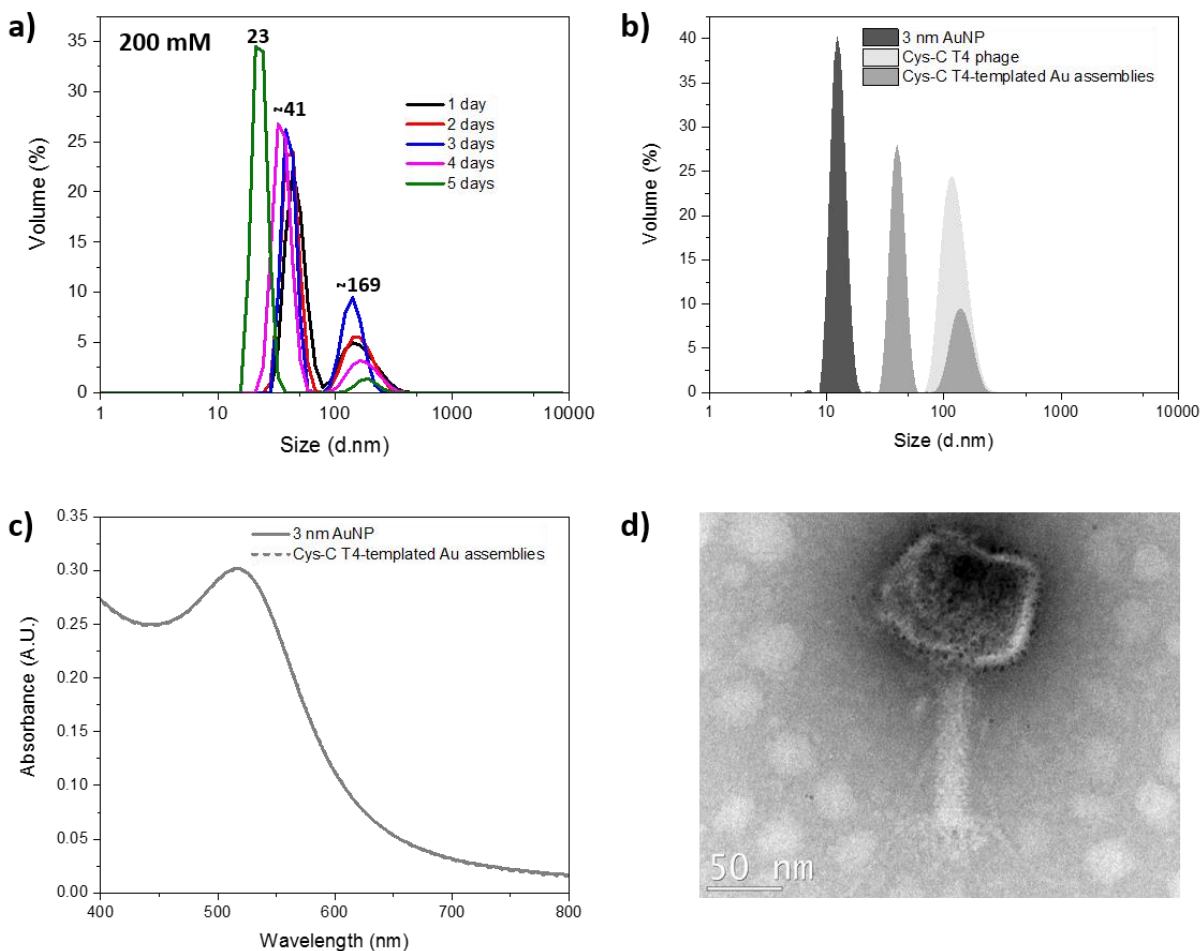


Figure 3.3.12 Characterization of 3-nm AuNPs self-assembled on Cys-C template. a) DLS histograms for volume based size analysis of Cys-C phage–3-nm AuNP solutions in 200 mM phosphate buffer. DLS histograms were recorded for a 5 day period. b) DLS histograms showing the size of 3 nm AuNP, Cys-C phage and Cys-C-templated gold assemblies after 2 days reaction. c) UV-Vis spectra of 3-nm colloidal AuNPs (solid line) and self-assembled on Cys-C phage template (dashed line) after 2 days reaction. d) TEM image of 3 nm AuNPs assembled on Cys-C phage.

The assembly of 9-nm AuNP in 50 mM phosphate buffer proceeded smoothly (Figure 3.3.13a). The main population in the DLS histograms of phage–AuNP binding reaction solutions was the colloidal AuNPs (~18 nm) and the relative proportion of the phage–AuNP assemblies in volume-based distribution

was only ~0.1%. The size of the population belonging to the phage–AuNP assemblies increased from 162 nm to 238 nm during the first 3 days of the reaction. The intensity-based size analysis of the reaction solutions clearly demonstrated the increase in the size of phage templates due to the assembly of AuNPs on their surfaces (Figure 3.3.13b). As the AuNPs were not stable enough on the third day, the assembly process was performed for 2 days period and the samples were characterized by UV-Vis spectroscopy and TEM imaging. Formation of Cys-C–AuNP assemblies was realized by a slight red shift and the broadening in the SPR band of the phage–AuNP binding solution (Figure 3.3.13c). Similarly to the observation made for Cys-N phage, imaging of 9 nm AuNPs assembled on Cys-C phage by electron microscopy resulted in phage particles partially covered with AuNPs which might be an indication of AuNP disassembly during TEM sample preparation.

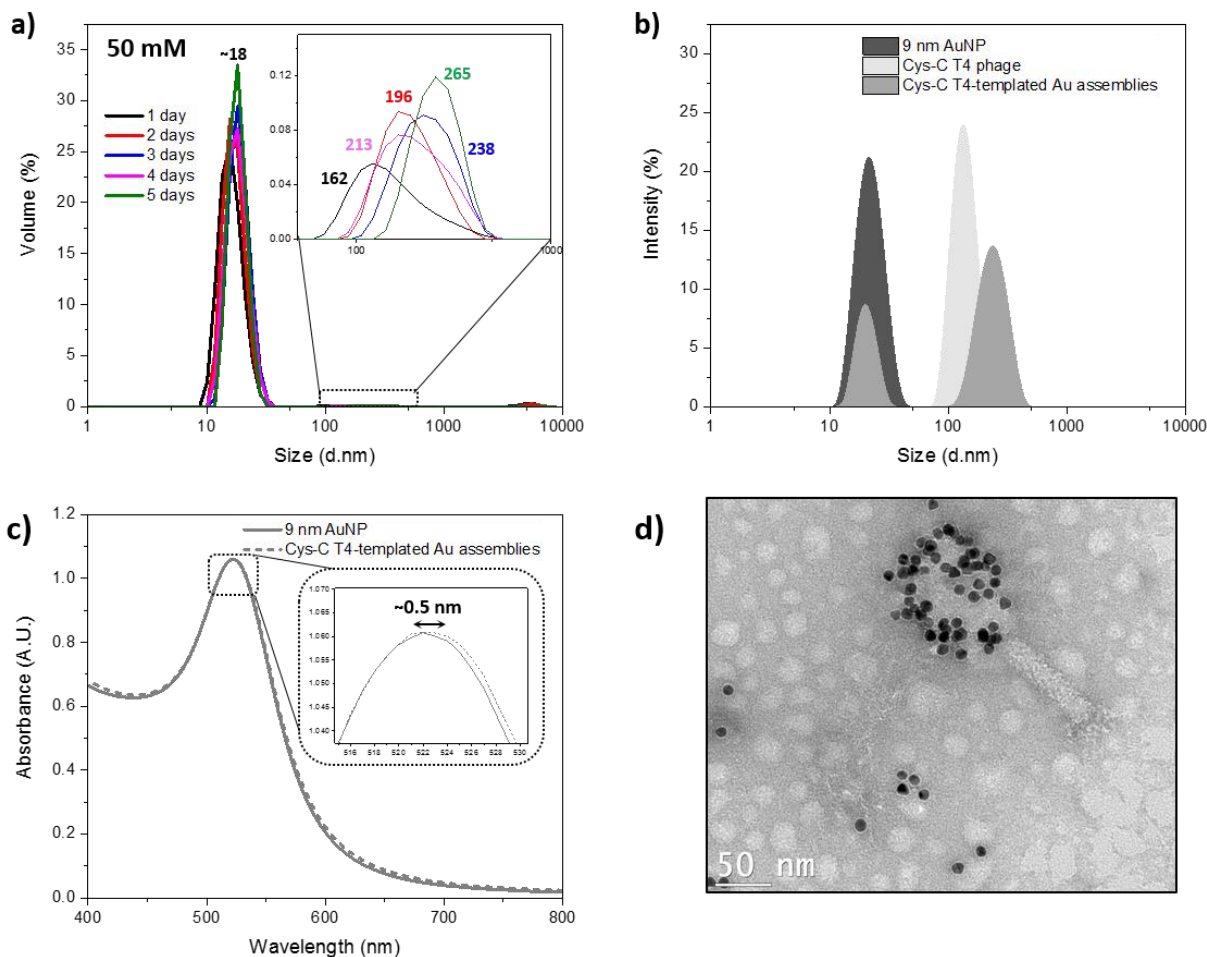


Figure 3.3.13 Characterization of 9 nm AuNPs self-assembled on Cys-C template. a) DLS histograms for volume based size analysis of Cys-C phage-9 nm AuNPs solutions in 50 mM phosphate buffer. DLS histograms were recorded for a 5 day period. b) DLS histograms showing the size of 9 nm AuNPs, Cys-C phage and Cys-C-templated gold assemblies after 2 days reaction. c) UV-Vis spectra of 9 nm colloidal AuNPs (solid line) and self-assembled on Cys-C phage template (dashed line) after 2 days reaction. d) TEM image of 9 nm AuNPs assembled on Cys-C phage.

The self-assembly process of 13-nm AuNPs was performed in 25 mM phosphate buffer over 2 days and resulted in the formation of phage–AuNP assemblies with a size of 293 nm (Figure 3.3.14a). The increase in the size of Cys-C phage template up on assembly of AuNPs was showed by intensity based size analysis of phage–AuNP reaction solutions (Figure 3.3.14b). Stability of 13-nm AuNPs was taken into account for optimization of phage–AuNP binding reaction time. The assembly process was carried out till the third day of the reaction that the AuNPs started to interact with each other strongly and form small aggregates. Characterization of Cys-C–AuNP assemblies by UV-Vis spectroscopy also showed the formation of assemblies which was creating a red shift and broadening in the SPR band of the reaction solution (Figure 3.3.14c).

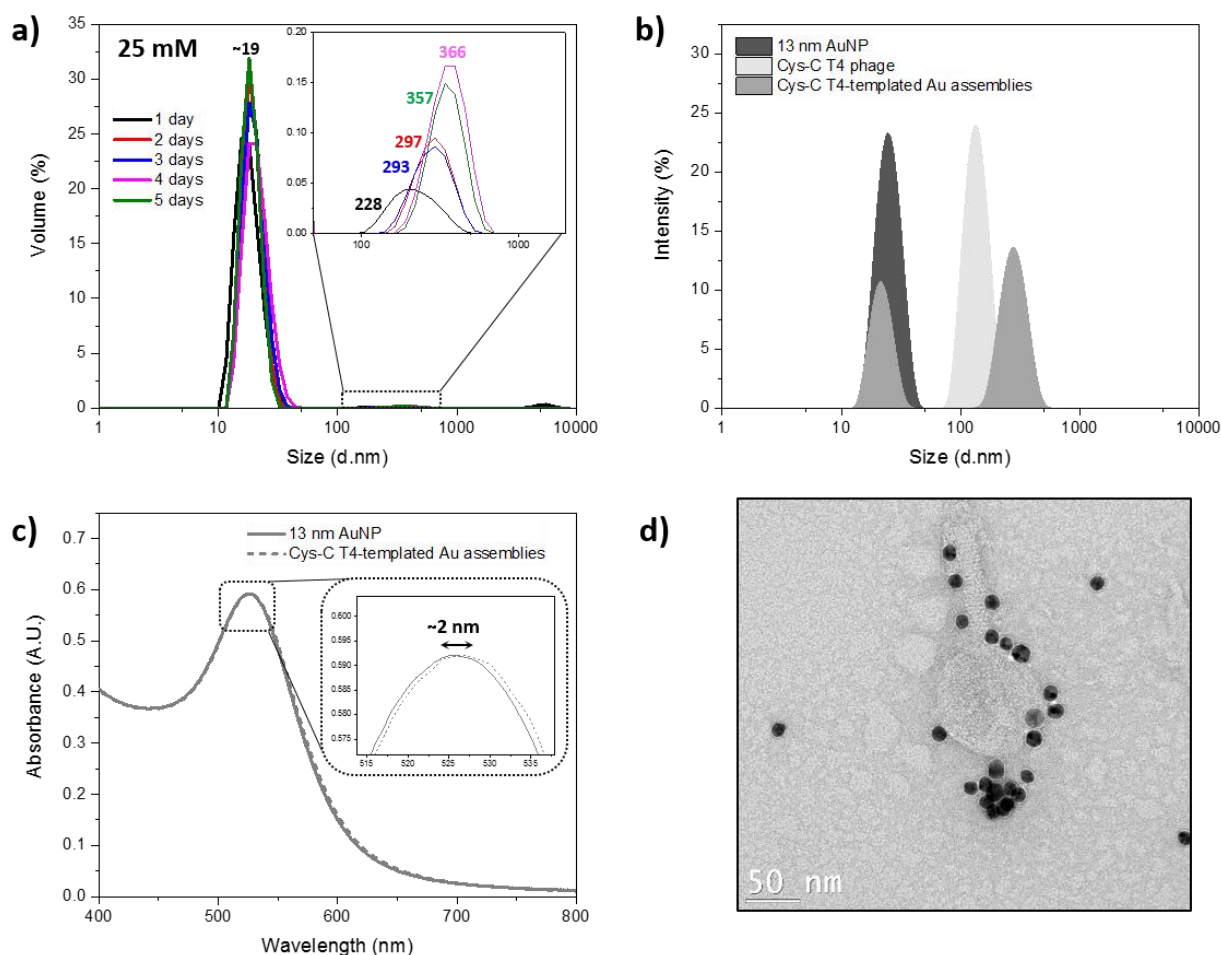


Figure 3.3.14 Characterization of 13-nm AuNPs self-assembled on Cys-C template. a) DLS histograms for volume based size analysis of Cys-C phage–13-nm AuNP solutions in 25 mM phosphate buffer. DLS histograms were recorded for a 5 day period. b) DLS histograms showing the size of 13-nm AuNPs, Cys-C phage and Cys-C-templated gold assemblies after 2 days reaction. c) UV-Vis spectra of 13-nm colloidal AuNPs (solid line) and self-assembled on Cys-C phage template (dashed line) after 2 days reaction. d) TEM image of 13 nm AuNPs assembled on Cys-C phage.

However, assembly of 13 nm AuNPs on Cys-C phage was not confirmed by TEM images. As observed for 9 nm AuNPs, in TEM images, phage particles were partially covered with AuNPs (Figure 3.3.14d). The results obtained from DLS and UV-Vis spectroscopy suggest that the AuNPs assembled on Cys-C phage were disassembled during sample preparation for TEM, most probably at drying step. Although, we could not confirm the assembly of AuNPs on Cys-N/C phage designs by TEM imaging, the results of DLS and UV-Vis spectroscopy suggest that display of cysteine residues on Soc protein of T4 phage resulted in template materials with gold binding affinity and enabled the attachment of AuNPs to phage capsid through thiol-gold interactions [240]. Compared to Cys-N design, TEM imaging of the AuNP assemblies templated on Cys-C phage resulted in higher numbers of phage particles covered with AuNPs. This observation might suggest that gold binding affinity of Cys-C phage was stronger than the affinity of Cys-N phage, therefore the assemblies templated on Cys-C could retain their stability up to a higher extent. Higher stability of Cys-C phage might be due to the fact that the C termini of Soc protein face each other at the trimeric junctions and enables the simultaneous interaction of AuNPs with 3 affinity moieties at each binding side.

Assembly of AuNPs on A3-gold binding peptide bearing T4 phage templates

The self-assembly reactions of AuNPs with the different T4 phage templates needed to be optimized on a case-by-case basis. As such, to avoid excessive repetition, in this part of the thesis only optimized reaction conditions of AuNP and T4 templates are shown. The DLS histograms of the reaction solutions with different ionic strengths are provided in Appendix A. Additionally, TEM imaging was not performed for characterization of the phage–AuNP assemblies due to the uncertainties related to the sample preparation for TEM observations. The effect of the drying process on stability of T4-templated AuNP assemblies is considered as a major problem influencing the images and complicates making concluding remarks regarding the prepared assemblies.

The assembly of 3-nm AuNPs on T4 phage templates displaying A3 gold-binding peptides were performed in 200 mM phosphate buffer over a 2 days reaction. Interactions of AuNPs with phage templates were dependent on the disposition of A3 peptide on phage surface. Assembly of AuNPs on A3-N phage, displaying gold-binding moieties on N-termini of Soc protein, generated phage–AuNP assemblies with a size of ~231 nm on the third day of the reaction (Figure 3.3.15a). While the colloidal AuNPs were not detectable in the reaction solution, a second population with a size of ~5000 nm was observed. Formation of the second population was due to the strong phage–AuNP interactions, which ultimately yielded large aggregates. UV-Vis spectroscopy of the reaction solution also confirmed the formation of

these clusters as the assembly process resulted in a red shift and broadening in the SPR band of AuNPs (Figure 3.3.15b). In case of A3-C phage, displaying A3 peptide on C-termini of Soc protein, phage–AuNP interactions were weaker. In addition to the phage–AuNP assemblies, the DLS histograms of reaction solutions showed a second population corresponding to the colloidal AuNPs (Figure 3.3.16a). As a result of weak particle interactions, a significant part of the colloidal AuNPs remained unbound in the reaction solution. Characterization of the phage–AuNP reaction solution by UV-Vis spectroscopy did not show any change in the SPR band of AuNPs (Figure 3.3.16b).

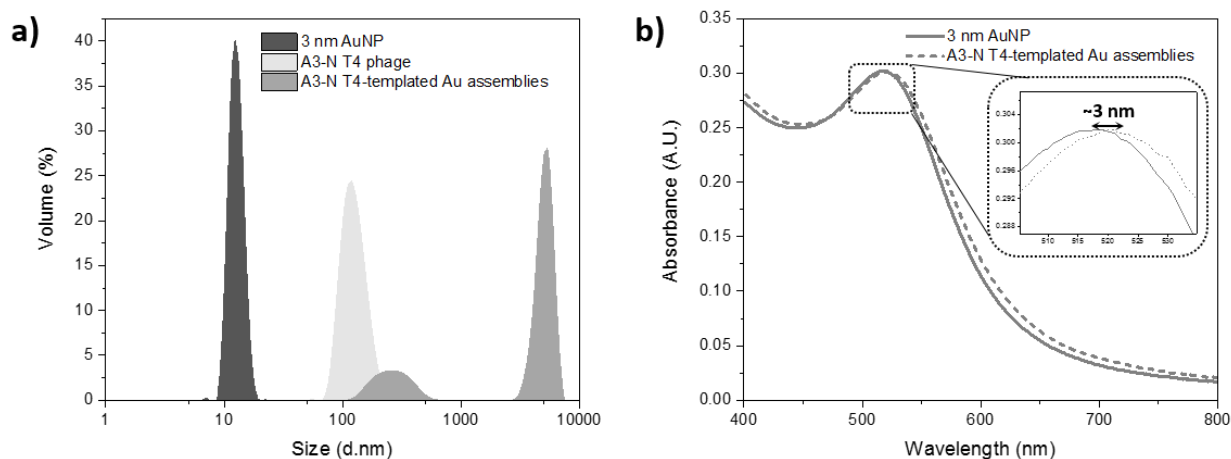


Figure 3.3.15 Characterization of 3 nm AuNPs self-assembled on A3-N template. a) DLS histograms showing the size of 3-nm AuNPs, A3-N phage and A3-N-templated gold assemblies after 2 days reaction. b) UV-Vis spectra of 3 nm colloidal AuNPs (solid line) and self-assembled on A3-N phage template (dashed line) after 2 days reaction.

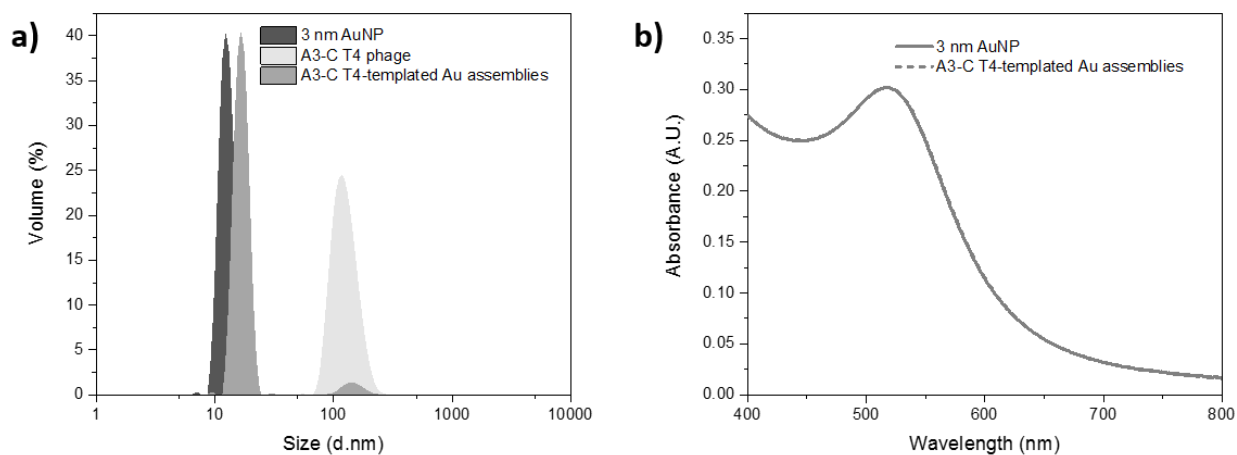


Figure 3.3.16 Characterization of 3-nm AuNPs self-assembled on A3-C template. a) DLS histograms showing the size of 3 nm AuNPs, A3-C phage and A3-C-templated gold assemblies after 2 days reaction. b) UV-Vis spectra of 3 nm colloidal AuNPs (solid line) and self-assembled on A3-C phage template (dashed line) after 2 days reaction.

The assembly of 9-nm and 13-nm AuNPs, was performed in 50 mM and 25 mM phosphate buffers, respectively. Characterization of reaction solutions by DLS demonstrated that interactions of AuNPs with A3-C phage was similar to the one with A3-N phage. Both template designs generated a population with a size slightly higher than the size of phage template after 2 days reaction (Figure 3.3.17a, Figure 3.3.18a, Figure 3.3.19a and Figure 3.3.20a). The slight red shift (~ 1 nm) and broadening in the SPR bands of the reaction solutions was an indication of phage-gold interactions and assembly of AuNPs on phage surface (Figure 3.3.17b, Figure 3.3.18b, Figure 3.3.19b and Figure 3.3.20b).

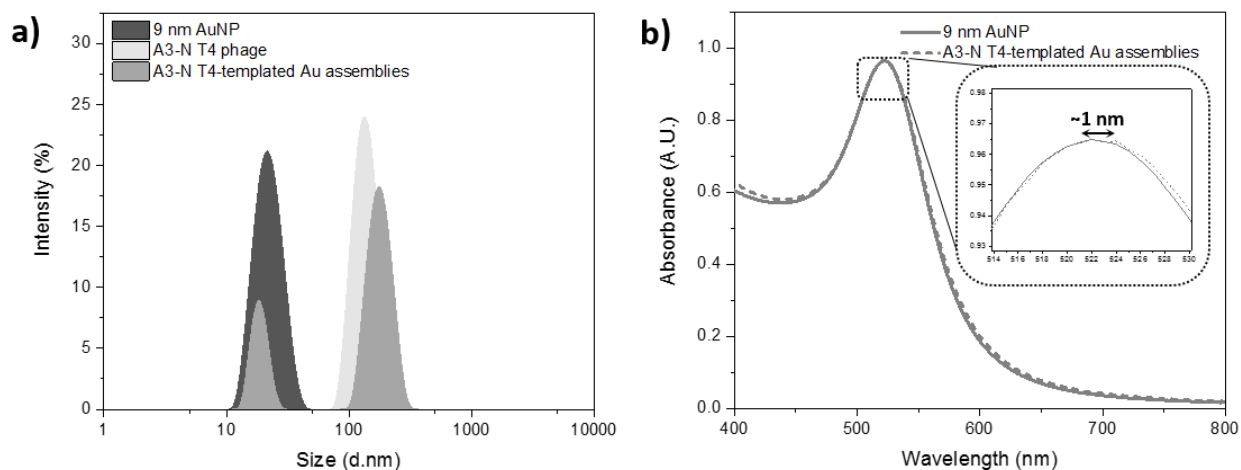


Figure 3.3.17 Characterization of 9-nm AuNPs self-assembled on A3-N template. a) DLS histograms showing the size of 9-nm AuNPs, A3-N phage and A3-N-templated gold assemblies after 2 days reaction. b) UV-Vis spectra of 9-nm colloidal AuNPs (solid line) and self-assembled on A3-N phage template (dashed line) after 2 days reaction.

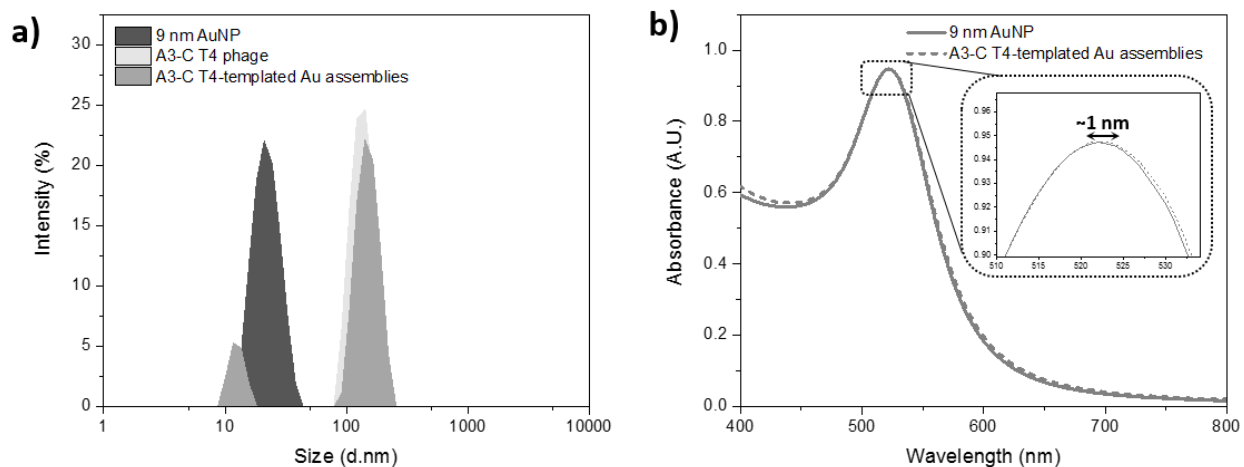


Figure 3.3.18 Characterization of 9-nm AuNPs self-assembled on A3-C template. a) DLS histograms showing the size of 9-nm AuNPs, A3-C phage and A3-C-templated gold assemblies after 2 days reaction. b) UV-Vis spectra of 9-nm colloidal AuNPs (solid line) and self-assembled on A3-C phage template (dashed line) after 2 days reaction.

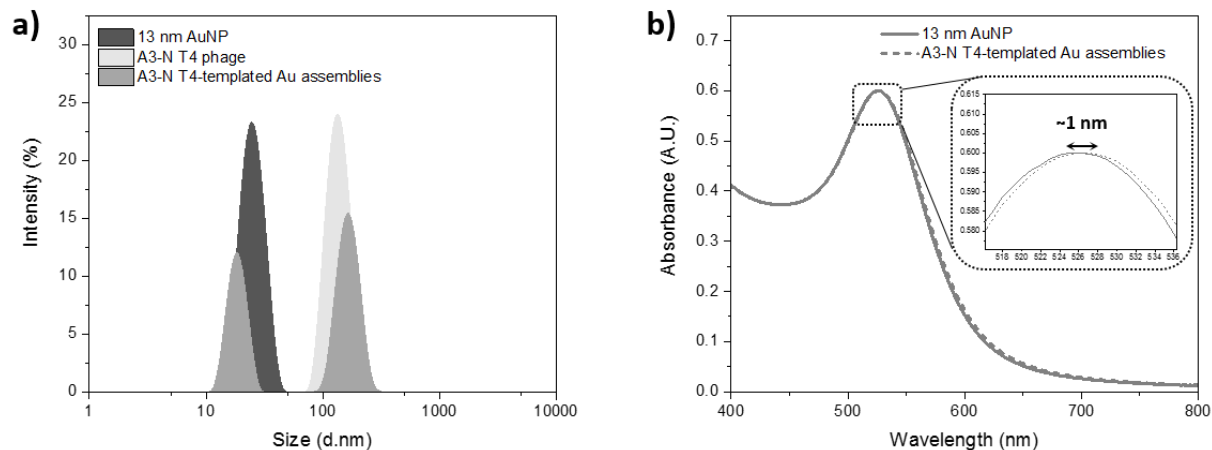


Figure 3.3.19 Characterization of 13-nm AuNPs self-assembled on A3-N template. **a)** DLS histograms showing the size of 13-nm AuNPs, A3-N phage and A3-N-templated gold assemblies after 2 days reaction. **b)** UV-Vis spectra of 13-nm colloidal AuNPs (solid line) and self-assembled on A3-N phage template (dashed line) after 2 days reaction.

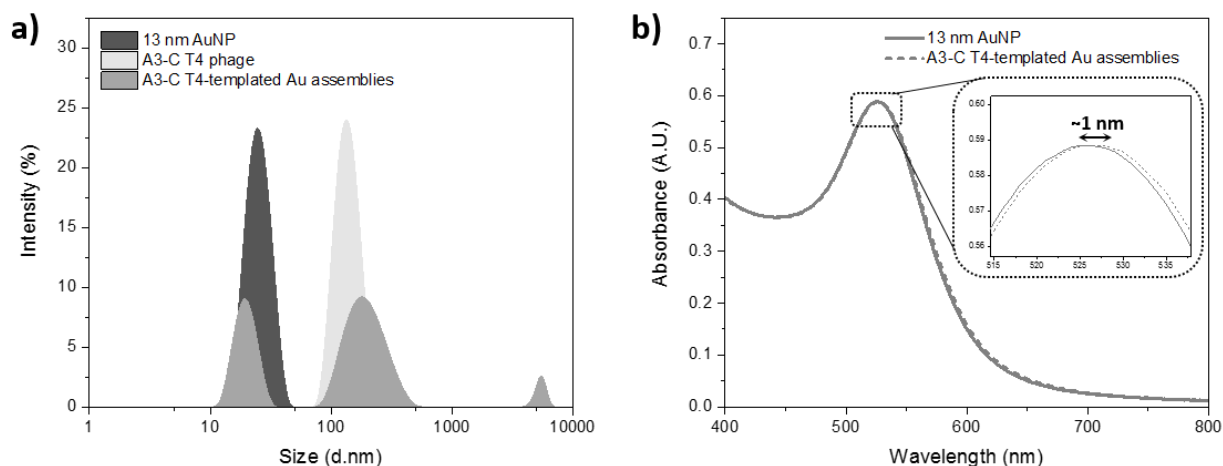


Figure 3.3.20 Characterization of 13-nm AuNPs self-assembled on A3-C template. **a)** DLS histograms showing the size of 13 nm AuNPs, A3-C phage and A3-C-templated gold assemblies after 2 days reaction. **b)** UV-Vis spectra of 13 nm colloidal AuNPs (solid line) and self-assembled on A3-C phage template (dashed line) after 2 days reaction.

It is worth mentioning that A3 peptide (AYSSGAPPMPFF) was screened on p3 minor coat protein of M13 phage and its binding affinity is attributed to the presence of the residues with aromatic side groups (tyrosine (Y) and phenylalanine (F)) and sulfur atoms (methionine (M)) which have strong gold binding energies [176]. In general, the screening of affinity moieties on p3 and p8 proteins of M13 phage with high copy numbers creates avidity problem which prevents the observation of binding affinity of individual fusion proteins and complicates the discrimination between low- and high-affinity binders [138]. Therefore, it is expected to observe different gold binding affinity for A3 peptide when it is displayed on Soc protein which results in different disposition and avidity on T4 phage capsid. In this manner, despite

the fact that DLS and UV-Vis spectroscopy results demonstrated the assembly of AuNPs on A3-N and A3-C templates, the stability of these assemblies still remains unclear. Although, it is crucial to evaluate their stability, their performance in future applications will clarify this uncertainty.

Assembly of AuNPs on GB gold-binding peptide bearing T4 phage templates

T4 phage templates displaying GB-gold-binding peptide were also studied to create phage–AuNP assemblies composed of 3, 9, and 13 nm AuNPs. As for the other T4 phage templates, assembly of 3 nm AuNPs on GB-N and GB-C phages was performed in 200 mM phosphate buffer over a 2-day period. Characterization of the reaction solutions by DLS demonstrated that a new population having a size of ~200 nm, which was higher than the size of T4 phage template (~126 nm), was formed (Figure 3.3.21a and Figure 3.3.22a). This new population was a result of AuNP assembly on phage template and was also confirmed by UV-Vis spectroscopy. Assembly of AuNPs on GB-C phage produced a red shift (~3nm) and broadening in the SPR band of AuNPs (Figure 3.3.22b). On the other hand, interactions of 3-nm AuNPs with GB-N phage did not create any change in the SPR band of the reaction solution (Figure 3.3.21b).

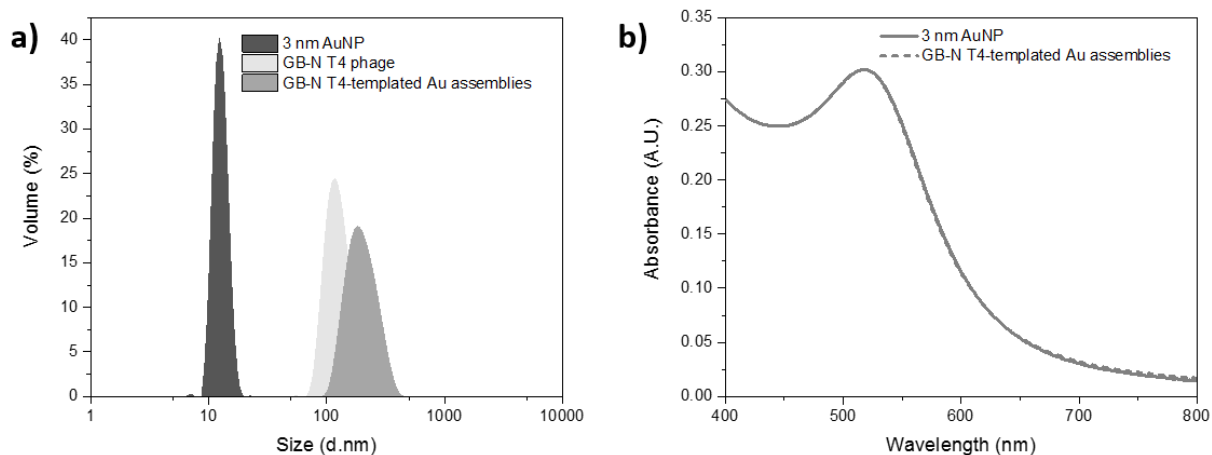


Figure 3.3.21 Characterization of 3-nm AuNPs assembled on GB-N template. a) DLS histograms showing the size of 3-nm AuNPs, GB-N phage and GB-N-templated gold assemblies after 2 days reaction. b) UV-Vis spectra of 3-nm colloidal AuNPs (solid line) and self-assembled on GB-N phage template (dashed line) after a 2-day reaction.

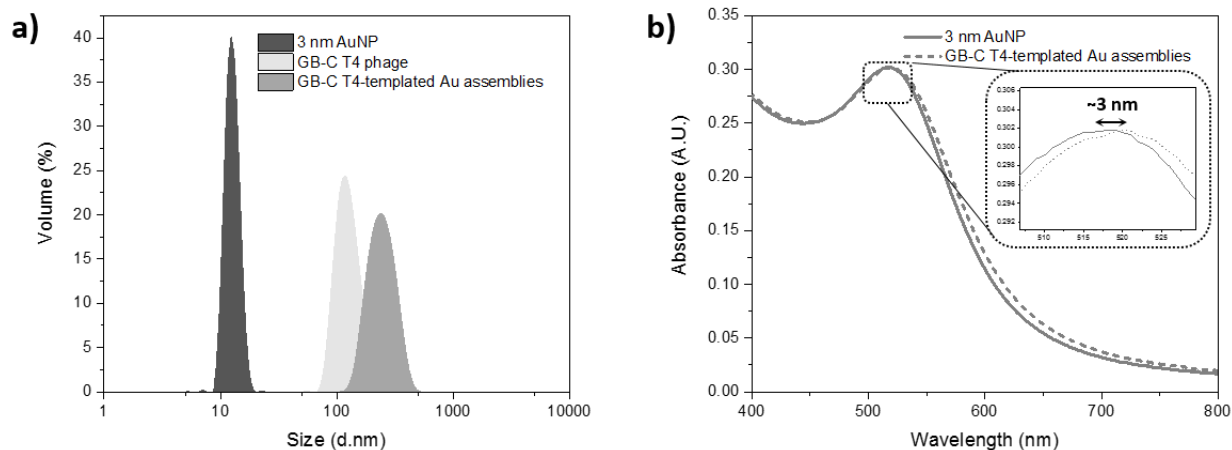


Figure 3.3.22 Characterization of 3-nm AuNPs self-assembled on GB-C template. a) DLS histograms showing the size of 3-nm AuNPs, GB-C phage and GB-C-templated gold assemblies after 2 days reaction. b) UV-Vis spectra of 3-nm colloidal AuNPs (solid line) and self-assembled on GB-C phage template (dashed line) after 2 days reaction.

The assembly of 9-nm AuNPs on GB-C and GB-N phage templates in 50 mM phosphate buffer yielded similar results. After 2 days reaction, DLS histograms showed that phage–AuNP assemblies templated by GB-N and GB-C phages had a size of 133 nm and 140 nm, respectively (Figure 3.3.23a and Figure 3.3.24a). A red shift (~1 nm) and broadening in the SPR band demonstrated the aggregation state of the AuNPs (Figure 3.3.23b and Figure 3.3.24b).

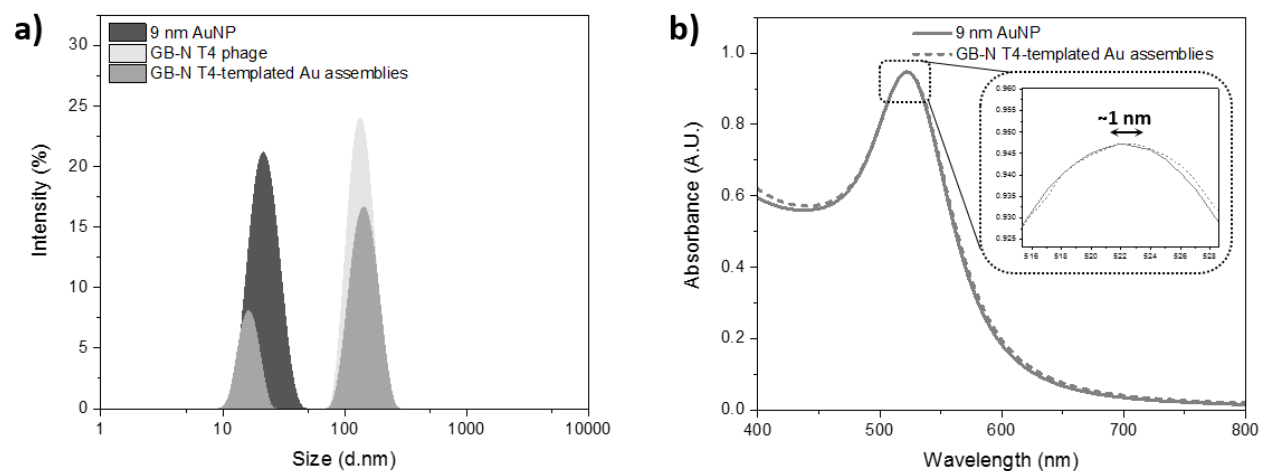


Figure 3.3.23 Characterization of 9 nm AuNPs self-assembled on GB-N template. a) DLS histograms showing the size of 9 nm AuNPs, GB-N phage and GB-N-templated gold assemblies after 2 days reaction. b) UV-Vis spectra of 3 nm colloidal AuNPs (solid line) and self-assembled on GB-N phage template (dashed line) after 2 days reaction.

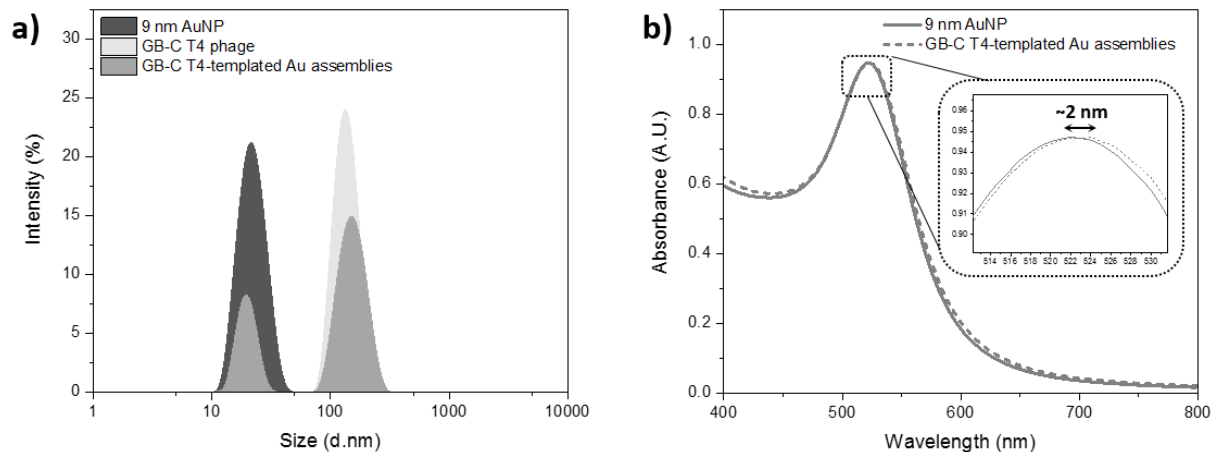


Figure 3.3.24 Characterization of 9 nm AuNPs self-assembled on GB-C template. a) DLS histograms showing the size of 9 nm AuNPs, GB-C phage and GB-C-templated AuNP assemblies after 2 days reaction. b) UV-Vis spectra of 3 nm colloidal AuNPs (solid line) and self-assembled on GB-C phage template (dashed line) after 2 days reaction.

The assembly of 13-nm AuNPs on GB-N and GB-C phages in 25 mM phosphate buffer over a 2 days period resulted in larger phage–AuNP assemblies, in comparison to those prepared with 9 nm AuNPs. Intensity-based size analysis of the reaction solutions demonstrated that GB-N and GB-C-templated AuNP assemblies with a size of 206 nm and 173 nm, respectively (Figure 3.3.25a and 3.3.26a). Self-assembly of AuNPs resulted in a red shift (~ 1 nm) and broadening in their SPR bands (Figure 3.3.25b and 3.3.26b).

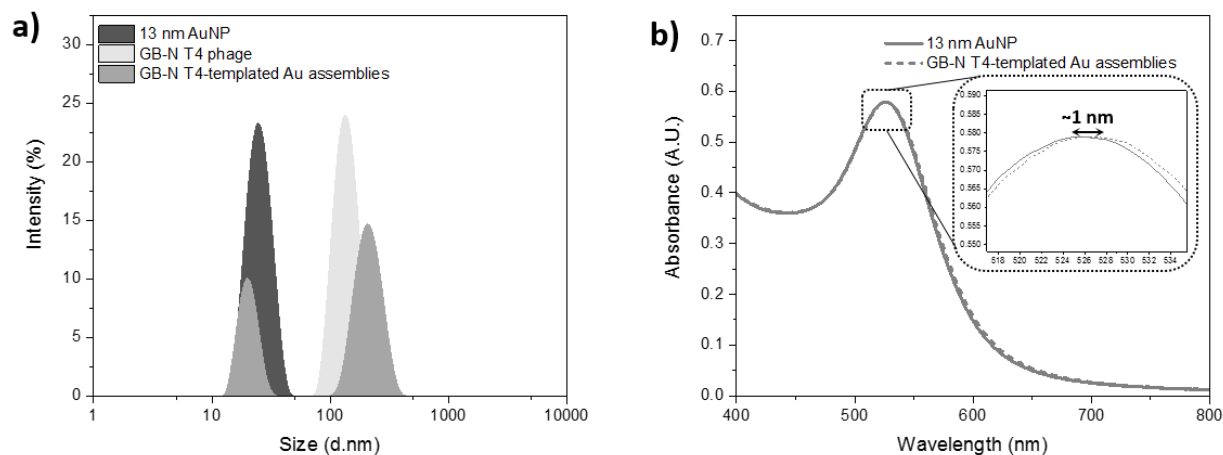


Figure 3.3.25 Characterization of 13 nm AuNPs self-assembled on GB-N template. a) DLS histograms showing the size of 13 nm AuNPs, GB-N phage and GB-N-templated AuNP assemblies after 2 days reaction. b) UV-Vis spectra of 3 nm colloidal AuNPs (solid line) and self-assembled on GB-N phage template (dashed line) after 2 days reaction.

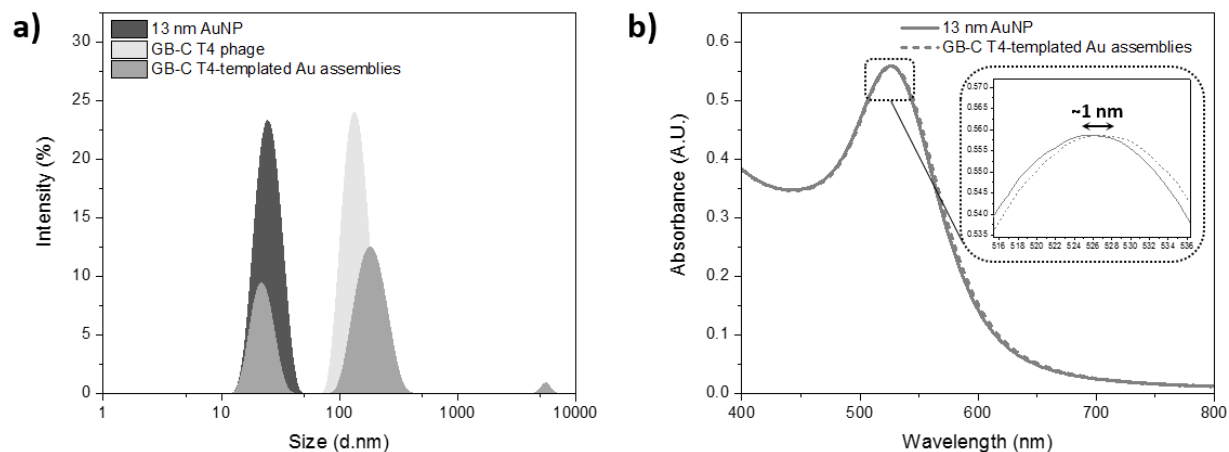


Figure 3.3.26 Characterization of 13 nm AuNPs self-assembled on GB-C template. **a)** DLS histograms showing the size of 13 nm AuNPs, GB-C phage and GB-C-templated AuNP assemblies after 2 days reaction. **b)** UV-Vis spectra of 3 nm colloidal AuNPs (solid line) and self-assembled on GB-C phage template (dashed line) after 2 days reaction.

GB peptide (VSGSSPDS) is another well-known gold-binding motif whose affinity is attributed to the presence of four serine (S) residues having hydroxyl groups on side chain [171]. Similar to the peptide sequences screened on p3 protein, an avidity problem could be also observed for GB peptide, which was selected by screening on p8 major coat protein of M13. In fact, the problem becomes more serious in the case of p8 protein given that a very high copy number of p8 protein (2700) is employed to display the peptide sequences. Therefore, GB peptide might exhibit different gold-binding affinity on Soc protein of T4 phage. So far, the results of DLS and UV-Vis spectroscopy demonstrated that GB-N/C phage designs have gold-binding affinity promoting the assembly of AuNPs on phage surfaces. However, it is necessary to study the stability of these assemblies to have better understanding on their feasibility for employment in different application.

3.4 Conclusion

In this chapter, different gold-binding moieties (cysteine, A3 and GB peptides) were displayed on Soc protein of T4 phage to design template materials for self-assembly of AuNPs. A3 peptide is a well-known gold-binding peptide screened on p3 minor coat protein of M13 phage whereas GB peptide was selected by screening on p8 major coat protein of M13. It is known that peptide motifs screened on a certain protein (as a result of different phage display platforms) can lose their functions when they are displayed on another protein [171]. This suggests that their disposition on the phage surface is important, which may indicate cooperativity of multiple peptides for the binding of a single AuNP. Actually, it was the

motivation of using two different gold binding peptides in this work to study this effect. Since they might exhibit different binding affinities on T4 surface, we aimed to investigate the binding affinities of both peptide sequence and choose the better binder.

Analysis of phage–AuNP assemblies was performed employing 3 different techniques (DLS, UV-Vis spectroscopy, and TEM imaging). While the employment of DLS enabled the observation of changes in size of phage templates due to the assembly of AuNPs on their surfaces, UV-Vis spectroscopy allowed us to study the occurrence of plasmon coupling between assembled AuNPs. Although TEM imaging was critical for better understanding of disposition of AuNPs on phage templates, as well as the stability of assemblies, difficulties were faced in electron microscopy observations. Most probably, these difficulties arise from the fact that the icosahedral structure of phage capsid got seriously affected from dehydration occurred during drying step of TEM sample preparations. As a result of dehydration, the shape of the phage capsid, as well as, the disposition of gold-binding moieties on capsid dramatically changed and resulted in disassembly of AuNPs. TEM observations, mostly, resulted in images of phage particles partially covered with AuNPs, phages without any AuNPs on their surface, and free AuNPs. Observation of phage particles with/without AuNPs on their surface in the same sample preparation suggested that the damage on phage capsid and corresponding AuNP assemblies was a random process. Therefore, TEM results were not conclusive to represent the samples. In this manner, the assemblies of AuNPs on T4 phage templates were assessed with the help of DLS and UV-Vis spectroscopy results which suggest that all gold-binding moieties displayed on Soc protein (Cysteine, A3 peptide and GB peptide) produced T4 phage templates with gold-binding affinity. Assembly of AuNP on phage templates were consistent with the observation of an increase in size of the phage templates. While the assembly of 3 nm AuNPs did not create a red shift in the position of SPR band for GB-N, A3-C, Cys-N, and Cys-C templated assemblies, the formation of phage–AuNP assemblies were mostly confirmed via a red shift due to the plasmon coupling between the AuNPs attached onto the phage capsids.

Display of gold-binding moieties on the tip of Soc protein introduced 810 functional groups to the phage surface, which were used to attach AuNPs. Both C- and N-termini of Soc protein were used to display gold-binding moieties. The disposition of the gold-binding peptides on the phage surface changed with the terminus employed in phage display. Consequently, the terminus of Soc protein employed in display of gold-binding moieties might significantly affect the attachment of AuNPs to the phage templates, as well as the stability of Au assemblies. TEM imaging was proposed as a tool not only to confirm the formation of phage–AuNP assemblies, but also to study their stability. However, the obtained

TEM images suggested that sample preparation seriously damaged the phage capsids and their AuNPs assemblies. Therefore, it is necessary to improve the sample preparation for TEM observation to be able to make conclusive analysis about formation of AuNP assemblies on phage templates. Fixation of phage–AuNP by chemicals such as glutaraldehyde might be used to preserve the assemblies and retain their stability during TEM observations.

To the extent of our knowledge, this is the first time that T4 phage has been employed as a template material to assist the self-assembly of AuNPs into clustered structures. As a natural recognition probe of *E.coli* cells, T4 phage been used in several biosensor applications. Lytic feature of T4 phage makes its employment in biosensor applications more interesting because of generating extra information through cell lysis for identification of the target cells [241]. In this regard, introduction of plasmonic properties to T4 phage by creating AuNP assemblies on capsid surface can open up new opportunities for phage-based biosensor applications.

4 PHAGE-TEMPLATED AuNP ASSEMBLIES AS SERS-IMAGING CONTRAST AGENTS

4.1 Introduction

4.1.1 Surface enhanced Raman scattering (SERS)

Raman scattering corresponds to the inelastic scattering of photons resulting from the interaction of light with the rotational/vibrational modes of molecules. These scattered photons have different energy than the incident photons, and this energy difference corresponds to the characteristic Raman-active modes of the molecules. The Raman spectra of molecules can be used as a fingerprint to identify compounds in e.g., chemical and biological systems [242] and, alternatively, Raman reporter molecules can be used as selective imaging contrast agents for hyperspectral imaging via their distinctive spectra (from the background matrix). However, statistically, only one in every 1–10 million scattered photons result from Raman scattering (the rest corresponding to elastic scattering), and thus signal intensity is a typical limiting factor for such applications [243], especially when the concentration of reporter molecule is very low compared to the background.

One approach to overcome this limitation is to bring the reporter molecule (or the molecule under investigation) in close proximity to metallic nanostructures, to enhance the Raman signal by the process of SERS [244]. Enhancement can result from two major mechanisms: 1) electromagnetic enhancement and 2) chemical enhancement. It is widely accepted that the major contributing mechanism to enhancement is electromagnetic enhancement. The latter originates from excitation of the surface plasmon of the metal by the laser, which generates an intense localized electromagnetic field around the metal surface. Due to field enhancement, both the excitation and emission rates of the Raman processes increase. In other words, molecules close to the metal surface obtain a large number of pathways for both excitation and emission [32]. The electromagnetic field enhancement generated around metal nanostructures decays exponentially as a function of distance from the metal surface. Therefore, high Raman signal enhancements are observed for molecules directly in contact or very close to the metal surface [21]. Because electromagnetic enhancement provides the same enhancement for all molecules within a given area, it is chemically non-selective. Thus, this mechanism of enhancement alone cannot explain all the feature of the SERS phenomenon. Chemical enhancement has been suggested as a second mechanism to describe the interactions between the molecules and the metal surface. According to this

mechanism, a charge-transfer state is created between the metal and the molecule adsorbed on it. The molecule–metal surface interaction induces novel charge-transfer intermediates that have higher Raman scattering cross-sections, which increase the probability of the Raman scattering. The chemical enhancement mechanism is molecule-dependent and is observed when the molecule is directly adsorbed to the metal surface [18, 245].

In systems designed to exploit SERS, the intensity of Raman scattering is dependent on several parameters including: i) the adsorption propensity between the molecules and nanostructures, ii) the excitation wavelength, and iii) the surface plasmon resonance features of nanostructures. Efficient adsorption of molecules on the nanostructure is crucial for reproducible SERS signal because it increases the number of molecules on the surface and creates correspondingly higher Raman signals [246]. The choice of excitation wavelength is dependent on the optical properties of the molecules and the nanostructure. The laser wavelength must not only excite the Raman scattering from the molecule, but also the surface plasmon of the nanostructures [247]. Indeed, the local electromagnetic field around the metal nanostructure is enhanced when the frequency of the incident light is resonant with the surface plasmon of the metal. In fact, oscillations of the electrons in the nanostructure becomes coherent with the light, which leads to redistribution of the local electromagnetic field and formation of locally-enhanced fields around the nanostructures, so-called “hot spot” [248]. As the electromagnetic enhancement mechanism is the dominant contribution to SERS, the features relevant to this mechanism become very important in the design of systems with strong SERS. As a consequence, the design of plasmonic nanostructures that produce local electromagnetic fields with high magnitudes has attracted significant attention. The properties of the materials e.g., size, shape, morphology, and arrangement, are critical parameters affecting plasmonic features. By tuning these parameters, electric field enhancements, and hence the Raman signal, can be amplified to yield highly Raman-emissive entities.

4.1.2 Plasmonic nano-architectures as SERS-active material

The preparation of SERS-active nano-structures is typically achieved by two main strategies: i) the top-down approach, and ii) the bottom-up approach. While bottom-up techniques use molecular or nanoscale building blocks to build-up the nano-structures, the top-down approaches start with a bulk material that is processed to create nanoscale features.

Top-down methods exploit computer-assisted design, and are very popular in the development of SERS-active planar (i.e., 2 dimensional) substrate materials. This is due to the fact that they enable the

fabrication of large-scale, reproducible, and high resolution (~ 10 nm) devices with a wide selection of geometries and sizes. In particular, reproducibility is critical for practical applications [249]. Techniques such as electron beam lithography (EBL), nanoimprint lithography, and photolithography have been used to create large arrays of nanostructures [250-252]. As another example, the Ag film over a nanosphere (AgFON) platform consists of the deposition of a silver film onto the surface of colloidal polystyrene particles, and is one of the most popular techniques used to create plasmonic arrays [253]. Alternatively, SERS-active arrays can be prepared by selective deposition or in situ reduction of metal nanoparticles on substrate surfaces including silicon, anodized aluminum oxide (AAO), or block copolymers [254-256]. Although these techniques can yield uniform SERS 'substrates' with large dimensions onto which test molecules can be deposited for analysis, the multiple fabrication steps make the entire process costly, time-consuming, and technically challenging. These caveats also complicate the development of more sophisticated multifunctional systems due to problems regarding the integration of these substrates into e.g., micro-channels. Furthermore, such planar substrates cannot be used as SERS-imaging contrast agents because they will indiscriminately enhance Raman scattering for any substance deposited into their hotspots. The surface of SERS substrates should be functionalized with receptor molecules to specifically capture the targets, however, it is quite challenging to place the receptor molecules precisely in hot-spots which will significantly affect the SERS signal. Therefore, exploring new methods to manufacture colloidal SERS materials with lower cost and simpler fabrication steps, and which permit the labelling of e.g., biological entities within complex sample environments, is an active area of research [21].

Some of the earliest platforms for SERS were produced via bottom-up approaches, which are relatively simple and low-cost in comparison to top-down techniques. In bottom-up approaches, individual building blocks, such as nanoparticles of variable size, geometry, or chemical composition are assembled into Raman-enhancing assemblies. Gold and silver nanoparticles are some of the most popular nanostructures employed [257-259]. For instance, ease of synthesis, stability, and biocompatibility are the most important features of AuNPs that make them favorable for biomedical applications. In fact, AuNPs have already been approved by the American Food and Drug Administration for clinical use in diagnostic applications [13]. In contrast, silver nanoparticles are not as popular for biomedical applications due to their potential toxicity [260]. Although individual nanoparticles have been reported to enhance Raman scattering, substantially higher SERS can be achieved when they are closely spaced, which allows their local SPR to couple. Plasmonic coupling within the nanometer-sized gaps between nanoparticles (so-called 'hot spots') gives rise to Raman signal enhancements as high as $\sim 10^9$ – 10^{11} . This can enable single molecule detection [261]. The Raman signals of molecules placed these small hot spots (1–5 nm)

contribute to a great extent to the total Raman signal (> 50%) [262]. Indeed, following the discovery of large Raman signal enhancements at plasmonic hot spots, SERS studies have focused on methods to fabricate nanostructures containing nanogaps that can accommodate intense electromagnetic field enhancements. The oldest and the simplest approach exploited is to induce the aggregation of nanoparticles, which produces randomly-generated hot spots. Aggregation of nanoparticles can be induced by several techniques, with the most common being the use of salts. Addition of electrolytes, e.g. KCl or NaCl, is commonly exploited for this purpose [263, 264]. Ethanol is another additive that induces the aggregation of metallic nanoparticles [265] by stripping their stabilizing surface ligands. An alternative approach is dye-induced aggregation, which relies on the replacement of stabilizing agents on the nanoparticle's surface by dye molecules, which reduces its colloidal stability (e.g., fuchsine basic, phthalazine, and rhodamine 6G) [266-268]. In this case, the dyes will act as Raman reporter molecules, owing to their presence in the gaps between nanoparticles. Finally, 'chemical-free' aggregation approaches, such as simply drying nanoparticle suspensions on a glass slide can also generate hot spots for SERS [269]. These aggregates are colloidal/dispersed entities, which make them suitable as imaging contrast agents (in comparison to planar substrates from above). As such, it is interesting to build upon these approaches and investigate means to enhance their SERS performance for this application.

In the preceding examples, nanoparticle aggregation is a random process, yielding an irregular number and disposition of hot spots. To better control the formation of hot spots and to improve reproducibility, several strategies have been developed to precisely assemble nanoparticles into larger clusters. For instance, the encapsulation of small nanoparticle aggregates into silica spheres is one approach that produces uniform aggregates for SERS. Formation of uniform aggregates is also achievable by carefully adjusting aggregation conditions (salt/dye amounts, pH, etc.) [270-272]. Alternatives to the silica shell are polymers such as polyvinylpyrrolidone (PVP), which are used to quench aggregation and stabilize the nanoaggregates [273]. These colloidal SERS assemblies can subsequently be functionalized with recognition molecules that target specific analytes thereby yielding SERS-imaging contrast agents. The assembly of nanoparticles on colloidal or dispersed support materials is an alternative way to control aggregation. Silver- or AuNPs can be deposited onto microbeads made of different materials such as silica, polymer, silver, or metallic nanowires. Grafting of nanoparticles on support materials can be achieved via covalent bonds [274], electrostatic interactions [275], by sputtering [276], or by *in situ* synthesis from the support materials [277-280]. Such SERS assemblies are usually modified with a Raman reporter molecule and then stabilized with silica shells. The resulting passivated assemblies can be subsequently functionalized with recognition molecules for use as contrast agents.

In addition to the aforementioned support materials, biological materials such as deoxyribonucleic acid (DNA), viruses, and bacteria, have also been employed as templates for the assembly of nanoparticles into plasmonic nano-structures with dense hot spots. For instance, the interaction of bacterial cells with metal ions results in the formation of random aggregated structures. In contrast, DNA and viruses are superior templates for the fabrication of highly-ordered SERS-active materials [281, 282]. Because of their chemistry it is possible not only to graft AuNPs to their surface, but also control their spacing, which has strong implications for SERS. In particular, DNA has gained great attention as a versatile nano-structure design material owing to the predictability of nucleobase pairing. In its simplest form, metal ions are reduced on double-stranded DNA templates using UV irradiation [283, 284]. DNA molecules act both a reducing agent and template in the preparation of these nanostructures. The SERS activity of these nano-structures arises from the short distance separating the nanoparticles on the DNA template [285]. DNA origami platforms, which are produced by assembling short DNA strands into large structures with pre-determined shape, also provide control of the size and spacing of the metallic nanoparticles over large dimensions [286]. Such DNA scaffolds can be adjusted to create SERS contrast agents with well controlled geometry and separation distance at the nanoscale [65, 287]. On their side, viruses correspond to colloidal templates that 'naturally' possess a precise disposition of functional groups on the surface, which can be (re-)engineered on the genetic level. M13 bacteriophage (a virus for bacteria) has been the most studied virus for the design of virus-templated SERS contrast agents. Metallic nanoparticles have been assembled on the p8 major coat protein of M13, which is a major component of the viral capsid with over 2700 copies per phage. The random self-assembly of nanoparticles can be directed by electrostatic interaction between negatively-charged M13 phage and positively-charged nanoparticles [29, 288, 289]. However, modification of the major coat protein (chemically or genetically) to display affinity moieties towards nanoparticles will result in more precise, stable, and reproducible phage-templated SERS contrast agents. For instance, M13 phage displaying a short dimer sequence (Proline-Aspartic acid) on p8 coat protein was employed to assemble 50 nm Au nanocubes (NC) to form a 1-dimensional chain assembly. While single AuNCs did not exhibit a distinguishable SERS signal, their assembly on phage surface resulted in hot-spots generating strong SERS signal intensity [33]. Self-assembly of SERS-active nanoparticles on phage surface can also be achieved through cysteine-rich peptides displayed on p8 protein. In a recent report, gold-coated magnetic nanostars (~35 nm) were assembled on M13 phage through thiol-gold affinity, and was later calcinated to form plasmonic mesoporous SERS substrates [181]. Formation of the mesoporous substrate resulted in clustered Au nanostructures with enhanced plasmon coupling, as well as enhanced SERS-activity.

Conjugation of DNA sequences to p8 coat protein via covalent binding is another approach to assemble SERS-active nanoparticles on phage template through DNA probes on particle surface. By doing so, large numbers of silver-coated AuNPs (20 nm) could be attached to phage surface and produced exponential gains in Raman signal due to their combinatorial effect rather than plasmon coupling [167].

Besides efforts to fabricate SERS-active materials from the aggregates of nanospheres, some research has focused on the design of single-nanoparticle-based SERS substrates, by controlling the shape of the metal nanoparticles. The fabrication of plasmonic nanostructures with sharp edges (e.g., nanostar, nanoflower, and nanocube) is one strategy to increase the electric field enhancement near the metallic particles [290-292]. As the electric field becomes more intense at the sharp edges of the material, an enhancement in the Raman signal is also observed. Using a related strategy, Cowpea mosaic virus (CPMV) has been coated with gold (via evaporation) to yield a structure with sharp edges, where strong electromagnetic fields can be generated [293]. Nano-shell structures are another type of plasmonic material that yields strong electromagnetic field enhancement. In these structures, the surface electromagnetic fields are localized through the pinholes in the hollow structures and creates enhanced Raman signal for SERS-based detection systems [294].

Overall, despite the interesting nature of the assemblies above, a need still exists for colloidal plasmonic assemblies that can be conveniently used for SERS-based contrast enhancement of biological entities in complex background matrices. This Chapter will therefore explore the opportunities and limitations of phage-templated AuNP assemblies as SERS contrast agents for bacteria, as model biological target. Phage naturally target bacteria and can therefore be used as contrast agents for these types of cells, though they can also be re-engineered to recognize a wide range of other targets. M13 and T4 phages with their distinct structures and geometries provide two different templates for AuNP assembly, and provide control over the local and long-range order of the AuNPs. In this study, we will examine very small AuNPs, which do not exhibit SERS on their own, or when 'randomly' aggregated. This will therefore not only contribute to the paucity of information regarding SERS with small AuNPs, but also provide the best contrast in images (no background from AuNPs not on the phage). Furthermore, small AuNPs will less interfere with the targeting process, which is an essential function for contrast agents.

4.2 Materials and Methods

4.2.1 Materials

T4 phage host *Escherichia coli* B (HER1024) were obtained from the Felix d'Herelle Reference Center for Bacterial Viruses (Université Laval, Quebec). Recombinant T4 phages stocks, so-called Cys-N, Cys-C, A3-N, A3-C, GB-N and GB-C were used, as prepared in Chapter 3. M13 phage host *Escherichia coli* strain ER2738 were obtained from New England Biolabs Inc. (Ontario). Recombinant M13 phage displaying gold binding moieties was used, as prepared in Chapter 2. All chemicals were obtained from Bioshop (Ontario, Canada) unless otherwise noted. They were of the highest grade available and were used as received without further purification. All aqueous solutions were prepared with deionized distilled water obtained from a Milli-Q water purifying system (18 M Ω /cm).

4.2.2 Preparation of Bacterial Strains and Bacteriophages

Escherichia coli B (HER1024) stock cultures were maintained in 35% glycerol and were kept at –80 °C. To prepare fresh bacterial cultures, an inoculum from a frozen glycerol stock was streaked onto a Luria Bertani (LB) (Miller) agar plate and incubated at 37 °C overnight. A single colony from the plate was inoculated into 10 mL of LB broth (Miller) and incubated overnight at 37 °C with shaking at 200 rpm. The viable bacteria number was calculated by preparing serial dilutions of culture and plating on LB agar plates. After overnight incubation, the colonies formed on agar plates were counted to calculate bacteria concentration, in the form of colony forming units (CFU). Prior to analysis, overnight bacterial suspensions were rinsed twice with distilled water, with centrifugation at 5000 rpm for 15 min after each rinse. The final cell pellet was suspended in phosphate buffer to reach 10⁶ CFU/mL.

In order to prepare *Escherichia coli* strain ER2738, a glycerol culture of bacteria was streaked onto a LB agar plate supplemented with tetracycline (10 μ g/mL) and incubated at 37 °C overnight. A culture for experiments was grown by inoculating 5 mL LB broth with a single colony from the plate and incubating overnight with shaking at 200 rpm at 37 °C. The next day, the viable bacteria number was calculated by preparing serial dilutions of culture and plating on LB agar plates. After overnight incubation, the colonies formed on agar plates were counted to calculate bacteria concentration as CFU. Similar to *Escherichia coli* B cell preparation, prior to analysis, overnight bacterial suspensions were rinsed twice with distilled water (?), with centrifugation after each wash, and diluted in phosphate buffer to reach 10⁶ CFU/mL.

4.2.3 Hydrophobic Treatment of Glass Slides

Before the hydrophobic treatment, the glass slides were cleaned. Initially, the glass slides (0.13–0.16 mm; Ted Pella Inc., CA, USA) were put in a beaker containing acetone and left for 30 min in an ultrasonic bath. Afterwards, the slides were thoroughly rinsed with distilled water and dried in the oven (60°C). In the second step, the slides were submerged in piranha solution (30% H₂O₂ in concentrated H₂SO₄ (3:1; Sigma Aldrich, Canada; **Caution:** piranha solution is very corrosive) and left for 30 min. Finally, the slides were rinsed with distilled water and dried in an oven (60°C).

A solution of trichloro(1H,1H,2H,2H-perfluorooctyl)silane solution (Alfa Aesar, MA, USA) (~1 mM) was freshly prepared in 100 mL toluene (Sigma Aldrich, Canada) in a 150 mL glass beaker. Freshly cleaned glass slides were immersed in this solution, the beaker covered with parafilm, and then stored in a fume hood for 3 hours. Afterwards, the slides were removed and successively rinsed with toluene and absolute ethanol (Commercial Alcohols, ON, Canada). Finally, the slides were dried in the oven (60°C) and stored in a box till they were used.

4.2.4 Preparation of Phage-templated Au Assemblies for SERS Analysis

M13-templated AuNP assemblies

As described in chapter 2, the stock of recombinant M13 phage displaying gold-binding peptide was already PEG-purified and stored at 4°C in TBS solution. The stock solution of phage was diluted in 100 mM phosphate buffer to a concentration of 10¹⁰ PFU/mL. The self-assembly of 3-, 9-, and 13-nm AuNPs on M13 phage templates was performed in 1 mL of 25 mM phosphate buffer (pH 7.0) including 100 µL of diluted phage solution (10¹⁰ PFU/mL in phosphate buffer) and 100 µL of nanoparticle stock solutions having concentrations of 2.8x10¹⁵ particle/mL, 5.7x10¹³ particle/mL, 3x10¹³ particle/mL for AuNPs with 3 nm, 9 nm and 13 nm diameters, respectively. After overnight incubation on a rotary shaker at room temperature, 100 µL of the reaction solution was rinsed twice with 25 mM phosphate buffer, with centrifugation at 3000 rpm for 5 min after each rinse. The final pellet was suspended in 30 µL of 25 mM phosphate buffer and a droplet of 3 µL of this solution was pipetted onto the hydrophobic glass slides and left to dry at room temperature.

Raman spectra of phage-templated AuNP assemblies were recorded in the absence and presence of bacterial cells. In order to prepare these samples, the phage–AuNP reaction solution was incubated

overnight and 100 μL of this solution was mixed with 1 mL of *Escherichia coli* ER2738 (10^6 CFU/mL in 25 mM phosphate buffer). After incubating the mixture for 1 h on a rotary shaker at room temperature, the sample solution was rinsed twice with 25 mM phosphate buffer, with centrifugation at 3000 rpm for 5 min after each rinse. The collected pellet including bacteria/phage-AuNP assemblies was suspended in 30 μL of 25 mM phosphate buffer and a droplet of 3 μL of this solution was pipetted onto the hydrophobic glass slides and dried at room temperature.

T4-templated AuNP assemblies

The stocks of recombinant T4 phages (Cys-N, Cys-C, A3-N, A3-C, GB-N, and GB-C) were column-purified as described in Chapter 3 and stored at 4 °C in 100 mM phosphate buffer (10^{10} PFU/mL) until used. The self-assembly of 3-, 9-, and 13-nm AuNPs on T4 templates was performed in 1 mL of phosphate buffer (pH 7; 200 mM, 50 mM, and 25 mM, respectively). The reaction solutions were prepared by adding 100 μL of phage stocks to 100 μL of nanoparticle stock solution. After 2 days incubation on a rotary shaker at room temperature, 100 μL of the reaction solution was rinsed twice with 25 mM phosphate buffer, with centrifugation at 3000 rpm for 5 min after each rinse. The pellet was suspended in 30 μL of 25 mM phosphate buffer and a droplet of 3 μL of this solution was pipetted onto the hydrophobic glass slides and left to dry at room temperature.

Raman spectra of T4-templated AuNP assemblies were also recorded in the presence of bacterial cells. One mL of *Escherichia coli* B suspension in 25 mM phosphate buffer (10^6 CFU/mL) was mixed with 100 μL of phage-AuNP reaction solution (aged for 2 days). The mixture was incubated for 15 min on a rotary shaker at room temperature, then the unbound AuNPs were removed from bacteria/phage-AuNP assemblies complex by rinsing twice with 25 mM phosphate buffer, with centrifugation at 3000 rpm for 5 min after each rinse. The pellet was suspended in 30 μL of 25 mM phosphate buffer and a droplet of 3 μL of this solution was pipetted onto the hydrophobic glass slides and dried at room temperature.

4.2.5 SERS Mapping on Glass Slides

Raman measurements were performed with a scanning probe microscope (AIST-NT CombiScope™ 1000) supporting Raman operating mode. A He-Ne laser, emitting at 632.8 nm, served as the excitation source. Unless otherwise mentioned, the laser had a power of 1.75 mW after the objective. The laser beam was focused onto the sample through a 20X objective lens with a numerical aperture of 0.45. Raman

spectra were collected from 0–1700 cm^{-1} with an exposure time of 1 s. The mapping area was $100 \times 100 \mu\text{m}^2$ with step size of 2.5 μm .

4.2.6 Determination of the SERS Enhancement Factor

In order to calculate the enhancement factor, SERS intensity of BSPP (Raman reporter) on phage-templated AuNP assemblies, I_{SERS} , was compared to the Raman intensity of BSPP in solution (145 mM in water), I_{Raman} . The enhancement factor EF was calculated using the following equation [295];

$$EF = \frac{I_{SERS} \times N_{Raman}}{I_{Raman} \times N_{SERS}}$$

where N_{Raman} and N_{SERS} are the numbers of BSPP in solution and on phage-templated AuNP assemblies, respectively.

Acquisition of the Raman spectrum of BSPP in solution was performed by placing a drop on a glass slide and measuring the signal under the same conditions as used for the SERS measurements of phage-templated AuNP assemblies. The excitation volume of laser was assumed as a cylinder and the height (h) was calculated by following equation [296];

$$\frac{h}{d} = \frac{3.28\eta}{NA}$$

where d is the diameter of laser beam (1.28 μm), η is the refractive index of water medium (1.33) [297] and NA is the numerical aperture of the objective (0.45). Afterwards, the calculated value of height was used to estimate the number of BSPP molecules in the excitation volume (N_{Raman}).

It should be noted that the number of phage-templated AuNP assemblies in the focal area of the laser was not known. As such, the number of hot spots and corresponding number of BSPP molecules placed in these hot spots was conservatively estimated as follows: The focal volume was assumed to be filled with a monolayer of AuNPs, and the entire surface area of the AuNPs were involved in generation of hot spots. Moreover, the surface of AuNPs was assumed to be covered with a monolayer of BSPP, with each BSPP molecule occupying an area of 0.5 nm^2 [298].

4.3 Results and Discussion

Because hyperspectral imaging experiments are typically conducted by casting dilute analyte solutions onto microscope slides from solution, an equivalent experimental approach was adopted herein to evaluate the phage-templated AuNP assemblies as SERS-imaging contrast agents for bacteria. For this purpose, conventional glass microscope slides were modified with a hydrophobic silane so that droplets of analyte solution would progressively shrink (and concentrated) during the drying process, due to the surface tension between the droplet and the surface (Figure 4.3.1).

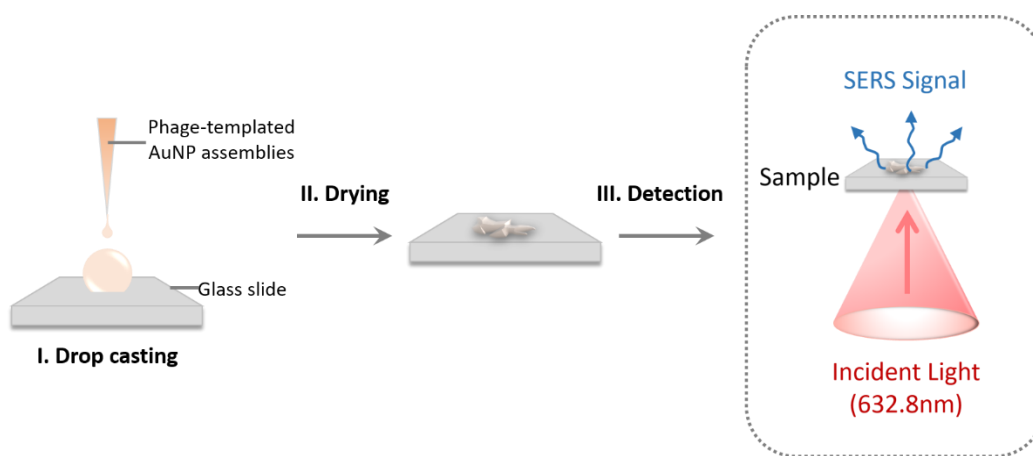


Figure 4.3.1 Schematic representation of sample preparation and SERS signal detection.

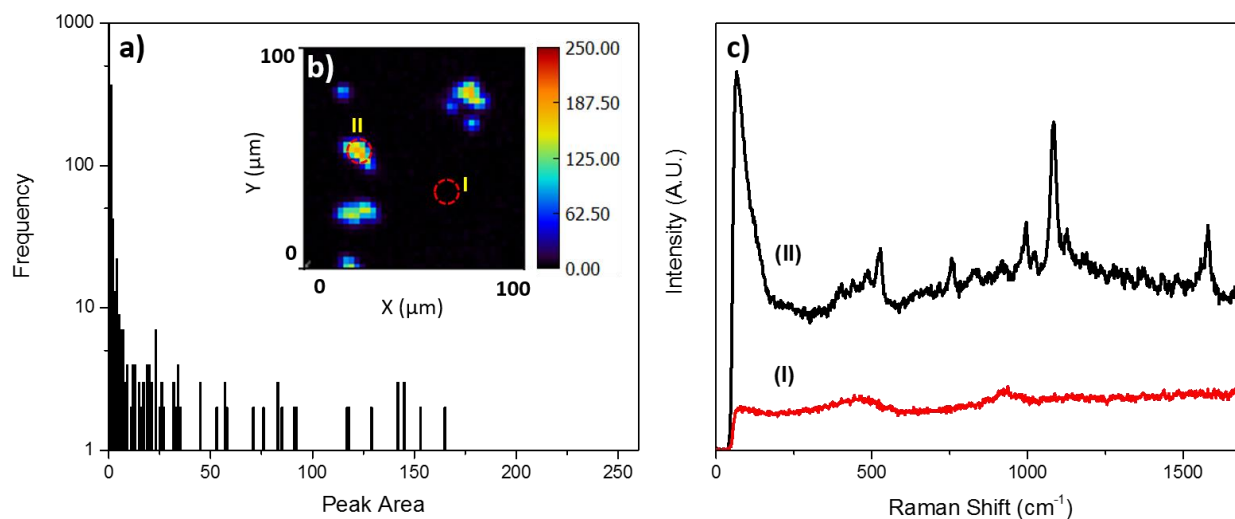


Figure 4.3.2 a) Representative histogram showing the SERS intensity distribution of 13 nm AuNPs assembled on M13 phage template. b) Corresponding SERS map of M13-templated Au assemblies used to plot the histogram. c) The SERS spectrums representing the background of the SERS map without hot spots (I) and the region of M13-templated Au assemblies with hot spots (II).

Thereafter, to acquire representative Raman intensity data from the dried droplet, a $100 \times 100 \mu\text{m}$ raster-scan in the center of the dry droplet was recorded, yielding a total of 1,600 Raman spectra for each sample. Statistical analysis of Raman intensity histograms obtained from this data were used to compare contrast enhancement of the different plasmonic and control samples (Figure 4.3.2).

4.3.1 SERS activity of M13-templated AuNP assemblies

In order to evaluate the SERS-activity of M13-templated AuNP assemblies, their Raman spectra were compared to those of isolated BSPP-stabilized AuNPs cast onto a microscope slide. BSPP is a common stabilizing agent for AuNP, which enables their controlled assembly on the phage, and will serve as Raman reporter herein. Figure 4.3.3a shows the Raman spectra of bulk (solid) BSPP and BSPP-passivated AuNPs (3 nm, 9 nm, and 13 nm diameters) cast onto a microscope slide.

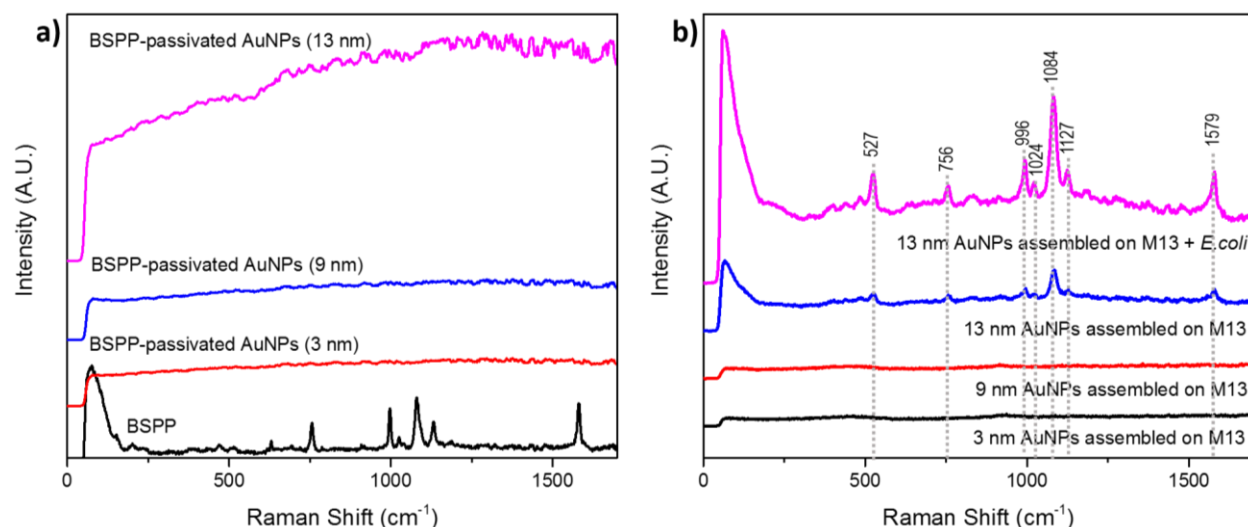


Figure 4.3.3 a) Representative Raman spectra of (bulk) BSPP (20x), and SERS spectra of BSPP adsorbed on 3–13 nm AuNPs (cast on microscope slide). b) Representative SERS spectra of M13-templated AuNP assemblies in the absence and presence of *E. coli* cell.

None of the peaks ascribed to the vibrational modes of BSPP were observed when adsorbed onto AuNPs. This was due to the small overall concentration of BSPP on the surface of the AuNPs (presumably a monolayer), and the fact that the diameters of the AuNPs employed in this work were too small to yield enhancement even when randomly aggregated (a process that can randomly generate hotspots). Indeed, it has been previously reported that SERS is highly-dependent on the size of AuNPs, as the particles smaller than 50 nm do not show any SERS signal in solution [299]. Higher SERS signals could be generated by employing particles with larger size [300], which produce larger local electromagnetic field enhancement

and which have larger surface area for adsorption, though this was not the focus of this study. For instance, it has been reported that 17 nm AuNPs are too small to produce sufficient enhancement to observe SERS peaks of Raman reporters such as 4-nitrothiophenol (4-NTP) or 4-aminothiophenol (4-ATP) upon their aggregation on glass slides [301]. In contrast, the Raman spectra of M13-templated AuNP assemblies (13 nm) displayed the characteristic peaks of BSPP (Figure 4.3.3b), and peaks associated with its aromatic ring (1579, 1084, 1024, 996, and 756 cm^{-1}) and sulfonate groups (1127 and 527 cm^{-1}) [30] were clearly visible compared to background noise. However, peaks from BPSS were not observed for the assemblies prepared with smaller AuNPs (3 or 9 nm). Because none of the individual AuNPs sufficiently promote SERS to observe the peaks of BSPP, the observation that the phage–AuNP assemblies do show BSPP peaks indicates that hotspots are indeed being created within the assemblies. More striking however is that it has been reported that aggregation of 14-nm AuNPs did not result in an increase of SERS signal [302]. Our results were also in agreement with this result. The size of AuNPs employed in this work (3 nm, 9 nm, and 13 nm) are comparatively small and did not generate any SERS signal upon their aggregation on glass slide during sample preparation. It is known that when the gap between the particles is smaller than 0.3 nm, new charge-transfer modes of light (tunneling) are observed, which push the electromagnetic field to the outside of the gap area and reduces the electromagnetic field enhancement [31, 32].

The Raman spectrum of M13–AuNP assemblies was also recorded after incubation with *E.coli* cells. Binding of the assemblies to bacterial cells did not produce any obvious change to the Raman spectrum in terms of number of observed peaks or their position (Figure 4.3.3b). This result suggest that SERS is generated within the gaps of the self-assembled AuNPs [33] and that the spectrum exhibits the fingerprint peaks of BSPP (located in these regions) rather than bacteria or other matrix proteins, which are outside these hot spots. As seen in Figure 4.3.4, the SERS signal intensities of M13–AuNP assemblies also remained unchanged after the interaction with *E.coli* cells which might therefore suggest that phage–AuNP assemblies maintain their SERS activity in the presence of bacterial cells and this feature might enable the use of phage–AuNP assemblies to probe their specific targets.

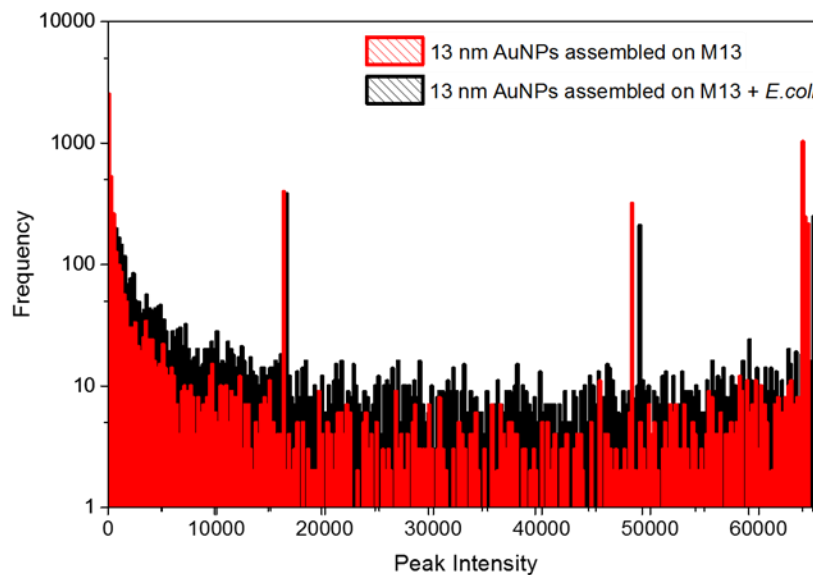


Figure 4.3.4 Histogram showing the SERS intensity distribution of 13 nm AuNPs assembled on M13 in the presence (black column) and in the absence of *E.coli* cell (red column).

The SERS enhancement factor for these assemblies alone (4.12×10^4) and with bacteria (4.79×10^4) were comparable to the values observed for metallic nanoparticles assembled on DNA-modified M13 phage. More-specifically, 20-nm AuNPs were coated with a silver shell having 10 nm thickness and assembled on M13 phage via DNA probes, yielding assemblies with an enhancement factor of 1.29×10^5 [167]. Thus, considering that the AuNPs here are substantially smaller, the observed enhancement is remarkable and emphasizes the importance of their spacing on the template. In fact, this result provides new perspectives for the design of SERS contrasts agents for use e.g., in the body, where smaller AuNPs are more easily eliminated with time once imaging is complete.

4.3.2 SERS-activity of T4-templated AuNP assemblies

Raman spectra were initially recorded for AuNP assemblies prepared with Cys-C and Cys-N. As shown in Figure 4.3.5a and Figure 4.3.5b, peaks characteristic of BSPP were observed only for assemblies prepared with 13-nm AuNPs. The addition of bacteria to these assemblies did not change the Raman spectra of the materials, in agreement with observations made above with M13 assemblies.

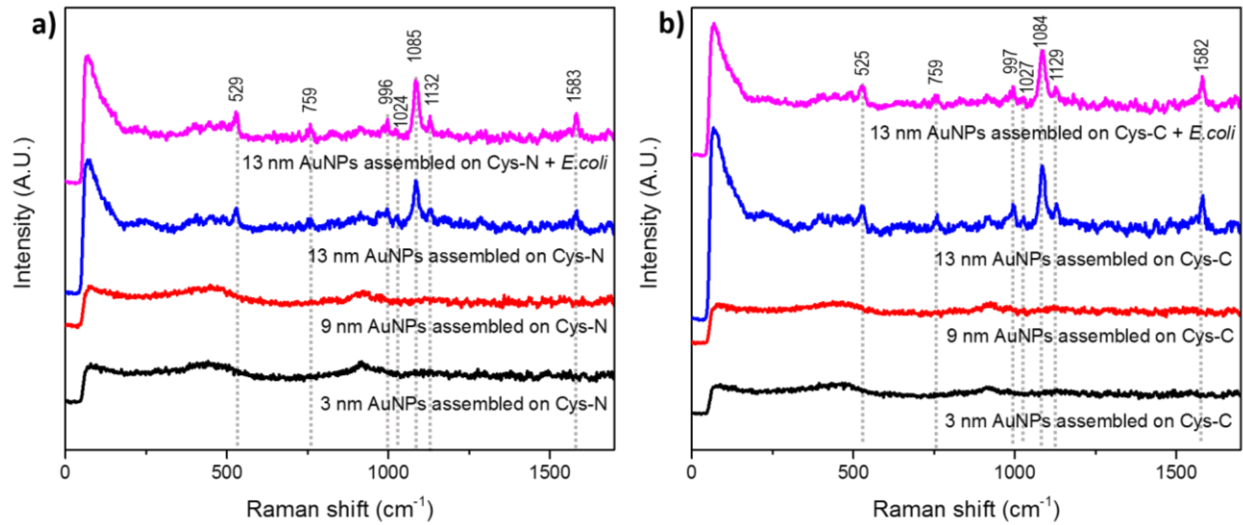


Figure 4.3.5 a) Representative SERS spectra of AuNPs assembled on Cys-N phage in the absence and presence of *E.coli* cell. b) Representative SERS spectra of AuNPs assembled on Cys-C phage in the absence and presence of *E.coli* cell.

Both assemblies prepared with Cys-C and Cys-N displayed SERS activity with enhancement factors estimated at 2.47×10^3 and 2.44×10^3 , respectively. The SERS signal intensities of the assemblies templated by these phage designs were compared by a one-way analysis of variance with statistical significance at $p < 0.05$. Analysis was performed employing the SERS maps constructed from the peak at $\sim 1085 \text{ cm}^{-1}$ and used to prepare the histograms to present average SERS intensity of the samples. It has been demonstrated that the average SERS intensities of Cys-C–AuNP assemblies was significantly higher than Cys-N–AuNP assemblies (Figure 4.3.6).

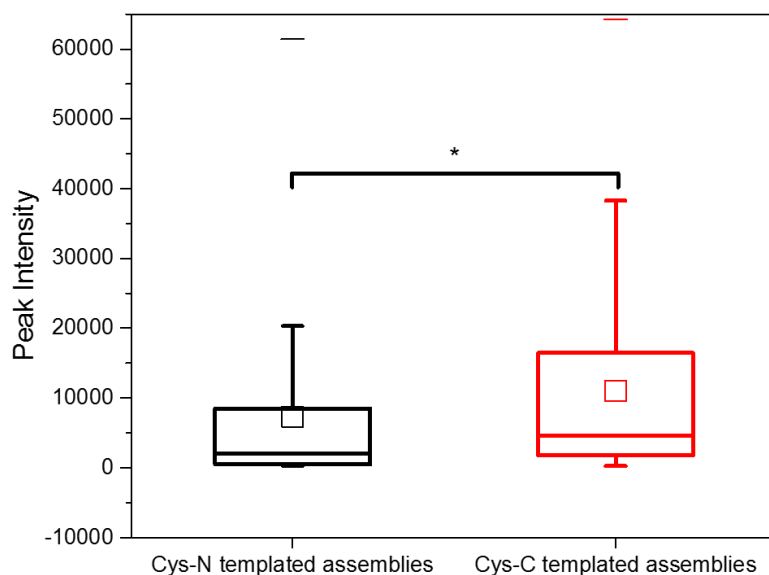


Figure 4.3.6 Representative distribution of SERS signal intensities of 13 nm AuNPs assembled on Cys-N (black) and Cys-C (red) templates. In each box, the top of the rectangle indicates the third quartile, a horizontal line near the middle of the rectangle indicates the median, and the bottom of the rectangle indicates the first quartile. The mean values and maximum values are represented by squares (\square) and lines (–) on the top, respectively. (* $P < 0.05$).

In fact, the binding moieties have slightly different disposition on the phage surface. For Cys-C, the binding moieties form trimeric junctions whereas Cys-N phage design results in dimeric junctions of gold binding moieties. Despite extensive testing, we were not able to observe intact T4 phage-templated AuNP assemblies by TEM. Images rather resembled phage templates partially covered with AuNPs, most probably due to the damage occurring during the drying step of sample preparation. It is important to note that TEM observations are performed under high vacuum with dried samples, which is very different than their colloidal form in solution. Under these circumstances, corresponding TEM images of phage-gold assemblies are far from presenting their actual states. Nonetheless, it was possible to use these images to estimate the distribution of AuNPs on T4 phage surface with respect to the disposition of Soc proteins on the phage capsid.

As illustrated below, it is known that the centers of adjacent Soc trimers are separated with a distance of $\sim 80 \text{ \AA}$ (Figure 4.3.7a) [213]. Moreover, the attachment of ring-shaped PA63 heptamer of anthrax toxin complex, with a diameter of 120 \AA , to the binding moieties displayed on N-terminal of Soc protein has been studied by cryo electron microscopy and provided useful information. Although protein structures have different degree of flexibility in comparison to rigid AuNPs, the disposition of PA63 heptamer on T4 capsid might provide us a platform to estimate the possible distribution of 13 nm AuNPs, which have a comparable size to PA63 heptamer.

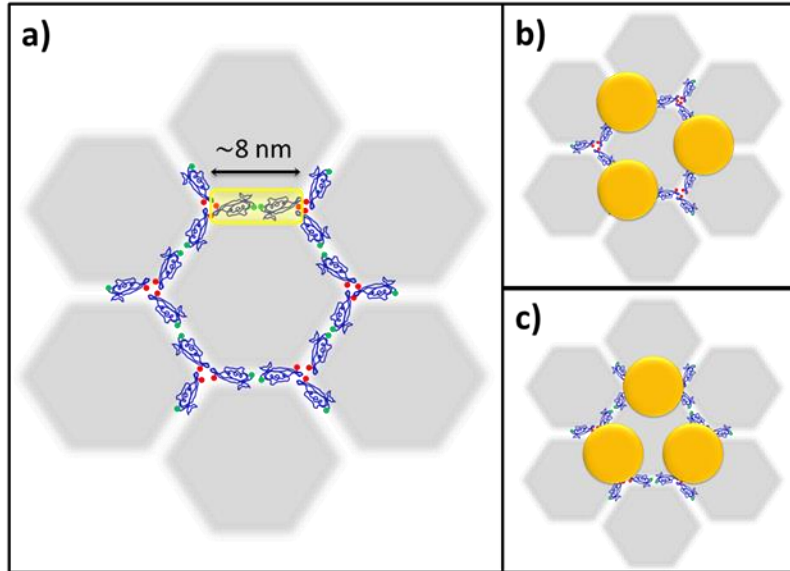


Figure 4.3.7 a) Schematic of T4 phage capsid structure showing the disposition of C- (red dot) and N-termini (green dot) of Soc protein (drawn in blue). The distance between the centers of two Soc trimeric junctions (~ 8 nm) is shown in yellow. **b)** Representative scheme showing the disposition of AuNPs centered on the Soc trimeric junctions. **c)** Representative image showing the disposition of AuNPs centered on the Soc dimeric junctions.

In this regard, the mentioned report suggests that for Cys-N the large diameter of AuNPs might result in a steric conflict for occupancy of each Soc dimeric junction by an AuNP. This would favor attachment of AuNPs randomly at positions centered on the trimeric junctions of Soc proteins (Figure 4.3.7b). However, it is important to mention that the spherical structure of AuNP is different than a ring shape structure, which might avoid interaction of AuNP with three dimeric junctions of Soc protein simultaneously. This feature might favor the disposition of AuNP centered on a single dimeric junction of Soc protein which will affect the total avidity of phage to AuNPs, as well as the spacing between them (Figure 4.3.7c). Furthermore, the angular positions of Soc proteins close to the 5-fold vertices of phage capsid would be different in comparison to the proteins in equatorial regions due to the difference in capsid curvature. Despite the fact that the steric hindrance might be the major limiting factor in distribution of AuNPs, the different angular positions of binding moieties might be also considered as another factor controlling the degree of occupancy. In case of Cys-C, similar factors would be involved in controlling the distribution of AuNPs on phage capsid. Consequently, the binding of AuNPs would occur through the binding moieties displayed on C-terminal of Soc protein, which are placed in the trimeric junctions. Similar to Cys-N, the disposition of AuNPs on Cys-C might change depending on how many AuNPs can fit to three Soc trimeric junctions. While the simultaneous binding of AuNPs to three Soc

trimeric junctions would result in a disposition as in Figure 4.3.7c, the disposition in Figure 4.3.7b would arise from the occupancy of a single trimeric junction in AuNP attachment.

It is obvious that the spacing between 13 nm AuNPs assembled on both Cys-N and Cys-C templates would be comparable to the spacing of 13 nm AuNPs assembled on M13 template (~3 nm). However, the AuNPs assembled on Cys-N and Cys-C phages showed relatively low SERS activities compared to the assemblies templated on M13 phage. The difference between the average SERS signal intensities of AuNPs assembled on each phage design was also demonstrated by statistical analysis (Figure 4.3.8). Indeed, the lower SERS activity of Cys-N/C-templated AuNP assemblies is due to the fact that, during the sample preparation, phage–AuNP assemblies are dried on glass slides and it is thought that drying step, as observed in TEM preparations, might destroy the assemblies. As a consequence, resulting SERS signals of Cys-N/C- templated AuNP assemblies might be considered as signals of destroyed assemblies instead of the signals of phage templates fully covered with AuNPs. In this regard, the results suggest that higher SERS activity of Cys-C–AuNP assemblies might be due to the higher numbers of hot spots remained after sample drying ,which might be an indication of stronger phage-gold binding affinity.

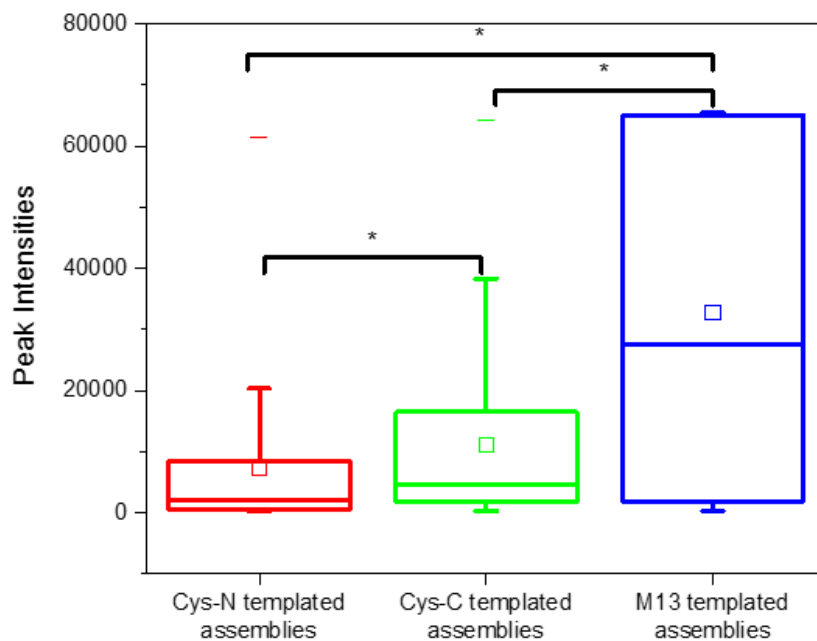


Figure 4.3.8 Representative distribution of SERS signal intensities of 13 nm AuNPs assembled on Cys-N (red), Cys-C (green), and M13 (blue) templates. In each box, the top of the rectangle indicates the third quartile, a horizontal line near the middle of the rectangle indicates the median, and the bottom of the rectangle indicates the first quartile. The mean values and maximum values are represented by squares (\square) and lines (–) on top of the rectangles, respectively. (* $P < 0.05$).

4.3.3 Effect of binding ligand

Because the anchoring chemistry between the phage and AuNP may affect the plasmonic properties of the AuNP as well as the surface available for BSPP adsorption, this parameter was varied in this section to examine how the phage–AuNP interface affects SERS. First, SERS activity was assessed for assemblies prepared from T4 displaying A3 peptide on Soc protein (A3-N and A3-C).

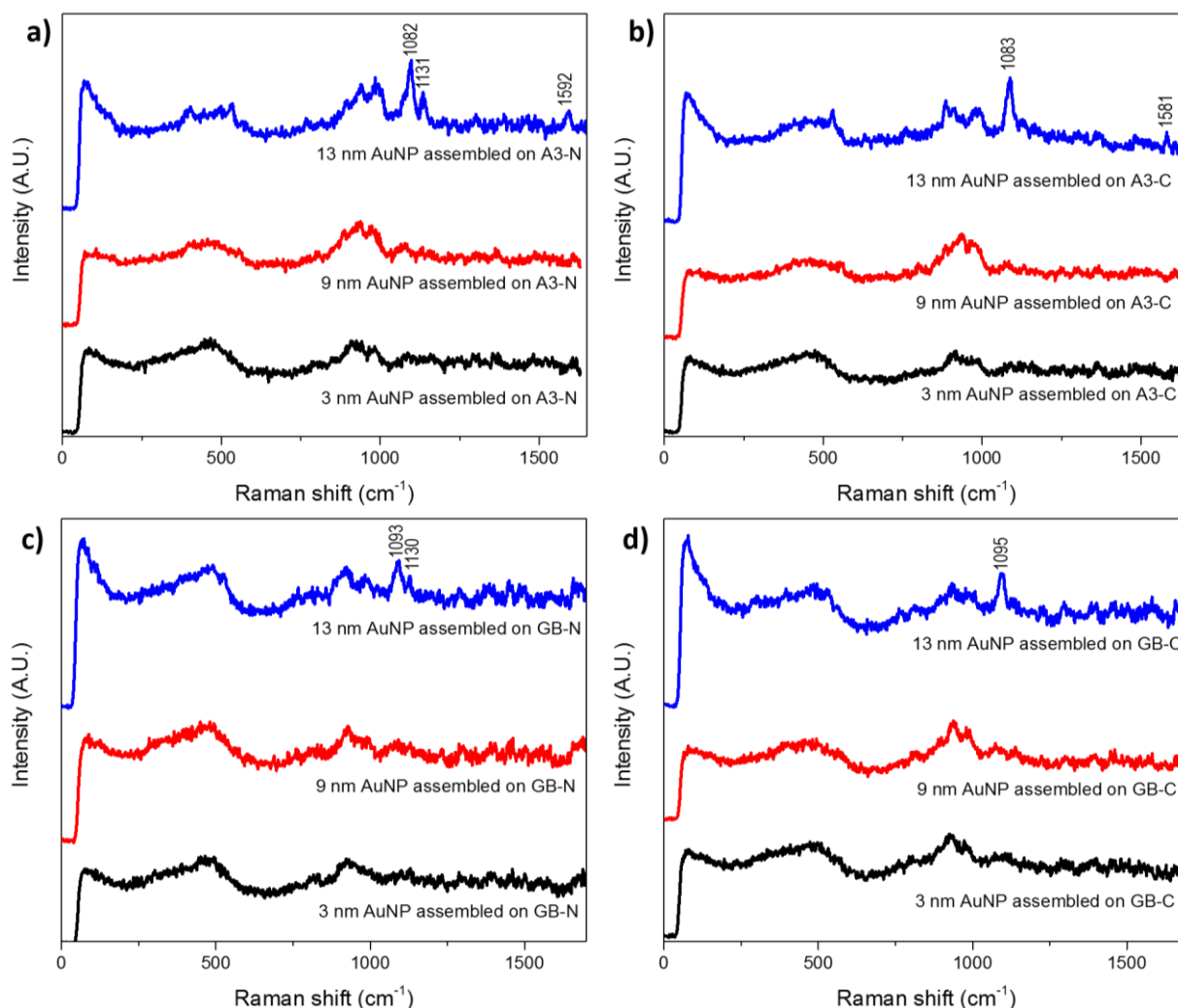


Figure 4.3.9 Representative SERS spectra of AuNPs assembled on A3-N phage (a), A3-C phage (b), GB-N phage (c), and GB-C phage (d).

As for Cys-C and Cys-N, SERS was only observed for 13-nm AuNPs. The resulting spectra displayed some features of BSPP (1592, 1131 and 1082 cm^{-1} for A3-N–AuNP assemblies, and 1582 and 1083 cm^{-1} for A3-C–AuNP assemblies), though the intensities of these peaks were very low (Figure 4.3.9a and 4.3.9b). Moreover, the Raman spectra lacked some peaks. Because the geometry and disposition of AuNPs are

expected to be the same as for Cys-N/C, respectively, this result suggests lower binding affinities of the phage towards AuNPs, leading to disassembly on the glass slide.

Second, AuNPs were assembled on phage templates displaying GB peptide (GB-C and GB-N phages), yielding assemblies with similar optical properties to A3. The Raman spectra of assemblies prepared with 13-nm AuNPs showed some features of BSPP (Figure 4.3.9c and 4.3.9d). Low binding affinity of GB peptide towards AuNPs may result in instability of the assemblies. Overall, despite the enhancement of some Raman peaks of BSPP using T4 displaying A3 or GB peptides, SERS signals in these samples were low compared to the other designs. Most probably, sample preparation for microscopy led to dissociation, indicating that these peptides are not suitable for preparing SERS-imaging contrast agents. It is worth mentioning that these two peptide sequences were identified in the literature using M13-phage display. Thus, their ability to bind AuNP may not be as high when displayed on T4 (herein), as this property may depend on their larger-scale arrangement on the phage (multiple peptides might be required for each AuNP). While A3 peptide was screened on p3 minor coat protein, GB peptide was screened on p8 major coat protein. It is known that the structures of the proteins on which the peptides are displayed can have a significant effect on the properties of the displayed peptide, which complicates the direct translation of these peptides to other display platforms, and which likely explains observations herein.

4.3.4 Chemical enhancement of SERS via graphitization of Reporter molecule

In the preceding section, the electromagnetic enhancement mechanism of SERS was examined. In this section, increasing laser power was exploited to graphitize BSPP within the hotspots, which, because of its high electron density, should produce a more intense Raman signal. In order to investigate this phenomenon, the Raman spectra of M13–AuNP assemblies (13 nm) were collected at different laser powers. The laser power was changed from 1.75 mW to 7.72 mW (after objective) by adjusting a neutral density filter placed between the laser and the microscope. As shown in Figure 4.3.10, increasing the laser power from 1.75 mW to 3.17 mW did not change the intensity or aspect of the Raman spectrum. However, at 7.72 mW, the intensity of the spectrum dramatically increased and was accompanied by a change in its shape. The change corresponded to the development of graphitic bands, known as the D and G bands of graphite. This phenomenon, called “graphitization”, occurs for carbon containing samples and is irreversible. As the Raman cross-section of graphite is large, the graphitic spectrum dominates the sample’s original spectrum and makes the identification of sample impossible [303].

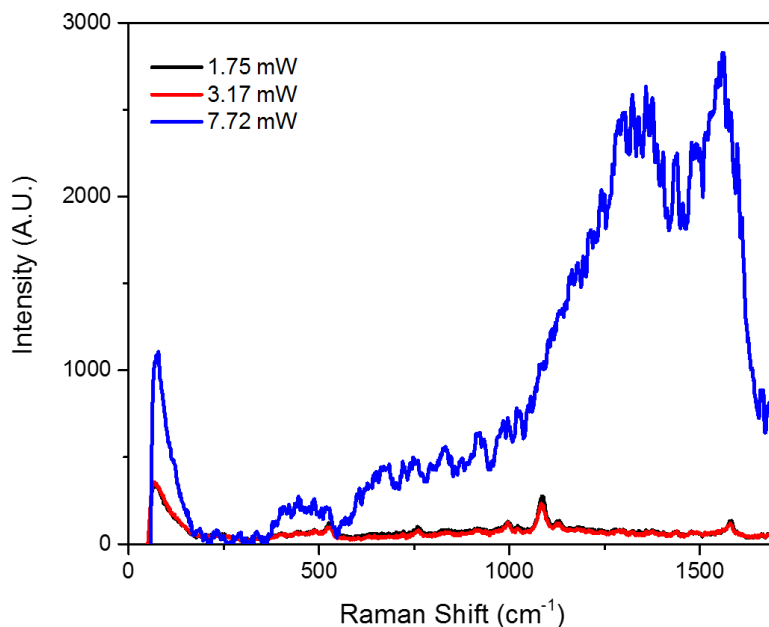


Figure 4.3.10 Representative SERS spectra of M13-templated AuNP assemblies at different laser powers demonstrating the effect of graphitization within the plasmonic hotspots.

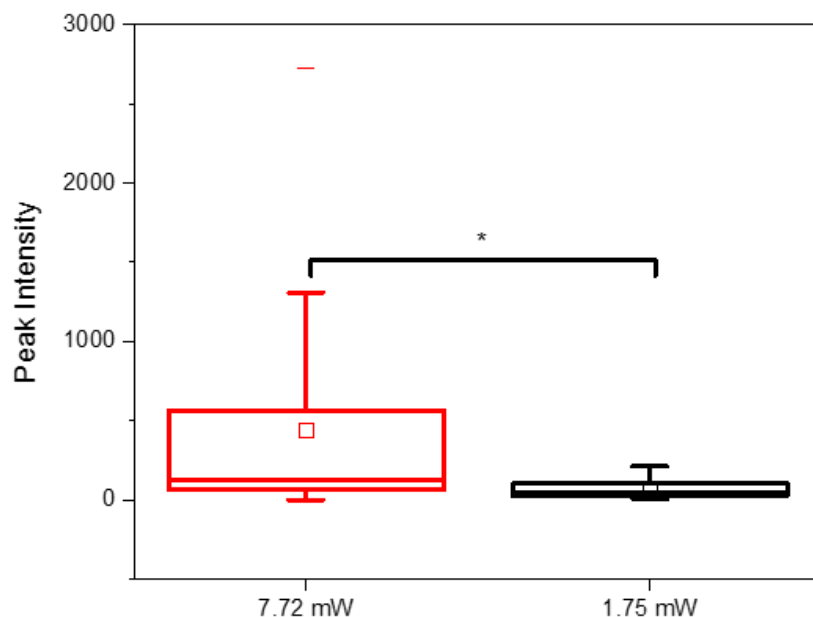


Figure 4.3.11 Representative distribution of SERS signal intensities recorded at high laser power (7.72 mW) and low laser power (1.75 mW) for 13 nm AuNPs assembled on M13 phage. In each box, the top of the rectangle indicates the third quartile, a horizontal line near the middle of the rectangle indicates the median, and the bottom of the rectangle indicates the first quartile. The mean values and maximum values are represented by squares (\square) and lines ($-$) on the top, respectively. (* $P < 0.05$).

In order to evaluate the effect of graphitization on sample's SERS signal intensity, one of the graphitic bands centered at $\sim 1560 \text{ cm}^{-1}$ (G band) was employed as reference peak to calculate the average SERS

signal intensity of the sample at high laser power and its intensity was compared with the reference BSPP peak centered at 1085 cm^{-1} . It has been shown that graphitization resulted in higher SERS signal intensities (438.1 a.u.) which was approximately six times higher than the SERS signal recorded at low laser powers (69.3 a.u.). The significance of the difference between the SERS signals was also determined by statistical analysis (Figure 4.3.11).

4.4 Conclusion

In this chapter, the SERS activity of phage–AuNP assemblies were investigated. It was shown that the assembly of 3 nm and 9 nm AuNPs on any given phage template did not produce sufficient enhancement (if any) to distinguish the spectrum from the control AuNPs alone. On the other hand, AuNPs with 13 nm diameter were found to create hot spots producing SERS enhancement of the spectrum of BSPP. Generation of hot spots between the AuNPs assembled on phage surface enabled the detection of the Raman reporter BSPP within the gaps. It is important to mention that none of the AuNPs used in this work showed SERS activity individually. Among all phage-templated AuNP assemblies, M13 showed the highest SERS activity.

Assemblies templated on T4, Cys-N, and Cys-C were the only designs that yielded stable assemblies with AuNPs. The two other gold-binding peptides on T4 phage (A3 and GB), had insufficient affinity towards AuNPs to stabilize the assemblies, resulting in lower (and less reproducible) signal enhancement. The enhancement factor calculated for M13–AuNP assemblies was higher than the enhancement factors determined for the assemblies templated by Cys-C or Cys-N. This difference could be explained with different spatial geometries provided by M13 and T4 phage templates for AuNP assembly, but was most likely a reflection of short-range ordering of AuNPs and overall stability of the assemblies. Although we did not observe phage–AuNP assemblies by microscopy after drying them on glass slides, TEM images of these phage designs clearly demonstrate their disassembly occurring during sample drying. M13 phage with flexible, thin, elongated structure is less affected from drying process than T4 phage with its icosahedral structure. Due to the drying process, dehydration of phage particles occurs which will change the structure of phage capsid as well as the position of gold-binding sites. Considering the angular positions of Soc proteins close to the 5-fold vertices of phage capsid, it is not surprising to observe the disassembly of phage–AuNP assemblies in sample preparation for SERS analysis.

It was interesting to observe that high laser powers resulted in “graphitization” of the sample, which manifested itself as the development of intense graphitic bands. Raman spectra recorded at high laser power (~7 mW) generated signals significantly larger than the SERS intensities recorded at low laser power (1.75 mW). Although graphitization results in irreversible damage to samples, which produces a loss of the peaks of the BSPP, higher SERS signals can be used to increase the sensitivity of sensing platforms at conditions that ensure specific capturing of the target molecules. Furthermore, because bulk BSPP is not affected by this laser power, graphitization is likely localized to the plasmonic hot spots and thus is consequently only a minor change to the overall chemical properties of the assemblies.

As previously demonstrated in Chapter 2, in addition to naturally recognizing bacterial, the minor coat protein of M13 phage can be easily modified to display peptide moieties to target different molecules, such as those over-expressed on the surface of e.g., cancer cells. Furthermore, as an example, the self-assembly of AuNPs on M13 did not affect the binding affinity of integrin-binding peptides displayed on the p3 coat protein. As a result, the phage–AuNP assemblies could be used as a contrast agents for Raman imaging, by displaying desired targeting ligand on p3 minor coat protein. Moreover, it has been demonstrated that SERS active materials can be generated using comparatively small AuNPs, which do not typically exhibit SERS activity individually. Thus, phage-templated SERS substrates could become more interesting for in vivo applications because small AuNPs, or serve as inspiration for the creation of other non-phage based plasmonic platforms. Furthermore, while described in the context of image contrast enhancement herein, similar principles are relevant for the use of such species as labels for bio-detection. AuNP size too big may interfere with this binding process, which is another advantage of having small AuNPs.

5 PHAGE-TEMPLATED AuNP ASSEMBLIES AS CONTRAST AGENT FOR NONLINEAR MICROSCOPY

5.1 Introduction

Optical microscopy is a fundamental tool for histological analysis of tissue, for characterizing populations of cells, and for quantitative analyses. In particular, the use of fluorescent contrast agents enables the discrimination of different types of cells within complex matrices, both in vitro and in vivo. Because fluorescence employs non-ionizing radiation, typically in the visible region of electromagnetic spectrum, it offers a margin of safety compared to other techniques such as e.g., x-ray computed tomography and positron emission tomography. In practice, the most common wavelengths used for exciting fluorescence are between 400–700 nm, and numerous fluorophores exist within this region. Unfortunately, biomolecules or naturally-occurring molecules are (or are composed of) chromo/fluorophores in the ultraviolet and visible regions (e.g., aromatic amino acid residues, nicotinamide adenine dinucleotide, flavins, lipofuscin, reticulin, hemoglobin, etc.). Absorption of light by these molecules reduces signal intensity, and fluorescence increases background noise. Moreover, light scattering contributes significantly to the background, and can reduce resolution or blur images, especially those taken deep within samples. For instance, tissue extraction and histological preparation can be employed to minimize the light scattering, though such approaches are not practical for imaging live tissues [304-306] and are not applicable for quantitative analyses. Due to these limitations, new fluorophores that can be excited in the near-infrared region (650–1000 nm) have been designed, and techniques for reducing background has been developed [307, 308]. For instance, confocal microscopy is an example of such a technique that achieves high resolution at depths of up to $\sim 100 \mu\text{m}$, due to elimination of background signal from out of the focal plane [309]. In addition, nonlinear optical microscopy, the imaging of nonlinear optical phenomena with a scanning microscope, is another solution to this multi-faceted problem [310]. The most widely-exploited optical process is the simultaneous multi-photon excitation of molecules (two or more photons) followed by a single photon emission with higher energy than the incident photons [311]. Of these, two-photon excitation fluorescence (2PEF) is the most widely known modality. Compared to fluorescence, nonlinear microscopy offers two major advantages [312]: photons generated in nonlinear processes have higher energies than the excitation photons. Consequently, longer wavelength light, which has greater penetration depth in tissues, can be used as excitation source [313]. In addition, the signal generated in nonlinear processes is proportional to the second or third power of the light intensity. As a consequence, only a very small spot within the focal

volume of the excitation source will produce a nonlinear process, thus eliminating out-of-focus excitation (i.e. background). This feature also makes nonlinear microscopy less sensitive to scattering, given that the density of background scattered photons will be too low to generate detectable signal and will not interfere with the signal of interest [314].

The absorption of two photons by an atom or molecule during a single quantum event was first predicted by Goepfert-Mayer in 1931. However, it was only confirmed experimentally in 1960, using pulsed ruby lasers [315]. Thereafter, two-photon excitation fluorescence was employed in molecular spectroscopy, and several molecules such as fluorescein, NADPH, flavoprotein, and naphthalene were studied [316-318]. Other important milestones were the development of commercially-available mode-locked femtosecond lasers and advances in laser scanning microscopy, which enabled 2PEF microscopy [319]. In the 90s, 2PEF was applied to fluorescence microscopy and its use in biology and neuroscience has increased steadily [320].

2PEF microscopy uses the principle of raster scanning, as in traditional confocal fluorescence microscopy. However, the differences in instrument design dramatically influence image quality. For instance, in a confocal microscope the fluorescent signal is excited by a tightly focused laser beam (providing x,y resolution), and a small pinhole blocks emission from outside of the focal plane (resolution along z)[321]. This detection geometry reduces background scattering and auto-fluorescence. On the other hand, in 2PEF microscopy, a focused femtosecond laser is used to excite the sample. Since the beam is concentrated in space (focusing) and in time (ultrafast), the signal is only generated within a very small region in the center of the focal spot, which significantly reduces background signal, obviates the need for a pinhole [312, 322], and reduces damage to sample. Because of the optical setup, all emitted photons (including scattered ones) are captured by the microscope objective and enhance the signal in thick samples. Furthermore, only a small volume of sample experiences the intense excitation source, which reduces photo-damage and photo-bleaching [323, 324]. Moreover, because near-infrared photons are typically employed to excite 2PEF better penetration depth due to their reduced scattering and reduced absorption are achieved [325]. In addition, photo-damage to living cells by UV light is also avoided in 2PEF, which enables long-term imaging of live preparations [326, 327]. With all these advantages, 2PEF microscopy has emerged as a promising modality for imaging in organs of living animals, including kidneys, eyes and brains, which can be examined in detail at imaging depths of up to 1 mm [328-330].

As a first step towards developing target-specific 2PEF contrast agents for imaging e.g., cell populations within tissues, this Chapter will first explore and optimize the 2PEF properties of phage–AuNP

assemblies. It has been previously demonstrated that gold nanoaggregates are good candidates as 2PEF probes due to the enhancement of 2PEF by strong local electric fields. In this manner, phage–AuNP assemblies are proposed herein as an alternative platform to form well-defined AuNP assemblies and investigate their performance as 2PEF contrast agent. M13 and T4 phages with their distinct structures and geometries provide two different templates for AuNP assembly, and provide control over the local and long-range order of the AuNPs. In addition to their ability to recognize their natural target bacteria, phage templates can be re-engineered to target a wide range of analytes. For this purpose, a more controlled model scenario is envisaged and in which the 2PEF intensity and robustness of the assemblies can be evaluated. As such, this Chapter will examine 2PEF signals emerging from samples drop cast and dried on microscope slides.

5.2 Materials and Methods

5.2.1 Materials

T4 phage host *Escherichia coli* B (HER1024) were obtained from the Felix d’Herelle Reference Center for Bacterial Viruses (Université Laval, Quebec). Recombinant T4 phages stocks, so-called Cys-N and Cys-C were used as they were prepared in Chapter 3. M13 phage host *Escherichia coli* strain ER2738 were obtained from New England Biolabs Inc. (Ontario). Recombinant M13 phage displaying gold binding moieties was used as it was prepared in Chapter 2. All chemicals were obtained from Bioshop (Ontario, Canada) unless otherwise noted. They were of the highest grade available and were used as received without further purification. All aqueous solutions were prepared with deionized distilled water obtained from a Milli-Q water purifying system (18 M Ω /cm).

5.2.2 Preparation of Bacterial Strains and Bacteriophages

Escherichia coli B (HER1024) stock cultures were maintained in 35% glycerol and were kept at –80 °C. To prepare fresh bacterial cultures, an inoculum from a frozen glycerol stock was streaked onto a Luria Bertani (LB) (Miller) agar plate and incubated at 37 °C overnight. A single colony from the plate was inoculated into 10 mL of LB broth (Miller) and incubated overnight at 37 °C with shaking at 200 rpm. The viable bacteria number was calculated by preparing serial dilutions of culture and plating on LB agar plates. After overnight incubation, the colonies formed on agar plates were counted to calculate bacteria

concentration, in the form of colony forming units (CFU). Prior to analysis, overnight bacterial suspensions were rinsed twice with distilled water, with centrifugation at 5000 rpm for 15 min after each rinse. The final cell pellet was suspended in phosphate buffer to reach 10^6 CFU/mL.

In order to prepare *Escherichia coli* strain ER2738, a glycerol culture of bacteria was streaked onto a LB agar plate supplemented with tetracycline (10 $\mu\text{g}/\text{mL}$) and incubated at 37 °C overnight. A culture for experiments was grown by inoculating 5 mL LB broth with a single colony from the plate and incubating overnight with shaking at 200 rpm at 37 °C. The next day, the viable bacteria number was calculated by preparing serial dilutions of culture and plating on LB agar plates. After overnight incubation, the colonies formed on agar plates were counted to calculate bacteria concentration as CFU. Similar to *Escherichia coli* B cell preparation, prior to analysis, overnight bacterial suspensions were rinsed twice with distilled water (?), with centrifugation after each wash, and diluted in phosphate buffer to reach 10^6 CFU/mL.

5.2.3 Hydrophobic Treatment of Glass Slides

Before the hydrophobic treatment, the glass slides were cleaned. Initially, the glass slides (0.13–0.16 mm; Ted Pella Inc., CA, USA) were put in a beaker containing acetone and left for 30 min in an ultrasonic bath. Afterwards, the slides were thoroughly rinsed with distilled water and dried in the oven (60°C). In the second step, the slides were submerged in piranha solution (30% H_2O_2 in concentrated H_2SO_4 (3:1; Sigma Aldrich, Canada; **Caution:** piranha solution is very corrosive) and left for 30 min. Finally, the slides were rinsed with distilled water and dried in an oven (60°C).

A solution of trichloro(1H,1H,2H,2H-perfluorooctyl)silane solution (Alfa Aesar, MA, USA) (~1 mM) was freshly prepared in 100 mL toluene (Sigma Aldrich, Canada) in a 150 mL glass beaker. Freshly cleaned glass slides were immersed in this solution, the beaker covered with parafilm, and then stored in a fume hood for 3 hours. Afterwards, the slides were removed and successively rinsed with toluene and absolute ethanol (Commercial Alcohols, ON, Canada). Finally, the slides were dried in the oven (60°C) and stored in a box till they were used.

5.2.4 Preparation of Phage-templated AuNP Assemblies for 2PEF Analysis

M13-templated AuNP assemblies

As described in chapter 2, the stock of recombinant M13 phage displaying gold-binding peptide was already PEG-purified and stored at 4°C in TBS solution (10^{12} PFU/mL). The stock solution of phage was diluted in 100 mM phosphate buffer to a concentration of 10^{10} PFU/mL. The self-assembly of 3-, 9-, and 13-nm AuNPs on M13 phage templates was performed in 1 mL of 25 mM phosphate buffer (pH 7.0) including 800 μ L of buffer solution, 100 μ L of diluted phage solution (10^{10} PFU/mL in phosphate buffer) and 100 μ L of nanoparticle stock solutions having concentrations of 2.8×10^{15} particle/mL, 5.7×10^{13} particle/mL, 3×10^{13} particle/mL for AuNPs with 3 nm, 9 nm and 13 nm diameters, respectively. After overnight incubation on a rotary shaker at room temperature, 100 μ L of the reaction solution was rinsed twice, with centrifugation at 3000 rpm for 5 min after each rinse. The pellet was suspended in 30 μ L of 25 mM phosphate buffer and a droplet of 3 μ L of this solution was pipetted onto the hydrophobic glass slides and left to dry at room temperature.

2PEF images of phage-templated AuNP assemblies were recorded in the absence and presence of bacterial cells. In order to prepare these samples, the phage–AuNP reaction solution was incubated overnight and 100 μ L of this solution was mixed with 1 mL of *Escherichia coli* ER2738 (10^6 CFU/mL in 25 mM phosphate buffer). After incubating the mixture for 1 h on a rotary shaker at room temperature, the solution was rinsed twice, with centrifugation at 3000 rpm for 5 min after each rinse. The collected pellet including bacteria/phage–AuNP assemblies was suspended in 30 μ L of 25 mM phosphate buffer and a droplet of 3 μ L of this solution was pipetted onto the hydrophobic glass slides and dried at room temperature.

T4-templated AuNP assemblies

The stocks of recombinant T4 phages (Cys-N, Cys-C, A3-N, A3-C, GB-N, and GB-C) were column-purified as described in Chapter 3 and stored at 4 °C in 100 mM phosphate buffer (10^{10} PFU/mL) until used. The self-assembly of 3-, 9-, and 13-nm AuNPs on T4 templates was performed in 1 mL of phosphate buffer (pH 7; 200 mM, 50 mM, and 25 mM, respectively). The reaction solutions were prepared by adding 100 μ L of phage stocks and 100 μ L of nanoparticle stock solution to 800 μ L of phosphate buffer. After 2 days incubation on a rotary shaker at room temperature, 100 μ L of the reaction solution was rinsed twice, with centrifugation at 3000 rpm for 5 min after each rinse. The pellet was suspended in 30 μ L of 25 mM phosphate buffer and a droplet of 3 μ L of this solution was pipetted onto the hydrophobic glass slides and left to dry at room temperature.

2PEF images of T4-templated AuNP assemblies were also recorded in the presence of bacterial cells. One mL of *Escherichia coli* B suspension in 25 mM phosphate buffer (10^6 CFU/mL) was mixed with 100 μ L of phage-AuNP reaction solution (aged for 2 days). The mixture was incubated for 15 min on a rotary shaker at room temperature, then the unbound AuNPs were removed from bacteria/phage-AuNP assembly complex by rinsing twice, with centrifugation at 3000 rpm for 5 min after each rinse. The pellet was suspended in 30 μ L of 25 mM phosphate buffer and a droplet of 3 μ L of this solution was pipetted onto the hydrophobic glass slides and dried at room temperature.

5.2.5 2PEF Microscopy of Samples on Glass Slides

The two-photon microscopy measurements were performed using a home-built optical system based on a laser scanning microscope (Till Photonics GmbH, Munich, Germany) equipped with a motorized XY stage (MLS203, Thorlabs). The pump beam provided by a titanium:sapphire oscillator (Tsunami, Spectra Physics, Santa Clara, USA) was used to generate \sim 180 femtosecond (fs) laser pulses with a central wavelength of 816.4 nm and a 80 MHz repetition rate. The fs laser beam was set to 15mW before being directed to the microscope and 8mW at focus. An Olympus UPlanSAPO 20X air immersion microscope objective with a numerical aperture of 0.8 was used to focus the light onto the sample. A telescope was used to increase the beam size to fill the back pupil of the objective, allowing to achieve an optimal spatial resolution of typically 600 nm (FWHM). The emission from the sample was collected using a condenser with a numerical aperture of 0.55, in the forward direction while the excitation laser was rejected by 380-700 nm filter (SEMRock, Rochester, NY, USA) and the wavelength of interest was selected by 661 ± 10 nm filter (SEMRock). 2PEF signal was detected using photomultiplier tubes (model R6357, Hamamatsu Corporation, New Jersey, USA) set at 700 V. The mapping area was $400 \times 400 \mu\text{m}^2$ with step size of 1 μm .

5.2.6 Quantification of 2PEF image signals

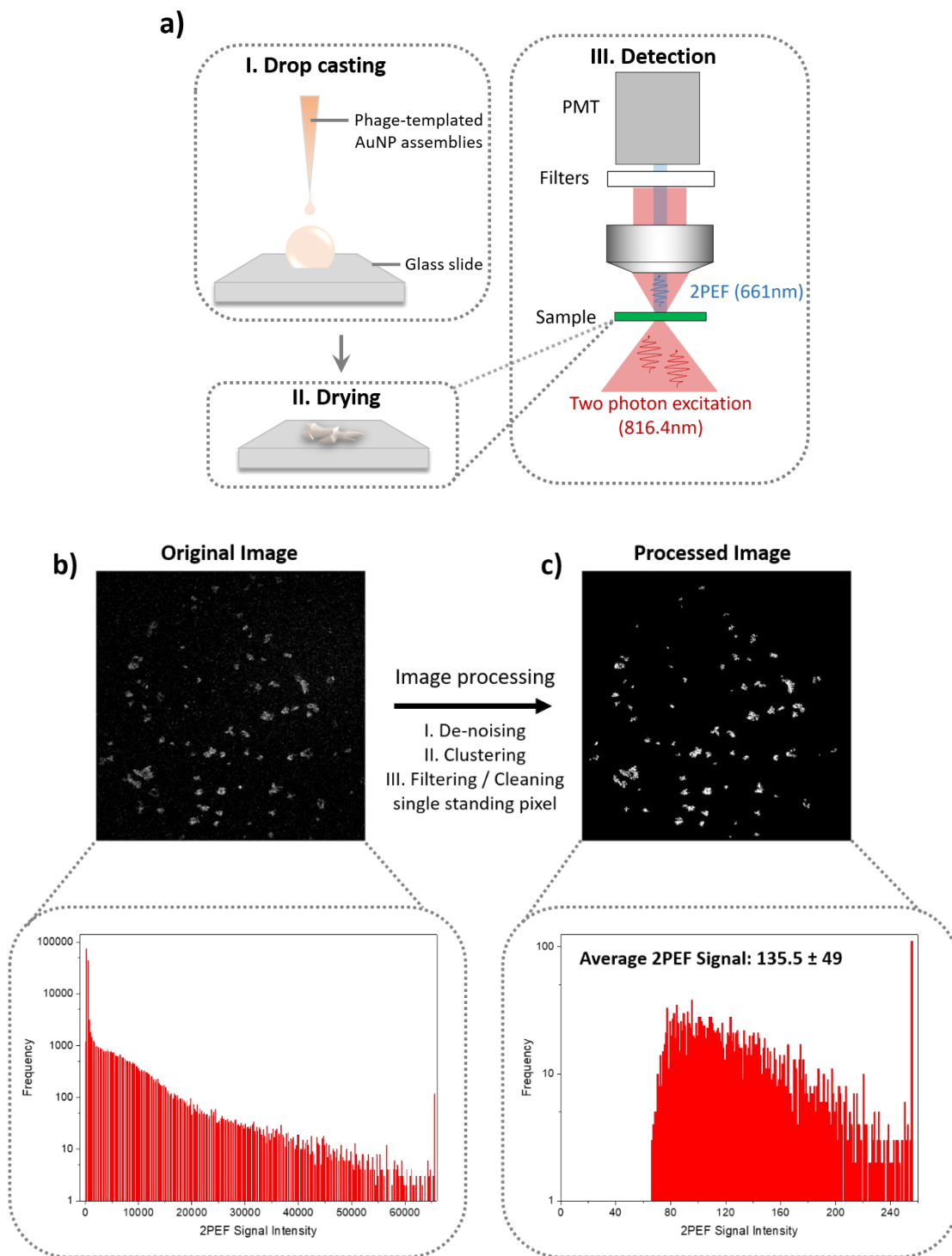
Quantification of 2PEF signals of images was performed by 2-step filtering and later k-means clustering to separate signal from the noise. Finally, very high intensity single-pixels (with no neighboring high intensity pixels) were removed. Image de-noising has been performed using Wiener filtering followed by 2-D bilateral filtering. Wiener filter performs 2-D adaptive noise-removal. It performs low pass filtering of an intensity image that has been corrupted by stationary additive noise [331] that is estimated based on statistics at a local neighborhood of each pixel. The bilateral filter is an edge-preserving nonlinear filter

that smooths a signal while preserving strong edges [332]. K-means separates the data into k groups (in our case 2) as such the sum of squares from points to the assigned cluster centers is minimized [333]. Briefly, the k-means algorithm is described as follows: 1) start with initial guesses for cluster centers, 2) for each data point, find closest cluster center, 3) replace each centroid by average of data points in its partition and 4) iterate step-1 and step-2 until stopping criteria met.

5.3 Results and Discussion

To evaluate 2PEF signal intensity and robustness of the assemblies, solutions of phage–AuNP assemblies (containing or not bacteria) were drop cast and dried on hydrophobic microscope slides. This process concentrates the otherwise very dilute solution into a small area on the slide, that can then be analyzed by 2PEF microscopy. This sample preparation will provide the essential background knowledge for the use of these new hybrid contrast agents for more complicated imaging experiments, beyond this thesis. Essentially, a drop of sample solution was cast onto a hydrophobic glass slide, which promotes the concentration of the sample at the center of the droplet during the drying process (Figure 5.3.1a). 2PEF images of the center of the dry droplet were acquired by scanning a $400 \times 400 \mu\text{m}$ area with a step size of $1 \mu\text{m}$, yielding 1,600 data-points for each sample.

Indeed, one of the key advantages of 2PEF versus other techniques, such as SERS, lies in imaging speed (~ 2 seconds for such an image). 2PEF signal intensity distributions were obtained by image processing to identify positive pixels from background noise, and remove isolated ‘hot’ pixels. The resulting histograms provide information on the average 2PEF intensity for a given sample, as well as the number of positive vs. negative pixels, which indirectly provides information on the robustness of the assemblies towards drying (Figure 5.3.1c).



5.3.1 2PEF of M13–AuNP assemblies

It is known that the efficiency of 2PEF of AuNPs depends on their level of aggregation. As such, 2PEF of isolated AuNPs were first compared to those of assembled on phage. As illustrated in Figure 5.3.2, representative histograms of processed data from isolated AuNPs were independent of size (3–13 nm) and corresponded to signal typically observed for background noise (Figure 5.2a-b-c). As such, isolated AuNPs (3–13 nm) were below the limit of detection, at least for this particular 2PEF system. This was also the case for M13–AuNP assemblies (3 nm). In contrast, M13–AuNP assemblies (9 and 13 nm) produced a signal that was substantially higher than the background, and increased with increasing AuNP size. The differences between assemblies prepared with 9 and 13 nm AuNPs were statistically significant, but small. The obtained results indicate that the threshold AuNP size for observing 2PEF enhancement for M13–AuNP assemblies lies somewhere between 3 nm and 9 nm. These values are quite small, considering that isolated AuNPs smaller than 40 nm typically do not exhibit 2PEF in solution (though can sometimes be observed when they are deposited on glass slides in an aggregated form) [334]. For the M13–AuNP assemblies (9 and 13 nm), the enhancement of 2PEF suggests formation of a plasmonic structure either due to short range or long range ordering of the AuNPs on M13. Indeed, the probability of the first intraband *sp-sp* transition during two photon excitation of the AuNP is related to the localized surface plasmon resonance of the particle. Due to the fact that the absorption cross-section of small spherical AuNPs at 816 nm is negligible, excitation of 2PEF at this wavelength is enabled only once the surface plasmon generates an absorption band at this wavelength. Inter-particle coupling is expected when the spacing between AuNPs is smaller than the particle's diameter, and is a crucial parameter to observe plasmon coupling, which is the case for 9 nm AuNP assemblies templated on M13 phage (~6.34 nm based on TEM analysis; Chapter 2).

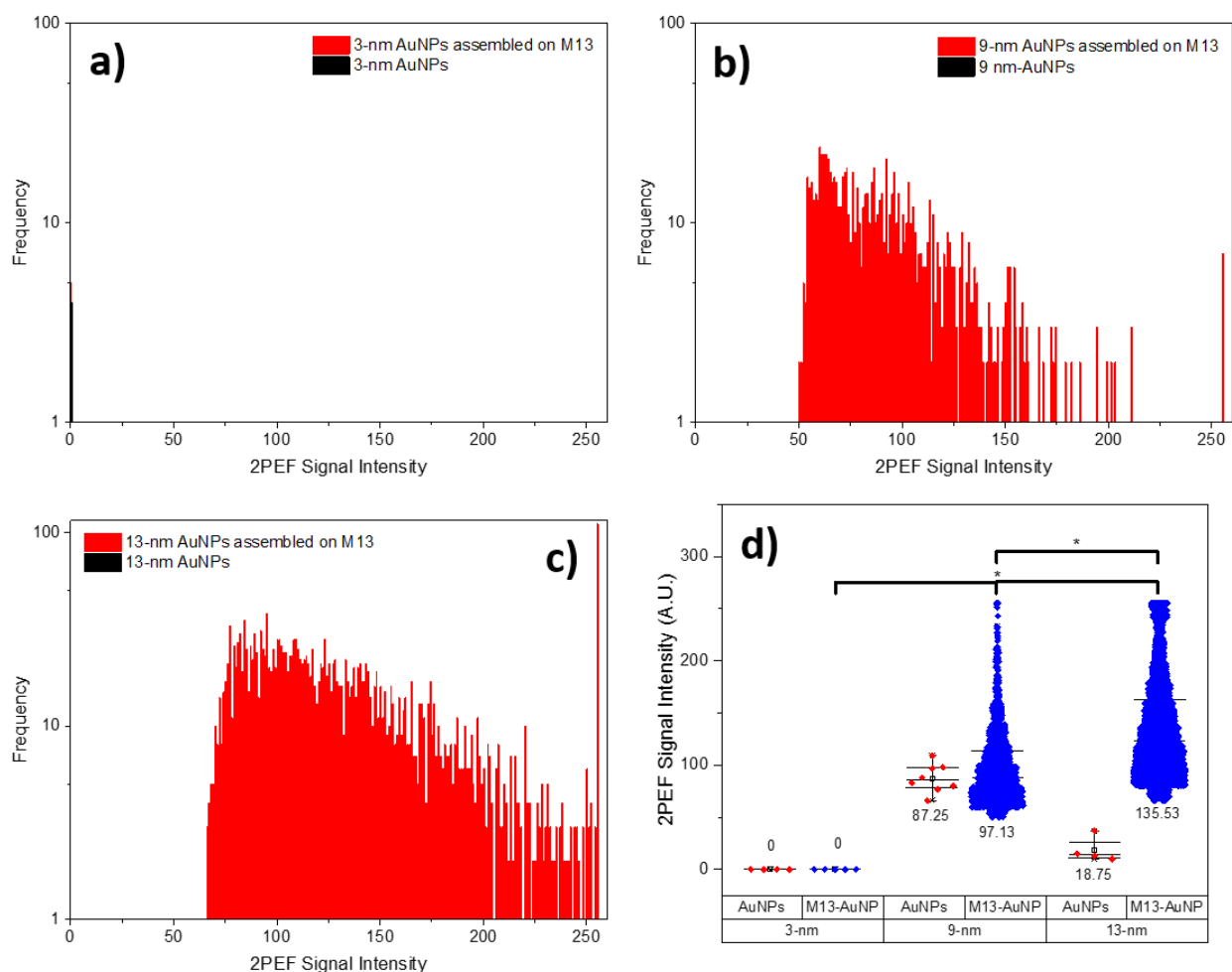


Figure 5.3.2 Representative 2PEF signal distribution histograms of isolated AuNPs and M13-templated AuNP assemblies with diameter of a) 3 nm, b) 9 nm, and c) 13 nm. d) The box chart plotted to compare the 2PEF signal intensities of isolated AuNPs with the 2PEF signal intensities of M13-templated AuNPs assemblies. In each box, the horizontal line on the top indicates the third quartile, a horizontal line near the middle indicates the median, and the horizontal line at the bottom indicates the first quartile. The blue and red diamonds overlapping with the boxes represent the entire data of the samples. The numerical values below each box indicate the mean value of the data set. (* $P < 0.05$).

Compared to the assemblies prepared with 9 nm AuNPs, higher 2PEF signal intensity was observed for those prepared with 13 nm AuNPs. The average 2PEF signal intensity of 13 nm AuNP assemblies was 135.53 A.U. where it was determined 97.13 A.U. for the assemblies prepared with 9 nm AuNPs (Figure 5.3.2d). This result is in agreement with data from the literature for which coupled 55 nm AuNPs produced higher 2PEF enhancement compared to aggregates of 20 nm AuNPs [335]. In this study, the coupling of AuNPs was induced by an oppositely charged polyelectrolyte, poly(diallyldimethylammonium chloride) (PDPA), and the 2PEF signals of the produced aggregates were recorded in solution. The resulting aggregates of 55 nm AuNPs had enhancement factor of 25-fold

whereas the aggregates of 20 nm AuNPs had 2PEF enhancement with factor of ~ 5 -fold. The size-dependent nature of 2PEF enhancement has been ascribed to the size-dependent electric field enhancement and size-dependent change in excitation wavelength. It is known that larger NPs have larger plasmon-induced electric-field, which creates stronger plasmon coupling and stronger electric field enhancements in their proximity. As a result of the strong plasmon coupling between the AuNPs, surface plasmons of the particles will be redshifted and result in an increase at the excitation wavelength (in the near infrared region), which will provide more intermediate states to induce two-photon excitation process.

In order to evaluate the effect of bacteria on the 2PEF intensity of M13–AuNP assemblies, images were acquired after incubating the assemblies with *E.coli* cells, which are the natural target of M13.

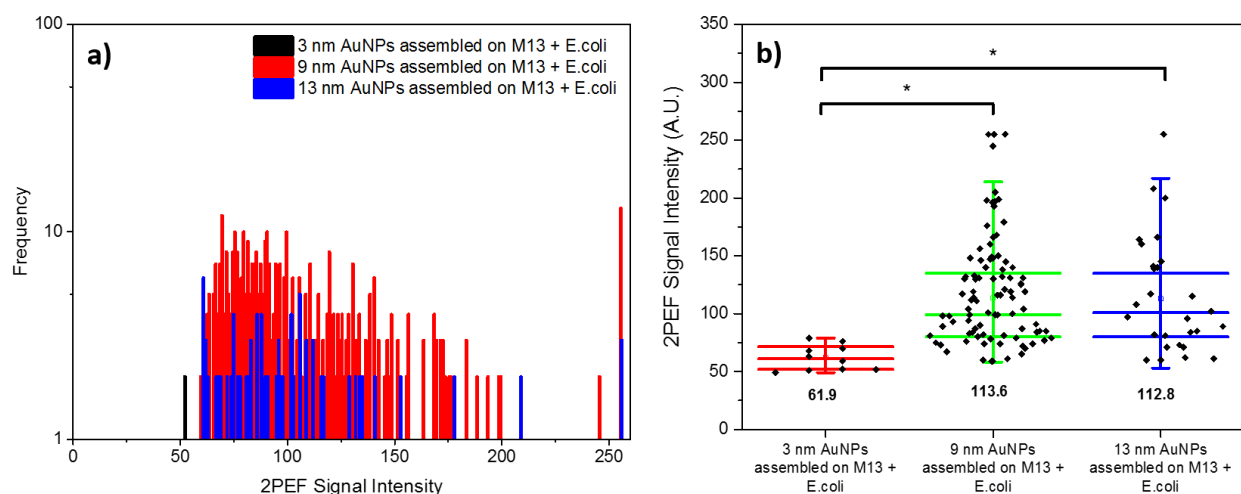


Figure 5.3.3 a) Representative 2PEF signal distribution histograms of M13-templated AuNP assemblies in the presence of *E.coli* cells. b) The box chart plotted to compare the 2PEF signal intensities of M13-templated AuNPs assemblies in the presence of *E.coli* cells. In each box, the horizontal line on the top indicates the third quartile, a horizontal line near the middle indicates the median, and the horizontal line at the bottom indicates the first quartile. The black diamonds overlapping with the boxes represent the entire data of the samples. The numerical values below each box indicate the mean value of the data set. (* $P < 0.05$).

Binding of the M13–AuNP assemblies to bacteria slightly affected the 2PEF signal intensity (Figure 5.3.3b). Quantitative analysis of the processed images revealed that assemblies prepared with 3 nm AuNPs revealed that the latter produced very few positive pixels, indicating that the average intensity of 2PEF for these assemblies, if occurring, falls largely in the regime of background noise. For M13–AuNP assemblies prepared with 9 nm and 13 nm AuNPs, the average 2PEF signal intensities of the processed images of these two samples were similar in the absence and presence of bacteria. Nevertheless, a slight increase of intensity was observed for assemblies prepared with 9 nm AuNP in the presence of bacteria.

Furthermore, the number of positive pixels for 13 nm assemblies declined, suggesting disassembly or that the 13 nm AuNPs pack effectively for 2PEF generation on M13. This observation might be due to dispersion of the assemblies which prevents contact-quenching of the assemblies that might occur in the absence of bacteria. In contrast, the average 2PEF signal of assemblies prepared with 13 nm AuNP decreased slightly in the presence of bacteria. Overall, this section demonstrates that selected M13–AuNP assemblies significantly enhance 2PEF to a level that is easily distinguishable from background, which is promising for their use as image contrast agents.

5.3.2 2PEF of T4-AuNP assemblies

In order to elucidate the influence of long-range ordering of AuNPs on 2PEF, assemblies were also templated on T4, for comparison with M13. In light of the poor relative stability of some assemblies of T4 templated AuNPs, as discussed in previous Chapters, only Cys-N and Cys-C designs were evaluated herein, as they produced the most stable assemblies. The other phage designs (A3-N, A3-C, GB-N, and GB-C) were not further investigated as they did not survive sample handling.

As shown in Figure 5.3.4, Cys-C-templated assemblies produced 2PEF signals intensities which were comparable, though slightly lower than those produced by the M13-templated assemblies. However, the number of positive signals for assemblies composed of 3 and 9 nm AuNPs was quite low, indicating that very few of the assemblies produce a positive signal. This either suggests that average 2PEF enhancement of these assemblies was either very low (equivalent to background signal), or that the assemblies dissociated during handling. In contrast, Cys-C assemblies produced with 13 nm AuNPs produced many positive pixels indicating that the assembly process reliably produced plasmonically-active assemblies. Moreover, the presence of bacteria had no effect on 2PEF signal intensity, except for assemblies prepared with 3 nm AuNPs, though the actual number of positive pixels was very small. Indeed, except for the assemblies prepared with 3 nm AuNPs, the difference between the average 2PEF intensity of Cys-C-templated AuNP assemblies, with/without *E.coli* cell, were not statistically significant. In general, the low signal intensities of Cys-C-templated assemblies might be due to the disposition of AuNPs on phage surface with inter-particle distance not favorable for strong plasmon coupling and 2PEF enhancement, correspondingly. As previously shown in Chapter 3, assemblies of 13 nm AuNPs templated on Cys-C phage were significantly affected from the drying step in sample preparation where the dehydration of phage particles resulted in disassembly of the assemblies. Therefore, the resulting 2PEF

emission of Cys-C templated assemblies might be concluded as the signal of remaining AuNPs assemblies after the sample was dropped cast on glass slides.

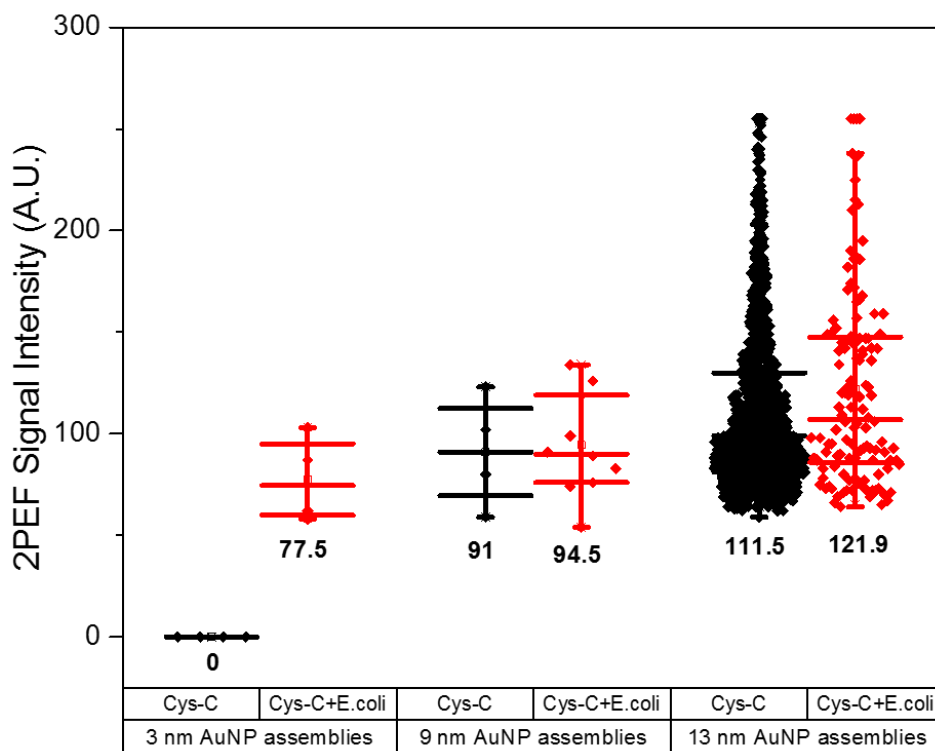


Figure 5.3.4 The box chart plotted to compare the 2PEF signal intensities of Cys-C-templated AuNPs assemblies in the absence and in the presence of *E.coli* cells. In each box, the horizontal line on top indicates the third quartile, a horizontal line near the middle indicates the median, and the horizontal line at the bottom indicates the first quartile. The black and red diamonds overlapping with the boxes represent the entire data of the samples. The numerical values below each box indicate the mean value of the data set. (* $P < 0.05$).

The 2PEF enhancement was also assessed for the assemblies prepared from Cys-N phage. As seen in Figure 5.3.5, assembly of AuNPs with different size (3 nm, 9 nm, and 13 nm) on Cys-N template did not result in structures with 2PEF distinguishable from the background. The histograms of AuNPs assembled on Cys-N phage had similar 2PEF signal intensity distribution, and interaction of *E.coli* cells did not change this situation. Indeed, as previously observed for Cys-C-templated assemblies, the few numbers of positive pixels suggests that Cys-N-templated assemblies do not exhibit 2PEF signals as the only detectable signal was the background noise of the images. It was interesting to observe that assembly of 13 nm AuNPs on Cys-N phage did not result in structures with 2PEF enhancement, in contrast to the observations made for 13 nm AuNPs assembled on Cys-C phage. This might be due to the fact that the binding moieties have slightly different disposition on Cys-N and Cys-C phage surfaces. For Cys-C, three cysteine residues come

together to form trimeric junctions with AuNPs, whereas only two cysteine residues come together on Cys-N to form dimeric junctions with AuNPs.

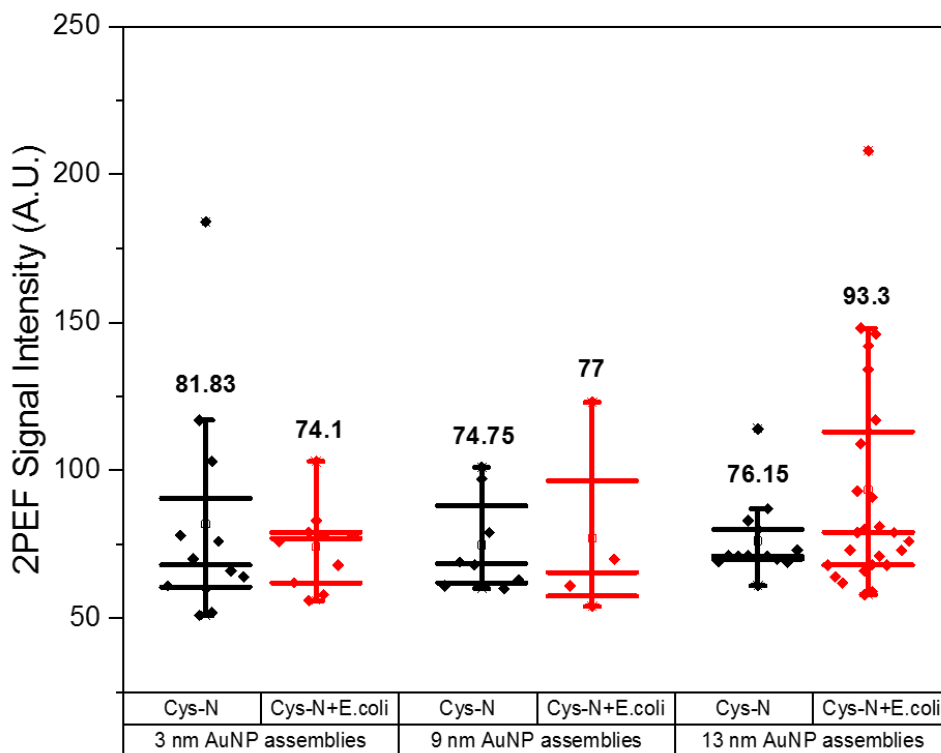


Figure 5.3.5 The box chart plotted to compare the 2PEF signal intensities of Cys-N-templated AuNPs assemblies in the absence and in the presence of *E.coli* cells. In each box, the horizontal line on top indicates the third quartile, a horizontal line near the middle indicates the median, and the horizontal line at the bottom indicates the first quartile. The black and red diamonds overlapping with the boxes represent the entire data of the samples. The numerical values below each box indicate the mean value of the data set. (*P<0.05).

Although, the disposition of AuNPs on these phage templates could not be visualized by electron microscopy, the relative distance between the binding sites on both T4 constructs is similar (~3 nm), which is smaller than the expected separation of binding sites on M13 phage. This could explain differences observed between the two phage platforms with regards to 2PEF intensity versus AuNP size. However, the lower number of positive pixels observed for T4 vs M13 suggests lower stability of the assemblies formed with the former. In this regard, the results suggest that Cys-C template might more strongly bind AuNPs than Cys-N, because of the greater number of thiols available per AuNP.

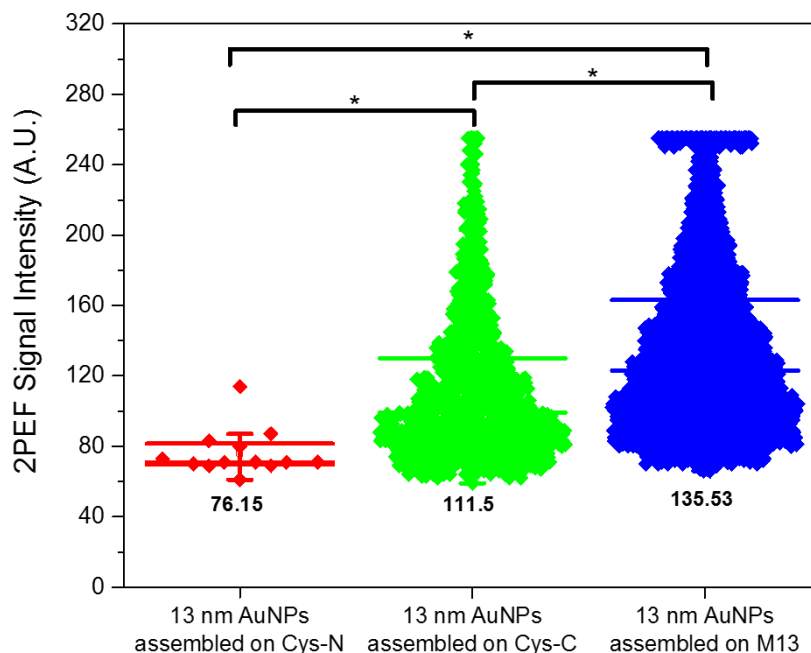


Figure 5.3.6 The box chart plotted to compare the 2PEF signal intensities of AuNPs assembled on Cys-N, Cys-C and M13 phages. In each box, the horizontal line on top indicates the third quartile, a horizontal line near the middle indicates the median, and the horizontal line at the bottom indicates the first quartile. The red, green and blue diamonds overlapping with the boxes represent the entire data of the samples. The numerical values below each box indicate the mean value of the data set. (* $P < 0.05$).

5.3.3 Comparison to other 2PEF contrast agents

The most widely used fluorophores exploited in 2PEF microscopy are either endogenous biomolecules or synthetic molecules used to label molecules. Endogenous 2PEF fluorophores include tryptophan and tyrosine residues in proteins, phycoerythrin protein of algae, serotonin, nicotinamides, and green fluorescent protein (GFP) [336-341]. Although, these biomolecules enable the non-invasive study of biological processes under physiological conditions, their overall abundance is limited in biological systems and their 2PEF intensity is generally low. Therefore, a variety of commercially available one-photon excitable fluorophores have been investigated as external 2PEF probes by screening their two-photon absorption cross sections. Rhodamine was one of the earliest fluorophores studied, and was followed by fluorescein, coumarin, and DAPI dyes [342]. As one-photon excitation and two-photon excitation have different selection rules, these commercial probes mostly exhibit low two-photon absorption cross sections, which limits their use in 2PEF microscopy. Moreover, those with relatively higher cross sections (e.g., rhodamine) suffer from low photo-stability [343]. As such, the development of fluorophores with better two-photon absorption properties is an exciting area of research that will enable

the use of lower intensity lasers, which will reduce the potential for photo-damage. Moreover, the fluorophores with sufficiently high two-photon cross-sections might exhibit 2PEM with common continuous wave lasers, thus reducing the cost of imaging system [344]. Research in this area has generated several fluorescent probes with two-photon absorption cross sections ca. two orders of magnitude larger than those of most common one-photon fluorophores [345]. Nevertheless, combining efficient 2PEF with other important physical characteristics, such as water-solubility, biocompatibility, ease of chemical modification, etc. still remains challenging [346].

As an alternative to organic 2PEF contrast agents, various other materials such as graphene (and its derivatives), up-converting nanoparticles, carbon dots, semiconductor nanocrystals, and metallic (silver and gold) nanoparticles have been studied and demonstrate excellent performance [347-353]. The most important advantages of these materials over organic dyes are their large two-photon absorption cross-section and high photo-stability. In particular, due to their favorable properties for biomedical applications (stability, easily modified surface chemistry, highly controllable shape and size), gold nanostructures have attracted great attention and have been extensively studied as contrast agents for 2PEF. The mechanism of 2PEF in gold nanostructures is based on radiative recombination of excited electrons in the *sp*-conduction band with holes in the *d*-band, as a result of the sequential absorption of two photons [354]. More specifically, during the excitation of gold nanostructures by femtosecond lasers, absorption of the first photon creates an intra-band transition in the *sp*-band leaving a hole in the *sp*-band below the Fermi level. Upon absorption of the second photon, an inter-band transition occurs that excites an electron from the *d*-band to recombine with the hole in the *sp*-band, which leaves a hole in the *d*-band. Thereafter, these electron-hole pairs recombine and produce the emission of a photon with higher energy than the separate excitation photons. While 2PEF is weak for bulk gold, gold nanostructures produce strong local electric fields that enhance 2PEF. The presence of enhanced local electric fields increases the probability of the first intra-band *sp-sp* transition, resulting in enhanced radiative recombination rates [10, 355] It is well known that the local electromagnetic fields around gold nanostructures can be enhanced when the frequency of the incident light is resonant with its surface plasmon. Therefore, structures with an SPR band in near infrared region can be conveniently excited by femtosecond lasers with appropriate wavelength [356]. In this manner, gold nanostructures whose plasmon modes are resonant at near-infrared frequencies such as nanorods, nanotriangles, nanobranched, nanowires, and nanoaggregates have been demonstrated to be good candidates as 2PEF probes [357-360]. In particular, aggregated AuNPs have been studied because of their significantly enhanced 2PEF signal compared to non-aggregated nanoparticles. While current research is focused on understanding the fundamental

mechanism of aggregation-induced 2PEF, several techniques have been employed to create better defined aggregates of gold nanoparticle. These include top-down nanofabrication techniques, drying induced random aggregation, and chemically induced controlled aggregates (ca. cysteine, poly(diallyldimethylammonium chloride), polymers, DNA, and peptides) [10, 335, 360-364].

5.4 Conclusion

In this chapter, M13 and T4 phage particles were proposed as template materials for the assembly of AuNPs to create structures with enhanced 2PEF emissions. The results demonstrate that several of the phage–AuNP assemblies survive the drying step on the microscope slides, which would be important for e.g., analysis of low concentration of bacteria in drinking water. Moreover, the influence of several design parameters on 2PEF intensity were established. It was shown that isolated AuNPs of the sizes employed (3–13 nm) do not exhibit 2PEF emission on their own. Upon their assembly on M13 phage, reproducible 2PEF enhancement was observed only AuNPs with 9 and 13 nm diameters. Only a small effect of AuNP size was observed, within the range of sizes examined. In contrast, assemblies prepared with T4 typically did not exhibit 2PEF and signals were only rarely distinguishable from the background. Nevertheless, Cys-C–AuNP assemblies (13 nm) produced reliable 2PEF signal, which was comparable in magnitude albeit slightly lower than that observed for equivalent assemblies prepared with M13. This difference could be explained with different spatial geometries of AuNP assemblies templated on M13 and T4 phages and their corresponding stabilities. The elongated and thin structure of M13 phage provides a flexible template material for AuNP assembly and enhance their stability against dehydration occurring at sample preparation. These results are most likely explained by a lack of stability of the assemblies. Indeed, it has been already shown that AuNP assemblies templated on Cys-C phage are not sufficiently stable to remain intact during the drying step of sample preparation.

This work sets the stage for the use of phage–AuNP assemblies for quantitative analyses of bacteria in drinking water. Moreover, phage–AuNP assemblies can be engineered to target specific molecules, which could also enable their use of imaging biological structures by 2PEF. From a more fundamental point of view, it would now be timely to address challenges associated with the study of 2PEF of the phage–AuNPs in solution, so as to better correlate structural features with 2PEF assembly, assisted by simulation. Finally, while 2PEF was examined here, the phage–AuNP may enhance the contrast for other nonlinear processes, such as optical harmonic generation, which occurs as a result of

simultaneous scattering of two or more photons by materials followed by emission of one photon with energy exactly equal to the sum of the excitation photons [365]. This type of nonlinear interaction is known as Second Harmonic Generation (SHG) or Third Harmonic Generation (THG) microscopies. Coherent Anti-Stokes Raman scattering (CARS) is yet another nonlinear optical process that generates contrast based on the Raman-active vibrational modes of the molecules. This technique employs two synchronized laser pulses to stimulate anti-Stokes Raman scattering. CARS microscopy is one of the most complex modalities used for nonlinear imaging and, although it pre-dates the other modalities above, has only recently seen a resurgence due to advances in laser technology [366].

6 CONCLUSION AND FUTURE WORK

6.1 Most significant findings and contribution to the advancement of knowledge

The most significant finding of this thesis is that very small AuNPs assembled on bacteriophage possess key features that are essential for their use as selective imaging contrast agents for SERS and 2PEF, in terms of signal enhancement, stability to sample handling, and ability to bind to a specific target. Compared to other systems that exist in the literature, the use of very small AuNPs (≥ 13 nm for SERS and $\geq 9-13$ nm for 2PEF) is advantageous because of they did not interfere with target binding, which is necessary for labeling specific biological targets. Furthermore, individual 'isolated' AuNPs of this size are much too small to produce a signal in SERS or 2PEF, which eliminates a possible source of background noise coming from assembly degradation. As such, the findings reported herein are original and contribute to the advancement of knowledge in an important area in which there is little data. This finding could be made on the basis of several additional important new findings and contributions to the advancement of knowledge established in this thesis. Namely, the

1) Establishment of experimental conditions for the assembly of very small AuNPs on bacteriophage.

2) Establishment of the effect of conjugation chemistry (disposition and type of AuNP binding moiety) on the stability of phage–AuNP assemblies.

3) The use of image processing tools to quantitatively analyze large amounts of data.

4) Analysis of the effect of inter-particle distance of AuNPs on plasmonic properties, achieved by varying the disposition of binding sites bacteriophage.

5) Analysis of the effect of long-range ordering of the AuNPs on plasmonic properties, using two bacteriophage with very different structures.

As a whole, the findings above rest on the analysis of a library of more than 21 unique phage–AuNP assemblies (prepared by permutation of phage type, conjugation chemistry, and AuNP size) analyzed by two different spectroscopic modalities. This provides some basis for generalizing the guidelines established above for future phage-templated AuNP assemblies. While the specific conclusions and guidelines have been discussed and presented in each relevant Chapter, overall, this thesis can conclude that specific assemblies, namely M13 and Cys-C, have been identified from this body of work as having

properties suitable for more complex analyses of their qualitative (i.e., imaging) and quantitative performance (i.e., bio-detection) in a variety of applications.

6.2 Future directions

The scientific content of this thesis sets the stage for future experiments, which can now be performed because of the refinement of the large library of phage–AuNP assemblies above. For instance, one major limitation of this work was the lack of stability of several phage–AuNP assemblies towards drying during sample preparation, which reduced the breadth of the conclusions that was expected to be established from the designed library. Unfortunately, analysis of the plasmonic properties of the assemblies in solution was technically challenging due to the high level of dilution, though solutions to this issue can be foreseen. Access to the SERS/2PEF properties of these meta-stable assemblies, possibly as a function of AuNP grafting density, would provide an additional dataset that could more readily be compared with plasmonic simulations. In addition, other non-linear spectroscopic modalities such as second harmonic generation or coherent anti-Stokes Raman scattering are accessible via minor modifications to the 2PEF system used, and would provide a more general view on the plasmonic properties of the assemblies for several techniques. Indeed, little or no data is currently available on the use of these techniques for the analysis of such samples.

Access to additional data and methodologies for analyzing the optical properties of the assemblies in their colloidal form (i.e., in solution), will in turn enable their analysis in more complex matrices. For instance, the quantitative signal from the assemblies could be exploited for the detection of bacteria in aqueous matrices such as drinking water/milk (or other). Furthermore, because capsid proteins not involved in AuNP-binding can be engineered to display targeting moieties for many other targets of biological significance, exploring their use as contrast agents within e.g., mixtures of cell populations would be interesting.

Finally, an unexpected observation was made in this thesis that warrants additional investigation. More specifically, in Chapter 2, M13–AuNP assemblies were analyzed by Enzyme-Linked Immunoassay for the ability of the phages to retain their targeting ability despite the presence of AuNP on their surface. In this assay, an anti-M13–[Horseradish peroxidase] conjugate was used as secondary antibody for quantification of the amount of target-bound assemblies. When the enzymatic substrate for Horseradish peroxidase was added to the sample wells, a dramatic enhancement of catalytic activity was observed

when AuNPs were bound to the phage. Indeed, while the enhancement of catalytic activity of some enzymes can be enhanced by adsorption to AuNPs, the observed enhancements are typically 2–4-fold [34–36]. The enhancement observed herein, 50–100-fold, is remarkable and may potentially be ascribed to facilitated electron transfer via plasmonic effects. As such, investigation of the underlying mechanism of this phenomenon as well as its potential applications are clearly of importance.

7 REFERENCES

1. Stewart, M.E., et al., *Nanostructured Plasmonic Sensors*. Chemical Reviews, 2008. **108**(2): p. 494-521.
2. Ghosh, S.K. and T. Pal, *Interparticle Coupling Effect on the Surface Plasmon Resonance of Gold Nanoparticles: From Theory to Applications*. Chemical Reviews, 2007. **107**(11): p. 4797-4862.
3. Petryayeva, E. and U.J. Krull, *Localized surface plasmon resonance: Nanostructures, bioassays and biosensing—A review*. Analytica Chimica Acta, 2011. **706**(1): p. 8-24.
4. Nath, N. and A. Chilkoti, *A Colorimetric Gold Nanoparticle Sensor To Interrogate Biomolecular Interactions in Real Time on a Surface*. Analytical Chemistry, 2002. **74**(3): p. 504-509.
5. Copland, J.A., et al., *Bioconjugated gold nanoparticles as a molecular based contrast agent: implications for imaging of deep tumors using optoacoustic tomography*. Molecular Imaging & Biology, 2004. **6**(5): p. 341-349.
6. Ding, H., et al., *Gold Nanorods Coated with Multilayer Polyelectrolyte as Contrast Agents for Multimodal Imaging*. The Journal of Physical Chemistry C, 2007. **111**(34): p. 12552-12557.
7. Huang, X., et al., *Plasmonic photothermal therapy (PPTT) using gold nanoparticles*. Lasers in Medical Science, 2007. **23**(3): p. 217.
8. Shanmukh, S., et al., *Rapid and Sensitive Detection of Respiratory Virus Molecular Signatures Using a Silver Nanorod Array SERS Substrate*. Nano Letters, 2006. **6**(11): p. 2630-2636.
9. Ming, T., et al., *Strong Polarization Dependence of Plasmon-Enhanced Fluorescence on Single Gold Nanorods*. Nano Letters, 2009. **9**(11): p. 3896-3903.
10. Guan, Z., L. Polavarapu, and Q.-H. Xu, *Enhanced Two-Photon Emission in Coupled Metal Nanoparticles Induced by Conjugated Polymers*. Langmuir, 2010. **26**(23): p. 18020-18023.
11. Stockman, M.I., et al., *Enhanced Second-Harmonic Generation by Metal Surfaces with Nanoscale Roughness: Nanoscale Dephasing, Depolarization, and Correlations*. Physical Review Letters, 2004. **92**(5): p. 057402.
12. Hou, W. and S.B. Cronin, *A Review of Surface Plasmon Resonance-Enhanced Photocatalysis*. Advanced Functional Materials, 2013. **23**(13): p. 1612-1619.
13. Mieszawska, A.J., et al., *Multifunctional Gold Nanoparticles for Diagnosis and Therapy of Disease*. Molecular Pharmaceutics, 2013. **10**(3): p. 831-847.
14. Huang, X. and M.A. El-Sayed, *Gold nanoparticles: Optical properties and implementations in cancer diagnosis and photothermal therapy*. Journal of Advanced Research, 2010. **1**(1): p. 13-28.
15. Sau, T.K. and C.J. Murphy, *Room Temperature, High-Yield Synthesis of Multiple Shapes of Gold Nanoparticles in Aqueous Solution*. Journal of the American Chemical Society, 2004. **126**(28): p. 8648-8649.
16. Loo, C., et al., *Gold nanoshell bioconjugates for molecular imaging in living cells*. Optics Letters, 2005. **30**(9): p. 1012-1014.
17. Gao, B., G. Arya, and A.R. Tao, *Self-orienting nanocubes for the assembly of plasmonic nanojunctions*. Nat Nano, 2012. **7**(7): p. 433-437.
18. Kumar, G.V.P., *Plasmonic nano-architectures for surface enhanced Raman scattering: a review*. Journal of Nanophotonics, 2012. **6**(1): p. 064503-1-064503-20.
19. Jain, P.K. and M.A. El-Sayed, *Plasmonic coupling in noble metal nanostructures*. Chemical Physics Letters, 2010. **487**(4): p. 153-164.
20. Kneipp, J., et al., *Gold Nanolenses Generated by Laser Ablation-Efficient Enhancing Structure for Surface Enhanced Raman Scattering Analytics and Sensing*. Analytical Chemistry, 2008. **80**(11): p. 4247-4251.

21. Yuan, Y., et al., *SERS-based ultrasensitive sensing platform: An insight into design and practical applications*. Coordination Chemistry Reviews, 2017. **337**: p. 1-33.
22. Flynn, C.E., et al., *Viruses as vehicles for growth, organization and assembly of materials*. Acta Materialia, 2003. **51**(19): p. 5867-5880.
23. Lee, S.-Y., J.-S. Lim, and M.T. Harris, *Synthesis and application of virus-based hybrid nanomaterials*. Biotechnology and Bioengineering, 2012. **109**(1): p. 16-30.
24. Rong, J., et al., *Self-assembly of viral particles*. Current Opinion in Colloid & Interface Science, 2011. **16**(6): p. 441-450.
25. Sambrook, J. and D.W. Russell, *Molecular Cloning A LABORATORY MANUAL*. Third Edition ed. 2001, Cold Spring Harbor, New York: Cold Spring Harbor Laboratory Press.
26. Zahr, O.K. and A.S. Blum, *Solution Phase Gold Nanorings on a Viral Protein Template*. Nano Letters, 2012. **12**(2): p. 629-633.
27. Shang, J. and X. Gao, *Nanoparticle counting: towards accurate determination of the molar concentration*. Chemical Society Reviews, 2014. **43**(21): p. 7267-7278.
28. Turkevich, J., P.C. Stevenson, and J. Hillier, *A study of the nucleation and growth processes in the synthesis of colloidal gold*. Discussions of the Faraday Society, 1951. **11**(0): p. 55-75.
29. Souza, G.R., et al., *Networks of gold nanoparticles and bacteriophage as biological sensors and cell-targeting agents*. Proceedings of the National Academy of Sciences of the United States of America, 2006. **103**(5): p. 1215-1220.
30. Ah, C.S., et al., *Colorimetric quantitative sensing of alkali metal ions based on reversible assembly and disassembly of gold nanoparticles*. Current Applied Physics, 2013. **13**(9): p. 1889-1893.
31. Savage, K.J., et al., *Revealing the quantum regime in tunnelling plasmonics*. Nature, 2012. **491**(7425): p. 574-577.
32. Yamamoto, Y.S., Y. Ozaki, and T. Itoh, *Recent progress and frontiers in the electromagnetic mechanism of surface-enhanced Raman scattering*. Journal of Photochemistry and Photobiology C: Photochemistry Reviews, 2014. **21**: p. 81-104.
33. Lee, H.-E., et al., *Virus Templated Gold Nanocube Chain for SERS Nanoprobe*. Small, 2014. **10**(15): p. 3007-3011.
34. Ansari, S.A. and Q. Husain, *Potential applications of enzymes immobilized on/in nano materials: A review*. Biotechnology Advances, 2012. **30**(3): p. 512-523.
35. Ding, S., et al., *Increasing the activity of immobilized enzymes with nanoparticle conjugation*. Current Opinion in Biotechnology, 2015. **34**(Supplement C): p. 242-250.
36. Johnson, B.J., et al., *Understanding enzymatic acceleration at nanoparticle interfaces: Approaches and challenges*. Nano Today, 2014. **9**(1): p. 102-131.
37. Lee, K.-S. and M.A. El-Sayed, *Gold and Silver Nanoparticles in Sensing and Imaging: Sensitivity of Plasmon Response to Size, Shape, and Metal Composition*. The Journal of Physical Chemistry B, 2006. **110**(39): p. 19220-19225.
38. Sun, Y. and Y. Xia, *Gold and silver nanoparticles: A class of chromophores with colors tunable in the range from 400 to 750 nm*. Analyst, 2003. **128**(6): p. 686-691.
39. Vieu, C., et al., *Electron beam lithography: resolution limits and applications*. Applied Surface Science, 2000. **164**(1): p. 111-117.
40. Cabrini, S., et al., *Focused ion beam lithography for two dimensional array structures for photonic applications*. Microelectronic Engineering, 2005. **78**: p. 11-15.
41. Guo, L.J., *Nanoimprint Lithography: Methods and Material Requirements*. Advanced Materials, 2007. **19**(4): p. 495-513.
42. Zhang, G. and D. Wang, *Colloidal Lithography—The Art of Nanochemical Patterning*. Chemistry – An Asian Journal, 2009. **4**(2): p. 236-245.

43. Wood, M.A., *Colloidal lithography and current fabrication techniques producing in-plane nanotopography for biological applications*. Journal of the Royal Society Interface, 2007. **4**(12): p. 1-17.
44. Boltasseva, A. and V.M. Shalaev, *Fabrication of optical negative-index metamaterials: Recent advances and outlook*. Metamaterials, 2008. **2**(1): p. 1-17.
45. Hamley, I.W., *Nanostructure fabrication using block copolymers*. Nanotechnology, 2003. **14**(10): p. R39.
46. Barth, J.V., G. Costantini, and K. Kern, *Engineering atomic and molecular nanostructures at surfaces*. Nature, 2005. **437**(7059): p. 671-679.
47. Kim, S., et al., *Controlling the microdomain orientation in block copolymer thin films via cross-linkable random copolymer neutral layer*. Polym J, 2016. **48**(4): p. 333-340.
48. Wang, D. and H. Mohwald, *Template-directed colloidal self-assembly - the route to 'top-down' nanochemical engineering*. Journal of Materials Chemistry, 2004. **14**(4): p. 459-468.
49. Sotiropoulou, S., et al., *Biotemplated Nanostructured Materials*. Chemistry of Materials, 2008. **20**(3): p. 821-834.
50. Lin, Y. and C. Mao, *Bio-inspired supramolecular self-assembly towards soft nanomaterials*. Frontiers of Materials Science, 2011. **5**(3): p. 247.
51. Fischlechner, M. and E. Donath, *Viruses as Building Blocks for Materials and Devices*. Angewandte Chemie International Edition, 2007. **46**(18): p. 3184-3193.
52. Galatsis, K., et al., *Patterning and Templating for Nanoelectronics*. Advanced Materials, 2010. **22**(6): p. 769-778.
53. Seeman, N.C. and A.M. Belcher, *Emulating biology: Building nanostructures from the bottom up*. Proceedings of the National Academy of Sciences, 2002. **99**(suppl 2): p. 6451-6455.
54. Busseron, E., et al., *Supramolecular self-assemblies as functional nanomaterials*. Nanoscale, 2013. **5**(16): p. 7098-7140.
55. Shen, L., et al., *Materials design using genetically engineered proteins*. Journal of Materials Chemistry, 2011. **21**(47): p. 18868-18876.
56. Sumper, M. and E. Brunner, *Learning from Diatoms: Nature's Tools for the Production of Nanostructured Silica*. Advanced Functional Materials, 2006. **16**(1): p. 17-26.
57. Seeman, N.C., *An Overview of Structural DNA Nanotechnology*. Molecular Biotechnology, 2007. **37**(3): p. 246.
58. Li, H., et al., *DNA-Templated Self-Assembly of Protein and Nanoparticle Linear Arrays*. Journal of the American Chemical Society, 2004. **126**(2): p. 418-419.
59. Han, D., et al., *DNA Origami with Complex Curvatures in Three-Dimensional Space*. Science, 2011. **332**(6027): p. 342.
60. Maune, H.T., et al., *Self-assembly of carbon nanotubes into two-dimensional geometries using DNA origami templates*. Nat Nano, 2010. **5**(1): p. 61-66.
61. Rogers, W.B., W.M. Shih, and V.N. Manoharan, *Using DNA to program the self-assembly of colloidal nanoparticles and microparticles*. 2016. **1**: p. 16008.
62. Schreiber, R., et al., *Hierarchical assembly of metal nanoparticles, quantum dots and organic dyes using DNA origami scaffolds*. Nat Nano, 2014. **9**(1): p. 74-78.
63. Nakao, H., et al., *Highly Ordered Assemblies of Au Nanoparticles Organized on DNA*. Nano Letters, 2003. **3**(10): p. 1391-1394.
64. Pinheiro, A.V., et al., *Challenges and opportunities for structural DNA nanotechnology*. Nat Nano, 2011. **6**(12): p. 763-772.
65. Kühler, P., et al., *Plasmonic DNA-Origami Nanoantennas for Surface-Enhanced Raman Spectroscopy*. Nano Letters, 2014. **14**(5): p. 2914-2919.

66. Luo, S.-C., et al., *Nanofabricated SERS-active substrates for single-molecule to virus detection in vitro: A review*. Biosensors and Bioelectronics, 2014. **61**: p. 232-240.
67. Liu, Z., et al., *Natural supramolecular building blocks: from virus coat proteins to viral nanoparticles*. Chemical Society Reviews, 2012. **41**(18): p. 6178-6194.
68. Pokorski, J.K. and N.F. Steinmetz, *The art of engineering viral nanoparticles*. Mol Pharm, 2011. **8**(1): p. 29-43.
69. Steinmetz, N.F., *Viral nanoparticles as platforms for next-generation therapeutics and imaging devices*. Nanomedicine: Nanotechnology, Biology and Medicine, 2010. **6**(5): p. 634-641.
70. Yildiz, I., S. Shukla, and N.F. Steinmetz, *Applications of viral nanoparticles in medicine*. Current Opinion in Biotechnology, 2011. **22**(6): p. 901-908.
71. Gao, J., et al., *Phage display and its application in vaccine design*. Annals of Microbiology, 2010. **60**(1): p. 13-19.
72. Lee, L.A., Z. Niu, and Q. Wang, *Viruses and virus-like protein assemblies—Chemically programmable nanoscale building blocks*. Nano Research, 2009. **2**(5): p. 349-364.
73. Koudelka, K.J. and M. Manchester, *Chemically modified viruses: principles and applications*. Current Opinion in Chemical Biology, 2010. **14**(6): p. 810-817.
74. Yang, S.H., et al., *Assembly of bacteriophage into functional materials*. Chem Rec, 2013. **13**(1): p. 43-59.
75. Moon, J.S., et al., *M13 Bacteriophage-Based Self-Assembly Structures and Their Functional Capabilities*. Mini Rev Org Chem, 2015. **12**(3): p. 271-281.
76. Bawden, F.C., et al., *Liquid Crystalline Substances from Virus-infected Plants*. Nature, 1936. **138**: p. 1501-1502.
77. Lee, S.W., B.M. Wood, and A.M. Belcher, *Chiral smectic C structures of virus-based films*. Langmuir, 2003. **19**(5): p. 1592-1598.
78. Dogic, Z. and S. Fraden, *Ordered phases of filamentous viruses*. Current Opinion in Colloid & Interface Science, 2006. **11**(1): p. 47-55.
79. Dogic, Z., *Filamentous Phages As a Model System in Soft Matter Physics*. Frontiers in Microbiology, 2016. **7**: p. 1013.
80. Lettinga, M.P., E. Barry, and Z. Dogic, *Self-diffusion of rod-like viruses in the nematic phase*. Europhysics Letters, 2005. **71**(4): p. 692-698.
81. Lettinga, M.P. and E. Grelet, *Self-diffusion of rodlike viruses through smectic layers*. Physical Review Letters, 2007. **99**(19): p. 197802.
82. Fraden, S., *Phase Transitions in Colloidal Suspensions of Virus Particles*, in *Observation, Prediction and Simulation of Phase Transitions in Complex Fluids*, M. Baus, L.F. Rull, and J.-P. Ryckaert, Editors. 1995, Springer Netherlands: Dordrecht. p. 113-164.
83. Lee, S.W. and A.M. Belcher, *Virus-based fabrication of micro- and nanofibers using electrospinning*. Nano Letters, 2004. **4**(3): p. 387-390.
84. Chung, W.J., D.Y. Lee, and S.Y. Yoo, *Chemical modulation of M13 bacteriophage and its functional opportunities for nanomedicine*. Int J Nanomedicine, 2014. **9**: p. 5825-36.
85. Li, K., et al., *Chemical modification of M13 bacteriophage and its application in cancer cell imaging*. Bioconjug Chem, 2010. **21**(7): p. 1369-77.
86. Niu, Z.W., et al., *Bacteriophage M13 as a Scaffold for Preparing Conductive Polymeric Composite Fibers*. Nano Research, 2008. **1**(3): p. 235-241.
87. Purdy, K.R. and S. Fraden, *Isotropic-cholesteric phase transition of filamentous virus suspensions as a function of rod length and charge*. Physical Review E, 2004. **70**(6): p. 061703.
88. Dogic, Z. and S. Fraden, *Development of model colloidal liquid crystals and the kinetics of the isotropic-smectic transition*. Philosophical Transactions of the Royal Society a-Mathematical Physical and Engineering Sciences, 2001. **359**(1782): p. 997-1014.

89. Tamerler, C. and M. Sarikaya, *Molecular biomimetics: utilizing nature's molecular ways in practical engineering*. Acta Biomater, 2007. **3**(3): p. 289-99.
90. Sarikaya, M., et al., *Molecular biomimetics: nanotechnology through biology*. Nature Materials, 2003. **2**(9): p. 577-585.
91. Lee, S.W., S.K. Lee, and A.M. Belcher, *Virus-based alignment of inorganic, organic, and biological nanosized materials*. Advanced Materials, 2003. **15**(9): p. 689-692.
92. Brown, S., *Metal-recognition by repeating polypeptides*. Nat Biotechnol, 1997. **15**(3): p. 269-72.
93. Brown, S., *Engineered iron oxide-adhesion mutants of the Escherichia coli phage lambda receptor*. Proc Natl Acad Sci U S A, 1992. **89**(18): p. 8651-5.
94. Whaley, S.R., et al., *Selection of peptides with semiconductor binding specificity for directed nanocrystal assembly*. Nature, 2000. **405**(6787): p. 665-8.
95. Seker, U.O., et al., *Adsorption behavior of linear and cyclic genetically engineered platinum binding peptides*. Langmuir, 2007. **23**(15): p. 7895-900.
96. Sanghvi, A.B., et al., *Biomaterials functionalization using a novel peptide that selectively binds to a conducting polymer*. Nature Materials, 2005. **4**(6): p. 496-502.
97. So, C.R., et al., *Controlling self-assembly of engineered peptides on graphite by rational mutation*. ACS Nano, 2012. **6**(2): p. 1648-56.
98. Pelle, B.R., et al., *Design criteria for engineering inorganic material-specific peptides*. Langmuir, 2005. **21**(15): p. 6929-33.
99. Hnilova, M., et al., *Effect of molecular conformations on the adsorption behavior of gold-binding peptides*. Langmuir, 2008. **24**(21): p. 12440-5.
100. Korkmaz Zirpel, N., T. Arslan, and H. Lee, *Engineering filamentous bacteriophages for enhanced gold binding and metallization properties*. J Colloid Interface Sci, 2015. **454**: p. 80-8.
101. Tamerler, C., et al., *Genetically engineered polypeptides for inorganics: A utility in biological materials science and engineering*. Materials Science & Engineering C-Biomimetic and Supramolecular Systems, 2007. **27**(3): p. 558-564.
102. Gaskin, D.J.H., K. Starck, and E.N. Vulfson, *Identification of inorganic crystal-specific sequences using phage display combinatorial library of short peptides: A feasibility study*. Biotechnology Letters, 2000. **22**(15): p. 1211-1216.
103. Sarikaya, M., et al., *Materials assembly and formation using engineered polypeptides*. Annual Review of Materials Research, 2004. **34**(1): p. 373-408.
104. Estephan, E., et al., *Peptides for functionalization of InP semiconductors*. J Colloid Interface Sci, 2009. **337**(2): p. 358-63.
105. Kriplani, U. and B.K. Kay, *Selecting peptides for use in nanoscale materials using phage-displayed combinatorial peptide libraries*. Curr Opin Biotechnol, 2005. **16**(4): p. 470-5.
106. Sano, K., H. Sasaki, and K. Shiba, *Specificity and biomineralization activities of Ti-binding peptide-1 (TBP-1)*. Langmuir, 2005. **21**(7): p. 3090-5.
107. Wang, S., et al., *Peptides with selective affinity for carbon nanotubes*. Nat Mater, 2003. **2**(3): p. 196-200.
108. Chen, H., et al., *QCM-D analysis of binding mechanism of phage particles displaying a constrained heptapeptide with specific affinity to SiO₂ and TiO₂*. Anal Chem, 2006. **78**(14): p. 4872-9.
109. Cui, Y., et al., *Chemical functionalization of graphene enabled by phage displayed peptides*. Nano Lett, 2010. **10**(11): p. 4559-65.
110. Galloway, J.M. and S.S. Staniland, *Protein and peptide biotemplated metal and metal oxide nanoparticles and their patterning onto surfaces*. Journal of Materials Chemistry, 2012. **22**(25): p. 12423-12434.
111. Mao, C., et al., *Virus-based toolkit for the directed synthesis of magnetic and semiconducting nanowires*. Science, 2004. **303**(5655): p. 213-7.

112. Nam, Y.S., et al., *Virus-templated iridium oxide-gold hybrid nanowires for electrochromic application*. *Nanoscale*, 2012. **4**(11): p. 3405-9.
113. Mao, C., et al., *Viral assembly of oriented quantum dot nanowires*. *Proc Natl Acad Sci U S A*, 2003. **100**(12): p. 6946-51.
114. Flynn, C.E., et al., *Synthesis and organization of nanoscale II-VI semiconductor materials using evolved peptide specificity and viral capsid assembly*. *Journal of Materials Chemistry*, 2003. **13**(10): p. 2414-2421.
115. Reiss, B.D., et al., *Biological routes to metal alloy ferromagnetic nanostructures*. *Nano Letters*, 2004. **4**(6): p. 1127-1132.
116. Yoo, P.J., et al., *Spontaneous assembly of viruses on multilayered polymer surfaces*. *Nat Mater*, 2006. **5**(3): p. 234-40.
117. Courchesne, N.M., et al., *Assembly of a bacteriophage-based template for the organization of materials into nanoporous networks*. *Adv Mater*, 2014. **26**(21): p. 3398-404.
118. Vera-Robles, L.I., et al., *Flexible Electroactive Nanomaterials Biotemplated with Versatile M13 Phage Platforms*. *Advanced Engineering Materials*, 2013. **15**(10): p. 954-961.
119. Rosant, C., et al., *Biosynthesis of Co₃O₄ electrode materials by peptide and phage engineering: comprehension and future*. *Energy & Environmental Science*, 2012. **5**(12): p. 9936-9943.
120. Nam, K.T., et al., *Virus-Enabled Synthesis and Assembly of Nanowires for Lithium Ion Battery Electrodes*. *Science*, 2006. **312**(5775): p. 885.
121. Nam, K.T., et al., *Stamped microbattery electrodes based on self-assembled M13 viruses*. *Proceedings of the National Academy of Sciences*, 2008. **105**(45): p. 17227-17231.
122. Lee, Y.J., et al., *Fabricating Genetically Engineered High-Power Lithium-Ion Batteries Using Multiple Virus Genes*. *Science*, 2009. **324**(5930): p. 1051.
123. Lee, Y.J., et al., *Biologically Activated Noble Metal Alloys at the Nanoscale: For Lithium Ion Battery Anodes*. *Nano Letters*, 2010. **10**(7): p. 2433-2440.
124. Frenkel, D. and B. Solomon, *Filamentous phage as vector-mediated antibody delivery to the brain*. *Proceedings of the National Academy of Sciences*, 2002. **99**(8): p. 5675-5679.
125. Yi, H., et al., *M13 Phage-Functionalized Single-Walled Carbon Nanotubes As Nanoprobes for Second Near-Infrared Window Fluorescence Imaging of Targeted Tumors*. *Nano Letters*, 2012. **12**(3): p. 1176-1183.
126. Ghosh, D., et al., *M13-templated magnetic nanoparticles for targeted in vivo imaging of prostate cancer*. *Nat Nanotechnol*, 2012. **7**(10): p. 677-82.
127. Ngweniform, P., et al., *Self-Assembly of Drug-Loaded Liposomes on Genetically Engineered Target-Recognizing M13 Phage: A Novel Nanocarrier for Targeted Drug Delivery*. *Small*, 2009. **5**(17): p. 1963-1969.
128. Oh, M.H., et al., *Genetically Programmed Clusters of Gold Nanoparticles for Cancer Cell-Targeted Photothermal Therapy*. *ACS Applied Materials & Interfaces*, 2015. **7**(40): p. 22578-22586.
129. Blum, A.S., et al., *Cowpea Mosaic Virus as a Scaffold for 3-D Patterning of Gold Nanoparticles*. *Nano Letters*, 2004. **4**(5): p. 867-870.
130. Radloff, C., et al., *Metal Nanoshell Assembly on a Virus Bioscaffold*. *Nano Letters*, 2005. **5**(6): p. 1187-1191.
131. Kuncicky, D.M., R.R. Naik, and O.D. Velev, *Rapid Deposition and Long-Range Alignment of Nanocoatings and Arrays of Electrically Conductive Wires from Tobacco Mosaic Virus*. *Small*, 2006. **2**(12): p. 1462-1466.
132. Slocik, J.M., et al., *Viral templates for gold nanoparticle synthesis*. *Journal of Materials Chemistry*, 2005. **15**(7): p. 749-753.
133. Choi, H.S., et al., *Renal Clearance of Nanoparticles*. *Nature biotechnology*, 2007. **25**(10): p. 1165-1170.

134. Chapman, S., et al., *Nanoparticles for cancer imaging: The good, the bad, and the promise*. Nano Today, 2013. **8**(5): p. 454-460.
135. Davis, M.E., Z. Chen, and D.M. Shin, *Nanoparticle therapeutics: an emerging treatment modality for cancer*. Nat Rev Drug Discov, 2008. **7**(9): p. 771-782.
136. Liu, J., et al., *Renal clearable inorganic nanoparticles: a new frontier of bionanotechnology*. Materials Today, 2013. **16**(12): p. 477-486.
137. Hemminga, M.A., et al., *Viruses: incredible nanomachines. New advances with filamentous phages*. European Biophysics Journal, 2010. **39**(4): p. 541-550.
138. Kehoe, J.W. and B.K. Kay, *Filamentous Phage Display in the New Millennium*. Chemical Reviews, 2005. **105**(11): p. 4056-4072.
139. Sidhu, S.S., *Engineering M13 for phage display*. Biomolecular Engineering, 2001. **18**(2): p. 57-63.
140. Clokie, M.R.J., et al., *Phages in nature*. Bacteriophage, 2011. **1**(1): p. 31-45.
141. Salmond, G.P.C. and P.C. Fineran, *A century of the phage: past, present and future*. Nat Rev Micro, 2015. **13**(12): p. 777-786.
142. Onodera, K., *Molecular Biology and Biotechnology of Bacteriophage*, in *Nano/Micro Biotechnology*, I. Endo and T. Nagamune, Editors. 2010, Springer Berlin Heidelberg: Berlin, Heidelberg. p. 17-43.
143. Tzagoloff, H. and D. Pratt, *The initial steps in infection with coliphage M13*. Virology, 1964. **24**(3): p. 372-380.
144. Held, H.A. and S.S. Sidhu, *Comprehensive Mutational Analysis of the M13 Major Coat Protein: Improved Scaffolds for C-terminal Phage Display*. Journal of Molecular Biology, 2004. **340**(3): p. 587-597.
145. Russel, M., H.B. Lowman, and T. Clackson, *Introduction to Phage Biology and Phage Display*, in *Phage Display: A Practical Approach*, T. Clackson and H.B. Lowman, Editors. 2004, Oxford University Press. p. 1-26.
146. Smith, G.P., *Filamentous fusion phage: novel expression vectors that display cloned antigens on the virion surface*. Science, 1985. **228**(4705): p. 1315.
147. Huang, J.X., S.L. Bishop-Hurley, and M.A. Cooper, *Development of Anti-Infectives Using Phage Display: Biological Agents against Bacteria, Viruses, and Parasites*. Antimicrobial Agents and Chemotherapy, 2012. **56**(9): p. 4569-4582.
148. Seker, U.O.S. and H.V. Demir, *Material Binding Peptides for Nanotechnology*. Molecules, 2011. **16**(2).
149. Merzlyak, A. and S.-W. Lee, *Phage as templates for hybrid materials and mediators for nanomaterial synthesis*. Current Opinion in Chemical Biology, 2006. **10**(3): p. 246-252.
150. Kriplani, U. and B.K. Kay, *Selecting peptides for use in nanoscale materials using phage-displayed combinatorial peptide libraries*. Current Opinion in Biotechnology, 2005. **16**(4): p. 470-475.
151. Garet, E., et al., *Rapid isolation of single-chain antibodies by phage display technology directed against one of the most potent marine toxins: Palytoxin*. Toxicon, 2010. **55**(8): p. 1519-1526.
152. Nanduri, V., et al., *SPR biosensor for the detection of L. monocytogenes using phage-displayed antibody*. Biosensors and Bioelectronics, 2007. **23**(2): p. 248-252.
153. Pasqualini, R. and E. Ruoslahti, *Organ targeting In vivo using phage display peptide libraries*. Nature, 1996. **380**(6572): p. 364-366.
154. Deutscher, S.L., *Phage Display in Molecular Imaging and Diagnosis of Cancer*. Chemical Reviews, 2010. **110**(5): p. 3196-3211.
155. Govarts, C., et al., *Frameshifting in the P6 cDNA Phage Display System*. Molecules, 2010. **15**(12): p. 9380.
156. Ghosh, D., et al., *Refactored M13 Bacteriophage as a Platform for Tumor Cell Imaging and Drug Delivery*. ACS Synthetic Biology, 2012. **1**(12): p. 576-582.

157. Gao, C., et al., *Making artificial antibodies: A format for phage display of combinatorial heterodimeric arrays*. Proceedings of the National Academy of Sciences, 1999. **96**(11): p. 6025-6030.
158. Pande, J., M.M. Szewczyk, and A.K. Grover, *Phage display: Concept, innovations, applications and future*. Biotechnology Advances, 2010. **28**(6): p. 849-858.
159. Makowski, L., *Phage display: structure, assembly and engineering of filamentous bacteriophage M13*. Current Opinion in Structural Biology, 1994. **4**(2): p. 225-230.
160. Smith, G.P., *Preface*. Gene, 1993. **128**(1): p. 1-2.
161. Lee, Y., et al., *Virus-templated Au and Au-Pt core-shell nanowires and their electrocatalytic activities for fuel cell applications*. Energy & Environmental Science, 2012. **5**(8): p. 8328-8334.
162. Yiran, Y., et al., *Viral-templated gold/polypyrrole nanopeapods for an ammonia gas sensor*. Nanotechnology, 2016. **27**(32): p. 325502.
163. Chen, P.-Y., et al., *Versatile Three-Dimensional Virus-Based Template for Dye-Sensitized Solar Cells with Improved Electron Transport and Light Harvesting*. ACS Nano, 2013. **7**(8): p. 6563-6574.
164. Chung Hee, M., et al., *Highly sensitive hydrogen sulfide (H₂S) gas sensors from viral-templated nanocrystalline gold nanowires*. Nanotechnology, 2014. **25**(13): p. 135205.
165. Moon, C.H., N.V. Myung, and E.D. Haberer, *Chemiresistive hydrogen gas sensors from gold-palladium nanopeapods*. Applied Physics Letters, 2014. **105**(22): p. 223102.
166. Vera-Robles, L.I., et al., *Using the M13 Phage as a Biotemplate to Create Mesoporous Structures Decorated with Gold and Platinum Nanoparticles*. Langmuir, 2015. **31**(33): p. 9188-9197.
167. Lee, J.H., et al., *M13 Bacteriophage as Materials for Amplified Surface Enhanced Raman Scattering Protein Sensing*. Advanced Functional Materials, 2014. **24**(14): p. 2079-2084.
168. Lee, J.H., D.W. Domaille, and J.N. Cha, *Amplified Protein Detection and Identification through DNA-Conjugated M13 Bacteriophage*. ACS Nano, 2012. **6**(6): p. 5621-5626.
169. Blaik, R.A., et al., *Gold-Coated M13 Bacteriophage as a Template for Glucose Oxidase Biofuel Cells with Direct Electron Transfer*. ACS Nano, 2016. **10**(1): p. 324-332.
170. Causa, F., et al., *Evolutionary screening and adsorption behavior of engineered M13 bacteriophage and derived dodecapeptide for selective decoration of gold interfaces*. Journal of Colloid and Interface Science, 2013. **389**(1): p. 220-229.
171. Huang, Y., et al., *Programmable Assembly of Nanoarchitectures Using Genetically Engineered Viruses*. Nano Letters, 2005. **5**(7): p. 1429-1434.
172. Stearns, L.A., et al., *Template-Directed Nucleation and Growth of Inorganic Nanoparticles on DNA Scaffolds*. Angewandte Chemie, 2009. **121**(45): p. 8646-8648.
173. Kim, J., M.J. Sadowsky, and H.-G. Hur, *Simultaneous Synthesis of Temperature-Tunable Peptide and Gold Nanoparticle Hybrid Spheres*. Biomacromolecules, 2011. **12**(7): p. 2518-2523.
174. Kim, J., et al., *Peptide-mediated shape- and size-tunable synthesis of gold nanostructures*. Acta Biomaterialia, 2010. **6**(7): p. 2681-2689.
175. Heinz, H., et al., *Nature of molecular interactions of peptides with gold, palladium, and Pd-Au bimetal surfaces in aqueous solution*. Abstracts of Papers of the American Chemical Society, 2009. **238**.
176. Yu, J., M.L. Becker, and G.A. Carri, *The Influence of Amino Acid Sequence and Functionality on the Binding Process of Peptides onto Gold Surfaces*. Langmuir, 2012. **28**(2): p. 1408-1417.
177. Tan, Y.N., J.Y. Lee, and D.I.C. Wang, *Uncovering the Design Rules for Peptide Synthesis of Metal Nanoparticles*. Journal of the American Chemical Society, 2010. **132**(16): p. 5677-5686.
178. Stearns, L.A., et al., *Template-Directed Nucleation and Growth of Inorganic Nanoparticles on DNA Scaffolds*. Angewandte Chemie-International Edition, 2009. **48**(45): p. 8494-8496.
179. Diamanti, S., et al., *Relative Functionality of Buffer and Peptide in Gold Nanoparticle Formation*. Journal of Physical Chemistry C, 2009. **113**(23): p. 9993-9997.

180. Ferguson, W.J., et al., *Hydrogen-Ion Buffers for Biological-Research*. Analytical Biochemistry, 1980. **104**(2): p. 300-310.
181. Nguyen, A.H., Y. Shin, and S.J. Sim, *Development of SERS substrate using phage-based magnetic template for triplex assay in sepsis diagnosis*. Biosensors & Bioelectronics, 2016. **85**: p. 522-528.
182. Liu, A., G. Abbineni, and C. Mao, *Nanocomposite Films Assembled from Genetically Engineered Filamentous Viruses and Gold Nanoparticles: Nanoarchitecture- and Humidity-Tunable Surface Plasmon Resonance Spectra*. Advanced Materials, 2009. **21**(9): p. 1001-1005.
183. Philip, D., *Synthesis and spectroscopic characterization of gold nanoparticles*. Spectrochimica Acta Part A: Molecular and Biomolecular Spectroscopy, 2008. **71**(1): p. 80-85.
184. Daniel, M.-C. and D. Astruc, *Gold Nanoparticles: Assembly, Supramolecular Chemistry, Quantum-Size-Related Properties, and Applications toward Biology, Catalysis, and Nanotechnology*. Chemical Reviews, 2004. **104**(1): p. 293-346.
185. Sapsford, K.E., et al., *Analyzing Nanomaterial Bioconjugates: A Review of Current and Emerging Purification and Characterization Techniques*. Analytical Chemistry, 2011. **83**(12): p. 4453-4488.
186. Amendola, V. and M. Meneghetti, *Size Evaluation of Gold Nanoparticles by UV-vis Spectroscopy*. The Journal of Physical Chemistry C, 2009. **113**(11): p. 4277-4285.
187. Tomaszewska, E., et al., *Detection Limits of DLS and UV-Vis Spectroscopy in Characterization of Polydisperse Nanoparticles Colloids*. Journal of Nanomaterials, 2013. **2013**: p. 10.
188. Hall, J.B., et al., *Characterization of nanoparticles for therapeutics*. Nanomedicine, 2007. **2**(6): p. 789-803.
189. Brydson, R., et al., *Analytical Transmission Electron Microscopy*. Reviews in Mineralogy and Geochemistry, 2014. **78**(1): p. 219.
190. Lin, P.-C., et al., *Techniques for physicochemical characterization of nanomaterials*. Biotechnology Advances, 2014. **32**(4): p. 711-726.
191. Wang, Z.L., *Transmission Electron Microscopy of Shape-Controlled Nanocrystals and Their Assemblies*. The Journal of Physical Chemistry B, 2000. **104**(6): p. 1153-1175.
192. Niikura, K., et al., *Gold Nanoparticle Arrangement on Viral Particles through Carbohydrate Recognition: A Non-Cross-Linking Approach to Optical Virus Detection*. Bioconjugate Chemistry, 2009. **20**(10): p. 1848-1852.
193. Pecora, R., *Dynamic Light Scattering Measurement of Nanometer Particles in Liquids*. Journal of Nanoparticle Research, 2000. **2**(2): p. 123-131.
194. Kato, H., et al., *Accurate Size and Size-Distribution Determination of Polystyrene Latex Nanoparticles in Aqueous Medium Using Dynamic Light Scattering and Asymmetrical Flow Field Flow Fractionation with Multi-Angle Light Scattering*. Nanomaterials, 2012. **2**(1): p. 15.
195. Hoo, C.M., et al., *A comparison of atomic force microscopy (AFM) and dynamic light scattering (DLS) methods to characterize nanoparticle size distributions*. Journal of Nanoparticle Research, 2008. **10**(1): p. 89-96.
196. Tscharnutter, W., *Photon Correlation Spectroscopy in Particle Sizing*, in *Encyclopedia of Analytical Chemistry*. 2006, John Wiley & Sons, Ltd.
197. Desgrosellier, J.S. and D.A. Cheresh, *Integrins in cancer: biological implications and therapeutic opportunities*. Nat Rev Cancer, 2010. **10**(1): p. 9-22.
198. Chen, X., et al., *Integrin $\alpha(v)\beta(3)$ -Targeted Imaging of Lung Cancer*. Neoplasia (New York, N.Y.), 2005. **7**(3): p. 271-279.
199. Yoo, S.Y., et al., *Facile patterning of genetically engineered M13 bacteriophage for directional growth of human fibroblast cells*. Soft Matter, 2011. **7**(2): p. 363-368.
200. Merzlyak, A., S. Indrakanti, and S.-W. Lee, *Genetically Engineered Nanofiber-Like Viruses For Tissue Regenerating Materials*. Nano Letters, 2009. **9**(2): p. 846-852.

201. Yoo, S.Y., A. Merzlyak, and S.-W. Lee, *Synthetic Phage for Tissue Regeneration*. Mediators of Inflammation, 2014. **2014**: p. 11.
202. Danhier, F., A. Le Breton, and V. Préat, *RGD-Based Strategies To Target Alpha(v) Beta(3) Integrin in Cancer Therapy and Diagnosis*. Molecular Pharmaceutics, 2012. **9**(11): p. 2961-2973.
203. Bidault, S. and A. Polman, *Water-Based Assembly and Purification of Plasmon-Coupled Gold Nanoparticle Dimers and Trimers*. International Journal of Optics, 2012. **2012**: p. 5.
204. Suzuki, K., K. Hosokawa, and M. Maeda, *Controlling the Number and Positions of Oligonucleotides on Gold Nanoparticle Surfaces*. Journal of the American Chemical Society, 2009. **131**(22): p. 7518-7519.
205. Suthiwangcharoen, N., et al., *M13 bacteriophage-polymer nanoassemblies as drug delivery vehicles*. Nano Research, 2011. **4**(5): p. 483-493.
206. Kooij, E.S., et al., *Ionic Strength Mediated Self-Organization of Gold Nanocrystals: An AFM Study*. Langmuir, 2002. **18**(20): p. 7677-7682.
207. Zimbone, M., et al., *Dynamic Light Scattering on Bioconjugated Laser Generated Gold Nanoparticles*. PLoS ONE, 2014. **9**(3): p. e89048.
208. Driskell, J.D., et al., *One-step assay for detecting influenza virus using dynamic light scattering and gold nanoparticles*. Analyst, 2011. **136**(15): p. 3083-3090.
209. Fontana, J., et al., *Virus-Templated Plasmonic Nanoclusters with Icosahedral Symmetry via Directed Self-Assembly*. Small, 2014. **10**(15): p. 3058-3063.
210. Kurzepa, A., et al., *Molecular modification of T4 bacteriophage proteins and its potential application — Review*. Folia Microbiologica, 2009. **54**(1): p. 5-15.
211. Sathaliyawala, T., et al., *Functional Analysis of the Highly Antigenic Outer Capsid Protein, Hoc, a Virus Decoration Protein from T4-like Bacteriophages*. Molecular microbiology, 2010. **77**(2): p. 444-455.
212. Sathaliyawala, T., et al., *Assembly of Human Immunodeficiency Virus (HIV) Antigens on Bacteriophage T4: a Novel In Vitro Approach To Construct Multicomponent HIV Vaccines*. Journal of Virology, 2006. **80**(15): p. 7688-7698.
213. Fokine, A., et al., *Cryo-electron microscopy study of bacteriophage T4 displaying anthrax toxin proteins*. Virology, 2007. **367**(2): p. 422-427.
214. Leiman, P.G., et al., *Structure and morphogenesis of bacteriophage T4*. Cellular and Molecular Life Sciences CMLS, 2003. **60**(11): p. 2356-2370.
215. Wilson, D.R. and B.B. Finlay, *Phage display: applications, innovations, and issues in phage and host biology*. Canadian Journal of Microbiology, 1998. **44**: p. 313-329.
216. Smith, G.P. and V.A. Petrenko, *Phage Display*. Chemical Reviews, 1997. **97**(2): p. 391-410.
217. Ren, Z.J., et al., *Phage display of intact domains at high copy number: A system based on SOC, the small outer capsid protein of bacteriophage T4*. Protein Science, 1996. **5**(9): p. 1833-1843.
218. Skerra, A. and A. Plückthun, *Secretion and in vivo folding of the Fab fragment of the antibody McPC603 in Escherichia coli: influence of disulphides and cis-prolines*. Protein Engineering, 1991. **4**(8): p. 971-979.
219. Bratkovič, T., *Progress in phage display: evolution of the technique and its applications*. Cellular and Molecular Life Sciences, 2010. **67**(5): p. 749-767.
220. Wu, J., et al., *Bacteriophage T4 nanoparticle capsid surface SOC and HOC bipartite display with enhanced classical swine fever virus immunogenicity: A powerful immunological approach*. Journal of Virological Methods, 2007. **139**(1): p. 50-60.
221. Ren, Z.-j. and L.W. Black, *Phage T4 SOC and HOC display of biologically active, full-length proteins on the viral capsid*. Gene, 1998. **215**(2): p. 439-444.
222. Oślizło, A., et al., *Purification of phage display-modified bacteriophage T4 by affinity chromatography*. BMC Biotechnol, 2011. **11**: p. 59-59.

223. Li, Q., et al., *Bacteriophage T4 Capsid: A Unique Platform for Efficient Surface Assembly of Macromolecular Complexes*. Journal of Molecular Biology, 2006. **363**(2): p. 577-588.
224. Jiang, J., L. Abu-Shilbayeh, and V.B. Rao, *Display of a PorA peptide from Neisseria meningitidis on the bacteriophage T4 capsid surface*. Infect Immun, 1997. **65**(11): p. 4770-4777.
225. Li, Q., et al., *Assembly of the Small Outer Capsid Protein, Soc, on Bacteriophage T4: a novel system for high density display of multiple large anthrax toxins and foreign proteins on phage capsid*. Journal of Molecular Biology, 2007. **370**(5): p. 1006-1019.
226. Gamkrelidze, M. and K. Dąbrowska, *T4 bacteriophage as a phage display platform*. Archives of Microbiology, 2014. **196**(7): p. 473-479.
227. Rao, V.B. and L.W. Black, *Structure and assembly of bacteriophage T4 head*. Virol J, 2010. **7**(1): p. 356.
228. Tao, P., et al., *Mutated and Bacteriophage T4 Nanoparticle Arrayed F1-V Immunogens from Yersinia pestis as Next Generation Plague Vaccines*. PLOS Pathogens, 2013. **9**(7): p. e1003495.
229. Shivachandra, S.B., et al., *In vitro binding of anthrax protective antigen on bacteriophage T4 capsid surface through Hoc-capsid interactions: A strategy for efficient display of large full-length proteins*. Virology, 2006. **345**(1): p. 190-198.
230. Alving, C.R., et al., *Liposomes containing glucosyl ceramide specifically bind T4 bacteriophage: a self-assembling nanocarrier formulation*. Journal of Liposome Research, 2011. **21**(4): p. 279-285.
231. Robertson, K.L., et al., *Engineered T4 Viral Nanoparticles for Cellular Imaging and Flow Cytometry*. Bioconjugate Chemistry, 2011. **22**(4): p. 595-604.
232. Liana, A.E., et al., *T4 bacteriophage conjugated magnetic particles for E. coli capturing: Influence of bacteriophage loading, temperature and tryptone*. Colloids and Surfaces B: Biointerfaces, 2017. **151**: p. 47-57.
233. Janczuk, M., et al., *Bacteriophage-Based Bioconjugates as a Flow Cytometry Probe for Fast Bacteria Detection*. Bioconjugate Chemistry, 2017. **28**(2): p. 419-425.
234. Shabani, A., et al., *Magnetically-assisted impedimetric detection of bacteria using phage-modified carbon microarrays*. Talanta, 2013. **116**: p. 1047-1053.
235. Xu, Z., et al., *Synthesis and magnetic property of T4 virus-supported gold-coated iron ternary nanocomposite*. Journal of Nanoparticle Research, 2012. **14**(12): p. 1267.
236. Hou, L., F. Gao, and N. Li, *T4 Virus-Based Toolkit for the Direct Synthesis and 3D Organization of Metal Quantum Particles*. Chemistry – A European Journal, 2010. **16**(48): p. 14397-14403.
237. Hou, L.I., et al., *SYNTHESIS AND ORGANIZATION OF PLATINUM NANOPARTICLES AND NANOSHELLS ON A NATIVE VIRUS BIOSCAFFOLD*. Nano, 2014. **09**(06): p. 1450058.
238. Adams, M.H., *Bacteriophages*. 1959: New York (& London): Inter-science Publishers. xviii + 592 pp.
239. Robertson, K., et al., *Deletion of the Hoc and Soc capsid proteins affects the surface and cellular uptake properties of bacteriophage T4 derived nanoparticles*. Biochemical and Biophysical Research Communications, 2012. **418**(3): p. 537-540.
240. Wang, Q., et al., *Natural Supramolecular Building Blocks*. Chemistry & Biology, 2002. **9**(7): p. 813-819.
241. Mejri, M.B., et al., *Impedance biosensing using phages for bacteria detection: Generation of dual signals as the clue for in-chip assay confirmation*. Biosensors and Bioelectronics, 2010. **26**(4): p. 1261-1267.
242. Jeon, T.Y., et al., *Nanostructured plasmonic substrates for use as SERS sensors*. Nano Convergence, 2016. **3**(1): p. 18.
243. Israelsen, N.D., C. Hanson, and E. Vargis, *Nanoparticle Properties and Synthesis Effects on Surface-Enhanced Raman Scattering Enhancement Factor: An Introduction*. The Scientific World Journal, 2015. **2015**: p. 12.

244. Fabris, L., *SERS Tags: The Next Promising Tool for Personalized Cancer Detection?* ChemNanoMat, 2016. **2**(4): p. 249-258.
245. Haynes, C.L., A.D. McFarland, and R.P.V. Duyne, *Surface-Enhanced Raman Spectroscopy*. Analytical Chemistry, 2005. **77**(17): p. 338 A-346 A.
246. Bailey, M.R., R.S. Martin, and Z.D. Schultz, *Role of Surface Adsorption in the Surface-Enhanced Raman Scattering and Electrochemical Detection of Neurotransmitters*. The Journal of Physical Chemistry C, 2016. **120**(37): p. 20624-20633.
247. Álvarez-Puebla, R.A., *Effects of the Excitation Wavelength on the SERS Spectrum*. The Journal of Physical Chemistry Letters, 2012. **3**(7): p. 857-866.
248. Wang, Y., B. Yan, and L. Chen, *SERS Tags: Novel Optical Nanoprobes for Bioanalysis*. Chemical Reviews, 2013. **113**(3): p. 1391-1428.
249. Shiohara, A., Y. Wang, and L.M. Liz-Marzán, *Recent approaches toward creation of hot spots for SERS detection*. Journal of Photochemistry and Photobiology C: Photochemistry Reviews, 2014. **21**: p. 2-25.
250. Cinel, N.A., et al., *E-Beam lithography designed substrates for surface enhanced Raman spectroscopy*. Photonics and Nanostructures - Fundamentals and Applications, 2015. **15**: p. 109-115.
251. Alvarez-Puebla, R., et al., *Nanoimprinted SERS-Active Substrates with Tunable Surface Plasmon Resonances*. The Journal of Physical Chemistry C, 2007. **111**(18): p. 6720-6723.
252. Zhang, Q., et al., *Hierarchical 3D SERS Substrates Fabricated by Integrating Photolithographic Microstructures and Self-Assembly of Silver Nanoparticles*. Small, 2014. **10**(13): p. 2703-2711.
253. Dempsey, W.P., S.E. Fraser, and P. Pantazis, *SHG nanoprobes: Advancing harmonic imaging in biology*. Bioessays, 2012. **34**(5): p. 351-360.
254. Qiu, T., W. Zhang, and P.K. Chu, *Aligned silver nanorod arrays for surface-enhanced Raman spectroscopy*. Physica B: Condensed Matter, 2009. **404**(8): p. 1523-1526.
255. Chan, S., et al., *Surface-Enhanced Raman Scattering of Small Molecules from Silver-Coated Silicon Nanopores*. Advanced Materials, 2003. **15**(19): p. 1595-1598.
256. Wang, Y., et al., *Nanostructured Gold Films for SERS by Block Copolymer-Templated Galvanic Displacement Reactions*. Nano Letters, 2009. **9**(6): p. 2384-2389.
257. Stamplecoskie, K.G., et al., *Optimal Size of Silver Nanoparticles for Surface-Enhanced Raman Spectroscopy*. The Journal of Physical Chemistry C, 2011. **115**(5): p. 1403-1409.
258. Nie, S. and S.R. Emory, *Probing Single Molecules and Single Nanoparticles by Surface-Enhanced Raman Scattering*. Science, 1997. **275**(5303): p. 1102.
259. Bich Ha, N., N. Van Hieu, and T. Hong Nhung, *Rich variety of substrates for surface enhanced Raman spectroscopy*. Advances in Natural Sciences: Nanoscience and Nanotechnology, 2016. **7**(3): p. 033001.
260. Chen, X. and H.J. Schluesener, *Nanosilver: A nanoparticle in medical application*. Toxicology Letters, 2008. **176**(1): p. 1-12.
261. Le Ru, E.C. and P.G. Etchegoin, *Single-Molecule Surface-Enhanced Raman Spectroscopy*. Annual Review of Physical Chemistry, 2012. **63**(1): p. 65-87.
262. Ding, S.-Y., et al., *Nanostructure-based plasmon-enhanced Raman spectroscopy for surface analysis of materials*. 2016. **1**: p. 16021.
263. Hu, J., et al., *Aggregation of Silver Particles Trapped at an Air-Water Interface for Preparing New SERS Active Substrates*. The Journal of Physical Chemistry B, 2002. **106**(25): p. 6500-6506.
264. Dong, X., H. Gu, and F. Liu, *Study of the surface-enhanced Raman spectroscopy of residual impurities in hydroxylamine-reduced silver colloid and the effects of anions on the colloid activity*. Spectrochimica Acta Part A: Molecular and Biomolecular Spectroscopy, 2012. **88**: p. 97-101.

265. Sun, L., et al., *Ethanol-Induced Formation of Silver Nanoparticle Aggregates for Highly Active SERS Substrates and Application in DNA Detection*. The Journal of Physical Chemistry C, 2008. **112**(5): p. 1415-1422.
266. Fang, J., et al., *Aggregation and surface-enhanced Raman activity study of dye-coated mixed silver-gold colloids*. Journal of Raman Spectroscopy, 2004. **35**(11): p. 914-920.
267. Vlčková, B., X.J. Gu, and M. Moskovits, *SERS Excitation Profiles of Phthalazine Adsorbed on Single Colloidal Silver Aggregates as a Function of Cluster Size*. The Journal of Physical Chemistry B, 1997. **101**(9): p. 1588-1593.
268. Kruszewski, S. and M. Cyrankiewicz, *Rhodamine 6G as a Mediator of Silver Nanoparticles Aggregation*. ACTA PHYSICA POLONICA A, 2013. **123**(6): p. 965-969.
269. Kahraman, M., K. Keseroğlu, and M. Çulha, *On Sample Preparation for Surface-Enhanced Raman Scattering (SERS) of Bacteria and the Source of Spectral Features of the Spectra*. Applied Spectroscopy, 2011. **65**(5): p. 500-506.
270. Huang, P.-J., et al., *Single-Domain Antibody-Conjugated Nanoaggregate-Embedded Beads for Targeted Detection of Pathogenic Bacteria*. Chemistry – A European Journal, 2009. **15**(37): p. 9330-9334.
271. Brown, L.O. and S.K. Doorn, *A Controlled and Reproducible Pathway to Dye-Tagged, Encapsulated Silver Nanoparticles as Substrates for SERS Multiplexing*. Langmuir, 2008. **24**(6): p. 2277-2280.
272. Huang, P.-J., et al., *Nanoaggregate-Embedded Beads as Novel Raman Labels for Biodetection*. Advanced Functional Materials, 2009. **19**(2): p. 242-248.
273. Braun, G.B., et al., *Generalized Approach to SERS-Active Nanomaterials via Controlled Nanoparticle Linking, Polymer Encapsulation, and Small-Molecule Infusion*. The Journal of Physical Chemistry C, 2009. **113**(31): p. 13622-13629.
274. Chen, S., et al., *Self-assembly of gold nanoparticles to silver microspheres as highly efficient 3D SERS substrates*. Nanoscale Research Letters, 2013. **8**(1): p. 168-168.
275. Wang, C., et al., *Monodispersed Gold Nanorod-Embedded Silica Particles as Novel Raman Labels for Biosensing*. Advanced Functional Materials, 2008. **18**(2): p. 355-361.
276. Eom, G., et al., *Nanogap-Rich Au Nanowire SERS Sensor for Ultrasensitive Telomerase Activity Detection: Application to Gastric and Breast Cancer Tissues Diagnosis*. Advanced Functional Materials, 2017. **27**(37): p. 1701832-n/a.
277. Kim, J.-H., et al., *Nanoparticle Probes with Surface Enhanced Raman Spectroscopic Tags for Cellular Cancer Targeting*. Analytical Chemistry, 2006. **78**(19): p. 6967-6973.
278. Li, J.-M., et al., *Poly(styrene-co-acrylic acid) core and silver nanoparticle/silica shell composite microspheres as high performance surface-enhanced Raman spectroscopy (SERS) substrate and molecular barcode label*. Journal of Materials Chemistry, 2011. **21**(16): p. 5992-5998.
279. Jun, B.-H., et al., *Surface-Enhanced Raman Spectroscopic-Encoded Beads for Multiplex Immunoassay*. Journal of Combinatorial Chemistry, 2007. **9**(2): p. 237-244.
280. Kim, K., et al., *Easy deposition of Ag onto polystyrene beads for developing surface-enhanced-Raman-scattering-based molecular sensors*. Journal of Colloid and Interface Science, 2008. **318**(2): p. 195-201.
281. Jia, K., et al., *Fixed Escherichia coli bacterial templates enable the production of sensitive SERS-based gold nanostructures*. Sensors and Actuators B: Chemical, 2015. **211**: p. 213-219.
282. Yang, D.-P., et al., *Bacteria-template synthesized silver microspheres with hollow and porous structures as excellent SERS substrate*. Green Chemistry, 2010. **12**(11): p. 2038-2042.
283. Yang, L.-b., et al., *Sunlight-induced formation of silver-gold bimetallic nanostructures on DNA template for highly active surface enhanced Raman scattering substrates and application in TNT/tumor marker detection*. Journal of Materials Chemistry, 2009. **19**(37): p. 6849-6856.

284. Kundu, S. and M. Jayachandran, *The self-assembling of DNA-templated Au nanoparticles into nanowires and their enhanced SERS and catalytic applications*. RSC Advances, 2013. **3**(37): p. 16486-16498.
285. Majumdar, D., et al., *DNA-Mediated Wirelike Clusters of Silver Nanoparticles: An Ultrasensitive SERS Substrate*. ACS Applied Materials & Interfaces, 2013. **5**(16): p. 7798-7807.
286. Pilo-Pais, M., et al., *Surface-Enhanced Raman Scattering Plasmonic Enhancement Using DNA Origami-Based Complex Metallic Nanostructures*. Nano Letters, 2014. **14**(4): p. 2099-2104.
287. Thacker, V.V., et al., *DNA origami based assembly of gold nanoparticle dimers for surface-enhanced Raman scattering*. 2014. **5**: p. 3448.
288. Scibilia, S., et al., *Self-assembly of silver nanoparticles and bacteriophage*. Sensing and Bio-Sensing Research, 2016. **7**: p. 146-152.
289. Lentini, G., et al., *Phage–AgNPs complex as SERS probe for U937 cell identification*. Biosensors and Bioelectronics, 2015. **74**: p. 398-405.
290. Indrasekara, A.S.D.S., et al., *Gold nanostar substrates for SERS-based chemical sensing in the femtomolar regime*. Nanoscale, 2014. **6**(15): p. 8891-8899.
291. Xie, J., et al., *The Synthesis of SERS-Active Gold Nanoflower Tags for In Vivo Applications*. ACS Nano, 2008. **2**(12): p. 2473-2480.
292. Rycenga, M., et al., *Generation of Hot Spots with Silver Nanocubes for Single-Molecule Detection by Surface-Enhanced Raman Scattering*. Angewandte Chemie, 2011. **123**(24): p. 5587-5591.
293. Hong, S., et al., *Bioinspired optical antennas: gold plant viruses*. Light Sci Appl, 2015. **4**: p. e267.
294. Chon, H., et al., *Highly Sensitive Immunoassay of Lung Cancer Marker Carcinoembryonic Antigen Using Surface-Enhanced Raman Scattering of Hollow Gold Nanospheres*. Analytical Chemistry, 2009. **81**(8): p. 3029-3034.
295. Lee, D. and S. Yoon, *Gold Nanocube–Nanosphere Dimers: Preparation, Plasmon Coupling, and Surface-Enhanced Raman Scattering*. The Journal of Physical Chemistry C, 2015. **119**(14): p. 7873-7882.
296. Lim, D.-K., et al., *Nanogap-engineerable Raman-active nanodumbbells for single-molecule detection*. Nat Mater, 2010. **9**(1): p. 60-67.
297. Wan, D.S., M. Rajadhyaksha, and R.H. Webb, *Analysis of spherical aberration of a water immersion objective: application to specimens with refractive indices 1.33–1.40*. Journal of Microscopy, 2000. **197**(3): p. 274-284.
298. Liu, A., et al., *Protein Cages as Containers for Gold Nanoparticles*. The Journal of Physical Chemistry B, 2016. **120**(26): p. 6352-6357.
299. Njoki, P.N., et al., *Size Correlation of Optical and Spectroscopic Properties for Gold Nanoparticles*. The Journal of Physical Chemistry C, 2007. **111**(40): p. 14664-14669.
300. Boca, S.C., C. Farcau, and S. Astilean, *The study of Raman enhancement efficiency as function of nanoparticle size and shape*. Nuclear Instruments and Methods in Physics Research Section B: Beam Interactions with Materials and Atoms, 2009. **267**(2): p. 406-410.
301. Hong, S. and X. Li, *Optimal Size of Gold Nanoparticles for Surface-Enhanced Raman Spectroscopy under Different Conditions*. Journal of Nanomaterials, 2013. **2013**: p. 9.
302. Krpetić, Ž., et al., *Importance of Nanoparticle Size in Colorimetric and SERS-Based Multimodal Trace Detection of Ni(II) Ions with Functional Gold Nanoparticles*. Small, 2012. **8**(5): p. 707-714.
303. Efrima, S. and L. Zeiri, *Understanding SERS of bacteria*. Journal of Raman Spectroscopy, 2009. **40**(3): p. 277-288.
304. Ye, T., D. Fu, and W.S. Warren, *Nonlinear Absorption Microscopy†*. Photochemistry and Photobiology, 2009. **85**(3): p. 631-645.
305. Helmchen, F. and W. Denk, *Deep tissue two-photon microscopy*. Nat Meth, 2005. **2**(12): p. 932-940.

306. Hong, G., A.L. Antaris, and H. Dai, *Near-infrared fluorophores for biomedical imaging*. 2017. **1**: p. 0010.
307. Chu, J., et al., *Non-invasive intravital imaging of cellular differentiation with a bright red-excitable fluorescent protein*. *Nat Meth*, 2014. **11**(5): p. 572-578.
308. Yu, D., et al., *A naturally monomeric infrared fluorescent protein for protein labeling in vivo*. *Nat Meth*, 2015. **12**(8): p. 763-765.
309. M. Shotton, D., *Confocal scanning optical microscopy and its applications for biological specimens*. *Journal of Cell Science*, 1989. **94**(2): p. 175.
310. Yue, S., M.N. Slipchenko, and J.X. Cheng, *Multimodal nonlinear optical microscopy*. *Laser & Photonics Reviews*, 2011. **5**(4): p. 496-512.
311. Williams, R.M., W.R. Zipfel, and W.W. Webb, *Multiphoton microscopy in biological research*. *Current Opinion in Chemical Biology*, 2001. **5**(5): p. 603-608.
312. Piston, D.W., *Imaging living cells and tissues by two-photon excitation microscopy*. *Trends in Cell Biology*, 1999. **9**(2): p. 66-69.
313. Squier, J. and M. Muller, *High resolution nonlinear microscopy: A review of sources and methods for achieving optimal imaging*. *Review of Scientific Instruments*, 2001. **72**(7): p. 2855-2867.
314. Carriles, R., et al., *Invited Review Article: Imaging techniques for harmonic and multiphoton absorption fluorescence microscopy*. *The Review of Scientific Instruments*, 2009. **80**(8): p. 081101.
315. Denk, W. and K. Svoboda, *Photon Upmanship: Why Multiphoton Imaging Is More than a Gimmick*. *Neuron*, 1997. **18**(3): p. 351-357.
316. Xu, C., et al., *Determination of absolute two-photon excitation cross sections by in situ second-order autocorrelation*. *Optics Letters*, 1995. **20**(23): p. 2372-2374.
317. Huang, S., A.A. Heikal, and W.W. Webb, *Two-Photon Fluorescence Spectroscopy and Microscopy of NAD(P)H and Flavoprotein*. *Biophysical Journal*, 2002. **82**(5): p. 2811-2825.
318. Gattermann, H. and M. Stockburger, *Two-photon and multi-photon excitation of naphthalene in the vapor phase, studied by excitation and fluorescence spectra*. *Chemical Physics*, 1977. **24**(3): p. 327-332.
319. Xu, C., et al., *Multiphoton fluorescence excitation: new spectral windows for biological nonlinear microscopy*. *Proceedings of the National Academy of Sciences*, 1996. **93**(20): p. 10763-10768.
320. Mertz, J., *Nonlinear microscopy: new techniques and applications*. *Current Opinion in Neurobiology*, 2004. **14**(5): p. 610-616.
321. Schermelleh, L., R. Heintzmann, and H. Leonhardt, *A guide to super-resolution fluorescence microscopy*. *The Journal of Cell Biology*, 2010. **190**(2): p. 165-175.
322. Oheim, M., et al., *Principles of two-photon excitation fluorescence microscopy and other nonlinear imaging approaches*. *Advanced Drug Delivery Reviews*, 2006. **58**(7): p. 788-808.
323. Diaspro, A., G. Chirico, and M. Collini, *Two-photon fluorescence excitation and related techniques in biological microscopy*. *Quarterly Reviews of Biophysics*, 2005. **38**(2): p. 97-166.
324. Yuste, R., *Fluorescence microscopy today*. *Nat Meth*, 2005. **2**(12): p. 902-904.
325. Xu, C. and F.W. Wise, *Recent advances in fibre lasers for nonlinear microscopy*. *Nat Photon*, 2013. **7**(11): p. 875-882.
326. Squirrell, J.M., et al., *Long-term two-photon fluorescence imaging of mammalian embryos without compromising viability*. *Nat Biotech*, 1999. **17**(8): p. 763-767.
327. Williams, R.M., et al., *Strategies for High Resolution Imaging of Epithelial Ovarian Cancer by Laparoscopic Nonlinear Microscopy*. *Translational Oncology*, 2010. **3**(3): p. 181-194.
328. Theer, P., M.T. Hasan, and W. Denk, *Two-photon imaging to a depth of 1000 μm in living brains by use of a Ti:Al₂O₃ regenerative amplifier*. *Optics Letters*, 2003. **28**(12): p. 1022-1024.
329. Imanishi, Y., K. Lodowski, and Y. Koutalos, *Two-photon microscopy: shedding light on the chemistry of vision*. *Biochemistry*, 2007. **46**(34): p. 9674-9684.

330. Ashworth, S.L., et al., *Two-photon microscopy: Visualization of kidney dynamics*. Kidney International, 2007. **72**(4): p. 416-421.
331. Lim, J.S., *Two-dimensional signal and image processing*. Prentice Hall signal processing series. 1990, Englewood Cliffs, N.J.: Prentice Hall. xvi, 694 p.
332. Tomasi, C. and R. Manduchi, *Bilateral filtering for gray and color images*. In: Proc. of International Conference on Computer Vision, IEEE, 1998: p. 839–846.
333. Bishop, C., *Pattern recognition and machine learning (information science and statistics)*. 1 ed. 2006, New York Springer.
334. Borglin, J., et al., *Insights on proximity effect and multiphoton induced luminescence from gold nanospheres in far field optical microscopy*. Applied Physics Letters, 2015. **107**(23): p. 234101.
335. Han, F., et al., *Size-Dependent Two-Photon Excitation Photoluminescence Enhancement in Coupled Noble-Metal Nanoparticles*. ACS Applied Materials & Interfaces, 2012. **4**(9): p. 4746-4751.
336. Chen, Z., et al., *Two-photon-induced fluorescence from the phycoerythrin protein*. Applied Optics, 1997. **36**(7): p. 1655-1659.
337. Lakowicz, J.R., et al., *Fluorescence anisotropy of tyrosine using one-and two-photon excitation*. Biophysical Chemistry, 1995. **56**(3): p. 263-271.
338. Lakowicz, J.R. and I. Gryczynski, *Tryptophan fluorescence intensity and anisotropy decays of human serum albumin resulting from one-photon and two-photon excitation*. Biophysical Chemistry, 1992. **45**(1): p. 1-6.
339. Shear, J.B., C. Xu, and W.W. Webb, *Multiphoton-Excited Visible Emission by Serotonin Solutions*. Photochemistry and Photobiology, 1997. **65**(6): p. 931-936.
340. Kierdaszuk, B., et al., *Fluorescence of reduced nicotinamides using one- and two-photon excitation*. Biophysical Chemistry, 1996. **62**(1): p. 1-13.
341. Potter, S.M., et al., *Intravital imaging of green fluorescent protein using two-photon laser-scanning microscopy*. Gene, 1996. **173**(1 Spec No): p. 25-31.
342. Sumalekshmy, S. and C.J. Fahrni, *Metal-Ion-Responsive Fluorescent Probes for Two-Photon Excitation Microscopy*. Chemistry of Materials, 2011. **23**(3): p. 483-500.
343. Yao, S. and K.D. Belfield, *Two-Photon Fluorescent Probes for Bioimaging*. European Journal of Organic Chemistry, 2012. **2012**(17): p. 3199-3217.
344. So, P.T.C., et al., *Two-Photon Excitation Fluorescence Microscopy*. Annual Review of Biomedical Engineering, 2000. **2**(1): p. 399-429.
345. Pawlicki, M., et al., *Two-Photon Absorption and the Design of Two-Photon Dyes*. Angewandte Chemie International Edition, 2009. **48**(18): p. 3244-3266.
346. Schafer-Hales, K.J., et al., *Fluorene-based fluorescent probes with high two-photon action cross-sections for biological multiphoton imaging applications*. Journal of Biomedical Optics, 2005. **10**(5): p. 051402.
347. Li, J.-L., et al., *Graphene Oxide Nanoparticles as a Nonbleaching Optical Probe for Two-Photon Luminescence Imaging and Cell Therapy*. Angewandte Chemie International Edition, 2012. **51**(8): p. 1830-1834.
348. Dong, N.-N., et al., *NIR-to-NIR Two-Photon Excited CaF₂:Tm³⁺, Yb³⁺ Nanoparticles: Multifunctional Nanoprobes for Highly Penetrating Fluorescence Bio-Imaging*. ACS Nano, 2011. **5**(11): p. 8665-8671.
349. Cao, L., et al., *Carbon Dots for Multiphoton Bioimaging*. Journal of the American Chemical Society, 2007. **129**(37): p. 11318-11319.
350. Yong, K.-T., et al., *Quantum Rod Bioconjugates as Targeted Probes for Confocal and Two-Photon Fluorescence Imaging of Cancer Cells*. Nano Letters, 2007. **7**(3): p. 761-765.
351. Zhang, X., et al., *Single-Layered Graphitic-C₃N₄ Quantum Dots for Two-Photon Fluorescence Imaging of Cellular Nucleus*. Advanced Materials, 2014. **26**(26): p. 4438-4443.

352. Aiboushev, A.V., et al., *Enhanced luminescence and two-photon absorption of silver nano-clusters*. *physica status solidi (c)*, 2009. **6**(S1): p. S162-S166.
353. Ramakrishna, G., et al., *Quantum-Sized Gold Clusters as Efficient Two-Photon Absorbers*. *Journal of the American Chemical Society*, 2008. **130**(15): p. 5032-5033.
354. Biagioni, P., et al., *Dependence of the two-photon photoluminescence yield of gold nanostructures on the laser pulse duration*. *Physical Review B*, 2009. **80**(4): p. 045411.
355. Beversluis, M.R., A. Bouhelier, and L. Novotny, *Continuum generation from single gold nanostructures through near-field mediated intraband transitions*. *Physical Review B*, 2003. **68**(11): p. 115433.
356. Cobley, C.M., et al., *Gold nanostructures: a class of multifunctional materials for biomedical applications*. *Chemical Society Reviews*, 2011. **40**(1): p. 44-56.
357. Wang, H., et al., *In vitro and in vivo two-photon luminescence imaging of single gold nanorods*. *Proceedings of the National Academy of Sciences of the United States of America*, 2005. **102**(44): p. 15752-15756.
358. Kim, H., et al., *Tunable Two-Photon Excited Luminescence in Single Gold Nanowires Fabricated by Lithographically Patterned Nanowire Electrodeposition*. *The Journal of Physical Chemistry C*, 2008. **112**(33): p. 12721-12727.
359. Gao, N., et al., *Shape-Dependent Two-Photon Photoluminescence of Single Gold Nanoparticles*. *The Journal of Physical Chemistry C*, 2014. **118**(25): p. 13904-13911.
360. Borglin, J., et al., *Peptide Functionalized Gold Nanoparticles as a Stimuli Responsive Contrast Medium in Multiphoton Microscopy*. *Nano Letters*, 2017. **17**(3): p. 2102-2108.
361. Hohenau, A., et al., *Spectroscopy and nonlinear microscopy of Au nanoparticle arrays: Experiment and theory*. *Physical Review B*, 2006. **73**(15): p. 155404.
362. Guan, Z., et al., *Huge Enhancement in Two-Photon Photoluminescence of Au Nanoparticle Clusters Revealed by Single-Particle Spectroscopy*. *Journal of the American Chemical Society*, 2013. **135**(19): p. 7272-7277.
363. Garai, M., et al., *Single Particle Studies on Two-Photon Photoluminescence of Gold Nanorod–Nanosphere Heterodimers*. *The Journal of Physical Chemistry C*, 2016. **120**(21): p. 11621-11630.
364. Yuan, P., et al., *Tuning Two-Photon Photoluminescence of Gold Nanoparticle Aggregates with DNA and Its Application as Turn-on Photoluminescence Probe for DNA Sequence Detection*. *ACS Applied Materials & Interfaces*, 2014. **6**(15): p. 13149-13156.
365. Sun, C.-K., et al., *Higher harmonic generation microscopy for developmental biology*. *Journal of Structural Biology*, 2004. **147**(1): p. 19-30.
366. Zipfel, W.R., R.M. Williams, and W.W. Webb, *Nonlinear magic: multiphoton microscopy in the biosciences*. *Nat Biotech*, 2003. **21**(11): p. 1369-1377.

8 APPENDICES

8.1 Appendix A: DLS histograms of phage/AuNP reaction solutions at different ionic strengths

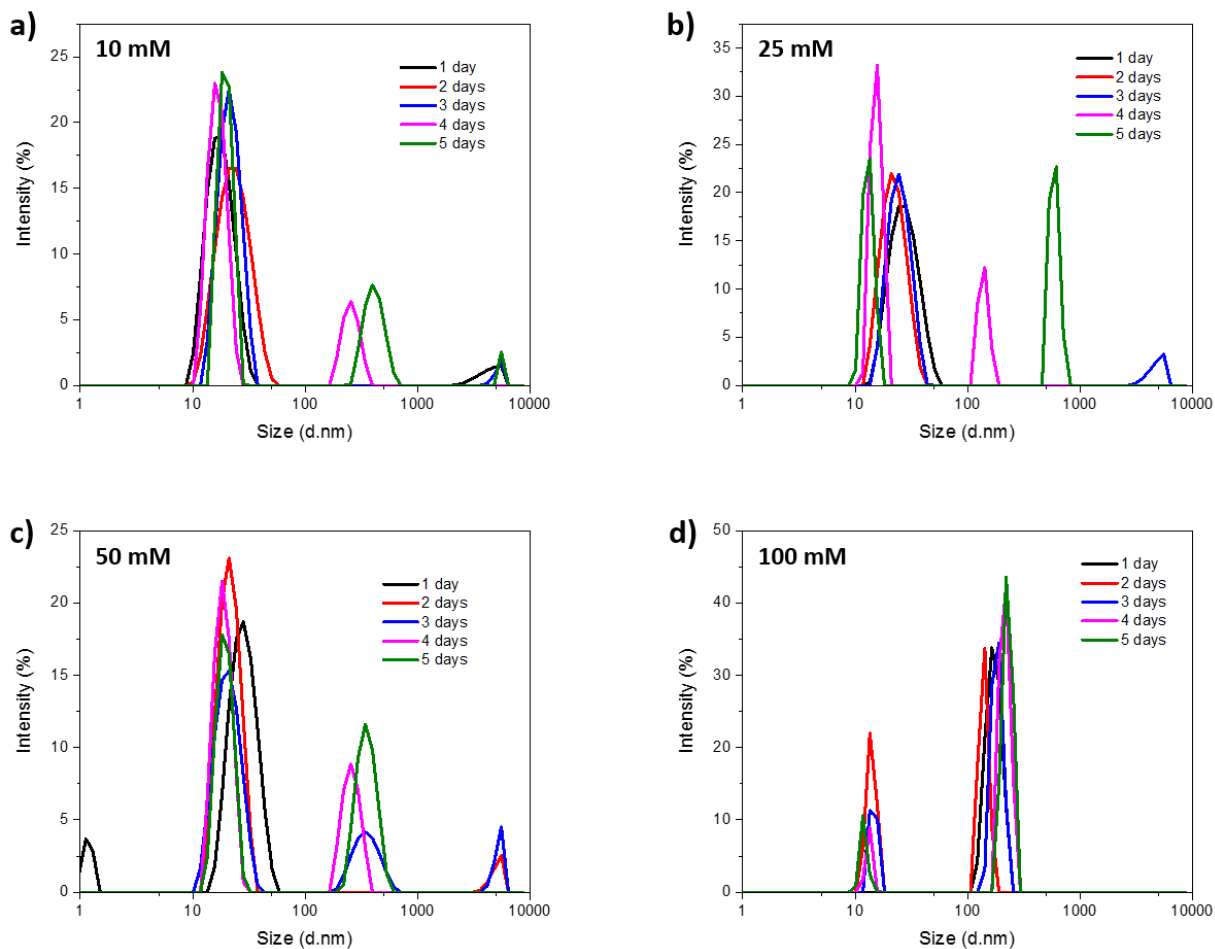


Figure A1. Stability of 9 nm AuNPs in various phosphate buffers. DLS histograms for intensity based size analysis of 9 nm AuNP solutions in phosphate buffers with a) 10 mM, b) 25 mM, c) 50 mM, and d) 100 mM ionic strengths. DLS histograms of each sample solution were recorded for a 5 day period.

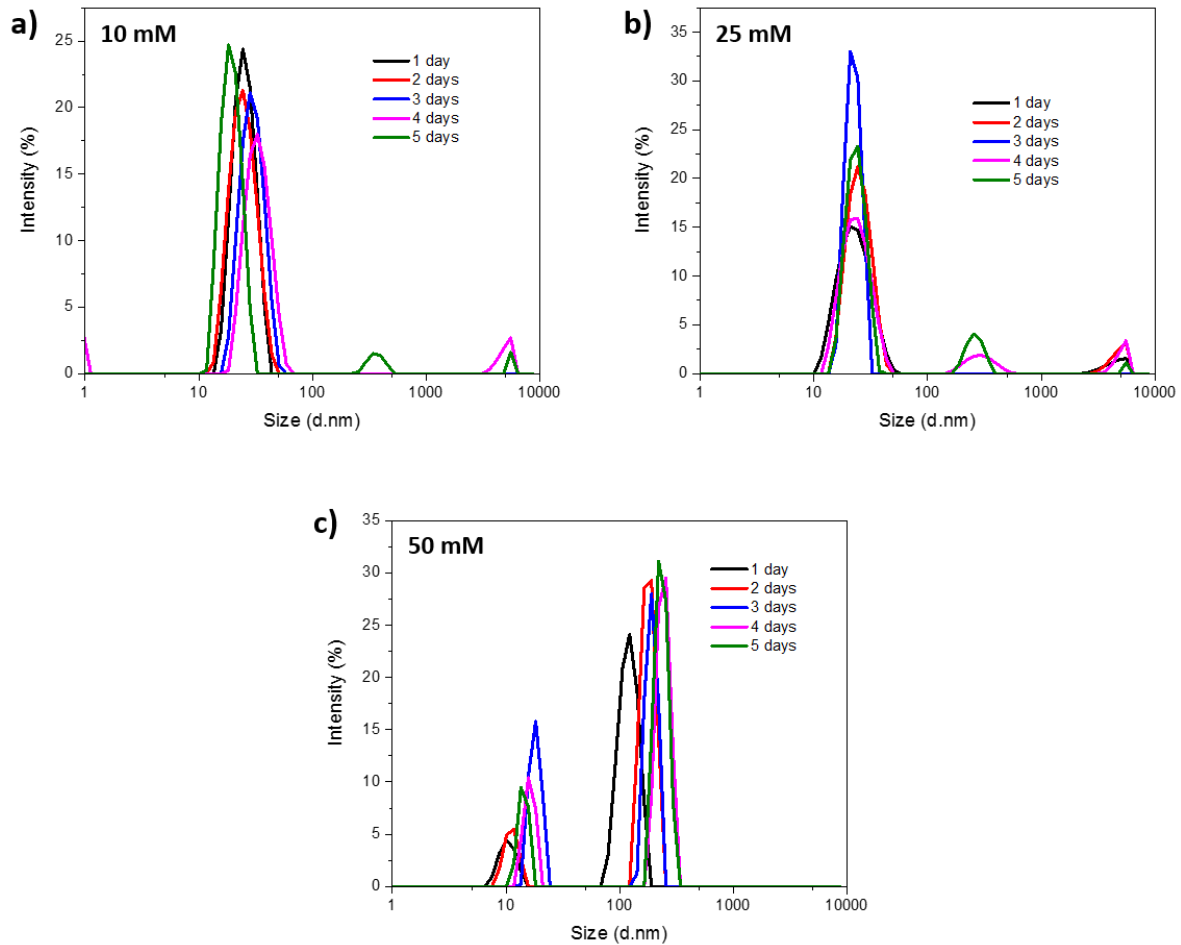


Figure A2. Stability of 13 nm AuNPs in various phosphate buffers. DLS histograms for intensity based size analysis of 13 nm AuNP solutions in phosphate buffers with a) 10 mM, b) 25 mM, and c) 50 mM ionic strengths. DLS histograms of each sample solution were recorded for a 5 day period.

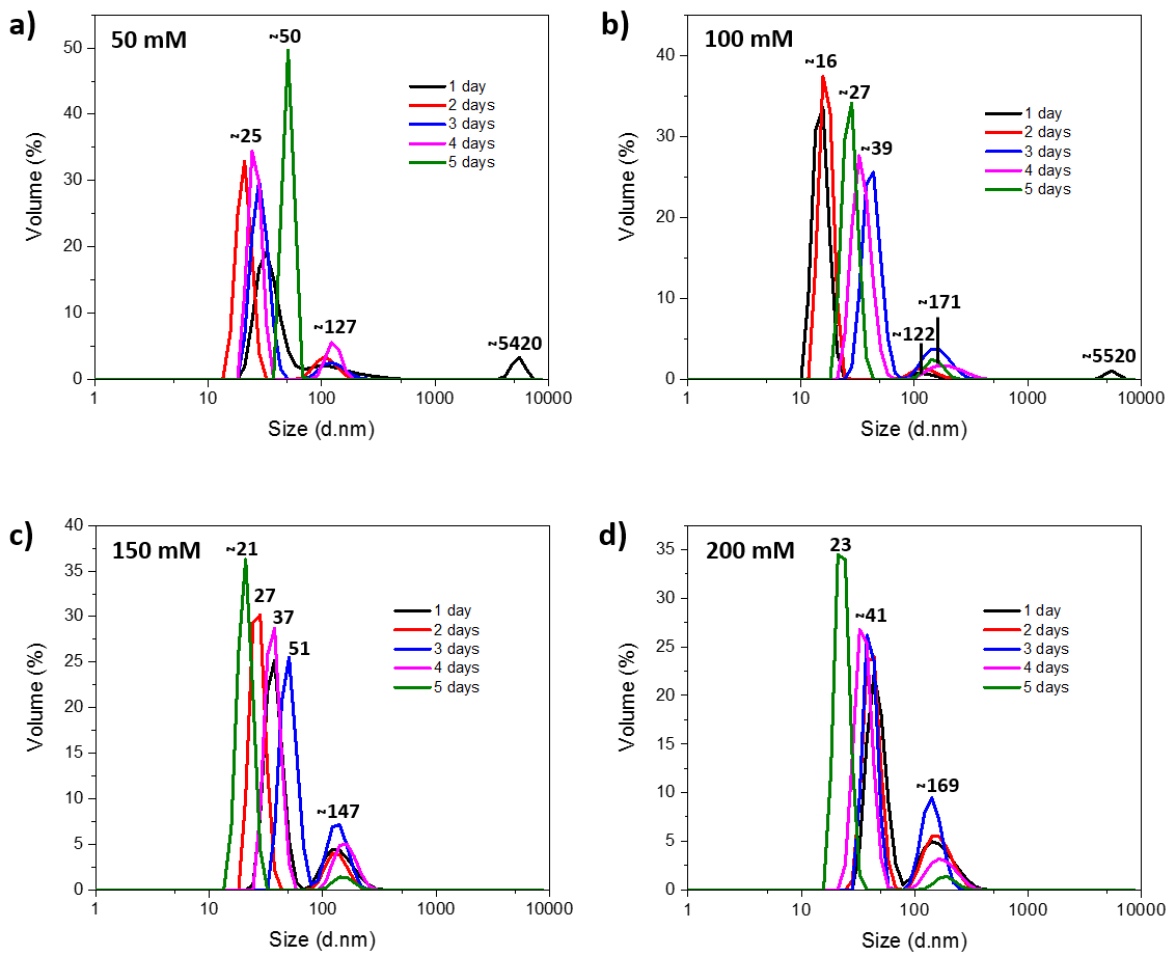


Figure A3. DLS histograms for volume based size analysis of Cys-C phage-3 nm AuNP solutions in phosphate buffers with a) 50 mM, b) 100 mM, c) 150 mM, and d) 200 mM ionic strengths. DLS histograms of each sample solution were recorded for a 5 day period.

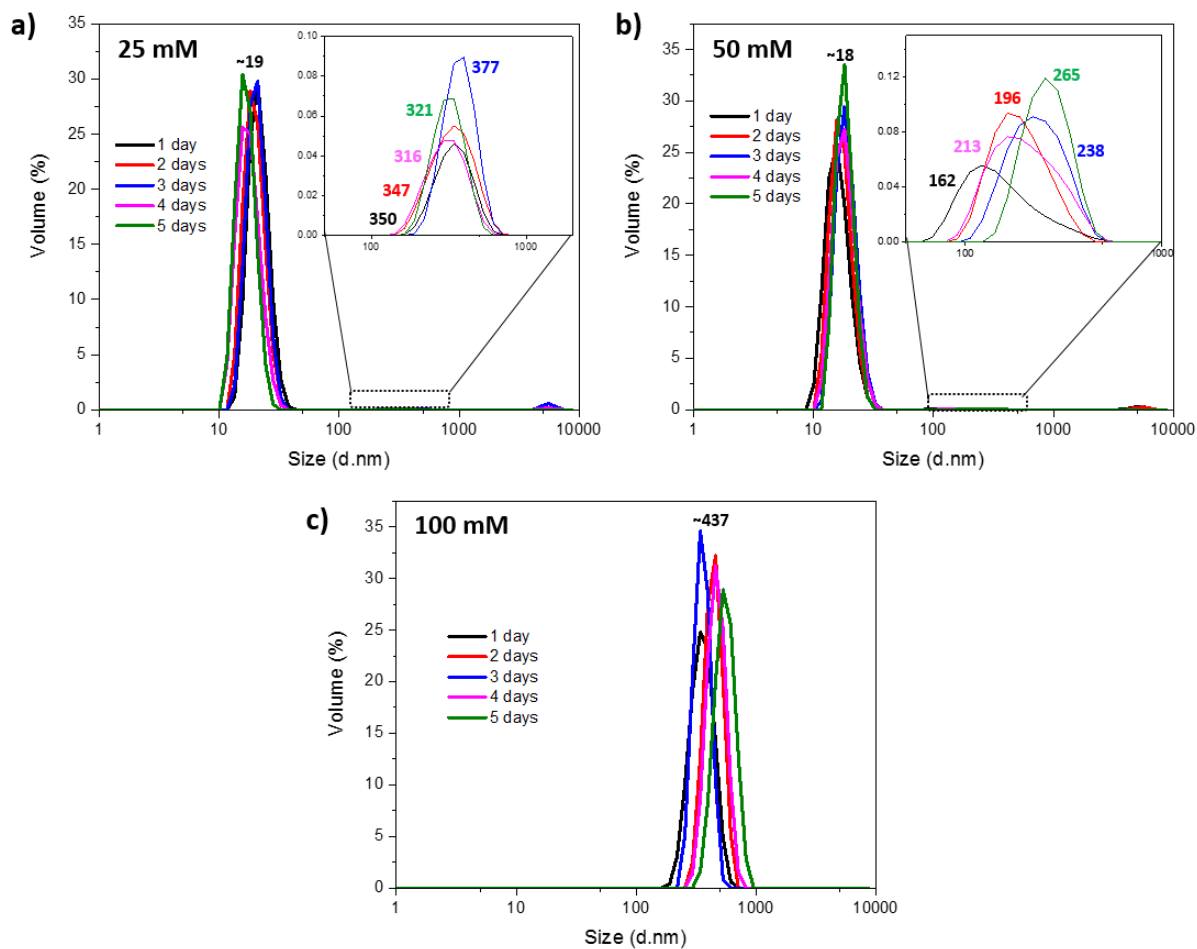


Figure A4. DLS histograms for volume based size analysis of Cys-C phage-9 nm AuNP solutions in phosphate buffers with a) 25 mM, b) 50 mM, and c) 100 mM ionic strengths. DLS histograms of each sample solution were recorded for a 5 day period.

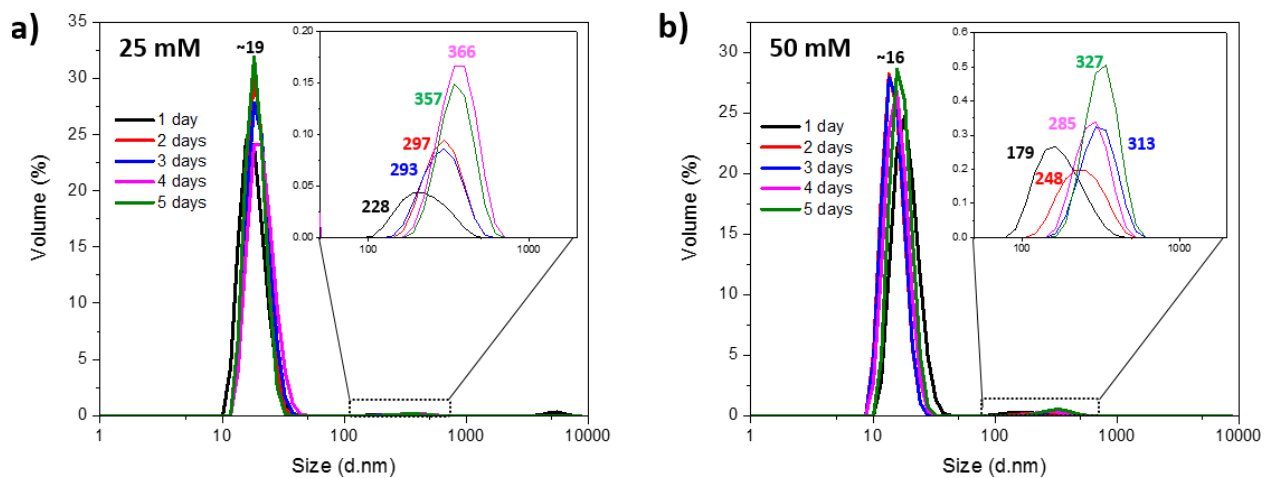


Figure A5. DLS histograms for volume based size analysis of Cys-C phage-13 nm AuNP solutions in phosphate buffers with a) 25 mM and b) 50 mM ionic strengths. DLS histograms of each sample solution were recorded for a 5 day period.

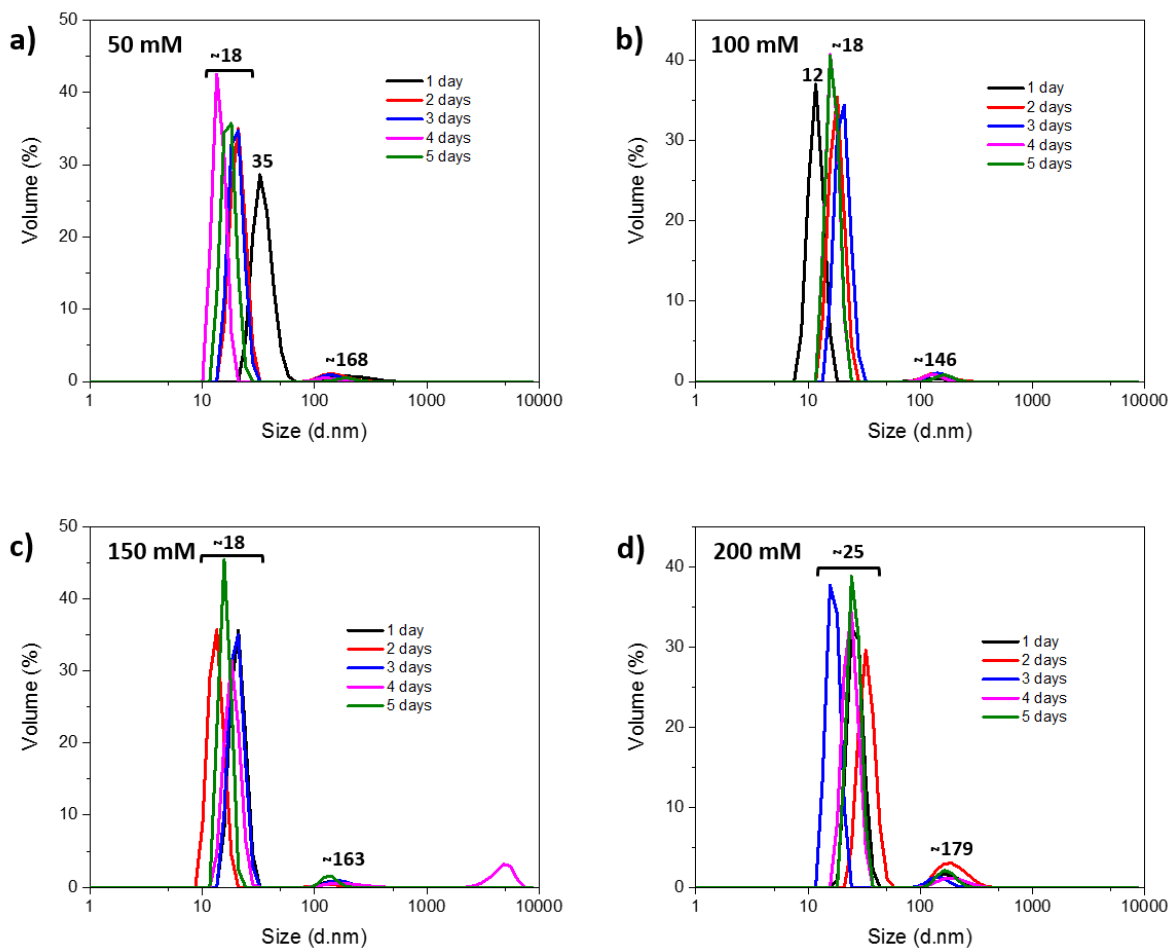


Figure A6. DLS histograms for volume based size analysis of A3-C phage-3 nm AuNP solutions in phosphate buffers with a) 50 mM, b) 100 mM, c) 150 mM, and d) 200 mM ionic strengths. DLS histograms of each sample solution were recorded for a 5 day period.

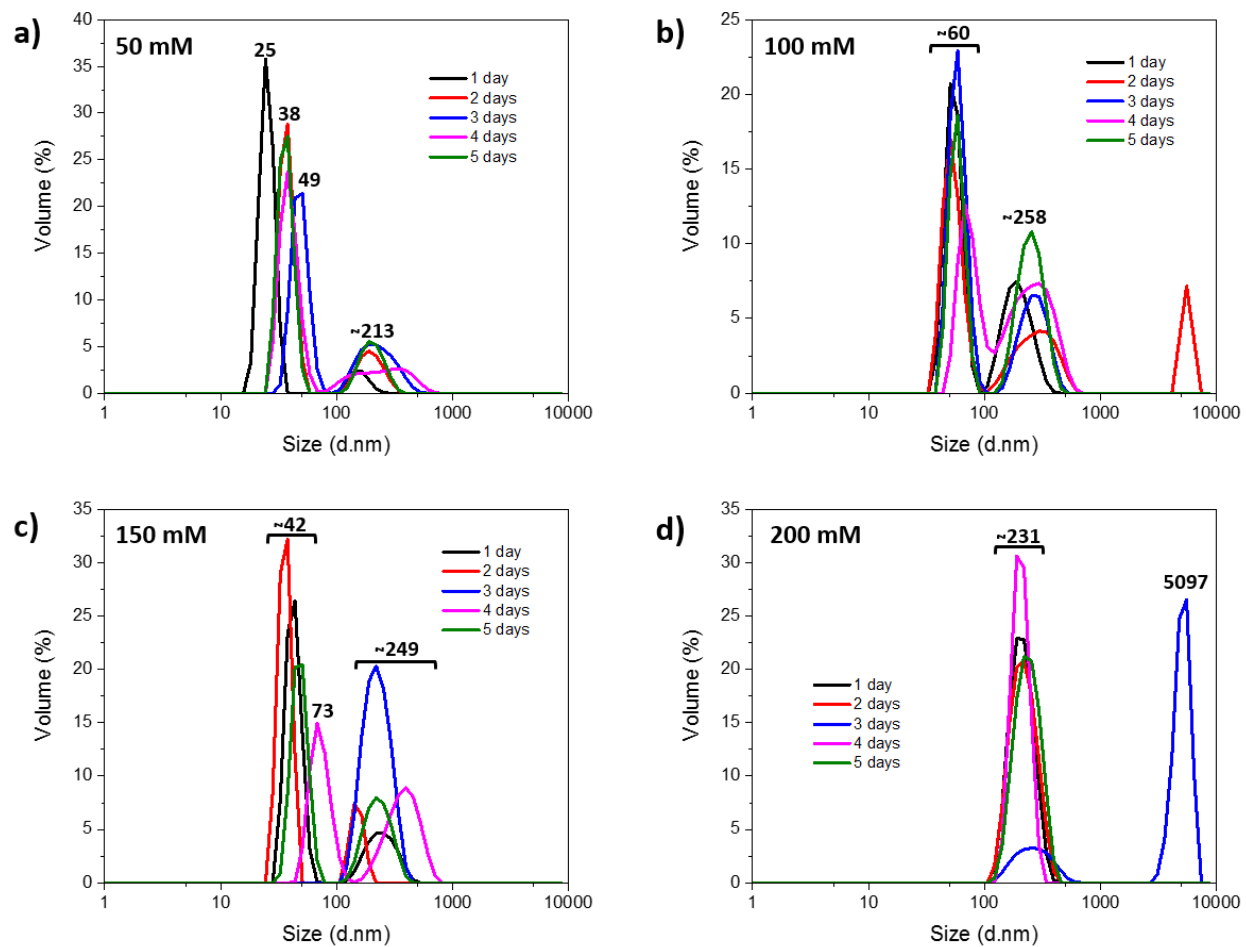


Figure A7. DLS histograms for volume based size analysis of A3-N phage-3 nm AuNP solutions in phosphate buffers with a) 50 mM, b) 100 mM, c) 150 mM, and d) 200 mM ionic strengths. DLS histograms of each sample solution were recorded for a 5 day period.

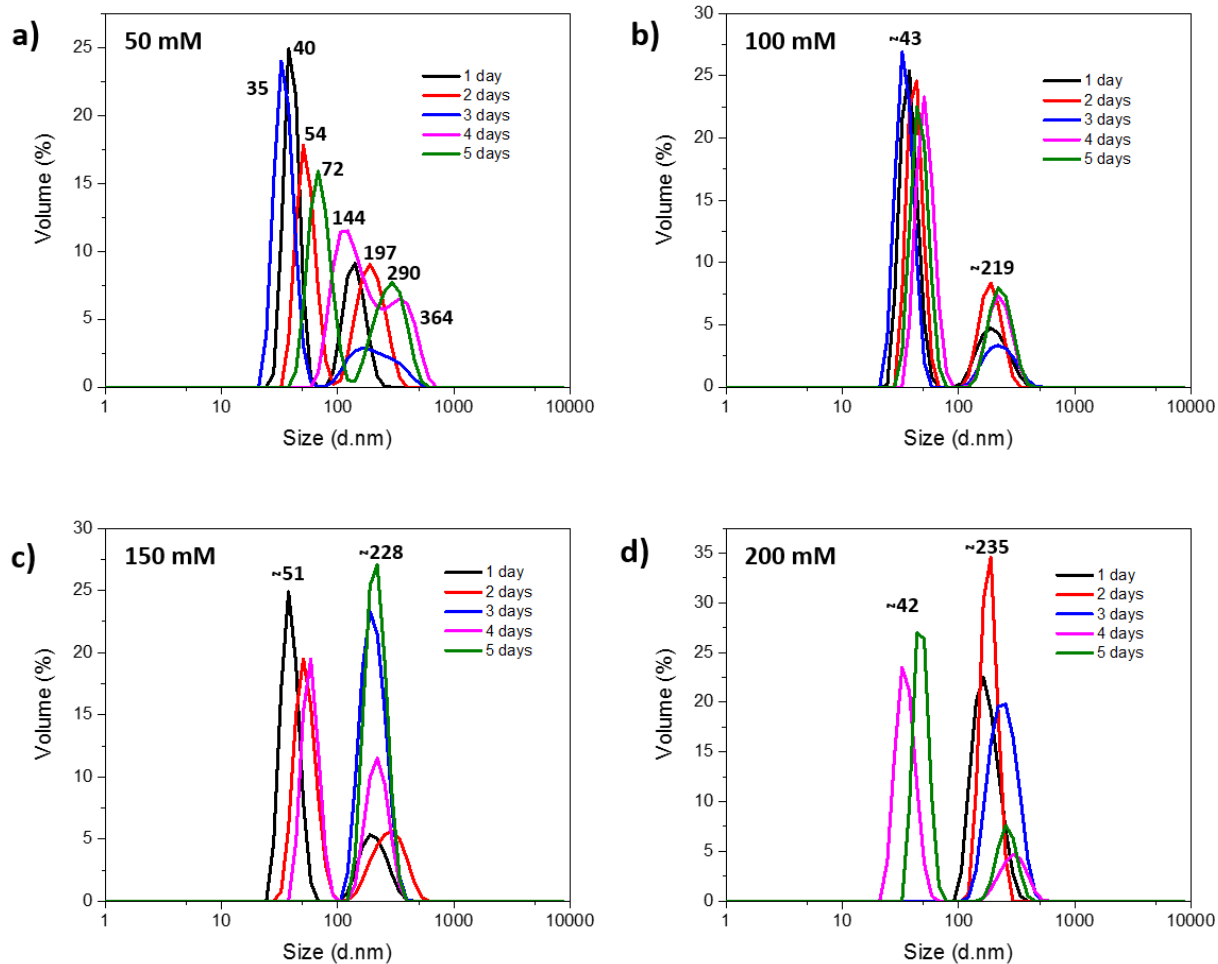


Figure A8. DLS histograms for volume based size analysis of GB-C phage-3 nm AuNP solutions in phosphate buffers with a) 50 mM, b) 100 mM, c) 150 mM, and d) 200 mM ionic strengths. DLS histograms of each sample solution were recorded for a 5 day period.

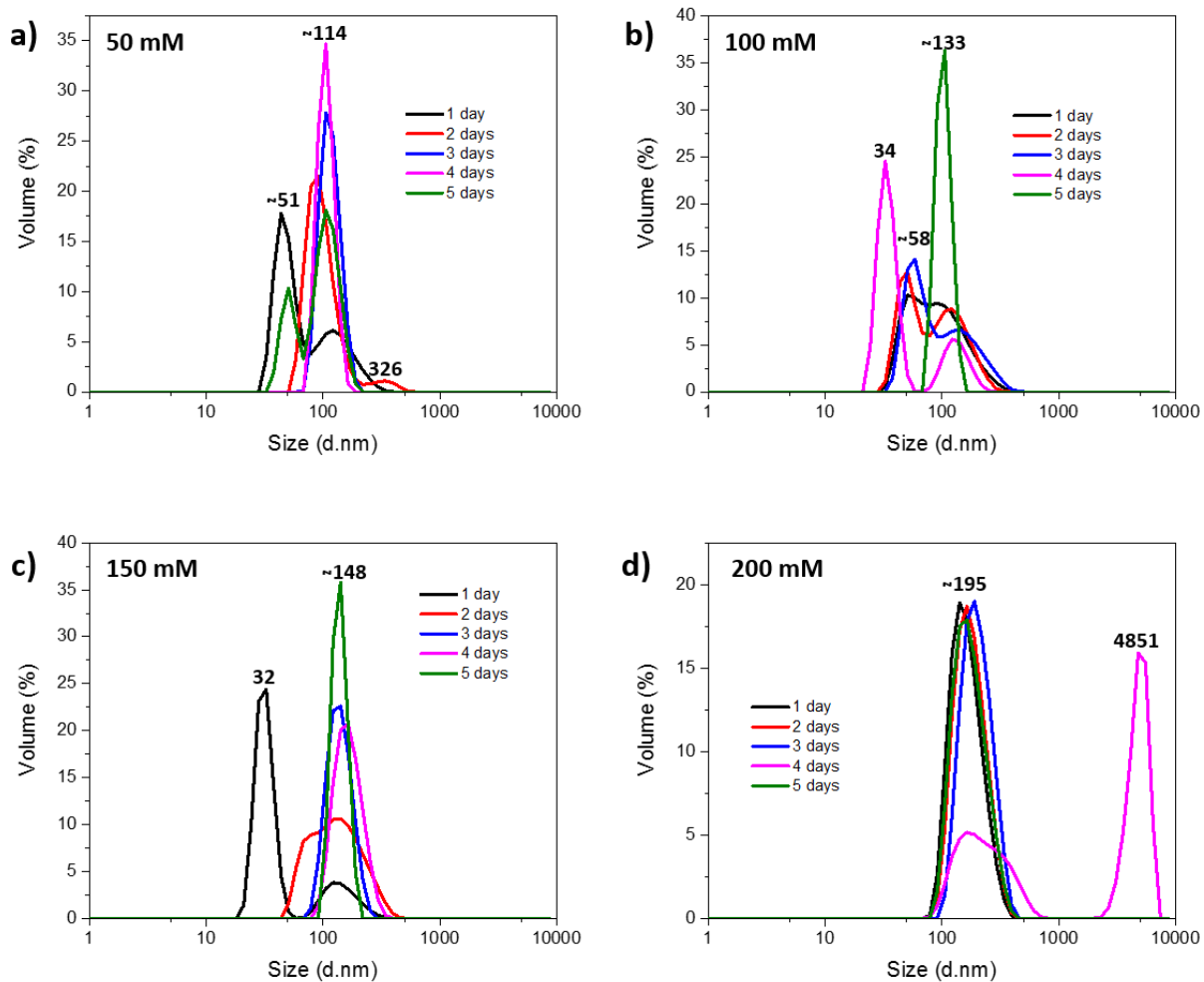


Figure A9. DLS histograms for volume based size analysis of GB-N phage-3 nm AuNP solutions in phosphate buffers with a) 50 mM, b) 100 mM, c) 150 mM, and d) 200 mM ionic strengths. DLS histograms of each sample solution were recorded for a 5 day period.

8.2 Appendix B: SERS maps of the samples analyzed in Chapter 4

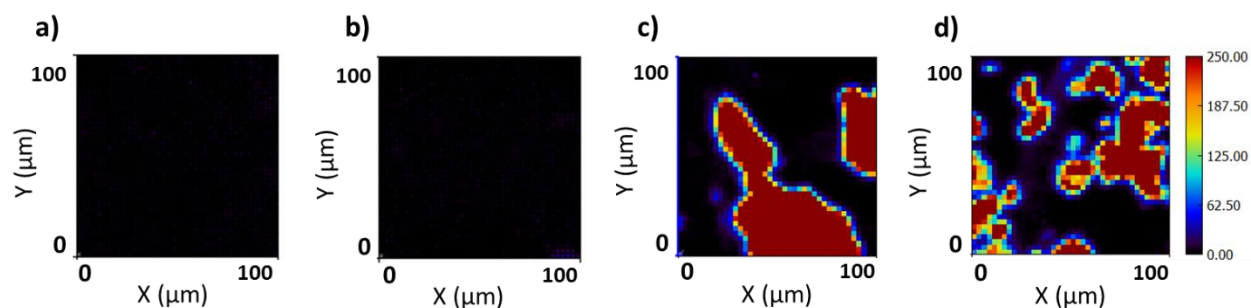


Figure B1. SERS maps constructed from the peak at 1085 cm⁻¹ for M13-templated AuNPs assemblies prepared from a) 3-nm, b) 9-nm, c) 13-nm AuNPs, and d) 13-nm AuNP assemblies incubated with *E. coli* cells.

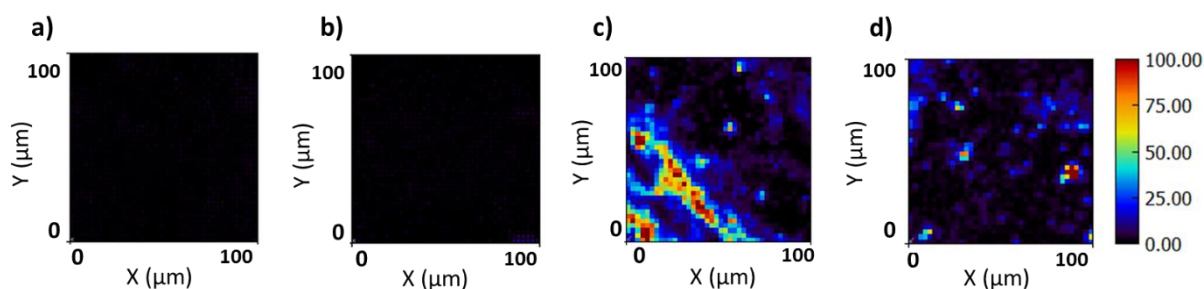


Figure B2. SERS maps constructed from the peak at 1085 cm⁻¹ for Cys-N-templated AuNPs assemblies prepared from a) 3-nm, b) 9-nm, c) 13-nm AuNPs, and d) 13-nm AuNP assemblies incubated with *E. coli* cells.

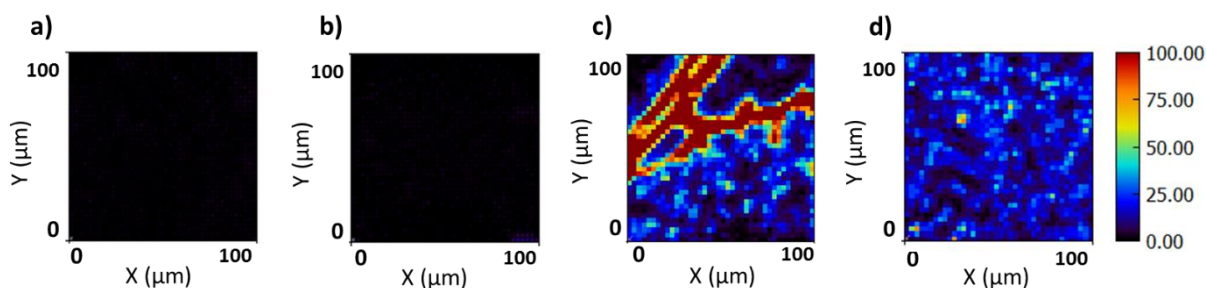


Figure B3. SERS maps constructed from the peak at 1085 cm⁻¹ for Cys-C-templated AuNPs assemblies prepared from a) 3-nm, b) 9-nm, c) 13-nm AuNPs, and d) 13-nm AuNP assemblies incubated with *E. coli* cells.

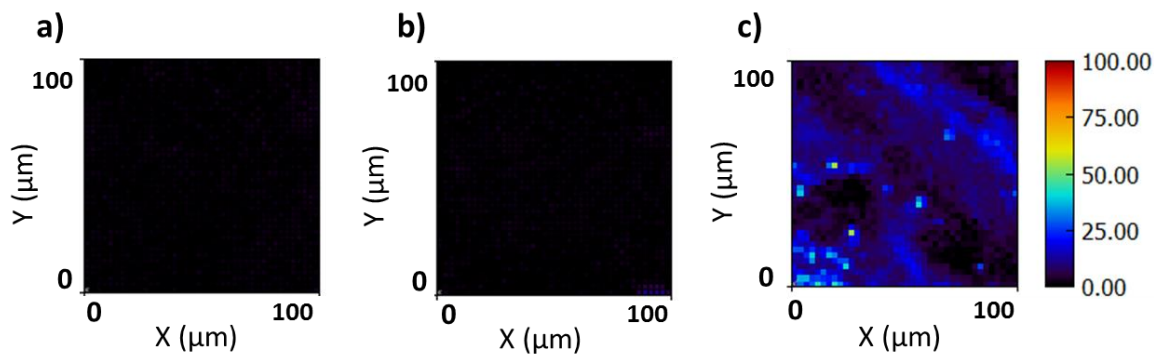


Figure B4. SERS maps constructed from the peak at 1085 cm^{-1} for A3-N-templated AuNPs assemblies prepared from a) 3-nm, b) 9-nm, and c) 13-nm AuNPs.

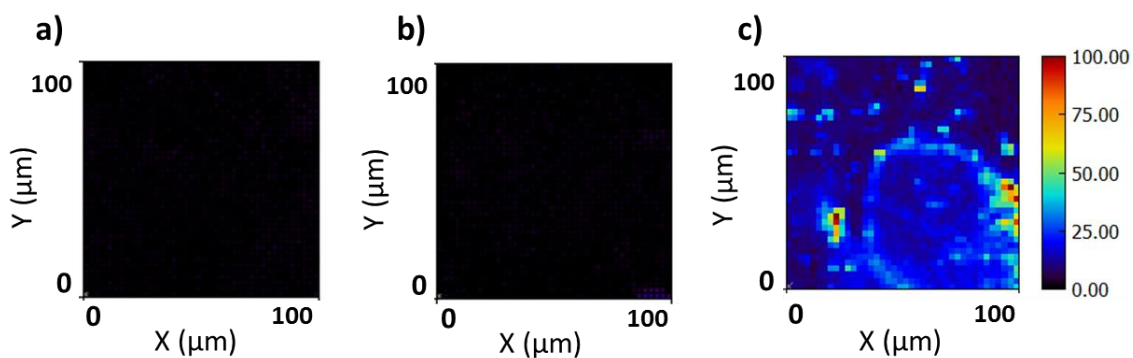


Figure B5. SERS maps constructed from the peak at 1085 cm^{-1} for A3-C-templated AuNPs assemblies prepared from a) 3-nm, b) 9-nm, and c) 13-nm AuNPs.

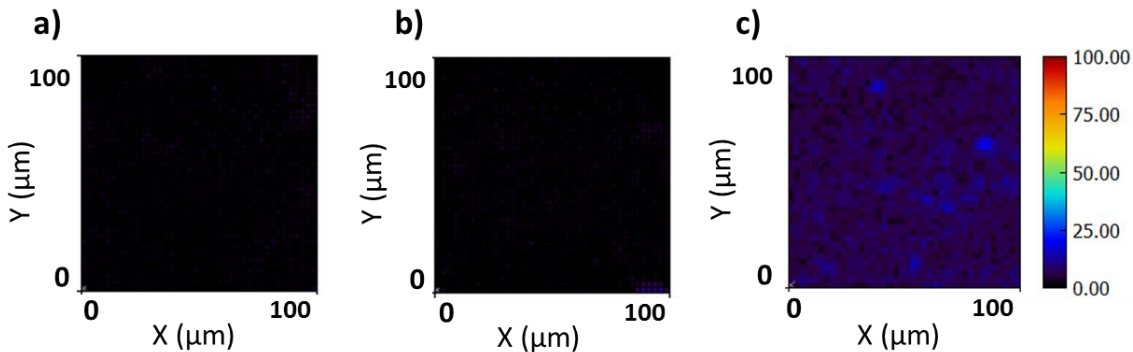


Figure B6. SERS maps constructed from the peak at 1085 cm^{-1} for GB-N-templated AuNPs assemblies prepared from a) 3-nm, b) 9-nm, and c) 13-nm AuNPs.

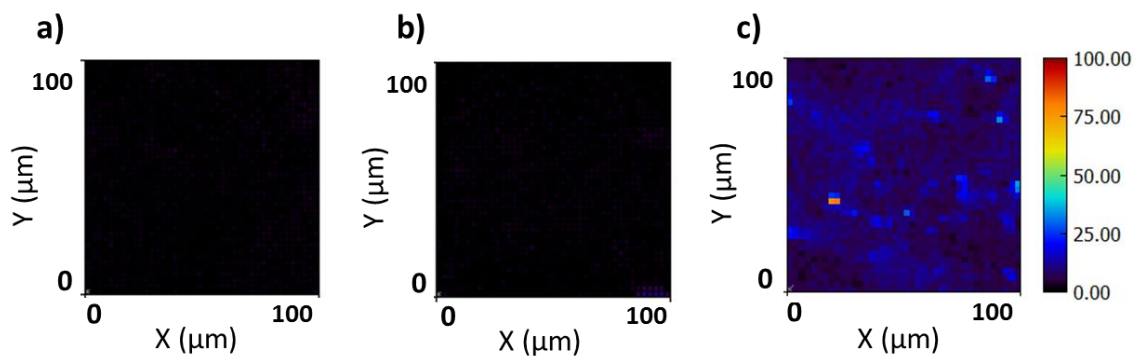


Figure B7. SERS maps constructed from the peak at 1085 cm^{-1} for GB-C-templated AuNPs assemblies prepared from a) 3-nm, b) 9-nm, and c) 13-nm AuNPs.

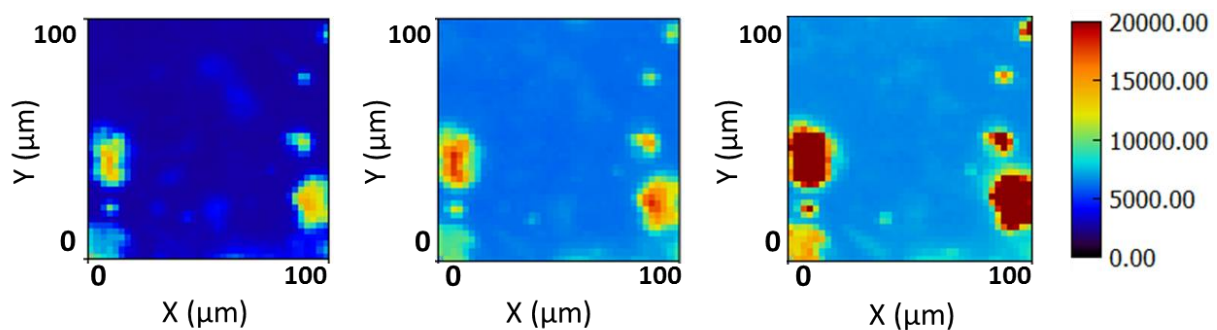


Figure B8. SERS maps constructed from the peak intensities around 1085 cm^{-1} of M13-templated AuNP assemblies prepared with 13 nm AuNPs. The maps were recorded at laser powers a) 1.75 mW, b) 3.17 mW, and c) 7.72 mW.

8.3 Appendix C. 2PEF images of the samples analyzed in Chapter 5

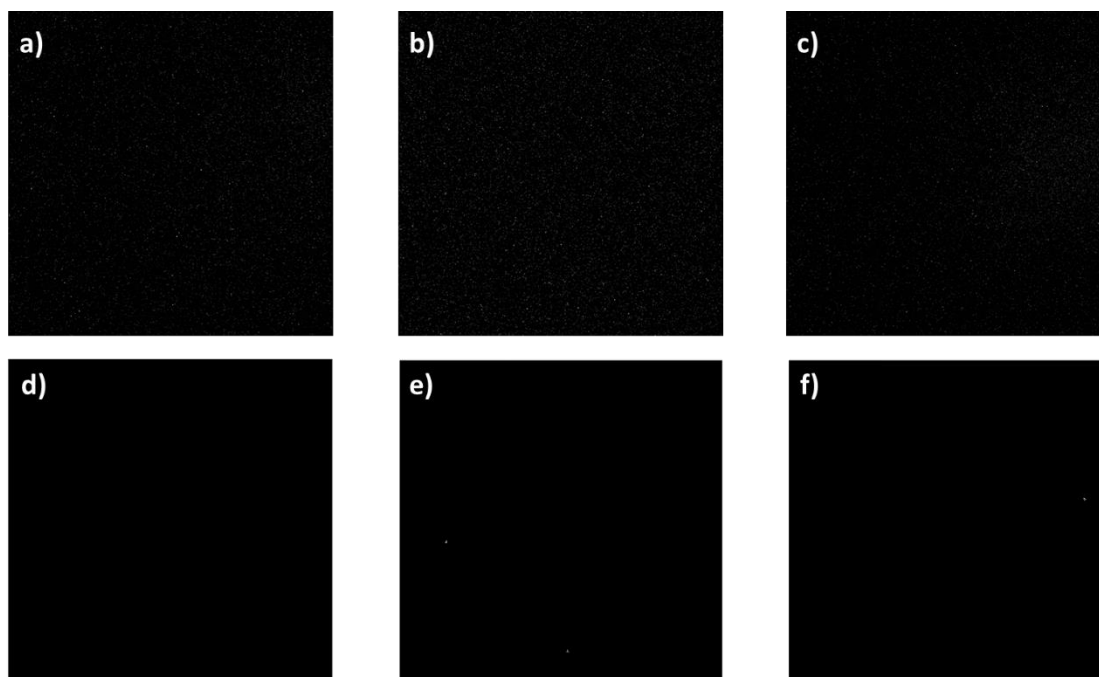


Figure C1. Original 2PEF images of AuNPs with size of a) 3-nm, b) 9-nm, and c) 13-nm. Processed 2PEF images of AuNPs with size of d) 3-nm, e) 9-nm, and f) 13-nm.

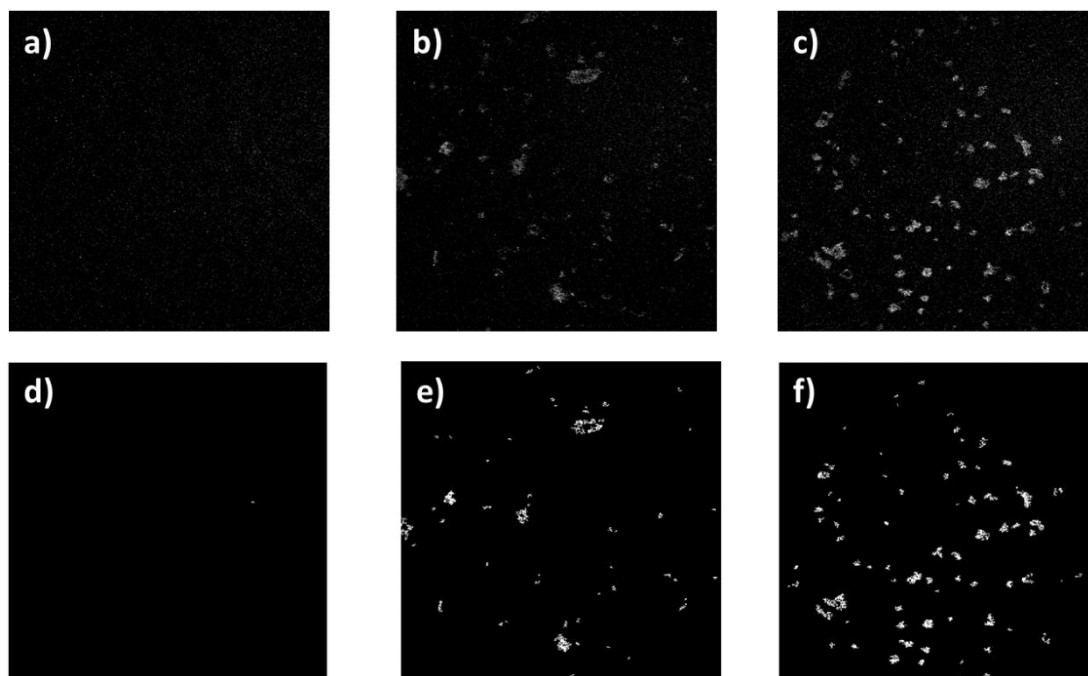


Figure C2. Original 2PEF images of M13-templated Au assemblies prepared with a) 3-nm, b) 9-nm, and c) 13-nm AuNPs. Processed 2PEF images of M13-templated Au assemblies prepared with d) 3-nm, e) 9-nm, and f) 13-nm AuNPs.

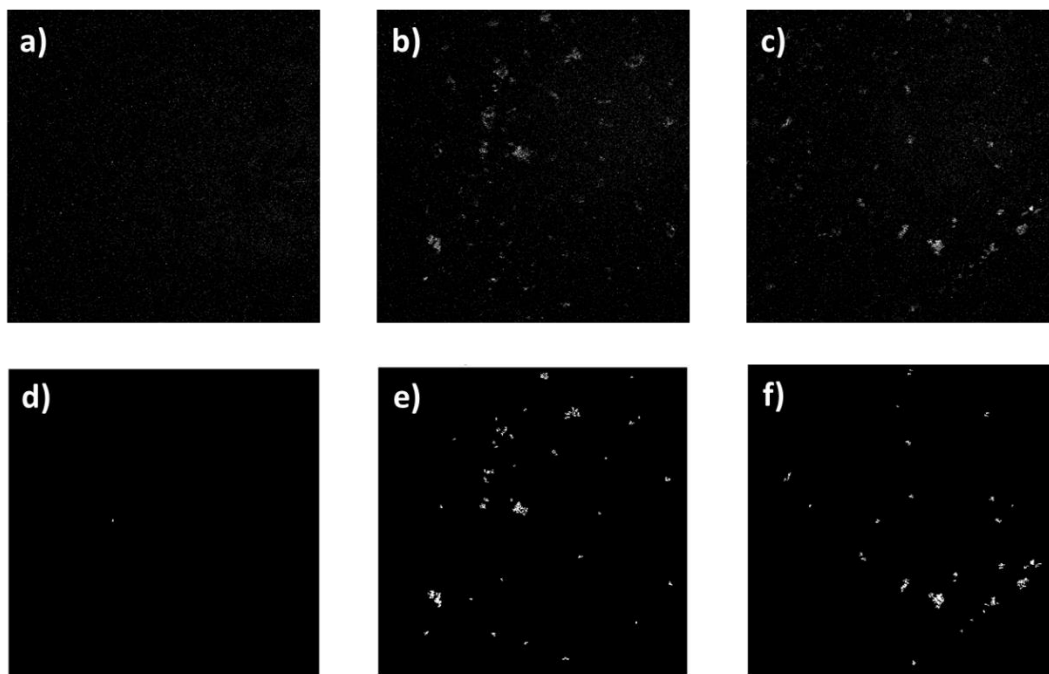


Figure C3. Original 2PEF images of *E.coli* cells incubated with M13-templated Au assemblies prepared with a) 3-nm, b) 9-nm, and c) 13-nm AuNPs. Processed 2PEF images of *E.coli* cells incubated with M13-templated Au assemblies prepared with d) 3-nm, e) 9-nm, and f) 13-nm AuNPs.

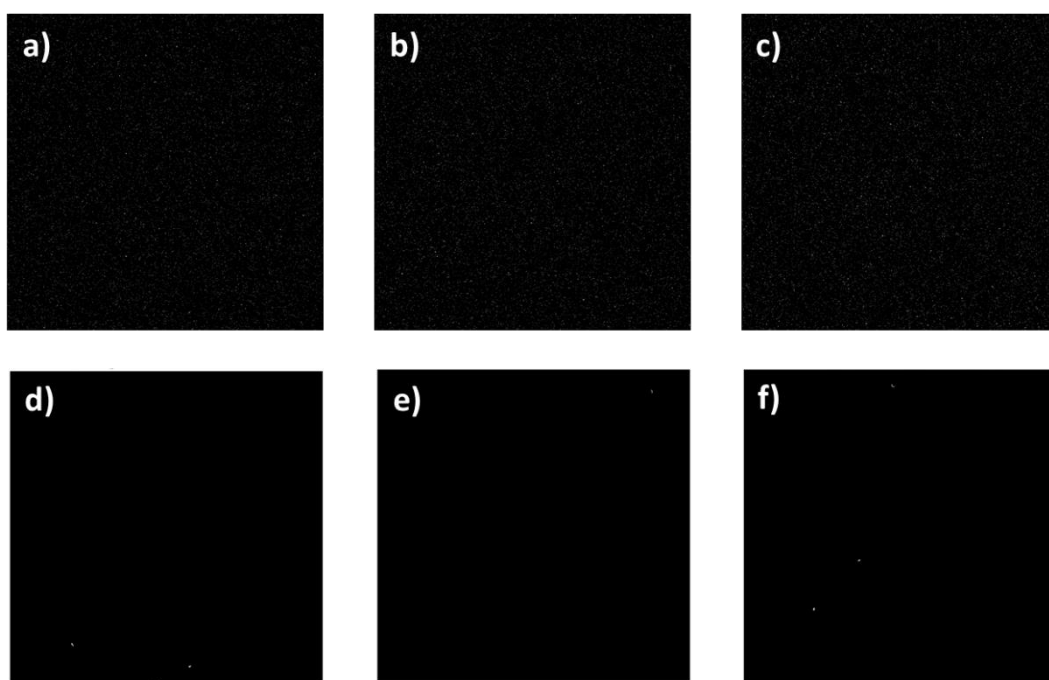


Figure C4. Original 2PEF images of Cys-N-templated Au assemblies prepared with a) 3-nm, b) 9-nm, and c) 13-nm AuNPs. Processed 2PEF images of Cys-N-templated Au assemblies prepared with d) 3-nm, e) 9-nm, and f) 13-nm AuNPs.

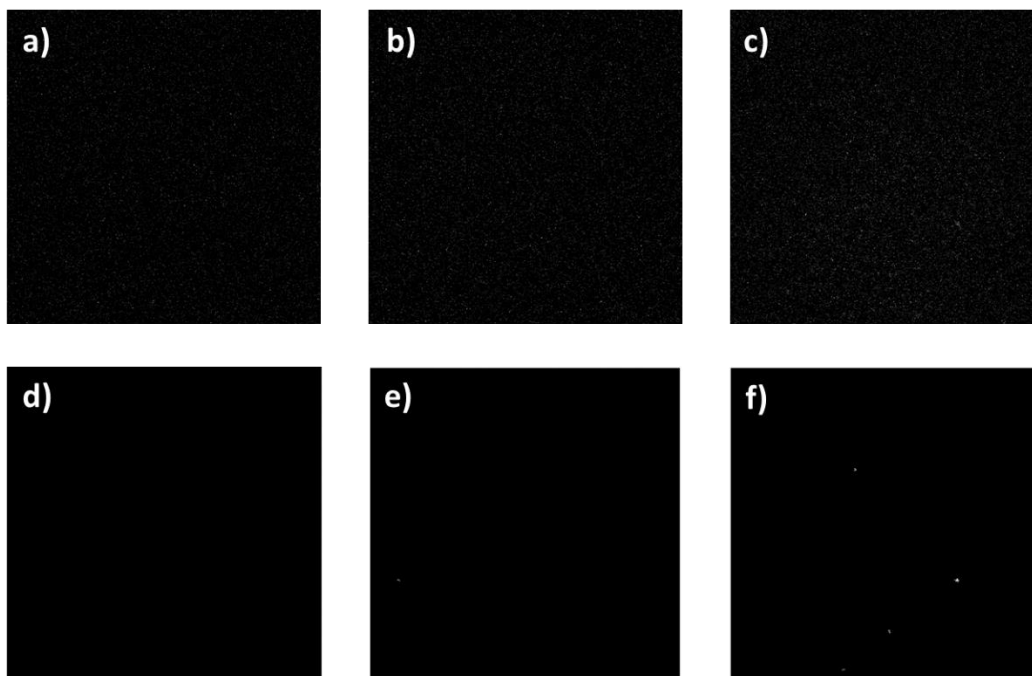


Figure C5. Original 2PEF images of *E.coli* cells incubated with Cys-N-templated Au assemblies prepared with a) 3-nm, b) 9-nm, and c) 13-nm AuNPs. Processed 2PEF images of *E.coli* cells incubated with Cys-N-templated Au assemblies prepared with d) 3-nm, e) 9-nm, and f) 13-nm AuNPs.

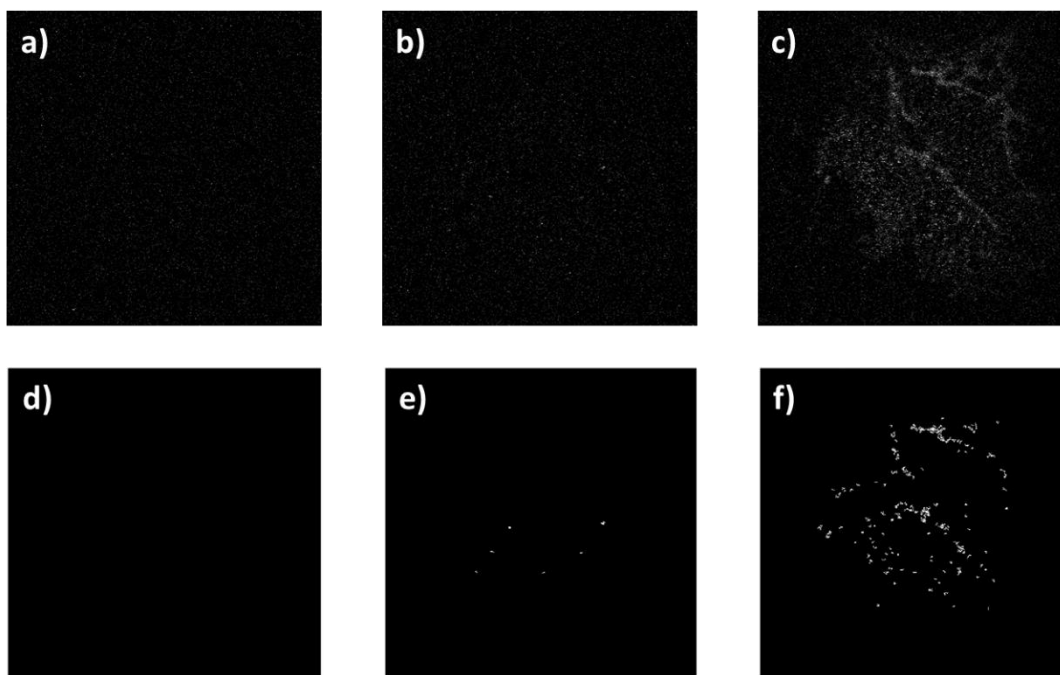


Figure C6. Original 2PEF images of Cys-C-templated Au assemblies prepared with a) 3-nm, b) 9-nm, and c) 13-nm AuNPs. Processed 2PEF images of Cys-C-templated Au assemblies prepared with d) 3-nm, e) 9-nm, and f) 13-nm AuNPs.

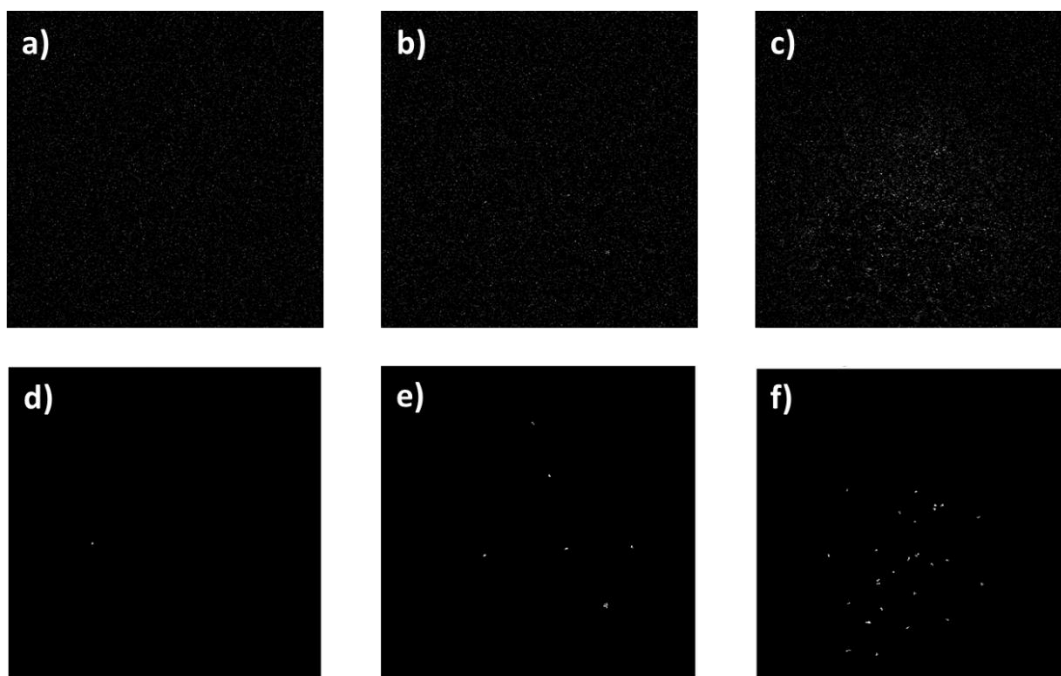


Figure C7. Original 2PEF images of *E.coli* cells incubated with Cys-C-templated Au assemblies prepared with a) 3-nm, b) 9-nm, and c) 13-nm AuNPs. Processed 2PEF images of *E.coli* cells incubated with Cys-C-templated Au assemblies prepared with d) 3-nm, e) 9-nm, and f) 13-nm AuNPs.